Sindre Bunkholt

Subgrain Growth, Recovery Kinetics and Nucleation of Recrystallization of Cold Deformed Aluminium Alloys

Thesis for the degree of Philosophiae Doctor

Trondheim, November 2013

Norwegian University of Science and Technology
Faculty of Natural Sciences and Technology
Department of Materials Science and Engineering

NTNU – Trondheim
Norwegian University of
Science and Technology

NTNU
Norwegian University of Science and Technology

Thesis for the degree of Philosophiae Doctor

Faculty of Natural Sciences and Technology
Department of Materials Science and Engineering

ISBN 978-82-471-4799-3 (printed ver.)
ISBN 978-82-471-4800-6 (electronic ver.)
ISSN 1503-8181

Doctoral theses at NTNU, 2013:330

IMT-Report 2013:192

Printed by NTNU-trykk

Preface

This thesis is submitted in partial fulfilment of the requirements for the degree of philosophiae doctor at the Norwegian University of Science and Technology (NTNU). This doctoral work has been performed at the Department of Materials Science and Engineering, NTNU, from August 2010 to September 2013. Professor Knut Marthinsen was the main supervisor and shared responsibility with co-supervisor Professor Emeritus Erik Nes. The doctoral work was financed through a Strategic Area Materials research fellowship granted by the Faculty of Natural Sciences and Technology, NTNU.

Parts of this doctoral work has been presented at and published in the proceedings of the following conferences:

- European Conference on Aluminium Alloys, 2011, Bremen
- 13$^{\text{th}}$ International Conference on Aluminum Alloys, 2012, Pittsburgh
- 5$^{\text{th}}$ International Conference on Recrystallization & Grain Growth, 2013, Sydney

I would like to acknowledge my main supervisor Professor Knut Marthinsen for his stimulating discussions, his support and dedication to my work. Knowing that he would answer any of my questions immediately and come with feedback to my work within hour or days has been great for efficiency and morale! I am also thankful for the guidance by Professor Emeritus Erik Nes who has happily shared his extensive scientific and metallurgical knowledge with me. I have been able to participate in the MOREAL project meetings (KMB project No.193179/II40), which I am grateful to project manager Dr. Yanjun Li at SINTEF Materials and Chemistry for.

For practical help I am indebted to Dr. Yanjun Li (TEM particle characterization), Dr. Olaf Engler (resistivity measurements), Torild Krogstad (HF etching) and Emmanuel Hersent, Ph.D. (Thermo-Calc).

My three years as a PhD candidate were wonderful, much thanks to my office mates Nagaraj Vinayagam Govindaraj, Ph.D., Qinglong Zhao, Ph.D., and Ning Wang. In addition, there are many more close co-workers at the department and team players on PolyCrystal Palace who made every day exciting.

To family and friends, thank you!

Trondheim, September 2013

Sindre Bunkholt

Abstract

The present PhD work gives a comprehensive overview of subgrain growth, nucleation of recrystallization, recrystallization texture and related annealing phenomena in 99.99 pure, binary Al-0.25Mn and commercial purity aluminium alloys. These aspects have been extensively investigated experimentally, with an emphasis on characterizing orientation dependent subgrain growth and the effect of interannealing on softening kinetics. The work is motivated by the need for better and more robust softening models that can handle the microchemistries of recycle based aluminium alloys and aims in particularly to give a better understanding of the mechanisms involved in subgrain growth.

The necessary driving force for recovery and recrystallization is here introduced through cold rolling. Characterization of the starting materials indicates that the amount of grain break-up during deformation is determined by the initial grain size. After deformation to strains of $\varepsilon = 2.6$ and $\varepsilon = 3.0$, all the investigated alloys exhibit typical pure metal deformation textures with a strong β-fibre.

Using a novel characterization method, subgrain growth during annealing at various temperatures was followed in reconstructed subgrain maps captured by EBSD. The growth mechanisms seem to be independent of the alloy system and the microchemistry only influences the coarsening kinetics. Orientation dependent subgrain growth, measured in lamellar bands of uniform orientation, occurs in three distinct ways depending of the size of the local orientation gradients. Subgrains with Cube and Goss orientations grow only marginally faster than other subgrains initially, despite the largest misorientations and orientation gradients. However, the misorientations are increasing during annealing and after an incubation period subgrains with mostly high-angle boundaries grow significantly faster than less misoriented subgrains. A bimodal size distribution develops and growth is somewhat discontinuous. For subgrain structures with slightly lower orientation gradients, Cu, S and Brass orientations are dominating. The subgrain growth rate is marginally weaker and constant throughout the annealing process. Growth is homogenous and there is no significant correlation between boundary misorientation and growth rate, though the average boundary misorientations are increasing a little. For orientation gradients less than $\sim 0.5^{\circ}/\mu m$, only observed for subgrain structures with S and Brass orientations, the misorientations are consistently decreasing during annealing. In this case growth results in a temporary bimodal size distribution, possibly because larger subgrains have a size advantage.

In the commercial purity alloy, general subgrain growth that is orientation independent is faster than the orientation dependent growth because more

growth occurs in regions near high-angle grain boundaries separating differently oriented lamellar bands. It appears as if subgrains misoriented by more than 3.5° have a growth advantage over less misoriented subgrains typically in the interior of lamellar bands. The average boundary misorientations are decreasing but the experimental results indicate that the individual boundary misorientations are actually increasing. Therefore, the decrease is interpreted as a shortening of the total boundary length of more misoriented boundaries, i.e. more subgrain coarsening in regions where the orientation gradients are larger.

In the high purity alloy, the recrystallization texture below 300 °C does not resemble a typical recrystallization texture. Nucleation of recrystallization occurs mainly at high-angle grain boundaries, often in relation with transition bands or micro-shear bands. The nucleated grains are typically oriented at or slightly beyond the edge of the orientation spread of their parent grains by a $\langle 111 \rangle$-rotation. Growth of a recrystallized grain occurs into a neighbouring, often more misoriented grain where the orientation relationship is a compromised $40°\langle 111 \rangle$-rotation. After recrystallization at 350 °C the Cube component is much stronger and the texture is also a characteristic Cube recrystallization texture.

In the commercial purity alloy, iron in solution has a strong retarding effect on the softening kinetics. The resulting recrystallization texture has a distinct Cube component but also some weak deformation texture components. By interannealing, the solute level is reduced by precipitation of Al_3Fe and some α_h-AlFeSi phases on the deformation microstructure. Precipitation is also enhanced by increasing deformation. With less iron in solid solution the softening kinetics are faster by a factor 10^3 and the recrystallization texture is slightly stronger with a pronounced Cube component and also an R component.

The present PhD work has clearly shown that the subgrain growth behaviour is complex, diverse and challenging to characterize, and thus even more so to model. Still, it is hoped that the present work has provided qualitative and quantitative results as well as some new understanding, which may be of value in improvements and further development of existing softening models. E.g. the present work has clearly identified the local orientation gradient as an important factor to the subgrain growth behaviour. Incorporating the variation of the local orientation gradient could be the key to make future softening models more sophisticated and applicable for a wider range of alloy systems.

Contents

List of Acronyms

Abbreviation	Phrase
BF	Bright Field
BSE	Back-Scattered Electrons
BUF	Break-Up Factor
CB	Cell Block
CI	Confidence Index
CSL	Coincident Site Lattice
DB	Domain Boundary
DP	Diffraction Pattern
DDW	Dense Dislocation Wall
DF	Dark Field
EBSD	Electron Backscatter Diffraction
ECD	Equivalent Circle Diameter
ED	Extrusion Direction
FCC	Face-Centred-Cubic
FE	Field Emission
GNB	Geometrically Necessary Boundary
GOS	Grain Orientation Spread
HAGB	High-Angle Grain Boundary
IDB	Incidental Dislocation Boundary
IQ	Image Quality
LAGB	Low-Angle Grain Boundary
LB	Lamellar Boundary
LOM	Light Optical Microscopy
MB	Microband
ND	Normal Direction

Abbreviation	Phrase
ODF	Orientation Distribution Function
PQ	Pattern Quality
PSN	Particle Stimulated Nucleation
RD	Rolling Direction
RT	Room Temperature
SE	Secondary Electron
SEM	Scanning Electron Microscope
SFE	Stacking Fault Energy
SIBM	Strain Induced Boundary Migration
TD	Transverse Direction
TEM	Transmission Electron Microscope
TTT	Time-Temperature-Transformation

Chapter 1

General Introduction & Motivation

Softening of deformed metals typically takes place by recovery, recrystallization and grain growth. Of the three mechanisms, recovery is the least understood and the term only started appearing frequently in literature after the Second World War. In one early paper by Crussard et al. [1950] it is described how heavily cold worked aluminium with a partially polygonized structure becomes softer during annealing due to annihilation of opposite sign dislocations and coarsening of the polygonized structure (recovery). Polygonization was followed by recrystallization which further decreased the yield point (elastic limit) or recrystallization could occur without any sign of previous polygonization at higher temperatures. Recovery, recrystallization and grain growth have since been extensively studied, particularly during the late 80'ies and 90'ies due to the introduction of the *electron backscatter diffraction* (EBSD) technique for *scanning electron microscope* (SEM) characterization. This new method made detailed studies of the substructure possible with far better statistics than previously achieved by *transmission electron microscopy* (TEM) and was important for an improved description of the softening mechanisms. However, despite a better understanding of recovery and recrystallization, which e.g. resulted in the development of several softening models [Humphreys, 1997; Sæter et al., 1998; Verdier et al., 1999], this area of aluminium metallurgy is still not fully understood.

Humphreys and Hatherly [2004] describe how low stacking fault energy metals may recrystallize without any significant recovery because dislocation climb and cross-slip is difficult. In high stacking fault energy metals like aluminium, on the other hand, the dislocations are much more mobile, making recovery a very important softening reaction. The kinetics of this thermodynamically irreversible transformation is influenced by several factors that are controlled by the chemical composition and the thermo mechanical processing. Obvious

factors are the degree of deformation and the annealing temperature, but the rate of recovery is also influenced e.g. by texture and the local orientation relationships [Barou et al., 2009; Brough and Humphreys, 2010a]. Maybe even more important is the effect from elements in solid solution. Solute atoms have a pinning effect on grain boundaries which change the mobility during recrystallization and grain growth [Huang and Humphreys, 2012]. This effect is not exclusive for grain boundaries but subgrain boundary mobilities (misorientation $<15°$) are also reduced by elements like Si and Fe in solid solution [Abtahi et al., 2001; Barou et al., 2009; Godfrey et al., 2001; Huang and Humphreys, 2000; Sæter, 1997].

Only 5% of the energy consumed during primary production is required to remelt aluminium and recycling of aluminium will be important in the future as bauxite resources are limited. However, introducing aluminium from post-consumer scrap increases the solute levels of impurity elements and alters the microchemistry in new ways. It is more important than ever to fully understand the mechanisms deciding the properties of aluminium as it will become more difficult to control the purity and chemical composition of alloys. Current softening models can successfully predict transformation kinetics and mechanical properties of several commercial alloys, both from heat- and non-heat-treatable alloy systems. Although most models incorporate physical mechanisms dictating the material's behaviour, tuning by fitting parameters is necessary to a large extent. With the even more complex chemistry of recycle-based alloys, current models may not capture the softening behaviour since a fully adequate understanding of the softening reactions is still missing. Hence, a better understanding of the underlying mechanisms controlling softening and a more comprehensive, quantitative description is needed.

This PhD work aims to continue the work on recovery and particularly reveal more of the fundamental parameters controlling subgrain growth kinetics by an experimental approach. Because recovery and subgrain growth kinetics are orientation dependent, it is necessary to make most of the investigations here orientation dependent in order to characterize possibly different growth mechanisms. While choosing industrially relevant processing parameters and keeping them nearly the same, variations of the chemical composition and microchemistry is an area of great interest. Thus, a high purity alloy, a high purity binary single phase alloy and commercial purity alloy are chosen for the experiments. In addition to subgrain growth, related phenomena like nucleation of recrystallization and development of recrystallization texture are also investigated.

While characterizing the softening kinetics of the commercial purity alloy, it became apparent that although the effect of iron on annealing of aluminium alloys is frequently described in literature the reports are more meticulous than comprehensive. Several aspects are not well understood, which is why it was

found necessary to characterize the effect of iron and interannealing on softening of the commercial purity alloys here in detail.

Structure of thesis

This monograph is loosely structured around the IMRAD format [Sollaci and Pereira, 2004]. After the short introduction on the previous pages, a theoretical background is presented in Chapter 2. Here, a general introduction to relevant metallurgical concepts and phenomena is given, hopefully giving a better understanding of the subsequent literature review on subgrain growth and the effect of iron during annealing of pure aluminium alloys. Then follows a description of the materials investigated and experimental methods used in this PhD work in Chapter 3. Chapter 4 is dedicated to characterization of the starting materials. This is done in order to better highlight the main experimental work presented in Chapter 5. In both Chapter 4 and Chapter 5, the results are presented in separate sections for the high and commercial purity alloys. In the high purity section, the results from high purity and high purity binary Al-Mn alloys are presented. The results from the two Al-Fe-Si alloys can be found in the commercial purity section. Because all alloys to some extent shed light on the problems to be addressed, the discussion in Chapter 6 is centred around the metallurgical phenomena which appear chronologically according to the process route.

Chapter 2

Theoretical Background

This chapter is divided into five parts. In the first part, general aspects related to production of semi-finished rolled aluminium products is presented. This includes material processing, how the material responds and what the main strengthening mechanisms are. The next three sections all give a detailed presentation of annealing, precipitation and texture, respectively. All topics which have been central in this PhD work and that give an understanding of some of the inherent challenges. The final part gives an even more in-depth discussion with an emphasis on literature of the two main aspects of this PhD work; i.e. subgrain growth and the effect of iron the softening behaviour of pure aluminium alloys.

It is noted that Section 2.1–Section 2.3 include some references to texture. The fundamentals and nomenclature of texture, however, are explained in more detail later in Section 2.4.

2.1 General Aspects

Laboratory processing of materials in this PhD work has been less complex than industrial processing in general and the steps included are presented graphically in Figure 2.1. Several, common industrial process steps for aluminium semi-finished rolled products are omitted and after casting the materials in this PhD work were only homogenized, cold rolled and annealed. The process route is completed by recycling. In the following, common aspect of metal processing and related metallurgical phenomena relevant to *face-centred-cubic* (FCC) metals are briefly presented starting with solidification during casting, the evolution of the microstructure during rolling and the four strengthening mechanism.

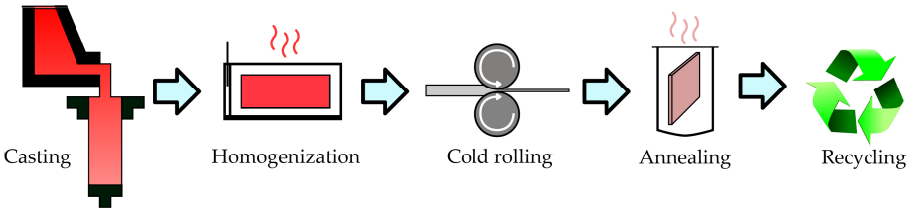

Figure 2.1: Schematic overview of the steps involved in lab-processing of aluminium, reflected by the scope of this thesis.

2.1.1 Solidification

In a liquid cooled below its equilibrium melting temperature there will be a driving force for solidification. The driving force arises from the Gibbs free energy of a solid which below this temperature is lower compared to that of the liquid. The formation of a solid is inherently associated with the creation of an interface toward liquid, leading to an increase of the energy and counteracting the volume Gibbs free energy reduction. Only when an infinitesimal size increase leads to a decrease in the Gibbs free energy can a solid nucleus be formed. Both contributions are size dependent, as shown in Figure 2.2(a), the negative contribution from the latent heat of fusion being proportional to r^3 while the positive contribution from interfacial energy is proportional to r^2. Hence, homogenous nucleation only takes place if the radius of the nucleus r is larger than a critical value r^*. Increasing the undercooling will make nucleation easier because r^* decreases. Yet, nucleation of solidification is seldom homogenous but typically starts heterogeneously on a surface which reduces the interfacial energy considerably.

During directional solidification, crystallites will form heterogeneously at the chilled surface and, due to the surface's roughness (usually a coated mould or crucible), the crystallites will have a more or less random orientation. However, the preferred growth direction of cubic metals is in the $\langle 100 \rangle$-directions [Kurz and Fisher, 1998]. During the whole growth process, and particularly in the initial stages, there will be a growth competition where crystallites which are oriented with one of the $\langle 100 \rangle$ growth directions perpendicularly to the isotherms will have an advantage over other crystallites. This is illustrated in Figure 2.2(b), albeit for an alloy developing dendritic grains but the principle remains the same also during planar growth. As long as heat is extracted through the already solidified metal, which it is in directional solidification, the solidification interface will be planar and stable. If the solid solubility at the solidification temperature is exceeded, the interface may become unstable due to constitutional undercooling and growth will be cellular or even dendritic. Equiaxed grains may further form in the bulk, ahead of the solidification front,

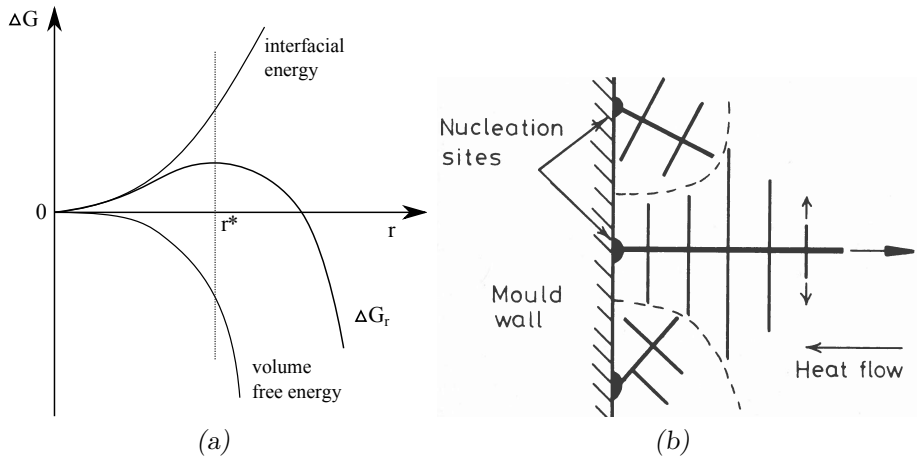

Figure 2.2: (a) Free energy ΔG_r as a function of radius during homogenous nucleation. (b) Competitive growth of dendritic grains nucleated heterogenously at a mould wall. [Porter and Easterling, 2004]

if an effective grain refiner is added to the melt.

In directional solidification of high-purity and dilute alloys, some of the crystallites formed at the chilled surface may enter the bulk due to turbulence during pouring. If the melt reaches the liquidus temperature soon after pouring, the free crystallites can continue to grow in the bulk. However, directionally solidified structures, as shown in Figure 2.3, typically consist of a chill zone with many, small crystallites and a columnar zone with their growth direction close to a ⟨100⟩-direction. This growth behaviour was characterized by Zhang et al. [2006] who studied directional solidification of 4N aluminium using a Bridgman configuration and no electromagnetic stirring. 30 mm from the chill, they observed 14 grains but due to fierce growth competition there were only 3 grains remaining 60 mm away from the chill and in fact the top of the casting was constituted by a single crystal. The columnar grains were found to deviate more from the ideal ⟨100⟩-type directions with an increasing growth velocity and a longer distance was needed to make the casting a "single crystal". New grains could also form during solidification, preferably at grain boundary corners, and grow at the expense other grains if oriented close to a preferred ⟨100⟩ growth direction. Thus, nucleation of new grains will not influence the number of columnar grains to a large extent.

2.1.2 Homogenization

The number of grains nucleating and segregation of alloy elements during casting is what determines the cast microstructure. However, this structure is

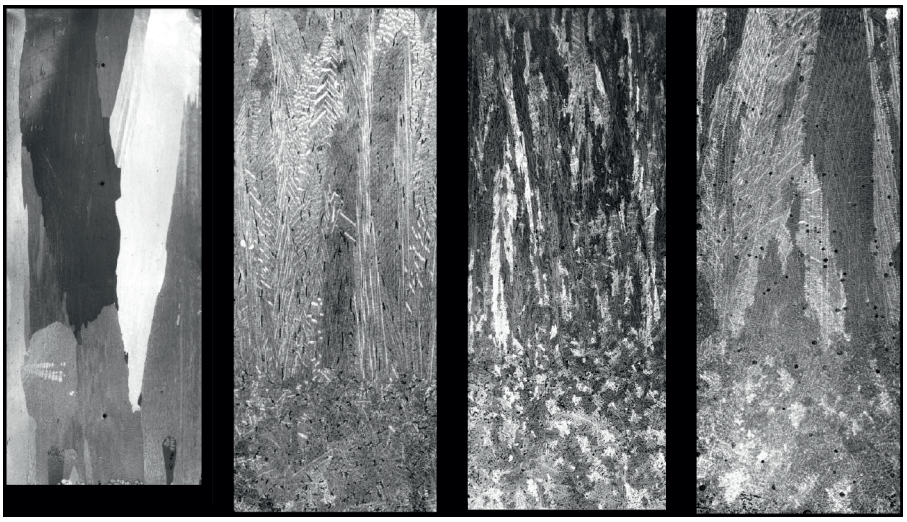

Figure 2.3: Growth competition observed in 4N Al (99.99% pure) with increasing silicon content left to right (3, 7 and 11 wt%) during directional solidification. Nucleation started at the chilled surface at the bottom of the pictures with a vertical growth direction for the columnar grains. Gandin [2000]

not necessarily ideal for further processing. Macrosegregations on the centimetre and meter scale are irreversible but microsegregations on the micrometre scale can be altered during a homogenization process. Parts of the microstructure does not change, i.e. the grain size and texture, even if homogenization is typically executed at 500–600 °C with different heating and cooling rates. Homogenization mainly affects the microchemistry, i.e. constituent particles and the distribution of solute and dispersoids, their composition and morphology. The microchemistry is important for both strengthening of softening mechanism, which is why homogenization influences the microstructure also in subsequent process steps.

The morphology of β-AlFeSi constituent particles in e.g. commercial purity alloys is sharp and plate-like and can cause nucleation of cracks during subsequent deformation. Through homogenization, a phase transformation to α-AlFeSi takes place which has a more rounded and less detrimental morphology [Kuijpers, 2003]. Another change that occurs during homogenization is a general levelling out of microsegregations. Depending on the distribution coefficient from the phase diagrams of aluminium and various alloy elements, solute is more readily deposited in the centre of grains or at the interface. Concentration profiles are generally levelled out but solute can also be precipitated. If the material is quenched from a high temperature, a high solute content can result and spontaneous precipitation at room temperature can happen. If, on the other hand, the temperature is lowered and held at an intermediate tempe-

rature over time, the system will try to reach phase equilibrium and solute will be precipitated as dispersoids and thereby stabilize the microchemistry.

2.1.3 Deformation by Cold Rolling

The rolling process under ideal conditions implies plane strain compression of a work piece plastically between two rolls. The deformation process is mainly one of compression, but some sheer commonly occurs close to the surface because of friction between the work piece and rolls. However, if the rolls are properly lubricated the deformation mode is close to plane strain compression. Industrially, cold rolling is often used as a finishing step because the sheets obtain a smooth surface finish and the final thickness can be controlled accurately. The sheet temperature during cold rolling is typically below 150 °C, making recovery processes slow. Thus, work hardening during deformation generally results in an increased strength after cold rolling.

The crystal lattices of metals are not perfect but the periodicity is interrupted by point defects and line defects, the latter better known as dislocations. When metals are deformed plastically, distinct regions of the crystal lattice are sliding relative to each other along definite crystallographic planes. This is called slip and principally occurs on the most densely packed planes in one of the closest packed directions. Twinning is another deformation mechanism, but is less important in aluminium where climb and cross-slip is easy because of the high stacking fault energy γ_{SFE}.

In a perfect lattice, slip would require the simultaneous movement of an indefinite number of atoms away from their minimum energy position. The theoretically necessary shear stress for such a deformation mode is larger than any values observed experimentally by two orders of magnitude. Instead, by moving a dislocation through the lattice as shown in Figure 2.4, the same displacement can be achieved at a much smaller shear stress. Moving a dislocation from one atomic plane to the next will only affect atoms in near vicinity to the dislocation and influenced by a continual shear stress, the dislocation will eventually reach a free surface. The two regions above and below the dislocation will be translated one atomic distance in the slip direction relative to each other. This slip distance is known as the Burgers vector b.

In FCC-metals, like aluminium, there are 12 possible combinations of densely packet planes and directions. They constitute what is defined as the $\{111\}\langle 110\rangle$-slip systems. Because there are so many possible slip systems, slip in FCC metals is easy and usually confined to one or more of these slip systems. Other systems may be activated at higher temperatures when dislocation climb is easier [Maurice and Driver, 1993]. Whereas a single crystal often is free to rotate in order to accommodate slip on only one slip system, grains in polycrystalline materials are constrained by neighbouring grains and the imposed shape change at the macroscale. This necessitates multislip to simultaneously main-

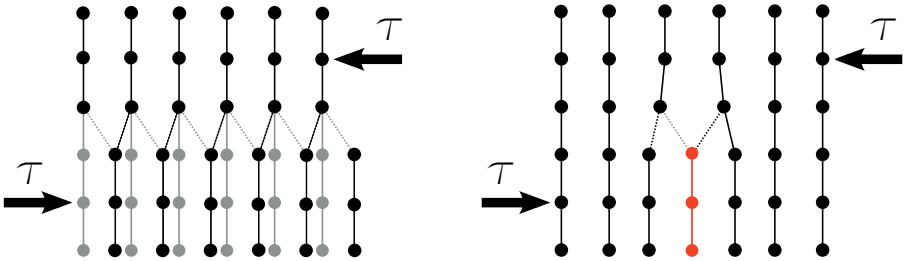

Figure 2.4: Deformation of a perfect lattice, as shown to the left, is more difficult than if deformation occurs by dislocation glide, i.e. shifting the red half-plane through the crystal (grey colour indicates old configurations and black, dotted lines are new bonds).

tain volume consistency and the macroscopic deformation state. Although, in polycrystalline materials under tension single slip has been observed [Huang and Winther, 2007].

However, during cold rolling of polycrystals it is safe to assume that multislip will occur in each grain and from the Taylor model, five independent slip systems are generally required to maintain homogenous deformation [Taylor, 1938]. Since slip occurs by dislocation glide, each slipped region is surrounded by at least one dislocation and mobile dislocations gliding on different slip systems will interact with each other or with sessile dislocations or other obstacles, e.g. particles, in the glide plane. These will act as dislocation sources (dislocation multiplication) and, hence, multislip produces a high density of dislocations on the operative slip systems.

Deformation Structures

Dislocations are defects in the crystal lattice and associated with an elastic stress field because of misfit between atomic planes. The energy per unit length is assumed to be similar to the line tension $\Gamma = {}^{Gb^2}/_2$ where G is the shear modulus and b the Burgers vector. Taking into account a normal dislocation density of 10^{10}–10^{14} ${}^{\text{cm}}/_{\text{cm}^3}$, the stored energy in the lattice can be substantial and, as elsewhere in nature, the system will try to minimise its energy. This is done in several ways. Rolling ingots will after casting have grains which typically assume more or less random orientations. Depending on the deformation mode, the grains will deform and rotate toward preferred orientations to minimise the local stress. The material is said to develop a texture and this will be discussed in greater detail in Section 2.4.

Because various parts of each grain are constrained differently, several slip system combinations act throughout each grain and homogenous deformation becomes localized in smaller regions. This results in a subdivision of the grains into smaller volume elements where the high density of tangled dislocations

forms lower energy configurations separating the distinct volume elements. In each new volume element, fewer operating slips systems are observed than those required by the Taylor model. Nevertheless, collectively the number of active slip systems is more than fulfilled [Bay et al., 1992a; Winther and Huang, 2007].

As deformation proceeds, the volume elements become increasingly refined, the boundaries sharpen and the misorientation between separate volume elements increases, at least for typical rolling strains [Bay et al., 1992a]. Increasing boundary misorientations are associated with increased boundary energy. However, the energy per dislocation will be reduced and so the total stored energy also decreases. At even higher strains, achieved through e.g. accumulated roll bonding, boundary spacing keeps on decreasing while boundary misorientations eventually saturates [Huang et al., 2003].

The substructural development is strain dependent and through extensive research on the topic, typical microstructures have been identified. An overview from small to large strains can be found in Bay et al. [1992b] and Humphreys and Hatherly [2004]. For a more detailed description, Bay et al. [1992a]; Rosen et al. [1995] and, most recently, Winther and Huang [2007] are well worth reading. At small strains (ε<0.3), the first features to form from the tangled dislocations are *cells* as pictured in Figure 2.5. They are formed statistically by mutual trapping of gliding and stored dislocations and are transient during deformation, i.e. trapping is counteracted by annihilation of dislocations. Such cell walls are called *incidental dislocation boundaries* (IDB) and differ from the higher angle boundaries of *cell blocks* (CB). Cell blocks develop from subdivision of grains, as described above and illustrated in Figure 2.6(a), and may themselves have a network of ordinary cells inside. The active slip system combinations of each cell block is the result of geometrical constraints, thus their boundaries are named *geometrically necessary boundaries* (GNB) in literature.

The morphology of the GNBs is strain dependent and appears different when viewed in a TEM. At low to moderate strains (0.3<ε<1.0), the cell block boundaries may adopt a narrow shape with a large misorientation across them called *dense dislocation walls* (DDW). These rotation boundaries of undissociated dislocations may continue for several cell blocks and are usually found at a $\pm 40^\circ$ angle to the rolling direction. At higher strains, the substructure develops an elongated appearance where layers of cell blocks as little as one cell in thickness are separated by long boundaries named *lamellar boundaries* (LB). These are typically aligned $\pm$ 15° with the rolling direction.

A third kind of GNBs present at most strains are *microbands* (MB). MBs are regions of small, pancake-shaped cells separating a regular network of cells. They tend to develop by splitting of DDWs and, hence, are also rotation boundaries. Within each microband, completely different sets of slip systems to the surrounding cell network are active. DDWs and MBs often interact with each other and delineate most of the CB-structure as shown in Figure 2.6. A less

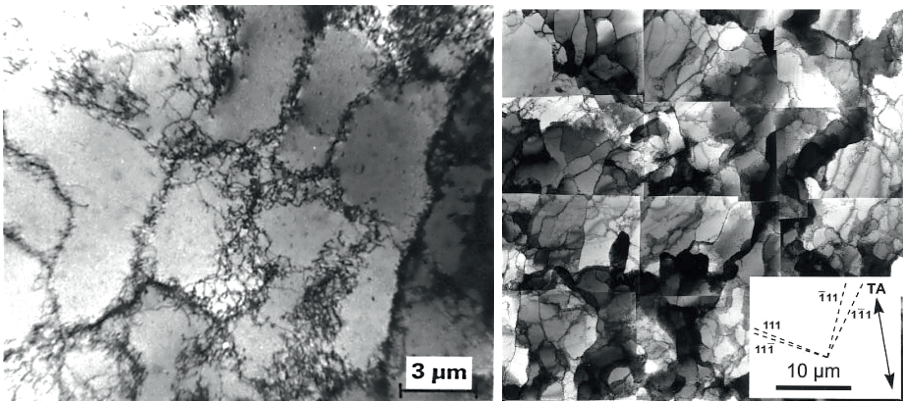

(a) Young et al. [1986]. *(b) Hansen and Huang [1997].*

Figure 2.5: Cell structure in high purity Al deformed 5% with loosely tangled dislocations (a) and 15% with a well-defined cell structure (b).

common type of MB, *second generation MB*, exists and often intersects MBs formed from DDWs, *first generation MBs*. A slightly higher stress level is required for them to be created by intersection of the cell network by dislocations gliding on a previously inactive slip system, forming narrow 2^{nd} generation MBs parallel to the {111} crystallographic planes.

The lattice rotation across DDW and MB boundaries increases as more dislocations are accommodated until misorientation almost saturates at 30–50% reduction. Dislocations generated by further deformation to large strains (ε>1.0) are absorbed by the normal cell walls, giving rise to increasing rotation angles and a heterogeneous stress distribution inside single CBs. Similar to what took place in grains at lower stress, the CBs will split into smaller volumes where different combinations of slip systems are active. A schematic drawing of this structure is given in Figure 2.7(a), where the microstructure consist of a banded cell or subgrain structure parallel to the rolling direct. The different lamellar regions, sometimes only one subgrain thick, are separated by LBs. During a transition period, going from intermediate to large strains, *micro-shear bands* having a pronounced S-shape emerge frequently. The micro-shear bands align closely with the {111} slip planes and intersect first generation MBs in localized regions.

The appearance of the deformation structure is, in addition to strain, influenced by solute. Solute atoms hinder dislocation motion and if sufficiently abundant, the friction stress becomes so large that recovery processes slow down and the reorganization of dislocations into low energy structures is impeded [Hughes, 1993]. Instead of forming cells, the dislocations can lower their energy somewhat by forming what is commonly known as a Taylor lattice [Kuhlmann-

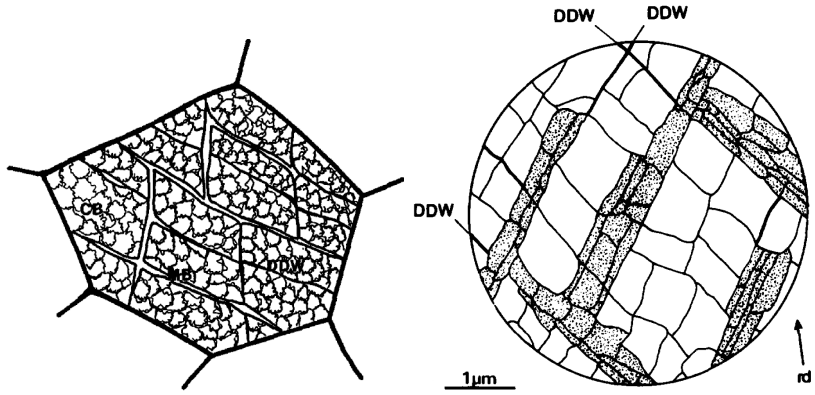

(a) Hughes [1993]. *(b) Bay et al. [1992b].*

Figure 2.6: Schematic drawings a substructure of CBs delineated by DDWs and MBs (a) and of DDWs and MBs (dotted) boundaries (b).

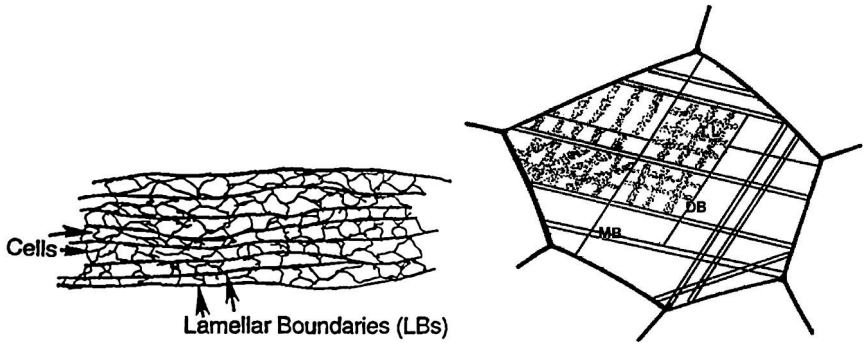

(a) Hughes and Hansen [1997]. *(b) Hughes [1993].*

Figure 2.7: Sketch of LBs parallel to the rolling direction with cells or subgrains at large strains (a) and a Taylor lattice with DBs and MBs along {111} slip planes (b).

Wilsdorf, 1989]. A similar structure also forms in low stacking fault energy materials. Figure 2.7(b) presents a sketch of a Taylor lattice composed of a regular array of trapped, incidental edge dislocations arranged in a three-dimensional network on {111} slip planes. To lower the energy, multiple Burgers vectors of dislocation are organised with alternating plus-minus rotations. Adjacent Taylor lattice regions are separated by DDWs parallel to the primary slip plane, dubbed *domain boundaries* (DB), and constituted by geometrically necessary dislocations. By replacing DDWs with DBs, the theory for substructure evolution is rather similar to that of cell forming materials. For instance, subdivision into finer volume elements is analogues and MBs are formed by splitting of DBs.

Since the microstructural evolution is strain dependent, it is natural that grain orientation is an important parameter too. Liu et al. [1998] found most features of the deformation structure to be orientation dependent, e.g. the scale of grain subdivision, CB morphology, orientation of GNBs (crystallographic or not) and the character, misorientation and rotation of dislocation boundaries. Grains with typical deformation texture components (Section 2.4.2) usually subdivided into cells and CBs, whereas Cube grains were also subdivided by MBs. Most boundaries were crystallographic with combination of tilt and twist, though in grains with near Cube orientation non-crystallographic boundaries were formed which were mainly of twist character. TEM pictures of crystallographic and non-crystallographic boundaries can be found in Figure 2.8.

Cube oriented regions also show a more rapid work hardening initially and they consist of more *high-angle grain boundaries* (HAGB). Later investigations have tried to create a more general picture, e.g. Hansen and Huang [1997] and Huang and Winther [2007] observed grains with typical β-fibre orientations or Cube orientation to form a CB structure with mostly non-crystallographic GNBs (both DDWs and MBs). Goss, Brass and rotated Cube grains, on the other hand, had a CB structure with interior cells where most of the GNBs (both DDWs and MBs) were straight and parallel and aligned on the primary slip planes. In more or less perfect Cube oriented grains, an equiaxed cell structure with relatively large boundary misorientations was observed.

2.1.4 Strengthening Mechanisms

The main focus of this thesis is on topics which are all related to annealing, a process which is applied industrially to make the material softer and which in the most basic fashion is characterized by the decrease in strength with time. To understand how annealing of a deformed material leads to a softer material, an insight into how aluminium resist deformation is useful. Inherent to plastic deformation of metals is glide of several mobile dislocations to accommodate the external stress state. The material becomes stronger when the mobility of such dislocations is retarded, which for aluminium is done either by introducing more dislocations by straining, adding solute atoms by alloying, forming fine

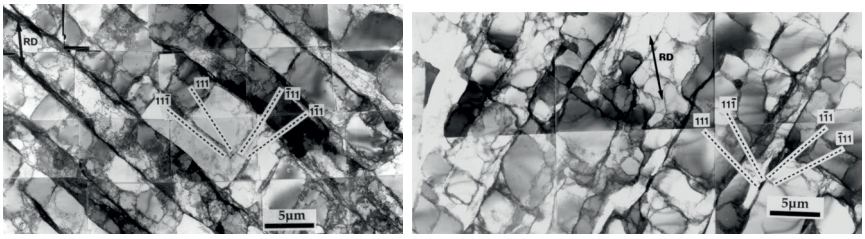

(a) (b)

Figure 2.8: Crystallographic (a) and non-crystallographic (b) GNBs (DDWs and MBs) in 10% cold rolled high purity Al. Liu et al. [1998]

precipitates through heat treatments or controlling the grain size. These four strengthening mechanisms of aluminium alloys are shown chronologically left to right in Figure 2.9 and will now be described shortly.

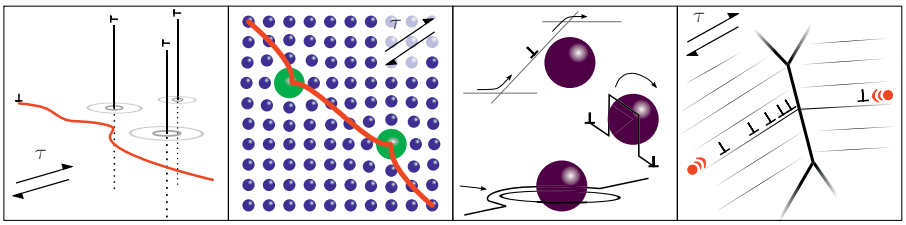

Figure 2.9: Graphical presentation of the four strengthening mechanism in aluminium. From left to right are strain, solute, precipitation and grain size hardening.

Strain Hardening

Individual dislocations are always associated with a strain field. Dislocation-dislocation interactions may result in energetically favourable configurations. The stress fields of different dislocations may interact in such a way as to reduce the free energy or the dislocations themselves rearrange and form sessile configurations. A gliding dislocation on one slip system can also meet a forest of stored dislocation on intersecting glide planes, which will lead to jog formations when cut by the gliding dislocation. Continued glide of a dislocation will in all the previous cases require an additional stress to be applied. Hence, slip is inhibited and strength increased. The strain hardening contribution to the flow stress is commonly assumed to follow the square root of the dislocation density as given by Equation 2.1, although more refined approaches exist. σ_y is the yield strength, σ_0 the friction stress, α a constant of order unity, G the shear modulus, b the Burgers vector and ρ the dislocation density.

$$\sigma_y = \sigma_0 + \alpha G b \rho^{\frac{1}{2}} \tag{2.1}$$

Solute Hardening

Substitutionally dissolved atoms in aluminium cause a misfit strain field of higher energy than the undistorted lattice which slows down gliding dislocations. The strain field can be of tensile or compressive character and the strengthening effect increases with increasing solid solubility at room temperature and the degree of misfit between the dissolved atom and the aluminium matrix. The solute atoms interact with dislocations elastically, due to the size misfit, by altering the local atomic interactions which affects the shear modulus and by segregating to stacking faults. The stacking fault energy γ_{SFE} becomes lower and the separation between partial dislocations increases.

The size misfit is often also referred to as elastic locking and is proportional to Gb^2 times the fractional change of the lattice constant with solute concentration for both edge a screw dislocations [Argon, 2007]. A screw dislocation has a pure shear strain field and will only interact with spherically symmetrical defects because of the nonlinear elastic behaviour of the core material. Similar interaction forces proportional to Gb^2 can be found for the relationships between edge and screw dislocations and the modulus misfit.

The effect of solute on the stacking fault energy, sometimes described as chemical locking, is less important for dilute alloys. In addition there exist several theories for the interaction between solute atoms and gliding dislocations, like the Friedel statistics for localized interaction with strong obstacles in dilute alloys [Friedel, 1964]. At higher concentrations, the diffuse interaction of weaker obstacles is described by Mott & Labusch statistics [Labusch, 1972; Mott, 1952].

Precipitation Hardening

The most effective strengthening is achieved by precipitation hardening. Through a heat treatment process called ageing, a fine distribution of precipitates is generated throughout the matrix. Optimum precipitation hardening requires a high solubility at the eutectic temperature and a rapidly decreasing solubility with falling temperature. During ageing, coherent Guinier-Preston zones form first followed by coherent and semi-coherent metastable phases and finally an incoherent stable phase is formed. Large coherency strain fields are introduced when the solute atoms start to group together and interact with gliding dislocations, slowing them down. The coherency strain field increases with precipitate size until coherency breaks down and a new surface is gradually formed and coherency vanishes completely for incoherent precipitates.

Growth of the precipitates also has a great influence on the coherency strain field strengthening. A maximum is reached when the precipitate spacing is identical to the critical dislocation curvature $r \approx {}^{Gb}/_{2\tau}$ where G is the shear modulus, b the Burgers vector and τ the applied shear stress. In this case, τ is known as Orowan stress τ_{Orowan} and given by Equation 2.2 where α is a geometrical factor and λ the average particle separation.

As the new precipitate take form it is initially coherent and shearable by passing dislocations. Whenever a precipitate is sheared, additional energy is required to form a new interface between precipitate and matrix. For ordered precipitates, additional energy is also necessary to create anti-phase boundaries and if the dislocation is dissociated into partial dislocations, the different stacking fault energy of the precipitate will change the separation between partials. When the precipitates finally become incoherent they cannot be sheared by the dislocation, which need to find a way to bypass the precipitates for glide to continue. Orowan bowing, climb and cross-slip are all possible ways for the dislocation to pass non-shearable precipitates but depend on an additional stress to be applied.

$$\tau_{Orowan} = \alpha \frac{Gb}{\lambda} \tag{2.2}$$

Grain Size Hardening

The strength from a grain boundary is caused by a mutual interference of slip within the two grains. A gliding dislocation cannot pass the high energy region of stored dislocations which create ledges constituting the grain boundary. Several gliding dislocations of equal sign can pile up at the grain boundary under a continued applied shear stress. The stress at the boundary intensifies proportionally to the number of dislocations in the pile up and eventually dislocation sources in the neighbouring grain will be activated, causing the neighbouring grain to yield. Grain boundary strengthening is commonly described by the Hall-Petch relationship given in Equation 2.3 where σ_y is the yield strength, σ_0 the friction stress, k the relative hardening constant and D the average grain diameter. It is important to remember that the Hall-Petch relationship is empirical and for aluminium the relationship breaks down for grain sizes in the range 10–20 nm [Morris, 2010].

$$\sigma_y = \sigma_0 + kD^{-\frac{1}{2}} \tag{2.3}$$

2.2 Annealing

Annealing is an important process subsequent to deformation often applied to alter the mechanical properties in order to improve formability, i.e. by re-

lieving internal stresses, lowering the flow stress and change texture. Though annealing may also be used to form unique structural features like annealing twins.

The textbook description of the microstructural evolution and release of stored energy during annealing is shown in Figure 2.10. After deformation, a dense network of tangled dislocations is separated into grains by old, original grain boundaries and new grain boundaries created by subdivision. Since each dislocation is associated with a strain field, this is a state of high energy that can be relaxed through microstructural changes which are thermally activated, like atomic diffusion. At an elevated temperature where the tangled dislocations are able to move, some dislocations will be annihilated while the rest rearrange themselves into lower energy configurations like cells and eventually subgrains. This process is known as recovery. The next step in the sequence of typical softening reactions is nucleation of recrystallization, where latent recrystallization nuclei form dislocation free grains. The final softening reaction is grain growth.

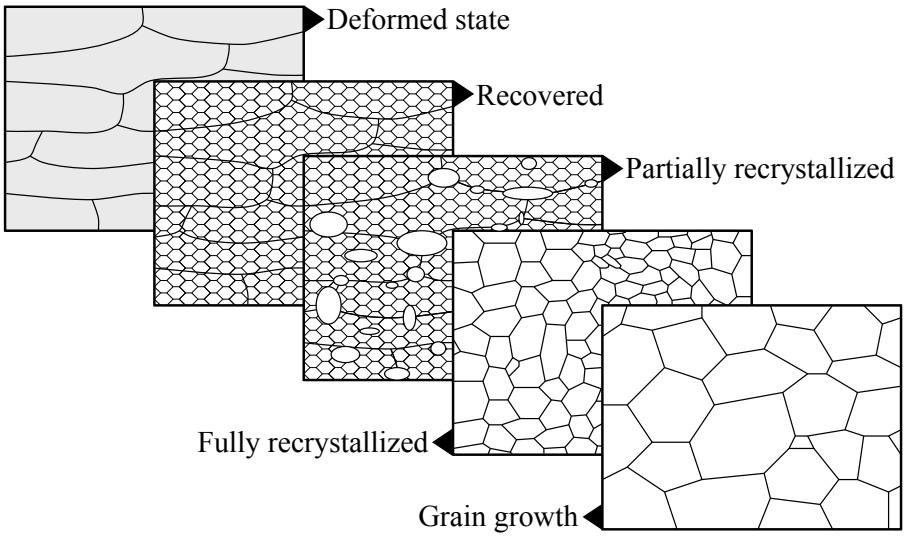

Figure 2.10: Schematic drawing of the microstructural evolution during annealing of deformed material; recovery, recrystallization and grain growth.

Recovery and recrystallization are actually competing mechanisms controlled by the strain state and temperature. Complete softening can theoretically be achieved by either process, although some recovery has typically taken place before the onset of recrystallization. However, recrystallization is extremely efficient at reducing the stored energy and cannot be succeeded by recovery. Newly formed grains will continue to grow during annealing. Some grains may experience more preferable growth conditions, e.g. highly mobile boundaries or surrounded by favourable misorientation gradients, and grow at the expense of

others. From the partially recrystallized state, the new grains will soon impinge and the material is fully recrystallized when all the deformed regions are consumed. For many years it was debated whether the final recrystallization texture was a result of oriented nucleation or oriented growth, but it is now widely accepted that both nucleation and growth are important factors [Engler et al., 1996b,c; Lücke, 1974]. After recrystallization, the stored energy can be further reduced by decreasing the total boundary area, i.e. grain growth.

Keeping in mind the strengthening mechanisms, in particular strain hardening and grain boundary hardening, it is clear why annealing is often described as softening. Annihilation of dislocation, subgrain growth, formation of dislocation free grains and grain growth make the material softer and is commonly characterized by hardness measurements due to its experimental simplicity. However, unlike e.g. yield stress, hardness is not a fundamental material property but is still often used to estimate the materials resistance to slip. It should also be noted that in the very beginning of annealing, the hardness might actually increase a bit before it decreases again. This phenomenon is hardly described in the literature, although it was discussed in the 1950s by Beck [1953] and Amin et al. [1970] who referred to it as recovery strengthening.

The effect of recovery and recrystallization on yield strength of an AA5754 alloy is exemplified in Figure 2.11.

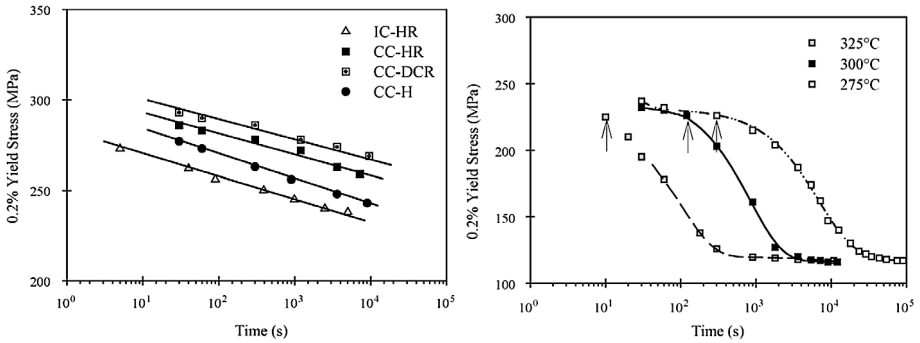

Figure 2.11: Decreasing yield strength during isothermal annealing of AA5754. Recovery kinetics at 200 °C in (a) after 80% deformation with different processing and recrystallization kinetics at higher temperatures of CC-HR (b). [Sarkar et al., 2004]

2.2.1 Recovery

The definition of the word *recovery* is "the process of returning to a normal condition". It is the evolution of the microstructure from a chaotic and high energy state, arising from e.g. deformation, into a well-defined, low energy

structure consisting of dislocation free subgrains through dislocation rearrangement. This may sound very similar to the formation of deformation structures. Indeed it is. There will always be a driving force for recovery during deformation of a polycrystalline material which results in some degree of dislocation annihilation, cell formation etc. This is commonly referred to as dynamic recovery and will not be discussed further. Static recovery, or simply recovery, on the other hand, takes place after the material has been deformed and will be discussed in more detail.

Light deformation on one single slip system can be fully recovered because it does not lead to local disorientations. For more severe plastic deformation, the fraction of recovery which can be expected depend on the amount of strain accumulated, the annealing temperature and the stacking fault energy γ_{SFE} of the material which controls the rate of dislocation climb and cross-slip. In high stacking fault materials like aluminium, dissociation of a unit dislocation into partial dislocations and the formation of a stacking fault is difficult. This is why a subgrain structure develops after moderate deformation of aluminium and why recovery will lead to such a structure if not already formed.

Network Growth

During annealing, dislocation network growth is responsible for the formation of a subgrain structure and depends on dislocation annihilation and rearrangement. The rate of both is controlled by dislocation glide, climb and cross-slip. The driving force for network growth arise from the dislocation line tension Γ and is given by Equation 2.4 where G is the shear modulus, b the Burgers vector and r scales with the mesh size and is $\approx {}^{1}/_{\sqrt{\rho}}$ [Friedel, 1964].

$$F \approx \frac{Gb^2}{r} \tag{2.4}$$

Network growth is highly complex and can be broken down into different rate controlling scenarios. In less pure alloys, solute atoms will induce a significant drag effect which potentially becomes rate controlling. An overview of the different rate controlling mechanism and the effect of solute drag is given by Nes [1995].

The mobility of heavily jogged screw dislocations can lead to thermally activated glide control. Without solute the rate controlling mechanism is climb of dislocation jogs. Climb of jogs depend on vacancy diffusion to and from jogs which may have different sign $(+/-)$, i.e. vacancies, from vacancy emitting jogs, diffuse to vacancy absorbing jogs. Local thermal equilibrium of vacancies is assumed. If solute atoms are present, a migration to jog sites in order to lower their misfit strain field is expected. This will lead to climb rate controlled by thermally activated diffusion of solute atoms away from the jogs if the relaxation time of the solute atoms at the jogs is smaller than the break-away of

the dislocation. During annealing, jogs will form by *cutting of trees* (e.g. a gliding edge dislocation crossing a perpendicular screw dislocation). In addition, opposite sign jogs can be annihilated. Hence, glide control with and without constant jog spacing may be envisioned. Lateral drift of jogs is likely in high stacking fault materials like aluminium. Taking into account the formation and annihilation of jogs, $l_j \approx \kappa r$ gives a good estimate of the average jog spacing, where κ is a geometric constant. The resulting network growth kinetics are expressed by Equation 2.5

$$\frac{r_0}{r} = \left[1 + \frac{t}{\tau_1}\right]^{-1} \tag{2.5}$$

where r_0 is the initial separation of dislocations and τ_1 is:

$$\tau_1 = \left[\sqrt{\rho_0} B_x \exp\left(\frac{\kappa\alpha G b^3}{kT}\right)\right]^{-1}$$

B_x is a temperature dependent parameter which accounts for the different diffusion mechanisms, i.e. vacancy bulk diffusion, vacancy core diffusion or solute diffusion. The solute may have a strong effect on the jog mobility, e.g. in commercial purity aluminium alloys, which might result in constant jog spacing during annealing (or in low stacking fault energy materials). The analytical approximate solution to recovery rate controlled by glide without lateral jog drift becomes

$$\frac{r_0}{r} = 1 - \frac{kT}{\kappa\alpha G b^3} ln\left(1 + \frac{t}{\tau_2}\right) \tag{2.6}$$

where τ_2 is:

$$\tau_2 = \left[\frac{\sqrt{\rho_0}\kappa\alpha G b^3 B_x}{kT} \exp\left(\frac{\kappa\alpha G B^3}{kT}\right)\right]^{-1}$$

This equation does only give reasonable fit with the numerical solution when $r_0/r > 0.4$ and $\kappa\alpha G B^3/kT > 20$.

The recovery kinetics can also be controlled by the dislocation annihilation reaction itself, which typically occurs at lower temperatures and depend on thermally activated cross-slip of screw dislocations. Friedel [1964] gives the relationship for a decay of the internal stress σ_i as:

$$\frac{\mathrm{d}\sigma_i}{\mathrm{d}t} \propto -\exp\left(-\frac{U_{cs}(\sigma_i)}{kT}\right)$$

According to Nes [1995] this equation leads to the following network growth law:

$$\frac{r_0}{r} = 1 - \frac{t}{\tau_3} \tag{2.7}$$

which predicts a power law decrease of the dislocation density ρ since $r_0/r = \sqrt{\rho/\rho_0}$ and linear hardness decrease because $\sigma_i \approx Gb\sqrt{\rho}$.

The final rate controlling mechanism which will be presented here is growth by dislocation climb. Even if glide and cross-slip are rate controlling initially, climb is occurring simultaneously and will rapidly determine the growth rate. Climb is a thermally activated process and the dislocation movement can be broken down into glide and climb steps where the climb rate depend on vacancy diffusion. The two extreme cases of vacancy transportation are bulk and dislocation core diffusion. In Equation 2.8 for network growth $a = 1/2$ and $a = 1/4$ gives dislocation climb controlled by vacancy diffusion through bulk and dislocation cores, respectively.

$$\frac{r_0}{r} = \left(1 + \frac{t}{\tau_4}\right)^{-a} \tag{2.8}$$

Of course, solute will have a great influence also on this growth mechanism. Instead of depending on vacancy diffusion, it is the migration rate of solute away from the dislocation itself which is rate controlling. An example could be Al-Mg alloys (5xxx) or even dilute alloys which contain small levels of iron. In fact, glide will be inhibited in the same way by any solute atoms and the drag effect on glide and climb is similar as long as the relaxation time for the solute atoms is less than that for break-away. The approximate solution for the growth kinetics is

$$\frac{r_0}{r} = 1 - \frac{kT}{\sqrt{\rho_0}\alpha l_s G b^4} \ln\left(1 + \frac{t}{\tau_4}\right) \tag{2.9}$$

where

$$\tau_4 = \left[\frac{\rho_0 \alpha l_s G b^4 B_x}{kT} \exp\left(\frac{\sqrt{\rho_0}\alpha l_s G b^4}{kT}\right)\right]^{-1}$$

and l_s is a function of the solute concentration among others parameters.

Subgrain Growth

At some point network growth will diminish and subgrain growth commence. The subgrain structure consists by definition of *low-angle grain boundaries* (LAGB), typically with a boundary misorientation decidedly smaller than the HAGBs with a threshold value at $\omega_m = 15°$. The driving force for subgrain growth arise from the subgrain boundary energy γ_{SB} and according to Ørsund [1989] this can be expressed as

$$F = \alpha \frac{\mathrm{d}}{\mathrm{d}r}\left(\frac{\gamma_{SB}}{r}\right) \tag{2.10}$$

where α is a geometrical constant, r is the average subgrain radius and γ_{SB} is given by the famous Read-Schockley [Read and Shockley, 1950] relationship with $\gamma_{GB} = 0.324$ $^{\mathrm{J}}/_{\mathrm{m}^2}$ [Murr, 1975].

$$\gamma_{SB} = \gamma_{GB}\frac{\omega}{15^\circ}\left[1 - \ln\frac{\omega}{15^\circ}\right]$$

A commonly applied solution to Equation 2.10 in the literature was formulated by Huang and Humphreys [1999] and gives the driving pressure for recrystallization explicit for average subgrain size δ and misorientations ω:

$$P_D = \frac{2\gamma_{SB}}{\delta} = \frac{2\gamma_{GB}}{\delta}\frac{\omega}{15^\circ}\left[1 - \ln\frac{\omega}{15^\circ}\right] \tag{2.11}$$

The mobility M of subgrain boundaries depends on the boundary misorientation ω and growth progress by atom diffusion and is according to Humphreys [1997] given by the empirical Equation 2.12. In this equation, M_m is the mobility of a high-angle grain boundary, A and B are constants and ω_m the misorientation of a HAGB, $\sim$15°. Larger misorientations induce more open space in the lattice and the mobility increases. According to Equation 2.11, the stored energy can be lowered by reducing the total boundary length and by decreasing the boundary misorientation. When the misorientation decreases, both the driving force and the boundary mobility become smaller and subgrain growth slows down.

$$M = M_m\left[1 - \exp^{-B(\omega/\omega_m)^A}\right] \tag{2.12}$$

There are two major theories for how subgrains are growing. Following the work by Hu [1962] and Li [1962], growth by rotation and coalescence gained momentum as an important mechanism for subgrain growth. However, sceptics claimed the experimental evidence, which was mainly from thin film investigations in TEM, could not be applicable for bulk growth and today this mechanism is considered to be less important for the overall subgrain growth kinetics [Nes, 1995; Smith and Dillamore, 1970].

Although the experimental work is ambiguous, subgrain coalescence is at least theoretically possible. By rotating toward a common orientation, two subgrains can eliminate their common LAGB. A subgrain has several neighbouring subgrains. Because $^{\mathrm{d}\gamma}/_{\mathrm{d}\rho}$ increase with decreasing misorientation, the most energetically favourable rotation is in a direction where the misorientation of higher angle boundaries increase while the lowest angle boundary decreases. This is particularly beneficial when one or more of the boundaries have high-angle character [Doherty and Cahn, 1972]. A HAGB will also be able to absorb dislocations from the LAGB by increasing the boundary energy notably. Hence, rotation and coalescence is most likely to occur in the vicinity of HAGBs, but has also been observed at low temperatures by Sandström et al. [1978].

A more widely accepted mechanism for subgrain growth is by low-angle boundary migration which is more similar to ordinary grain growth in that small subgrains will be consumed by larger ones. However, because the energy of LAGBs is sensitive to misorientation, unlike most HAGBs, subgrain growth should also be treated differently from normal grain growth. The most obvious effect of the varying boundary energy can be seen at triple junctions where the equilibrium configuration is not necessarily with a 120° angle between the boundaries. Subgrain growth kinetics have long been expressed by an empirically derived exponential growth law. However, the exponents are found to scatter significantly and good fit with experimental data is sometimes difficult. That is why Furu et al. [1995] suggested a different, more physically based model. Subgrain coarsening is by Furu et al. [1995] described as migration of flexible boundaries through lateral drift of thermally activated boundary ledges. The rate controlling mechanisms are then thermally activated climb in high purity alloys and diffusion of solute away from glide of climbing ledges in less pure alloys. The resulting growth rate from this approach can then be described by the differential equation

$$\frac{\mathrm{d}d}{\mathrm{d}t} = C\sinh\left(\frac{A_x}{dkT}\right) \tag{2.13}$$

where d is the average subgrain diameter and A_x a parameter which accounts for different rate controlling mechanisms. For pure climb $A_x = 2\alpha\kappa Gb^4$ and for solute drag $A_x = 2\alpha l_s Gb^3$ where l_s is the spacing between solute atoms along the dislocation length.

In Humphreys and Hatherly [2004] a distinction between subgrain growth in an orientation gradient and in the absence of an orientation gradient is made. When there is no orientation gradient, the stored energy is lowered by a combination of shortening the total boundary length and lowering the average boundary misorientation. This has been confirmed by models and is also seen experimentally. The presence of an orientation gradient is however more common in a polycrystalline material and then the average boundary misorientation increases with subgrain growth, i.e. the opposite behaviour. For an orientation gradient larger than 5°/μm, the growth rate also becomes significantly faster.

Another important aspect of growth in an orientation gradient is discontinuous subgrain growth. Normal growth occurs by a more or less continuous process where the size distribution at any point during the annealing process will show only one major peak. However, under most circumstances the subgrain structure consists of subgrains with a certain misorientation spread. The most misoriented subgrains have a growth advantage over their neighbours and rapid growth with increasing misorientations follow. It has been shown experimentally at 300 °C that subgrains with 5° misoriented boundaries have 14 times as high mobility as those with 3° boundary misorientations [Ferry and

Humphreys, 1996]. This growth process leads two a bimodal size distribution and appear similar to recrystallization but involves only migration of low-angle grain boundaries. Discontinuous subgrain growth has been confirmed to be more feasible than continuous subgrain growth theoretically but there is a lack of experimental evidence. According to Humphreys and Hatherly [2004] this is because very little subgrain growth is usually observed before the onset of recrystallization making relevant experiments difficult.

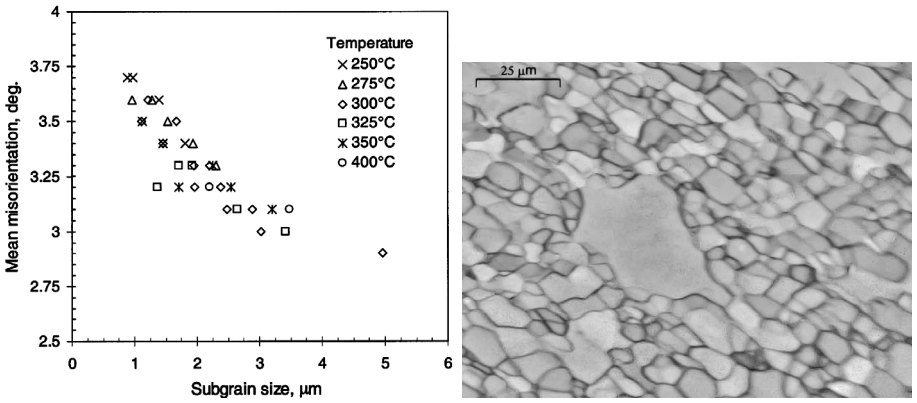

Figure 2.12: Decreasing average boundary misorientations during annealing of 70% cold deformed Al-0.05% Si (a) and discontinuous subgrain growth in 70% hot deformed Al-0.05% Si (b). [Huang and Humphreys, 2000]

Zener Drag

With an extremely fine distribution of particles with spacing similar to the mesh size of the dislocation network, dislocation annihilation and rearrangement, and thus network growth, would be inhibited. Though, such situations are rarely encountered. A coarse particle distribution where the spacing scales with the subgrain size is much more common and has a great influence on recovery kinetics. The effect is somewhat similar to the effect of solute. The particles pin mobile subgrain boundaries because their interaction is energetically favourable. The retarding force or pinning pressure depend on the energy and nature of the boundary (e.g. triple junctions) and the shape, size, interface, spacing and volume fraction of the particles. By assuming a random distribution on non-coherent, spherical particles of radius R and a particle spacing significantly smaller than the subgrain diameter, the pinning pressure condenses down to the well-known Zener drag pressure P_Z [Smith, 1948].

$$P_Z = \frac{3F_V\gamma_{SB}}{2R}$$

where F_V is the volume fraction of particles and γ_{SB} is the subgrain boundary energy. Zener drag will dominate the subgrain growth kinetics which can be expressed by the resulting driving force when a Zener pressure is operating. The velocity of a boundary is proportional to the net pressure and by multiplying with the temperature dependent mobility M the subgrain growth rate follows:

$$\frac{\mathrm{d}r}{\mathrm{d}t} = MP_{net} = M(P_D - P_Z) = M\left(\frac{\omega\gamma_{SB}}{r} - \frac{3F_V\gamma_{SB}}{2R}\right) \tag{2.14}$$

The Zener drag effect discussed above assumes a planar subgrain boundary. However, the subgrain boundaries will bow out between particles in order to relax locally. The effect of particles also depends on when they are formed. E.g. similar spacing between particles and subgrains after deformation may stabilize the structure during subsequent annealing. If precipitation occurs during annealing, known as concurrent precipitation, precipitates may form on the subgrain boundaries. Here they may exert a stronger pinning force than for a random lattice distribution and stabilize the subgrain structure. Further network growth is then controlled by coarsening of the particles, which often leads to extended recovery.

2.2.2 Recrystallization

Recrystallization, as opposed to recovery, is a discontinuous process. Nuclei can be what appear to be random subgrains or subgrains in the vicinity of heterogeneities like grain boundaries, shear bands or particles in the microstructure. Nucleation of recrystallization is illustrated for a cold deformed annealed AA1050 alloy in Figure 2.13. Nuclei grow at the expense of the deformed or recovered microstructure and leave behind new, strain free crystallites. Recrystallization nuclei are often found to be subgrains with a size larger than a critical value, particularly true for subgrains with Cube orientation. A large subgrain size can be associated with a lower stored energy and growth of overcritical Cube oriented subgrains into e.g. S, which have a smaller subgrain size and larger stored energy, is energetically favourable as the total stored energy is decreased.

Nucleation is followed by grain growth. Though, as long as there are unrecrystallized regions left behind, nucleation can occur at any point in time during the recrystallization process. Recrystallization may not necessarily appear that different from subgrain growth but a recrystallized grain has by definition high-angle boundaries toward its surroundings whereas subgrains have low-angle boundaries. The higher mobility of HAGBs generally makes recrystallization progress faster than recovery and subgrain growth. Growth of nuclei with a Cube or R orientation is particularly fast because they have a $40°\langle 111\rangle$-rotation relationship with S oriented regions. This $\Sigma 7$ boundary is highly mobile and, in

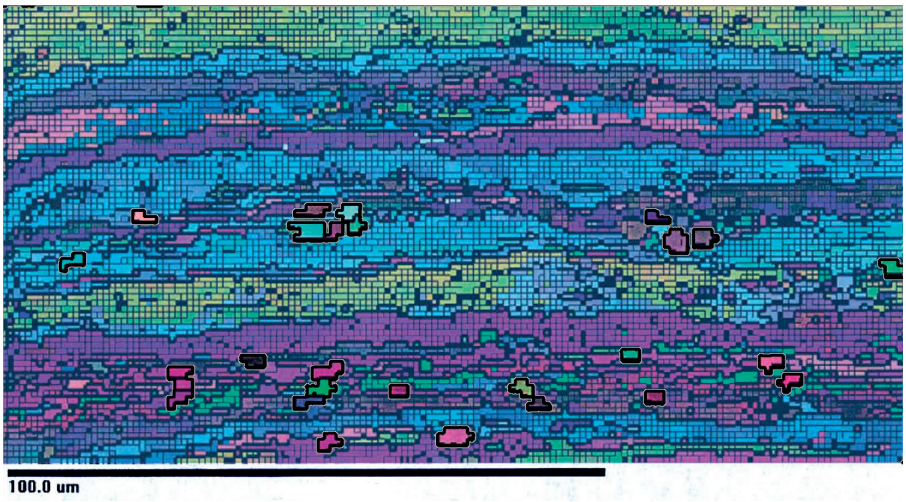

Figure 2.13: Orientation micrograph from EBSD scan of 90% cold rolled AA1050 alloy annealed at 250 °C for 300 seconds with superimposed recrystallization nuclei. After Vandermeer and Juul Jensen [2001].

addition, S is one of the deformation texture components and usually abundant in the deformation microstructure.

There might however be a transition period where only one or some of the boundaries have high-angle character. This is particularly true for discontinuous subgrain growth, where subgrains with misorientations deviating from their surroundings have a misorientation advantage. In sites of high strain energy with an orientation gradient, rapid recovery is expected and subgrain growth will produce HAGBs early. These are then nearly strain free subgrains with partially mobile HAGBs in a preferable growth environment, i.e. perfect recrystallization nuclei. These quasi-recrystallized grains are vaguely defined and can cause some confusion.

A different nucleation mechanism is *strain induced boundary migration* (SIBM), first described by Beck and Sperry [1950]. At low to medium strain, either side of a HAGB will usually have different strain levels due to different orientations initially or after rotations during grain break-up. A curved segment of a HAGB extending over several subgrains can consume the higher energy area by a bulging movement of the boundary either by extending some of the substructure or leaving behind a low-angle boundary. Either way, the newly claimed areas either have coarser substructure than before or are completely dislocation free and represent a significant decrease in stored energy. When the stored energy difference across the HAGB is large, SIBM by a single subgrain is more likely because the necessary curvature $R_{crit} > {}^{2\gamma}/_{\delta E}$ is easier to obtain over a short distance when there is no substructure holding the bulge back. The orien-

tation of the recrystallized region left behind by the bulging grain boundary will usually be similar to the orientation of the grain on the concave side of the bulge. However, at strains larger than 40% the recrystallized grains may have orientations different from either of the grains involved in SIBM [Beck and Sperry, 1950].

Single grain SIBM is somewhat similar to "homogenous nucleation" of recrystallization by a subgrain with a misorientation advantage described earlier, which in the vicinity of a HAGB would also have an immediate and even larger growth advantage [Hutchinson, 1989]. This is also true for transition bands where there is a particularly large orientation gradient. Recovery and subgrain growth is rapid in a transition band due to the large driving force and large misorientations are easily accumulated. In shear bands there are also large orientation gradients and usually larger subgrains with more highly misoriented boundaries due to the large amount of strain. The exact nucleation mechanism is however less understood. The orientations of the recrystallized grains are helpful in this respect but are found to be very case dependent [Nes and Hutchinson, 1989].

In alloys containing a certain amount of alloying elements, large particles forms during casting that are non-deformable. They are not removed by subsequent homogenization but can break up during deformation. If their size after deformation is still larger than a critical diameter determined by the strain level, *particle stimulated nucleation* (PSN) can occur. Their size must typically be larger than $\approx$1 μm, though larger sizes might be necessary or more efficient. This is because recrystallization nucleates within the deformation zone surrounding the particles, or other types of particles or second phase elements for that matter. The particles must be large enough to lead to inhomogeneous deformation and local accumulation of strain. In the deformation zone there are smaller than average and highly rotated subgrains and extremely large orientation gradient, which are ideal for rapid recovery and subgrain growth. Thus, viable recrystallization nuclei form with a different orientation than their surrounding matrix, i.e. separated by mobile HAGBs favourable for growth.

2.3 Precipitation

In aluminium, the solid-solid phase transformations have received great attention because aluminium does not have allotropes under industrial circumstances. A solid-solid phase transformation is initiated by the nucleation of a second phase and growth of this solid phase in the aluminium matrix. Inherent to precipitation in a specific alloy is a decrease of the solubility of at least one component with decreasing temperature and precipitation leads to a local change of the atomic structure, composition and mechanical properties. The rather nice image in Figure 2.14(a) presents a detailed view of the atomic

structure of a precipitate, the surrounding matrix and interphase relationship. This is only one of several sequences of the precipitation process which leads to the stable phase and is different for different alloy systems.

Like any other phase transformation, solid-solid phase transformations are controlled by the Gibbs Free energy. Similarly to the solid-liquid phase transformation, i.e. solidification, formation or precipitation of a second phase can occur uniformly in the matrix or at heterogeneities which are more energetically favourable. Precipitation will occur when the free energy of formation is less than zero. The volume free energy of the nucleus is negative and counteracted by an increase in energy from creating a new surface and a strain field due to a lattice misfit of the new phase (see Figure 2.2(a)). The critical size for nuclei to be stable increases with increasing surface energy and strain energy, but precipitation is enhanced by undercooling as long as diffusion of solute atoms is not too slow. Heterogeneous precipitation at vacancy clusters, dislocations and subgrain or grain boundaries facilitates the nucleation of precipitation by reducing the surface and strain energies. Figure 2.14(b) shows how solute clusters form on grain boundaries and even dislocation lines, which under favourable conditions will form precipitates. Heterogeneous nucleation can be so efficient that incoherent, equilibrium phases form directly, a phenomenon which is rarely the case for homogenous nucleation. Instead, homogenous nucleation typically takes place by clustering and formation of fully coherent Guinier-Preston zones, followed by a sequence of metastable transition phases until finally the stable phase is formed. One such metastable precipitate with partial coherency with the aluminium matrix is illustrated in Figure 2.14(a).

During heating of a sample with a quenched in metastable, super saturated solid solution, decomposition of the alloy can occur by nucleation and growth or spinodal decomposition. During nucleation and growth a distinct interface is always present and matrix solute atoms reach the interface through diffusion in a negative concentration gradient. Spinodal decomposition, on the other hand, requires transport of solute in a positive concentration gradient. The growth of initially small concentration perturbations is gradual and relies on fluctuations in concentration and the effect of coherency strain fields and gradient energy. When a spinodal composition is reached, there is no thermodynamic barrier to growth which is only controlled by diffusion. Eventually, spinodal decomposition also leads to a distinct interface and further growth of the precipitates is controlled by diffusion from the supersaturated matrix to the depleted zone around the particle or the rate at which solute atoms reach the interphase. For small precipitates, growth is interphase controlled but as the diffusion distance increases diffusion becomes rate controlling. Eventually the matrix will be at equilibrium and further growth occurs by dissolution of smaller particles (particle coarsening).

Quenched-in vacancies, dislocations and subgrain and grain boundaries have

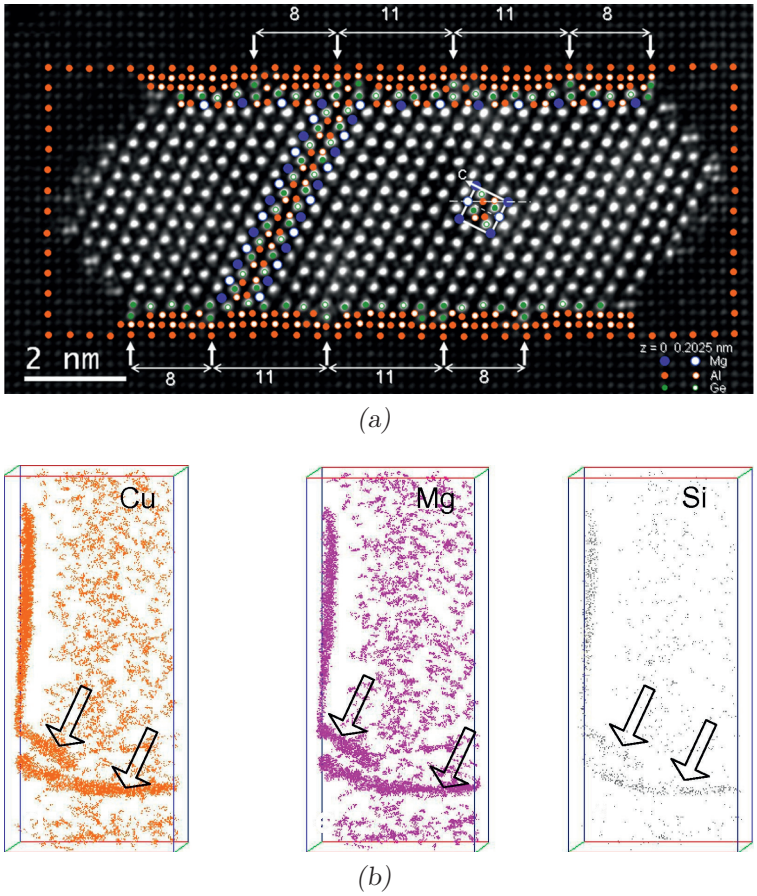

Figure 2.14: Filtered HAADF STEM image in (a) of a U1-Ge precipitate with superimposed atomic model [Bjørge et al., 2011]. Atom-probe tomography maps of AA2024 alloy aged at 170 °C for 0.5 hours in (b) showing cluster at a grain boundary (vertical) and two dislocation segments (arrows) after the removal of matrix solute atoms. [Sha et al., 2011]

a profound effect on the nucleation and growth kinetics of precipitation. They all act as heterogeneous nucleation sites and speed up diffusion significantly. The more open lattice structure at such imperfections reduces the activation energy for diffusion at low temperatures by as much as 50% over lattice diffusion in the case of grain boundaries. Figure 2.14(b) clearly show how grain boundaries and dislocations are preferential sites for precipitation. The volume fraction of grain boundaries is however relatively low. Dislocations, in addition to subgrain boundaries, in a heavily deformed material are plentiful and lead to pipe diffusion where the cross sectional area fraction of dislocations typically is $\approx 10^{-7}$. Pipe diffusion is less sensitive to temperature than lattice diffusion and can at low temperature be the sole diffusion path in addition to grain boundaries. Not only do dislocations and grain boundaries aid diffusion but they also attract solute due to a relaxation of the misfit strain fields surrounding solute atoms. Hence, solute concentrations and diffusion rates are both expected to be higher at microstructural heterogeneities like vacancies, dislocations and subgrain and grain boundaries.

2.3.1 Concurrent Precipitation

Knowing how dislocations and subgrain boundaries act as sinks and diffusion paths for solute atoms, it should come as no surprise that precipitation on the deformation substructure during annealing has been observed experimentally in several alloy systems [Hornbogen, 1977; Hutchinson and Duggan, 1978; Marshall et al., 1991; Morris and Duggan, 1978]. Precipitation mainly occurs on low-angle boundaries where the precipitates exert a pinning effect retarding the softening reactions. This phenomenon is known as concurrent precipitation and is important for recovery and recrystallization kinetics as long as recrystallization is not complete before the onset of precipitation.

Precipitates on the substructure can prevent growth to occur through the Zener drag as discussed in Section 2.2.1 and can prevent recrystallization from happening. This is illustrated by regime I in Figure 2.15. However, depending on the annealing process, the precipitates may grow and even coarsen sufficiently to destabilize the substructure and lead to continued recovery and possibly recrystallization. After cold rolling, the precipitates form on the lamellar substructure and if the structure recrystallizes the grains usually become elongated in the rolling direction due to a lower Zener drag between the horizontal lamellas. As can also be seen from the *time-temperature-transformation* (TTT) diagram in Figure 2.15, the heating rate is important and controls the fraction precipitates which will be encountered initially by the recrystallization front.

If recrystallization has already started and precipitation then commence, i.e. regime II in Figure 2.15, a slightly different microstructure to the elongated grains appears. It is more inhomogeneous as recrystallization is sensitive to the

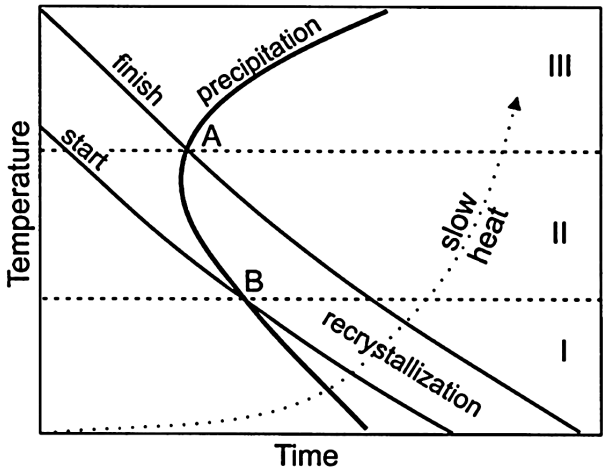

Figure 2.15: Schematic time-temperature-transformation (TTT) diagram for recrystallization and precipitation in supersaturated and deformed aluminium. [Humphreys and Hatherly, 2004]

local driving force and Zener drag. Recrystallization will be facilitated when the driving force is large and the Zener drag low. If the opposite is true, the deformation structure will be retained for longer times. In addition, preferential nucleation can occur on random boundaries while special boundaries are less susceptible to Zener drag, an aspect which may have a great influence on the texture. Concurrent precipitation is sometimes observed to favour nucleation of recrystallization by the SIBM mechanism. In regime III, recrystallization into a fine grained and equiaxed structure is finished before any precipitation can occur, a situation where the only remaining nucleation cites for precipitation are HAGBs. Because the grain interiors are dislocation free, diffusion is also slow but solute can be redistributed to the grain boundaries by a sweeping action of mobile grain boundaries [Sulonen, 1960; Turnbull, 1955].

2.4 Texture

A polycrystalline material is, as the name suggests, composed of several crystallites which are oriented in a particular way relative to the sample geometry. The crystallites are called grains when they are separated by high-angle boundaries and subgrains when the angle is below 15°. The grain or subgrain orientations influence mechanical properties and are one reason for anisotropic behaviour. The grains may have nearly random orientations, i.e. after casting with grain refiner, but during deformation or heat treatments certain orientations are more energetically favourable and a non-random distribution of

orientations develop which is called a texture. Depending on the material and processing, certain preferred textures form that consists of a few typical orientations with specific names. Aluminium is typically deformed either by extrusion or rolling and the sample symmetry {S} is then defined by the *extrusion* or *rolling direction* (ED or RD), the short *transverse direction* (TD) and the *normal direction* (ND) in the thickness direction.

2.4.1 Representing Texture

The crystal lattice {C} is usually defined by low index orthogonal vectors like the ⟨001⟩-directions. The exact orientation of each grain can then be specified by a matrix rotation which represents the necessary rotations to make the sample coordinate system and crystal lattice coincide. The orientation of each individual grain has to be obtained from diffraction experiments, e.g. by TEM, EBSD or X-ray measurements, and related to the sample symmetry either by an axis of rotation and a rotation angle, a triplet of Euler angles or by a set of Miller indices. In this work, the Euler angles with Bunge's notation $(\varphi_1, \Phi, \varphi 2)$ are used and will be further explained [Bunge, 1982]. φ_1 is the rotation about the ND axis to bring RD into the plane spanned out by two of the crystal vectors. Keeping RD in the plane, Φ is then the rotation about RD to make ND parallel to one of the crystal axes. Finally, to make the two systems coincide, φ_2 is the rotation angle about ND.

Now that all the individual orientations can be represented mathematically, the question is how to present them graphically? The simplest way is to plot each individual orientation in a stereographic projection. An imaginary unit sphere is created around the sample coordinate system. For every grain in the sample, the unit cell is placed at the origin of the sample coordinate system and the intersection of a set of plane normals $\{hkl\}$ with the northern hemisphere noted. The points of intersection are connected to the south pole by poles. In the stereograph projection, or pole figure, the intersection of theses poles with the equatorial plane is plotted. To describe an orientation unambiguously, at least two poles are necessary. For cubic crystals, the lowest indexed planes {001} have three poles, thus, any pole figure can describe the orientation satisfactory.

EBSD maps of the microstructure often give colourful presentations of the grains. Such maps can be inverse pole figure maps where the colour represents the rotation necessary to bring the sample coordinate system into the crystal lattice. Each corner of the unit triangle ([001], [011] and [111]) are given a colour and all other orientation within the triangle are defined by a mix of the corner colours. To have any meaning, the unit triangle must be related to one of the specimen directions ND, TD or RD, i.e. the colour give the pole which is parallel to the chosen sample direction.

The two previously mentioned presentation techniques give the orientations in 2D only. Hence, in order to describe the texture, that is the complete orien-

tation distribution of the sample, a stronger tool is necessary. With the Euler angles already at hand, the most common way to present texture is by an *orientation distribution function* (ODF) in the 3D Euler space. An ODF cannot be plotted directly but must be calculated from pole figures or inverse pole figure data. However, in such EBSD or X-ray measurements, the necessary data for polar angles of more than 70–80° can be difficult to obtain. The pole figure data must be manipulated mathematically and the most common method is by spherical harmonic functions. For a cubic material, this method requires data from at least three different pole figures.

For FCC samples of orthotropic sample symmetry, the texture is presented in the 90° Euler space with constant φ_2 at 5° intervals. Orientation intensities in the φ_1-Φ plane can be presented in colours, greyscale or isointensity contour lines or a combination as shown in Figure 2.16. From ODFs it is possible to quantify the texture and identify the intensity along certain texture fibres. Also the volume fractions of individual texture components can be readily calculated. One of the drawbacks with ODFs is that each orientation is defined by three different rotations.

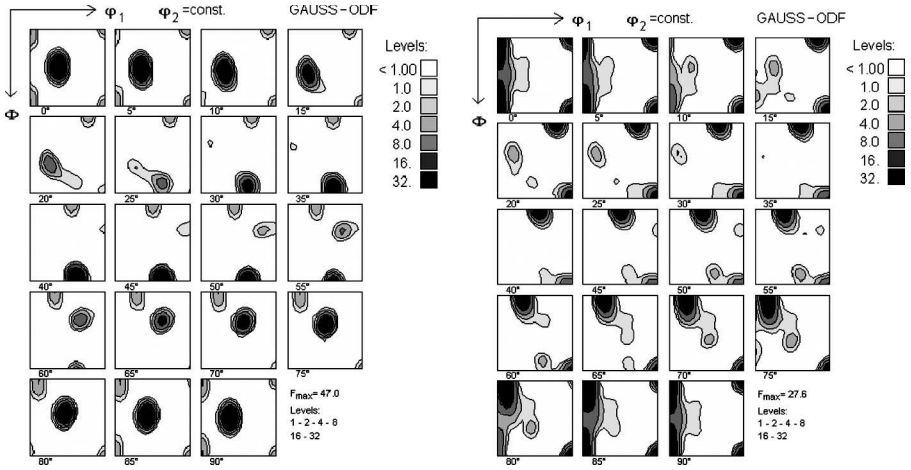

Figure 2.16: Typical deformation (left) and recrystallization (right) textures in aluminium as presented by ODFs. [Achani et al., 2011]

2.4.2 Textures in Aluminium

Orientation changes take place during deformation of aluminium due to geometrical constraints and because plastic deformation is easier in certain slip systems, i.e. crystallographic constraints. Which slip systems are activated and to what extent depend on the mode of deformation. The deformation texture also has a great influence on the recrystallization texture. Whatever initiates

nucleation of recrystallization, the nuclei must be present in the microstructure after deformation. The texture may also develop during growth of the recrystallized grain because certain boundaries have a growth advantage over others. In addition, recrystallization textures are particularly sensitive to changes in microchemistry. Industrial processing leads to a few well recognized orientations that constitute the most typical texture components found in FCC materials. In Table 2.1 these are categorized as deformation or recrystallization texture components and listed with their respective Miller indices and Euler angles.

*Table 2.1: Ideal components of the deformation and recrystallization textures in aluminium. * according to Engler [1999].*

	Miller indices	**Euler angles**		
Texture components	{hkl}⟨uvh⟩	φ_1	Φ	φ_2
Deformation				
Copper, Cu	{112}⟨111⟩	90°	35°	45°
S	{123}⟨634⟩	59°	37°	63°
Brass, B	{011}⟨211⟩	35°	45°	0/90°
Goss, G	{110}⟨001⟩	0°	45°	0/90°
Recrystallization				
Cube, C	{100}⟨001⟩	0°	0°	0/90°
ND-rotated Cube	{001}⟨110⟩	45°	0°	0/90°
Goss, G	{110}⟨001⟩	0°	45°	0/90°
CG	{520}⟨001⟩	0°	22.5°	0/90°
P	{011}⟨122⟩	65°	45°	0°
R*	{124}⟨211⟩	60°	35°	55°

Deformation

Because rolling is the preferred mode of deformation in this PhD work, only rolling textures will be considered in the following. In FCC materials there are two major rolling textures, the pure metal texture and the alloy texture. Which texture will be present is mainly decided by the deformation mechanism, i.e. slip or twinning. The determining factor is the stacking fault energy γ_{SFE} which is influenced by the solute level, hence the name for the different textures.

Pure metal texture is to be expected for high stacking fault energy materials like pure aluminium. This texture is characterized by several orientations which form a continuous tube in Euler space. These orientations are Brass, S and Copper and together they form what is known as the β-fibre. For lower stacking fault energy materials the β-fibre continues from Brass to Goss in what is known as the α-fibre. Both fibres and their position in Euler space are illustrated in Figure 2.17(a). Furthermore, a τ- and γ-fibre are also observed in the alloy texture.

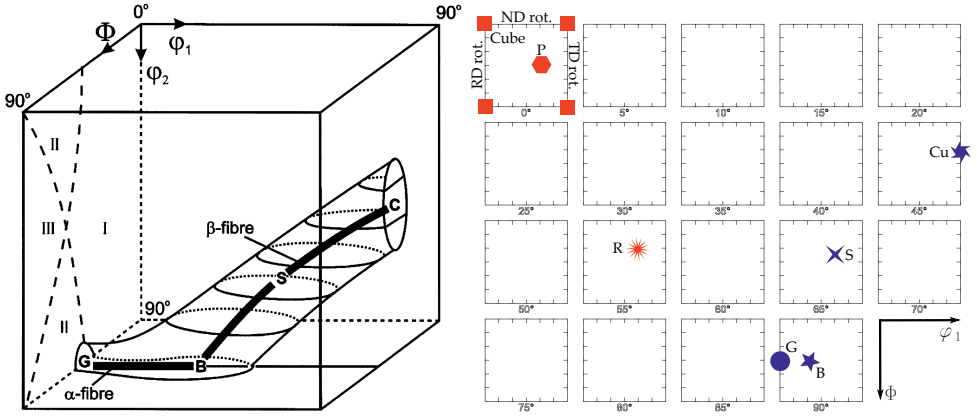

Figure 2.17: α- and β-fibre of FCC rolling texture in the 90° Euler subspace (a) [Humphreys and Hatherly, 2004] and some of the deformation (blue) and recrystallization (red) texture components indicated in an ODF with constant φ_2 (b).

Recrystallization

The recrystallization textures are more complex than the deformation textures in the sense that they originate from the deformation texture as well as being greatly influenced by the annealing temperature, boundary mobilities and microchemistry. Even so, the main component in a typical recrystallization texture for heavily cold rolled aluminium is very often Cube. The Cube component is strengthened by increasing temperature and deformation up to a certain point. The Cube orientation is not stable during cold rolling but must be present after deformation if the recrystallization texture is to have a Cube component. Hence, in severely cold rolled aluminium the Cube component may be suppressed because Cube rotates in the RD direction toward Goss. The reason for the strong Cube texture is debated. Cube subgrains are often found to have a larger than average size, possibly due to a low Taylor factor. Or Cube subgrains have an enhanced recovery rate which effectively creates dislocation free Cube nuclei surrounded by high energy regions which provides a strong driving force for recrystallization. It is also extensively documented that Cube subgrains have a growth advantage when narrow Cube bands are neighboured by regions of S-orientations because these two orientations form a low energy Σ7 boundary, better known as the $40°\langle 111\rangle$ orientation relationship.

According to Daaland and Nes [1996], a $40°\langle 111\rangle$ orientation relationship can also be responsible for the ND-rotated Cube texture component, particularly at low annealing temperatures when recrystallization is influenced by concurrent precipitation. The ND-rotated Cube texture has a $40°\langle 111\rangle$ orien-

tation relationship with the Cu orientation and nuclei form early and are not as influenced by precipitation as for examples nuclei formed at large second phase particles.

Large constituent particles may have a pronounced effect on recrystallization textures. The particles ought to be larger than a couple of micrometres and must be present before deformation. This is the PSN effect previously mentioned, where large, non-deformable particles induce deformation zones of large strains typically at the equatorial plane parallel to the rolling direction. Slip taking place in the particle deformation zone is more chaotic than in the matrix and, although the nuclei have an orientation relationship with the matrix, there is a larger spread of the orientations resulting in a randomization of the rolling texture, i.e. pure metal texture. There are however also some evidence of selected nucleation of ND-rotated Cube and P texture components from these deformation zones [Engler et al., 1996c; Sjølstad, 2003].

Particles smaller than 1 μm, like dispersoids, also influence the recrystallization texture. Small, deformable particles lead to an anisotropic behaviour during deformation with formation of shear bands in which Goss and P oriented grains nucleate. The resulting texture can still be strongly influenced by Cube. The mechanism for recrystallization if the particles are small and present during deformation is SIBM. For narrow Cube bands which have a lower stored energy but are surrounded by higher energy regions, SIBM is a favourable recrystallization mechanism. Growth of Cube in a Zener drag situation is less influenced possibly due to a decreased drag effect on the special Cube boundaries or other low energy, low index *coincident site lattice* (CSL) boundaries, suppressing other texture components [Humphreys and Hatherly, 2004].

Alternatively, by exhibiting a Zener drag on the boundaries, dispersoids stabilize the deformation structure and promote extended recovery. Viable recrystallization nuclei are pinned and the texture is mainly constituted by a component similar to the rolling texture components. This is the retained rolling texture R which resembles the S deformation texture. There are two variants of R used ambiguously in literature. One nucleates from within the spread of the deformation texture component by continuous recrystallization, or extended recovery, and retains the S orientation. The second type of R is more misoriented from S and has the position in Euler space given in Table 2.1. It nucleates by SIBM and has a well-defined orientation due to growth selection ($40°\langle 111\rangle$) [Engler, 1999]. This causes some confusion when referring to observations in literature since the R orientation is seldom given precisely. The R texture component is also reported to be promoted by iron in solid solution in commercial purity alloys by solute drag or precipitation on the recrystallization front and thereby slow down the growth of Cube grains [Humphreys and Hatherly, 2004].

2.5 Literature Review

Now that general theory and fundamental concepts have been introduced, a more detailed background and literature review on recovery and annealing phenomena which are relevant to the scope of this PhD work is given. First, several of the most important publications on subgrain growth and nucleation of recrystallization are presented to give an overview of the many interesting aspects of softening reactions, evolution of typical properties like boundary misorientations and characteristics of differently oriented microstructures. The second and last section is dedicated to the effect of dissolved iron on annealing behaviour in commercial and high purity aluminium alloys. Iron is an important element because it is hard to remove by refining; it has a low solubility at RT and is a very slow diffusing element in aluminium. These properties make high and commercial purity alloys sensitive to iron and the processing parameters.

2.5.1 Subgrain Growth

In the beginning of the 1950s, Heidenreich [1949, 1951] did some pioneering studies on the formation of recovery domains by TEM in aluminium. The recovery domains were followed by the formation of a polygonized structure with 1–2 μm large subgrains that were only slightly misoriented from each other. TEM studies of subgrains continued in the 1970s when numerous papers on the growth mechanisms and kinetics were published [Exell and Warrington, 1972; Jones et al., 1979; Modéer and Odén, 1975]. Sandström [1977a,b] presented models for recovery by different mechanisms based on theoretical studies. Model predictions were later backed up by experimental results from extensive TEM work on subgrain growth in pure aluminium and a binary Al-Mn alloy [Sandström et al., 1978]. Figure 2.18 shows experimental data from the 1% Mn case and predicted growth to follow the parabolic growth law; $D^2 - {D_0}^2 = ct$ where $n = 2$ and c is a temperature dependent constant. The next decade saw only sporadic work on recovery in aluminium, but due to the industrial importance of knowing the softening behaviour for hot and cold worked aluminium, recovery received new attention in the beginning of the 1990s e.g. by Nes [1995], Furu et al. [1995] and Humphreys [1997] which also introduced a new characterization method. The EBSD technique.

Throughout the 1990s the EBSD technique developed fast and made it possible to study microstructures in greater detail. Pattern acquisition speeds increased, ensuring that subgrains could be characterized much more extensively. Although EBSD could not reveal the same details as TEM, measurements of orientations, misorientations and growth kinetics were still quite accurate. F. J. Humphreys in particular utilized the EBSD technique to gain improved knowledge of recovery and subgrain growth, work which is summarized along with an extensive literature review in the book by Humphreys and Hatherly

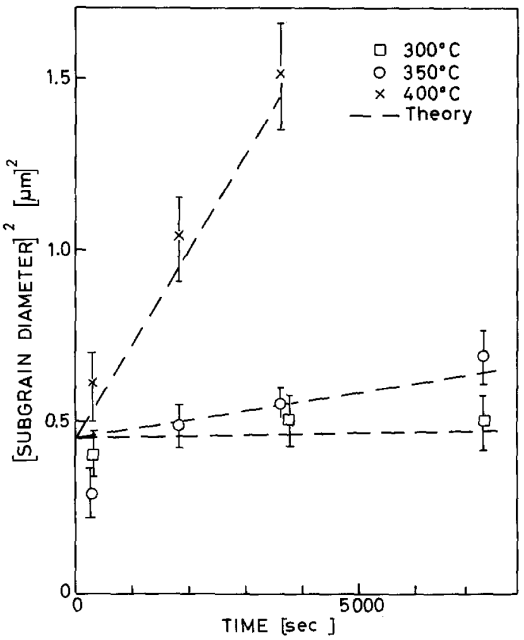

Figure 2.18: Subgrain growth following the parabolic growth law at various temperatures after 80% cold rolling of Al-1% Mn alloy. [Sandström et al., 1978]

[2004].

Somerday and Humphreys [2000] investigated recovery in an Al-1.3 wt.% Mn alloy. Samples were cold rolled to 90% reduction and subsequently annealed at temperatures ranging from 300 °C to 550 °C. Only temperatures below 450 °C were interesting with respect to recovery, and precipitation and recovery processes were occurring simultaneously. At 300–350 °C precipitation occurred immediately at LAGB and effectively pinned the boundaries. Although some growth was observed, both subgrain sizes and misorientations remained relatively constant with annealing time. At 375 °C some precipitation free boundaries were present, mostly prior high-angle twin boundaries, which nucleated recrystallization by SIBM.

Subgrain growth and low-angle boundary mobilities were studied by Huang and Humphreys in two Al-0.05 wt.% Si single-phase, single crystals from reconstructed EBSD maps after annealing at temperatures between 250 °C and 450 °C. In Huang and Humphreys [2000], a $\{110\}\langle001\rangle$ crystal was compressed in a channel die to a reduction of 30% (cold) and 70% (cold and hot), after which the microstructure consisted of almost equiaxed subgrains with more or less the same $\{110\}\langle001\rangle$ orientation and no long range orientation gradients. Huang et al. [2000] covered only deformation at elevated temperatures, where a $\{100\}\langle001\rangle$ single crystal was deformed by PSC at different strain rates to a to-

tal reduction of 75%. As opposed to the $\{110\}\langle001\rangle$ orientation, the $\{100\}\langle001\rangle$ orientation was not stable during PSC, particularly at low temperatures and high strain rates, and long range orientation gradients were introduced.

For the growth curves in Figure 2.19, the accompanying mean misorientations in the $\{110\}\langle001\rangle$ single crystal was found to decrease upon annealing, i.e. for larger average subgrain sizes, in accordance with theoretical predictions [Huang and Humphreys, 2000]. Subgrain growth took place discontinuously with slower kinetics deviating from the parabolic law as found by Sandström et al. [1978] with various, larger n-values. Highly misoriented subgrains became less misoriented upon growth, thus decreasing the driving force, while other subgrains found themselves in a better growth environment. Subgrain coarsening in the deformed $\{100\}\langle001\rangle$ single crystal was relatively homogenous within bands of similar subgrain size. However, the amount of growth varied a lot from one band to another and substantial growth was observed within localized bands. The mean subgrain misorientations increased because the long range orientation gradients remained almost constant upon annealing and were unaffected by subgrain growth. In the $\{110\}\langle001\rangle$ single crystal case, no particular correlation was found between subgrain size and mean misorientation. On the other hand, size and misorientation were strongly correlated in the hot deformed $\{100\}\langle001\rangle$ case and highly misoriented grains also grew most rapidly. Hot and cold deformation seems to alter the subgrain growth mechanism as Huang and Humphreys [2001] found annealing of hot deformed $\{110\}\langle001\rangle$ single crystals also to produce a microstructure where the largest subgrains were also the most misoriented.

The growth results from the $\{110\}\langle001\rangle$ single crystal were fitted to a new cellular growth model. The migration of subgrain boundaries seemed to be controlled by a thermally activated mechanism and the corresponding activation energy was found to be 134 kJ/mol for LAGBs and 150 kJ/mol for HAGBs. Both energies are higher than the activation energy for self-diffusion in aluminium, but close to that for lattice diffusion of silicon in aluminium. The misorientation related to a boundary was also found to have a strong effect on the mobility. LAGBs had a much lower mobility than HAGBs, which again had a much lower mobility compared to $40°\langle111\rangle$ tilt boundaries. For larger misorientations observed in deformed $\{100\}\langle001\rangle$ single crystals, the mobility did not increase that much with increasing misorientation but formed a plateau for misorientations from 15° to 20°. In contrast to the $\{110\}\langle001\rangle$ case, an increase in activation energy with misorientation up to 15° misorientation was clearly observed. The activation energies for the different samples investigated were in the range of 135–160 kJ/mol, also in support of a migration mechanism controlled by solute diffusion.

Huang and Humphreys [2001] also investigated recovery in $\{110\}\langle100\rangle$ and $\{100\}\langle100\rangle$ oriented single crystals of Al-0.05 wt.% Si. Samples were deformed

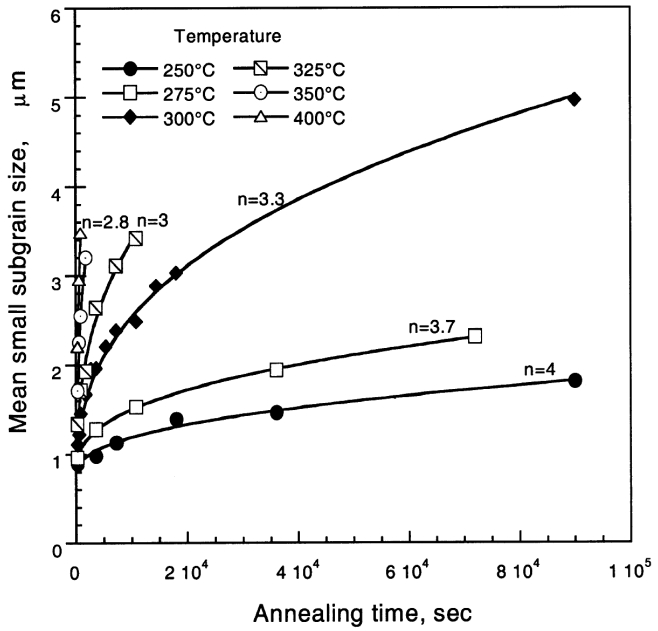

Figure 2.19: Subgrain growth in isothermally annealed {110}⟨001⟩ single crystal aluminium with 0.05 wt.% Si after 70% cold deformation. [Huang and Humphreys, 2000]

and annealed similarly to previous work [Huang and Humphreys, 2000; Huang et al., 2000]. Again, a strong correlation between subgrain size and misorientation was found and not only for the {100}⟨100⟩ case, as already described in Huang and Humphreys [2000], but also in the deformed {110}⟨100⟩ single crystals. For {110}⟨100⟩, it could however not be concluded whether large subgrains also were the most misoriented [Huang et al., 2000]. Continuous subgrain growth found in the {110}⟨100⟩ single crystal was also observed and differed from the discontinuous growth described previously by Huang and Humphreys [2000] on similar materials. However, the seemingly contradicting results were explained by different annealing conditions resulting in very different growth factors. Other results, like the rapid increase of the mobility with increasing misorientation which finally saturated at 15° and the activation energies for boundary migration were in agreement with previous work [Huang and Humphreys, 2000; Huang et al., 2000].

It is described by Hasenclever [2002] how the heating rate during annealing influence the recovery and recrystallization behaviour of an Al-1.0 wt.% Mn alloy. A heating rate of more than ∼2 °C/s was required to prevent precipitation and obtain a fine grained recrystallization structure after annealing at 400 °C. Slower heating rates resulted in a coarse grained material. Discontinuous subgrain growth, where some subgrains grow significantly larger than

their neighbours, can occur also in single-phase aluminium according to model predictions made by Holm et al. [2003]. From an analytical model of abnormal subgrain growth, a recrystallization model was derived and simulations suggested that abnormal subgrain growth was due to non-uniform boundary mobility. Anisotropic boundary energy, sometimes believed necessary, was not required.

Another mechanism for nucleation of recrystallization was considered by Sabin et al. [2003]. They characterised the orientations in the vicinity of triple junctions before and after annealing to yield recrystallization nuclei in high purity aluminium. Half of the recrystallization nuclei found had orientations within the spread from one of the deformed grains, but several nuclei were also found to be rotated about an axis close to $\langle 111 \rangle$ relative to one of the original grains. A mechanism for the $\langle 111 \rangle$ rotated nuclei was not found, although the normal of slip planes predicted to be highly active during deformation correlated with the rotation axis. For subgrains with deformation texture orientations which turned into recrystallization nuclei, the mechanism was recognised as subgrain coalescence and SIBM. Nucleation by SIBM is also observed from Cu and Goss bands by Brough and Humphreys [2010a]. However, when the recrystallized grains grew into regions of similar orientation, growth almost ceased.

In an AA3103 alloy with different amounts of Mn in solid solution, Tangen et al. [2010] found PSN to play a significant role in the nucleation of P and ND-rotated Cube texture components. The few Cube oriented grains found after recrystallization were assumed to be a result of grain fragmentation and to nucleate from Cube subgrains within transition bands. Prior to recrystallization, the Cu and S texture components were reported to sharpen with increasing annealing time and generally an increasing amount of Mn in solid solution resulted in smaller and less misoriented subgrains. During annealing at 350 °C precipitation did not occur in the 0.31 wt.% alloy, but both the 0.42 wt.% Mn and, especially, the 0.5 wt.% Mn alloys were influenced by concurrent precipitation.

The recrystallization behaviour of high purity Al-1.3 wt.% Mn and Al-0.3 wt.% Mn was investigated by Somerday and Humphreys [2003a] and Somerday and Humphreys [2003b], respectively. Recrystallization was found to be influenced by concurrent precipitation also here. At annealing temperatures in the range 400–550 °C in the 1.3 wt.% Mn alloy, the main recrystallization mechanism was broad front SIBM of HAGB segments, resulting in a microstructure of equiaxed grains. However, at temperatures below 400 °C precipitation took place earlier in the softening process and at 375 °C both precipitation and recrystallization took place within 1 minute. Rather than $\Sigma 3$ twin boundaries as found by Somerday and Humphreys [2000], it was special boundaries like $\Sigma 7$, where precipitation is difficult, which stayed mobile and initiated recrystallization by SIBM. Recrystallization was more difficult at 350 °C and HAGBs (and LAGBs after long annealing times) were pinned by precipitates. Only a slight

increase in subgrain size and misorientation was observed in this case.

In the leaner Al-0.3 wt.% Mn alloy, the effect of different grain sizes before deformation was investigated. Annealing at 275–350 °C did not lead to precipitation in any of the two samples, the grain size did however have an influence on softening. The microstructure of the coarse grained material became very inhomogeneous after deformation with several new HAGB due to grain fragmentation. Also, the Goss texture component was more pronounced after deformation in the coarse grained material compared to the fine grained. In fragmented grains, the subgrain size was rather small (0.75 μm) and the average misorientation quite high (5°). Here, nucleation of recrystallization was easy due to many HAGBs making SIBM from single subgrains the primary nucleation mechanism. The amount of fragmentation of a grain depended on the original orientation and caused heterogeneous recrystallization. Grains with unstable deformation texture orientations became more fragmented and recrystallized easily, resulting in fine grained regions with orientations close to P and ND-rotated Cube. The recrystallized regions grew into regions with stable orientations like Copper S and Goss that were not yet recrystallized. When stable Cu, S and Brass regions eventually recrystallized, the grain structure was coarse due to few nuclei (lack of mobile HAGBs).

Similarly, Xing et al. [2006] found large subgrains within bands with unstable orientations to grow into bands with the stable Cu, S and Brass orientations. Coarsening also seemed to be more pronounced near or at HAGBs, the mechanism assumed to be subgrain coalescence or a combination of subgrain coalescence and SIBM. In an Al-0.1 wt.% Mg alloy hot deformed to a strain $\varepsilon = 1.6$ and annealed at about 280–300 °C, Brough and Humphreys [2010a] correlated subgrain growth and nucleation of recrystallization with orientation. The average subgrain misorientation was approximately 3.9° in Bs, Cu and S components and 4.8° in the Cube component. The Cube-subgrains also coarsened significantly faster than subgrains with other orientations (including Goss). Cube grains nucleated by SIBM grew easily into bands with S orientation due to the $40°\langle 111\rangle$-rotation between them.

By 3-Dimensional synchrotron X-Ray Diffraction (3DXRD), Gundlach et al. [2004] studied in-situ growth of subgrains with a spatial resolution of 0.3 μm. The commercial purity aluminium AA1050 alloy was deformed by cold rolling to a reduction of 38% and had an average subgrain size of 2.4 μm after deformation. Figure 2.20 illustrates the growth sequence of a recrystallization nucleus. After 3 minutes of annealing at 300 °C the subgrain size increased to 3.2 μm, while after 181 minutes of annealing only a minimal additional increase to 3.4 μm was observed. Although a limited number of subgrains were measured, no support for a classical curvature driven growth model where the large grains grow at the expense of the small was found. In fact, some of the smallest subgrains were found to grow the most, while some of the largest were found not

to change size or even shrink. Also, within the accuracy of the method (0.3°) no rotation of the subgrains (coalescence) was observed during annealing.

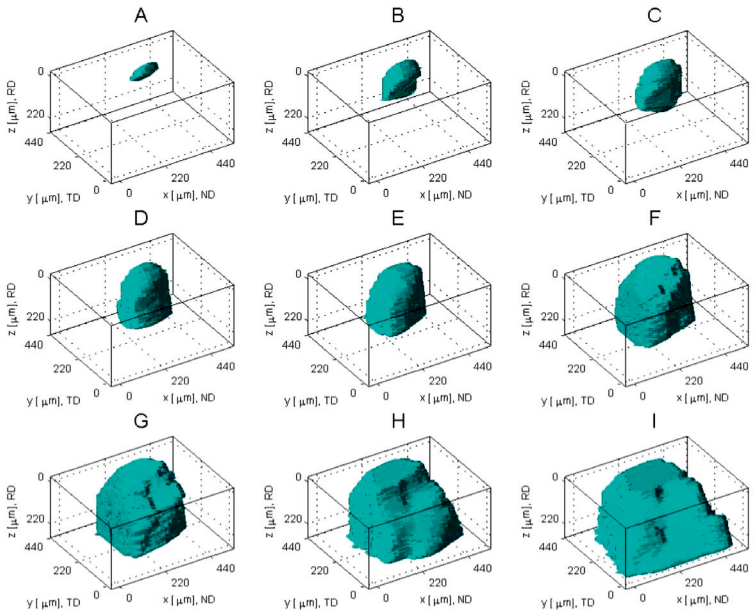

Figure 2.20: Subgrain growth, recrystallization and grain growth followed by 3DXRD. [Schmidt et al., 2004]

Considerable work has been done on activation energy considerations and accurate measurements of boundary mobilities. E.g. Driver, Maurice and co-workers have published several papers on grain and subgrain growth. For HAGBs, Lens et al. [2005] found migration in Al-0.1 wt.% Mn and Al-0.3 wt.% Mn ($\varepsilon = 1.1$) to be controlled by solute drag during annealing at temperatures in the range 200–450 °C, although in the 0.1 wt.% Mn alloy some boundaries were also partially free from solute. With most activation energies in the range 120–160 kJ/mol, and some in the range 150–190 kJ/mol for particularly slow migrating boundaries in the 0.1 wt.% Mn alloy, diffusion of dissolved Mn is believed to be rate controlling. The activation energies for boundary migration are in between that of the 211.4 kJ/mol for lattice diffusion of Mn in aluminium and the ∼50% lower activation energy for boundary diffusion of Mn [Hood and Schultz, 1971]. High activation energies of 175 kJ/mol were later also found when the Al-0.1 wt.% Mn alloy was deformed to a strain $\varepsilon = 1.6$ by Driver et al. [2006] making it reasonable to assume boundary migration to be controlled by solute Mn.

Activation energies for general boundary migration are reported to be similarly high as the HAGB values presented above. Both in a commercial purity AA1200 alloy investigated by Ekström et al. [2004] and an AA3103 alloy studied

by Ekström et al. [2006], were the activation energies for boundary migration closely correlated with the lattice diffusion of iron and manganese, respectively. Even for subgrain boundaries with LAGB character have Huang and Humphreys [2001] calculated the activation energy for boundary migration to vary from 125–160 kJ/mol with increasing misorientation from 2–15°. Thus, there seems to be no difference between HAGBs and LAGBs since these values were in the range of the activation energy for lattice diffusion of silicon in aluminium and the migration rate is suggested to be controlled by solute diffusion.

However, for LAGBs, i.e. subgrain boundaries, in the Al-0.1 wt.% Mn alloy (at strain $\varepsilon = 1.6$) during in-situ annealing at 150 °C to 300 °C, Driver et al. [2006] found significantly smaller activation energies of about 60 kJ/mol. A similar activation energy was later confirmed by Barou et al. [2007] during annealing experiments of the same materials in an air circulation furnace. Somewhat surprisingly, Driver et al. [2006] also found sub-boundary mobilities in the range 10^{-14}–10^{-15} m^4/Js, in line with sub-boundary mobilities in Al-0.05 wt.% Si alloy [Huang and Humphreys, 2001]. By an improved characterization method with better resolution, Barou et al. [2009] got much lower sub-boundary mobilities and slightly lower activation energies of 48 kJ/mol and 52 kJ/mol for sub-boundary migration in the 0.1 wt.% Mn and 0.3 wt.% Mn alloys, respectively. In these publications the normal grain growth kinetic law ($d^2 \propto t$) was used. However, the diffusion coefficient for Si in aluminium is several orders of magnitude larger than that of Mn at 300 °C yet in both alloy systems solute drag is assumed to be rate controlling. Later work using the Nes kinetic law (Section 2.2.1) gave activation energies compatible with solute diffusion control [Barou et al., 2012]. The proposed explanation by Barou et al. [2007] considers the orientation spread which is almost two times larger in the polycrystalline Al-Mn alloy than the single crystal Al-Si alloy and that large orientation gradients are favourable for subgrain growth.

In EBSD studies, misorientations below 2° are sometimes excluded. By TEM characterization of subgrain growth with an angular resolution of 0.2°, Xing et al. [2006] have illustrated how the angular resolution significantly influences misorientation distribution measurements. Samples from an AA1200 alloy were deformed to a strain $\varepsilon = 2$ and annealed at temperatures up to 280 °C. Xing et al. [2006] were able to characterize the misorientation distributions of subgrains with different orientations. A regular structure of lamellar boundaries was found in most bands except those with Cube orientation after deformation. In the Cube oriented bands, subgrains were more equiaxed. Average boundary misorientation and orientation spread were found to be smaller in the rolling texture components (Cu, S and Brass) than other components. Initially, upon low temperature annealing, the spacing of incidental dislocation boundaries (mostly low-angle boundaries) increased marginally, while the spacing between geometrically necessary boundaries (mostly high-angle boun-

daries) coarsened significantly. The different growth rates of high- and low-angle boundaries resulted in a more equiaxed structure. In bands with other orientations than the rolling textures components, more coarsening occurred because of a higher fraction of boundaries with larger misorientation angles and a higher stored energy.

By EBSD, Barou et al. [2009] were able make accurate observation of orientation dependent subgrain growth. Both the misorientation spread, average subgrain misorientation and the number of HAGBs decreased upon annealing, most likely due to the elimination of high energy and high mobility subboundaries. The growth rate was slower in the 0.3 wt.% Mn alloy than the 0.1 wt.% Mn alloy because of pinning by precipitates formed at the lowest temperatures. However, both alloys appeared to recrystallize by SIBM. The results reproduced in Figure 2.21 for subgrains with Bs, Cu and S orientations are rather similar and found to be smaller and have lower growth rates than subgrains with Goss orientation. In Barou et al. [2012] the experimental data are analysed in light of the logarithmic growth law and solute drag mechanism proposed by Nes [1995] and the model data fit rather well with the 0.1 wt.% Mn variant. Additional fitting was necessary to achieve good fit for the 0.3 wt.% Mn alloy, indicating that the solute drag approach to subgrain growth seems fundamentally correct but further refinement is required to make it handle variations in the microchemistry.

2.5.2 The Effect of Iron in Pure Aluminium Alloys

Iron is an element which is difficult to remove from aluminium alloys and has a tendency to accumulate e.g. as a consequence of recycling post-consumer scrap. If other alloy elements are abundant, these will be deciding for the properties. However, iron will usually be present, often as the major element, in commercial purity and even high purity alloys. The effect of iron on the softening behaviour is mainly related to solute drag and precipitation during intermediate annealing. Recrystallization texture is of course a result of the softening behaviour and the discussion is usually whether iron in solid solution or precipitated as clusters or particles enhances or reduces the formation of Cube texture. Even extremely small amounts of iron are found to have a pronounced effect on recovery kinetics and recrystallization texture. In the following a review of available literature on these two topics will be given.

Interannealing and Precipitation

Figure 2.22 exemplifies the effect of different interannealing processes on commercial purity alloys with iron initially in solid solution. The solute content before final annealing and the tensile strengths (Rm) after 1 hour final annealing at 280 °C were measured and there is a strong correlation between the two.

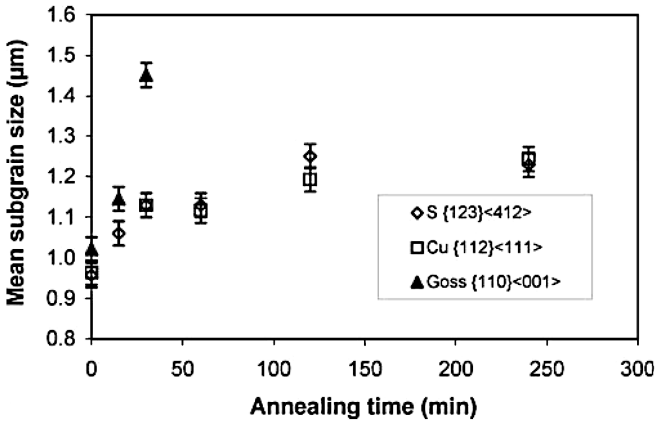

(a) 0.1 wt.% Mn at 200 °C.

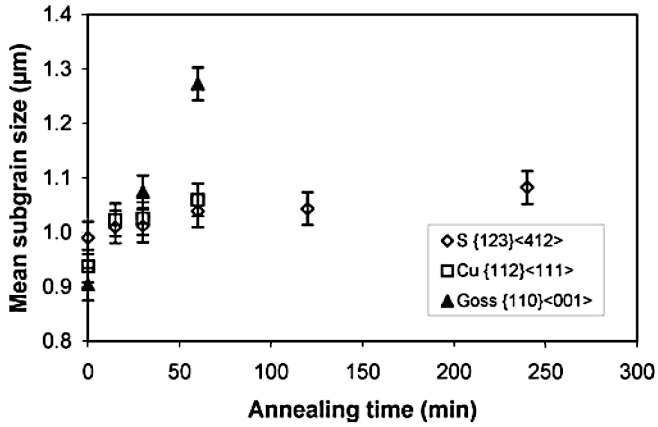

(b) 0.3 wt.% Mn at 275 °C.

Figure 2.21: Orientation dependent subgrain growth of Al-Mn alloy after channel-die compression to Von Mieses strain 1.8 and subsequent annealing. [Barou et al., 2009]

Intermediate coil annealing at 300 °C resulted in the weakest material and better stability was obtained in the other alloys due to more iron in solid solution which precipitated and caused dislocation pinning during the final annealing.

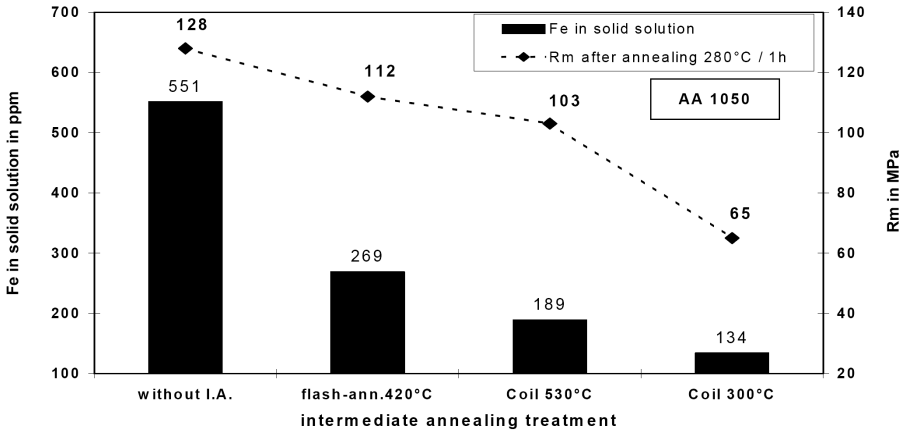

Figure 2.22: Effect of different interannealing processes on the level of iron in solid solution and on tensile strength after final annealing. [Hasenclever, 2006]

Iron related to softening and the effect of interannealing was thoroughly investigated by Marshall et al. [1991]. They were interested in the subsequent softening kinetics of 88% cold rolled commercial pure (99.5%) Al after interannealing in the range 320–550 °C. The goal was to strike a balance between retaining strength during stoving at intermediate temperatures and obtaining a fine grain size after high temperature recrystallization. A threshold was found between 400 °C and 450 °C which clearly showed the effect of iron and interannealing on subsequent annealing processes. Figure 2.23 illustrates how slow softening kinetics result after annealing at T>400 °C and the much faster kinetics below 400 °C. The two sheets interannealed at 360 °C and 400 °C softened by a combination of recovery and recrystallization by PSN at coarse Al_3Fe particles. At higher interannealing temperatures, i.e. 450 °C and 500 °C, the samples experienced extended recovery to fully soft condition although some PSN did take place in the 450 °C case at 240 °C after 10 minutes and became widespread at 270 °C.

The authors speculated whether the different behaviour was related to nucleation of recrystallization. Evidence of enhanced precipitation of iron rich particles was not observed. The behaviour was rather attributed to solute drag on dislocations and subgrain boundaries by increasing levels of iron in solid solution. For their investigations, Marshall et al. [1991] assumed a maximum solubility of 0.052 wt.% iron at RT and interannealing at temperatures above 400 °C to dissolve fine precipitates of Al_3Fe and AlFeSi formed during homogenization. Hence, a higher solute level was attained which retarded the recovery

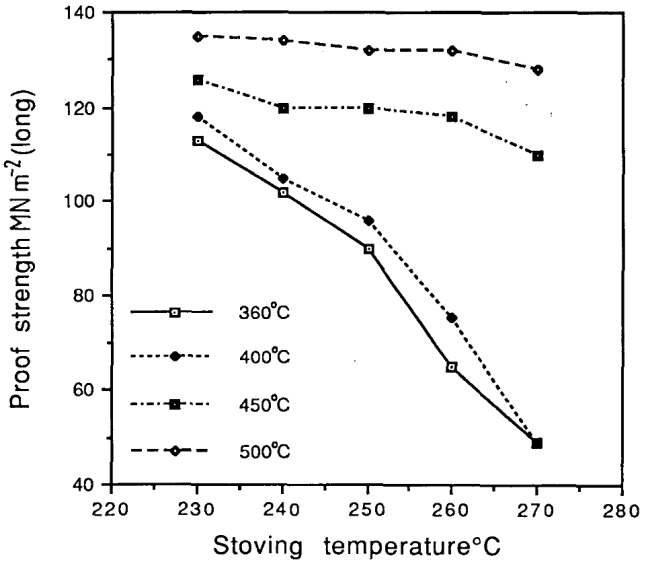

Figure 2.23: Effect of interannealing temperature on annealing response after 10 minutes of soaking at various temperatures. [Marshall et al., 1991]

process by solute drag. It is claimed that the solute level was maintained during annealing due to a large barrier toward homogenous nucleation, although other literature disagree.

Studies of iron segregation and possible clustering or precipitation are challenging due to the low solute levels, although a higher solubility limit is expected at grain boundaries and other imperfections due to a more open crystal lattice. Characterization methods like microprobe (wavelength dispersive spectroscopy) and atom-probe tomography are useful. However, alternative methods based on etching have been proposed and applied with success.

It has long been known that iron has a negative effect on corrosion and particularly the pitting potential of aluminium. Bond et al. [1966] studied the effect of the residual impurity elements Fe, Si and Cu on the pitting potential in 4N, 5N and 6N aluminium alloys with 20, 2 and ∼0.3 ppm (zone refined) iron, respectively. The samples were single crystals directionally solidified at two different growth rates where the fastest growing had a hexagonal substructure. Pitting was not observed in the 6N materials at all. In both 4N and 5N, on the other hand, pitting was observed at nodes as illustrated in Figure 2.24. The samples were also deformed 75% and annealed 1 hour at 200 °C and 25 hours at 600 °C. The pitting behaviour did not change for as-deformed samples or samples annealed at 200 °C. After annealing at 600 °C, more and smaller pits were observed in 4N and 5N cellular material but also in the 4N non-cellular samples. Hence, even at these low solute concentrations, segregation

to lattice imperfections is taking place and can be detected by changes in the surface properties. In fact, Wyon and Marchin [1955] found single dislocations to be revealed by etching due to solute segregation in high purity aluminium containing 40 ppm iron and 50 ppm silicon.

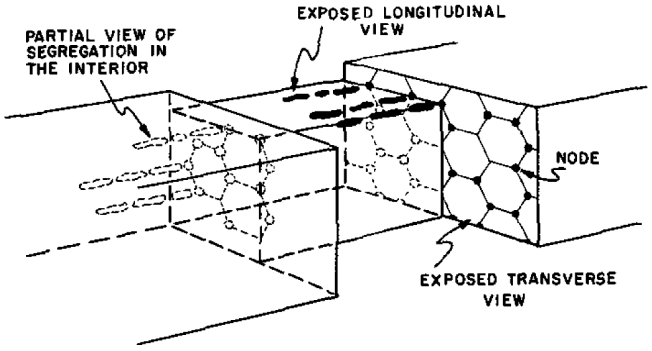

Figure 2.24: Illustration of segregation pattern of impurities on cellular substructure in high purity aluminium. [Bond et al., 1966]

Vandermeer [1967] utilized an etchant to reveal the presence of impurity elements (like iron) during annealing of 4N aluminium at 65 °C, 100 °C and 187 °C after extrusion with a 71.5% reduction ratio. They observed pits in the recrystallized microstructure and particularly at grain boundaries. However, very few or no etch pits were observed in the centre of the recrystallized grains. These findings were explained by the low diffusivity of impurities (iron) in a perfect lattice and a redistribution of iron to dislocations by lateral diffusion through the migrating grain boundaries. Vandermeer [1967] explained the observation by the rate at which the boundaries migrate. Initially, the rate is larger than the speed of lateral diffusion and no segregation occurs. Thus, as the boundary slows down during growth, it is possible for the solute at the boundary to be redistributed at dislocations left behind by the recrystallized front. An alternative interpretation could be that a certain concentration of impurities has to accumulate at the boundary before redistribution on dislocations in front of the boundary (recrystallization leaves behind dislocation free grains) is possible.

The results of Vandermeer [1967] confirm that a redistribution of solute may occur during annealing, although Vandermeer [1967] did not elaborate more on the reason for pit formation than indicating a clustering effect. In commercial purity alloys, precipitation was recognized by Grewen and Heimendahl [1968]. However, for high purity alloys there is less evidence of precipitation in literature. Metzger and Levy [1985] confirmed formation of widely spaced ($\sim$1 μm) clusters on subgrain boundaries in aluminium alloys containing 5 ppm and up to 120 ppm iron which was made possible by pipe diffusion. Suzuki et al. [1985]

and Kubota et al. [2001] have annealed and analysed iron containing high purity (4N) aluminium alloys by Mössbauer Spectroscopy. Based on their results on deformed and heat treated samples containing 22 ppm and 55 ppm iron, Suzuki et al. [1985] found precipitation of metastable Al_6Fe and possibly equilibrium Al_3Fe. Their study was on texture development and they suggested different textures were observed due to diffusion of solute along subgrain boundaries exerting a solute drag effect and ensuing precipitation. Kubota et al. [2001] gives a more thorough description of the precipitation behaviour, this time in a solution heat treated 50 ppm Fe alloy cold rolled 97% and annealed at various temperatures. Precipitation of Al_6Fe was initiated at 120 °C and at 500 °C all the iron was in solution again. As shown in Figure 2.25, maximum precipitation was observed at 310 °C. Samples from the same material that were not cold rolled did not show any sign of precipitation, leading the authors to conclude that a high density dislocation network was essential for precipitation to occur.

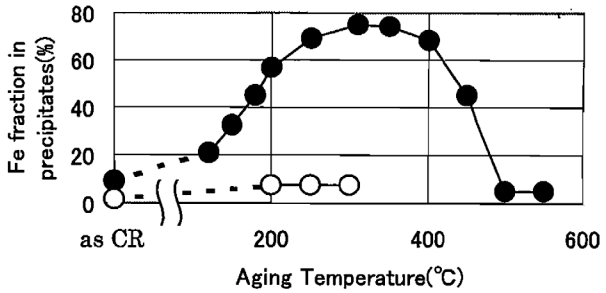

Figure 2.25: Effect of 97% cold rolling (black dots) versus no deformation (white dots) on precipitation behaviour of high purity aluminium with 50 ppm Fe after 6 hours of annealing at various temperatures. [Kubota et al., 2001]

The precipitation sequence and the possibility of other metastable phases have been investigated. Holm and Hornbogen [1970] found Al_3Fe in undeformed Al-0.042 wt.% Fe to precipitate heterogeneously at grain boundaries as almost incoherent particles of irregular shape and homogenously as semi-coherent needles. In 50% deformed material preferential nucleation on special dislocation nodes with large misorientations were observed and resulted in spherical particles with incoherent interfaces. Increasing amounts of deformation also lead to earlier precipitation. In an alloy of similar iron content, Stickels and Bush [1971] found Al_6Fe, with some coherency to the matrix, to form most readily in 88.9% cold rolled samples at 320–370 °C. In samples not exerted to deformation, Al_6Fe formed in the early stages but was reverted to Al_3Fe during continued annealing. Precipitation of Al_3Fe was most rapid at 470 °C and the removal of iron in the undeformed samples was half the rate of that in deformed samples. Davies et al. [1998] found Al_3Fe to have a spherical morphology. These observations were partially confirmed by Yamamoto et al. [2004] in a

4N alloy with 0.03 wt.% Fe. Precipitation of Al_6Fe was enhanced by deformation and lead to partially coherent needles and was followed by precipitation of partially coherent Al_3Fe in deformed samples. The rate of precipitation of Al_3Fe was not accelerated by deformation. Al_3Fe could also form directly in non-deformed samples.

In addition to iron, both commercial purity and high purity alloys also contain some silicon. In work on alloys with substantially more iron, i.e. commercial purity alloys, precipitation of the already mentioned phases have been observed in addition to AlFeSi phases. 0.05 wt.% additions of Si was also found to improve the nucleation rate of Al_3Fe by lowering the activation energy for diffusion of iron [Miki and Warlimont, 1968]. Ito et al. [1982] observed a similar effect of Si also on other phases. Si additions e.g. lead to the formation of the metastable α-AlFeSi phase at 280 °C in deformed materials. At 280 °C, Al_6Fe was also observed and when the temperature was raised to 400 °C α-AlFeSi, Al_6Fe and Al_3Fe were all coexisting.

Recrystallization and Texture

Precipitation during annealing tends to stabilize the deformation structure and slow down recovery and inhibit recrystallization as discussed in Section 2.2.1 (Zener drag). However, segregation of dissolved iron to dislocations and subgrain boundaries also exert a strong drag effect (solute drag). Both drag mechanism influence continuous recrystallization (or extended recovery) by stabilizing the deformation texture, which results in a strong R texture. On the other hand, if normal, discontinuous recrystallization is possible the resulting texture in pure aluminium typically has a strong Cube component.

Masing et al. [1956] have shown how additions of impurity elements in the range 0.01 at.% may slow down recrystallization kinetics by a factor 10^{11}. The effect is due to elastic interactions between solute atoms and the matrix and becomes larger with increasing deformation and when the misfit, i.e. size difference, increases. In addition, large constituent particles containing iron will of course also influence recrystallization and texture (PSN) but are less important for pure metals and will not be considered here.

There has been much debate to which extent these two aspects influence the industrially important Cube texture and it is not trivial to study the effect of iron on the annealing behaviour. Marshall and Ricks [1993] did observe a higher annealing temperature with the addition of 40 ppm iron with no particular change up to 0.02 wt.%. As graphically illustrated in Figure 2.26, for 0.47 wt.% Fe, the alloys contained constituent particles and the annealing temperature was reduced. Still, recovery was even slower than in the alloys containing particles and this behaviour was explained by the possibility of higher solute levels in particle containing alloys. Due to the different microstructures it is thus challenging to say anything about the effect of dissolved iron on texture

evolution. The initial texture was also different and, as shown in Table 2.2, the particle containing alloys have a significantly stronger Cube texture. Taking this into account and comparing the Cube fraction after various times of annealing at 300 °C, it appears that more iron in solution dramatically impedes the formation of the Cube texture component.

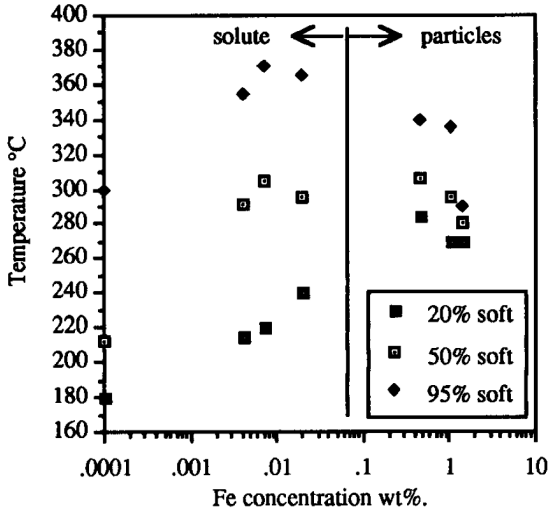

Figure 2.26: Annealing response of aluminium as a function of the Fe concentration. [Marshall and Ricks, 1993]

Table 2.2: Volume fraction of texture components from 15° spread about ideal orientation during annealing at 300 °C. [Marshall and Ricks, 1993]

Alloy	Time	Cube	Goss	Cu	Bs	S	Random
0.007% Fe	As-deformed	0.2	3.5	23.2	12.1	36.0	25
	2 h	5.7	1.5	15.5	5.3	27.6	44.4
	24 h	11.5	1.6	11.3	5.5	18.5	51.5
1.06% Fe	As-deformed	3.5	5.4	20.6	11.8	34.3	24.3
	1 h	5.6	4.3	20.4	9.8	34.1	25.8
	2 h	8.1	4.3	16.3	7.8	26.7	36.8
	24 h	9.5	4.3	13.1	7.1	23.4	42.6

According to work by Ito et al. [1976] on Al-Fe alloys with 0.04 and 0.16 wt.% Fe, in the recrystallization texture the R component is promoted while Cube is strongly inhibited by iron in solid solution during annealing. Both the R and Cube texture components grow by the motion of $40°\langle 111\rangle$ boundaries, which make the authors suggest the effect of dissolved iron is most significant on the nucleation process of Cube. A more detailed study on high purity alloys with 50 and 400 ppm iron was made by Ito et al. [1983a] where the effect of precipitation

was considered in greater detail. As long as iron remained in solid solution during the annealing process, the resulting texture was dominated by the R component. Earlier in this section, 360 °C was found to be in the range where iron precipitated readily in deformed high purity alloys during annealing and Ito et al. [1983a] observed then a minimum Cube fraction and also a strongly suppressed R texture. They concluded that this was due to precipitation of iron on the substructure. Ito et al. [1983b] also investigated the effect of Si additions to a high purity Al-Fe alloy containing 0.034 wt.% Fe. Si speeded up the precipitation kinetics and the amount of precipitation during annealing was found to increase with Si additions. This led to faster recrystallization and a more random texture.

Similar behaviour to that found by Ito et al. has also been observed by others [Bunk, 1965; Rogers and Roberts, 1974]. E.g. Suzuki et al. [1985] followed the texture evolution and solute content of iron and found a supersaturated solid solution of iron and subsequent concurrent precipitation during annealing to promote the R texture component. Further, if precipitation was nearly complete and the solute level low, the R component was replaced by a strong Cube component. Ekström et al. [1990] do however introduce some doubt about this behaviour. They observed in commercial purity alloys that removal of iron from solution strengthened the Cube texture but, rather contradicting, the strongest Cube texture was detected in samples processed in order to have high solute levels of iron. The reason for which is speculated to be low, industrial heating rates during batch annealing or constituent particles.

Li and Saimoto [1998] have also found somewhat contradicting results. In a pure aluminium alloy containing among others 90 ppm Fe, continuous recrystallization and a strong R texture component was only observed when the solute level of iron was below 1 ppm. Low solute levels of Fe can according to Li and Saimoto [1998] be achieved in different commercial alloys by pre-straining and annealing at 230 °C. With extremely low solute levels of iron (<0.1 ppm), dynamic recrystallization resulted in a prominent Goss component. At higher solute concentrations (>1 ppm), random boundaries are more severely pinned than special boundaries like $\Sigma 7$ (like the boundary between Cube and S), thus promoting the Cube component. With decreasing levels of dissolved iron, the solute drag can be neglected and the intrinsic mobility of the boundary becomes rate controlling, i.e. random HAGBs are more mobile than the special CSL boundaries. Consequently, growth of the Cube component is then not due to a highly mobile CSL boundary but rather because segregated Fe atoms are less effective at pinning $\Sigma 7$ boundaries compared to other boundaries. This could explain the observations by Ekström et al. [1990] of a large Cube fraction even when a large amount of dissolved iron was present.

However, if taken a step further, CSL boundaries have a particularly well defined interface and are automatically denser than other random boundaries

with a more open structure. This could mean less iron is segregated to such boundaries during annealing due to a lower solubility. During interannealing when precipitation of iron on the substructure is observed, precipitation may not occur as readily on CSL boundaries which during the initial stages of annealing are strongly pinned by solute. The more random boundaries, on the other hand, are less influenced, although experiencing a Zener drag from the precipitates, and have a higher mobility resulting in the observed R texture.

Chapter 3

Materials & Methods

The experimental work involves numerous methods that will be described after a presentation of the materials. From bulk materials like ingots and rolled sheets, smaller samples were cut in order to fit characterization equipment, e.g. sample holders for SEM. Due to the plane-strain deformation mode of rolling, the microstructure will appear different depending on which cross sectional plan is being investigated. Hence, it is necessary to define the sample surface in relation to the rolling geometry. The terminology is as follows; the length of the sheet is parallel to the rolling direction (RD), the width of the sheet is parallel to the rolls and called the transverse direction (TD). Finally, parallel to the sheet's thickness and normal to the sheet plane, is the normal direction (ND). Figure 3.1 depicts the typical subgrain structures in the sample planes relative to the rolling geometry.

3.1 Materials

In the present work several different materials have been investigated to various extents. These can be categorized into two groups; high purity and commercial purity alloys. The materials, their composition and how they are processed, is described on the next few pages.

3.1.1 High Purity Alloys

For the high purity part of the experimental work, four aluminium alloys were used. One was a 99.99% Al variant and the three others were binary alloys containing 0.25 wt%, 0.5 wt% and 1.0 wt% manganese, respectively. A pre-alloy was made by mixing 99.99% pure Al and 99.9% pure Mn in the ratio 10:1. The pre-alloy was then melted in vacuum at a temperature of 1309 °C in a 99.7% pure Al_2O_3 sintered pot. The actual alloys were mixed in melting pots made from graphite clay coated with Al_2O_3, burned at 1200 °C and finally

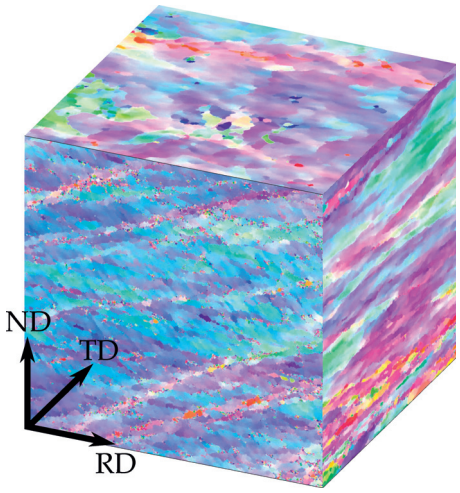

Figure 3.1: Visualization of the substructures in the three sample cross sections relative to the rolling coordinate system.

coated with boron-nitride. A complete overview of the chemical composition of the four alloys is given in Table 3.1.*

Table 3.1: Chemical composition of the four high purity alloys [wt.%].

Alloy	**Al**	**Mn**	**Si**	**Fe**	**Cu**	**Mg**	**N**
Al4N	99.9900	-	0.0011	0.0005	0.0017	0.0003	<0.00005
Al-0.25Mn	99.7407	0.2493	0.0011	0.0005	0.0017	0.0003	<0.00005
Al-0.5Mn	99.4821	0.5075	0.0011	0.0005	0.0017	0.0003	<0.00005
Al-1.0Mn	98.9649	1.0242	0.0010	0.0005	0.0017	0.0003	<0.00005

The alloys were cast into rolling ingots measuring $7 \times 7.5 \times 20$ cm by directional solidification. Prior to deformation, the alloys were heated (200 °C/h) and homogenized at 635 °C for 16 hours and subsequently quenched in water. Next, the ingots were cold rolled in several passes with lubricated rolls to a total reduction of 80%, equivalent to a strain $\varepsilon = 1.6$.

Primarily made for a different project, only limited amounts of high purity material was available for this PhD work, and only in as-deformed state. Further cold rolling to increase the driving pressure for recovery was then done down to a thickness of 1 mm, i.e. 95% reduction and a strain $\varepsilon = 3.0$. Due to the directional solidification process, the materials were found to be very co-

*Processing was executed several years ago in unpublished work by Professor Bjørn Holmedal, NTNU.

arse grained and the microstructures of the two alloys at strain 1.6 and 3.0 are pictured in Figure 3.2. This is an advantage with respect to characterizing the relationship between orientation and subgrain growth kinetics but also make the materials less suitable for direct comparison with industrially processed alloys. It is clear from the micrographs in Figure 3.2 that there are wide areas with similar orientation (same colour) and that the materials are very heterogeneous at both strain levels. For instance, the left and right pictures do not correlate very well with respect to the number of bands with same orientation. This may influence to which extent compositional variations can be identified.

Subsequent to cold rolling, the softening behaviour of each alloy was characterized by hardness measurements and electrical conductivity measurements in order to select proper annealing temperatures resulting in a fair degree of recovery for later studies of recovery kinetics and subgrain growth. The isothermal back-annealing was performed in oil baths at temperatures ranging from 180 °C to 240 °C. After being immersed for a designated time in the range 2–10^6 seconds, the samples were quenched in water. For short annealing times or thick specimens it is important to have convection in the annealing medium in order to maintain a high temperature gradient across the liquid-sample interface. This was shown by Furu [1992] for salt baths as illustrated in Figure 3.3. However, it is less important in oil baths, which have automatic stirring.

3.1.2 Commercial Purity Alloys

Two commercial purity aluminium alloys were produced by Hydro Aluminium Sunndal. The two alloys in question, named A1 and A2, are lean on alloying elements. Both contain nominally 0.15 wt.% Fe and they differ only in the level of silicon. Alloy A1 was intended to have 0.05 wt.% Si whereas alloy A2 was supposed to have 0.15 wt.% Si. The exact composition is given in Table 3.2. From the billets measuring 220 mm in diameter, rolling ingots were machined with dimensions L = 200 mm, W = 80 mm and H = 30 mm which first had to be homogenized.

Table 3.2: Chemical composition of the two commercial purity alloys in [wt.%].

Alloy	**Al**	**Si**	**Fe**	**Cu**	**Mn**	**Mg**	**Zn**	**V**
A1	99.7308	0.0670	0.1458	0.0008	0.0025	0.0042	0.0050	0.0105
A2	99.6653	0.1457	0.1384	0.0007	0.0022	0.0043	0.0050	0.0106

Homogenization

Homogenization is necessary in order to decrease the level of microsegregations and spherodize the constituent, iron-rich particles. Initially, the soaking

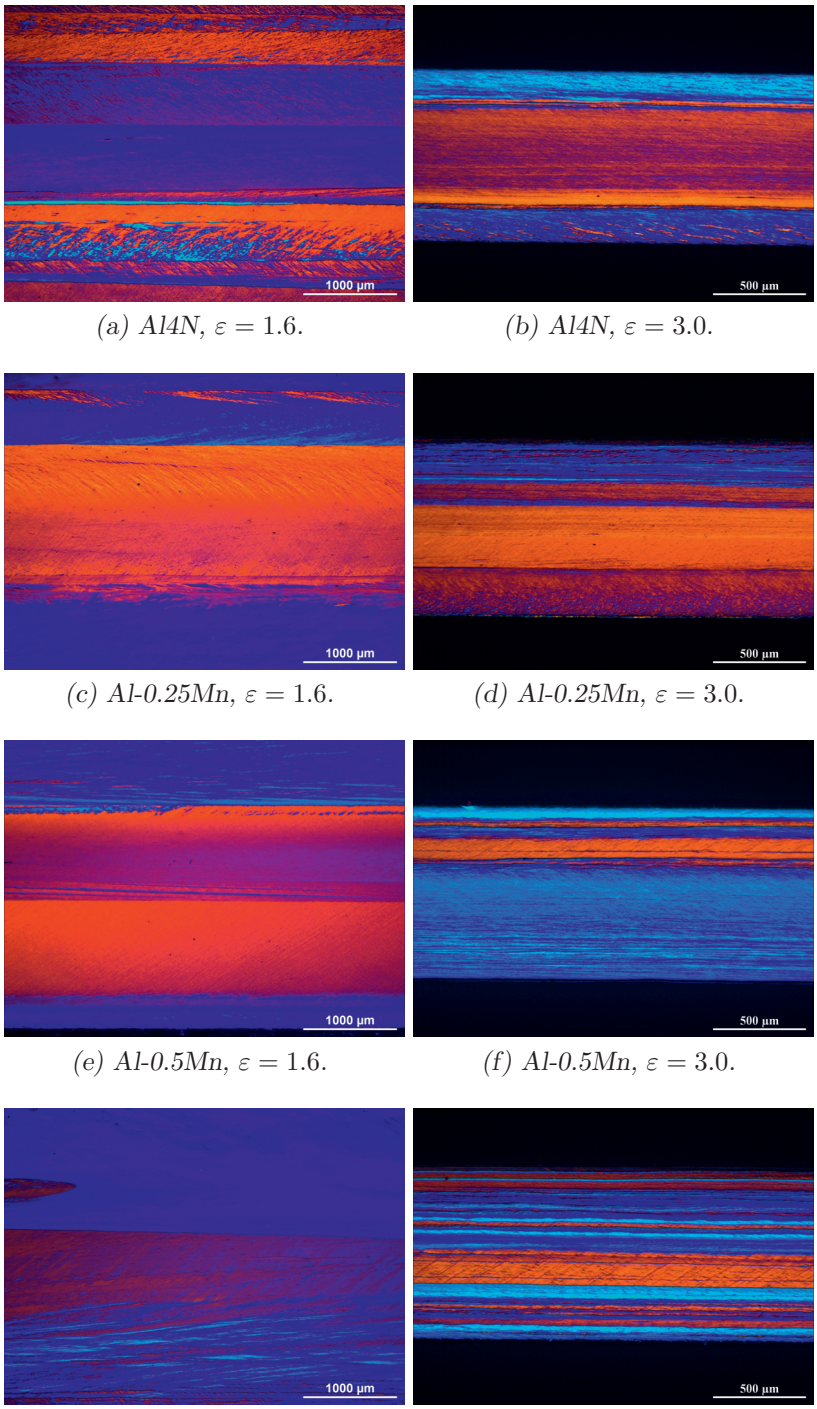

(a) Al4N, $\varepsilon = 1.6$. *(b) Al4N, $\varepsilon = 3.0$.*

(c) Al-0.25Mn, $\varepsilon = 1.6$. *(d) Al-0.25Mn, $\varepsilon = 3.0$.*

(e) Al-0.5Mn, $\varepsilon = 1.6$. *(f) Al-0.5Mn, $\varepsilon = 3.0$.*

(g) Al-1.0Mn, $\varepsilon = 1.6$. *(h) Al-1.0Mn, $\varepsilon = 3.0$.*

Figure 3.2: Micrographs of anodized RD-ND cross sections of as-deformed microstructure in Al4N, Al-0.25Mn, Al-0.5Mn and Al-1.0Mn.

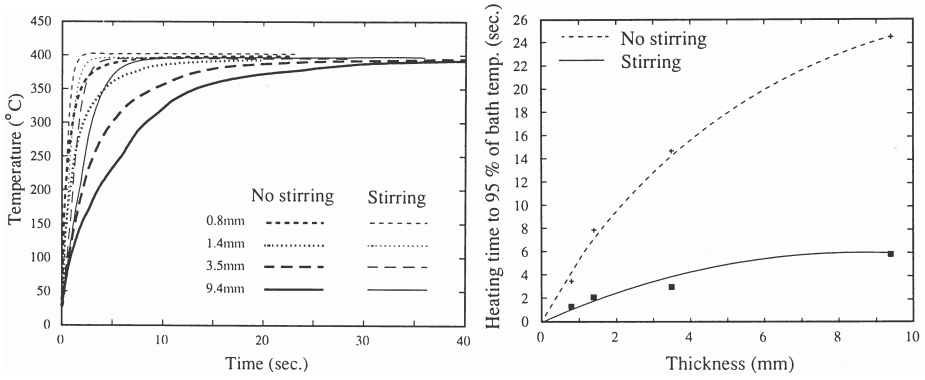

Figure 3.3: (a) Heating curves to 400 °C in a salt bath for samples of varying thickness, with and without stirring. (b) Time to 95% of bath temperature as a function of thickness, with and without stirring. [Furu, 1992]

temperature was set to 600 °C. However, at this temperature the A2 alloy, which had a much finer as-cast grain structure than A1, experienced abnormal grain growth. This material will be referred to as $A2^{hom}_{600}$. After heating to both 580 °C and 560 °C and holding for 24 hours, abnormal grain growth still occurred and the soaking temperature had to be lowered to 540 °C for abnormal grain growth to cease. Both A1 and A2 were thus soaked at 540 °C for 24 hours before they were log-cooled to 450 °C and held there for 36 hours according to the schedule given in Figure 3.4. The A2 alloy homogenized at 540 °C is referred to simply as A2.

Deformation & Annealing

The A1 and A2 alloys were already characterized to some extent by Sande [2012]. Some of the results are reproduced here, including EBSD scans of $A1^{rex}_{450}$ sample and hardness and conductivity measurements of A1 and A2 homogenized at 600 °C, deformed 92.5% and annealed at 275-375 °C.

In this PhD work, the A1 and A2 billets homogenized at 540 °C were cold rolled from 30 mm to 2.25 mm in several passes in a laboratory mill with lubricated rolls. This is equivalent to a 92.5% reduction or a strain $\varepsilon = 2.6$. After cold rolling, samples were cut and annealed at 250 °C in an oil bath with constant stirring for 2 seconds and up to 10^5 seconds. 250 °C balanced the need for significant subgrain growth without giving much recrystallization, ideal for characterizing subgrain growth in the A1 alloy. The A1 samples measured 2×1 cm with the long direction parallel to RD.

After 10^5 seconds at this low temperature, the samples were not fully soft

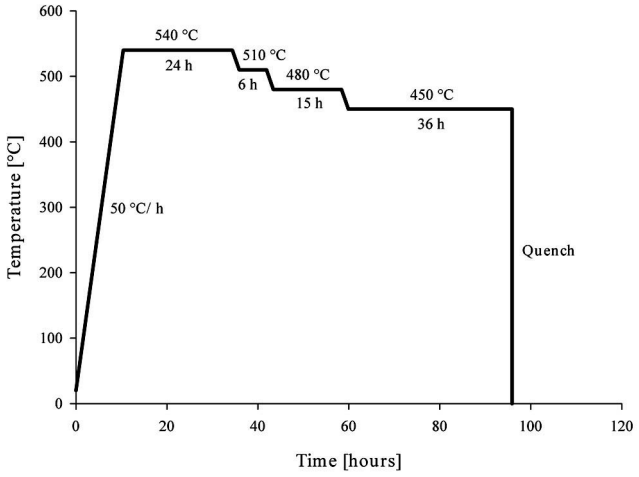

Figure 3.4: Temperature variation during homogenization process for A1 and A2 alloys.

and only partially recrystallized. Hence, the recrystallized grain size and texture were investigated in samples annealed at 350 °C for 1000 seconds in a salt bath. These were heat treated in an oil bath for intervals in the range 2–10^5 seconds and subsequently quenched in water.

Previous work had indicated relatively slow recovery of the A1 and A2 alloys during annealing at temperatures in the range 275–375 °C. In order to investigate the effect of grain size prior to deformation, an A1 sample was deformed 50% and annealed to fully recrystallized state at 450 °C for 100 seconds in a salt bath. This lead to a smaller grain size and the sample, labelled $A1^{rex}_{450}$, was then cold rolled 92.5% and annealed at 300 °C to compare the recovery kinetics with those of the coarse grained material.

The effect of iron in solid solution on softening was investigated by performing an intermediate annealing step to reduce the solute level by precipitation. The softening behaviour of samples with high and low solute contents was then compared. Lower solute content was achieved by deforming homogenized A1 billet material 50% and anneal it to fully soft state at 300 °C for 10^5 seconds. Subsequently, the material was further deformed by cold rolling to 50 and 92.5% reduction and annealed at 300 °C. Similar deformation and annealing was done to samples without any previous annealing and the hardness and electrical conductivities compared.

Processing of A1 with High Solute Content

Due to slow recovery kinetics caused by iron in solid solution, another experiment was arranged in which the level of iron in solid solution was significantly higher and the potential for increased kinetics by precipitation larger than before. According to Thermo-Calc (COST 507 dataset) at 620 °C, Al_3Fe is the only stable phase and the solubility limit is 0.032 wt % Fe. At the finishing temperature of 450 °C during the previous homogenization, both α-AlFeSi and Al_3Fe are stable and the solubility limit is 0.003 wt % Fe. Thus, homogenization at 620 °C followed by quenching represents a tenfold hike in the level of dissolved iron over the former homogenization process. Hence, an A1 rolling ingot, L = 200 mm, W = 80 mm and H = 30 mm, went through a complete homogenization sequence as illustrated schematically in Figure 3.5.

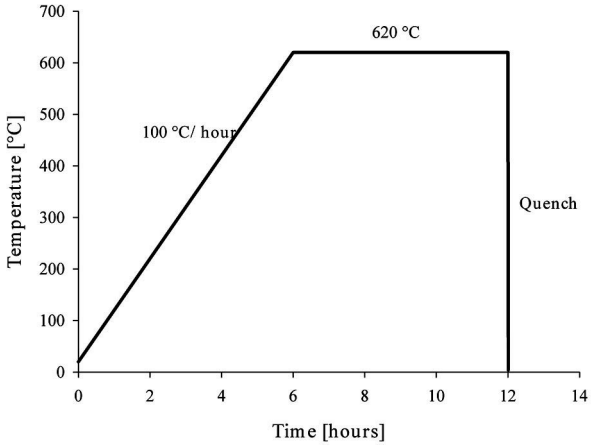

Figure 3.5: Temperature variation during high-temperature homogenization of A1.

After homogenization, the rolling ingot was cut and cold rolled to two different strain levels with lubricated rolls; $\varepsilon = 0.7$ and $\varepsilon = 2.6$. This is similar to the previous experiment and equivalent to 50% and 92.5% deformation, respectively. Due to the higher solute level of iron, slower kinetics during annealing was expected. Annealing was consequently done at 320 °C for the samples deformed 50% and 300 °C for the 92.5% deformed samples in order to make the two strain cases fully soft after similar annealing times.

Some samples for further deformation were annealed to fully soft condition for 10^5 seconds at 320 °C from both strain variants. The 50% deformed and back-annealed material was further deformed 50% and 92.5% and annealed at 320 °C and 300 °C, respectively. The 92.5% deformed sample was only deformed 50% and annealed at 320 °C. A complete list of the processing history for the

five initial states and annealing temperatures is given in Table 3.3.

Table 3.3: Processing done prior to final annealing at the designated temperature for the five different states of A1 homogenized at 620 °C.

Initial state of sample	**Annealing temp. [°C]**
Def. 50%	320
Def. 50% + 10^5 s/320 °C + def. 50%	320
Def. 92.5% + 10^5 s/320 °C + def. 50%	320
Def. 92.5%	300
Def. 50% + 10^5 s/320 °C + def. 92.5%	300

3.2 Characterization Methods

After the samples were cut to size, metallographic sample preparation was necessary and always incorporated several common steps. These were typically sample embedding and curing in ClaroCit resin, followed by grinding with SiC paper of consecutively increasing grit size (smaller carbide particles). The final step was mechanical polishing using diamond spray, generally with 3 µm and then 1 µm small particles. In between the different grinding steps it is favourable to clean the samples with ethanol in an ultrasonic bath to remove any remains from the previous step.

Light Optical Microscopy

One of the most fundamental characterization methods for metals is *light optical microscopy* (LOM). It is a relatively simple, low-cost method which provides a large field of view but only with low resolution. There are several techniques which combine various sample preparation methods and operation modes of the microscope that together make LOM a versatile and efficient characterization tool. As always, sample preparation is the key factor for good results. In this PhD work, LOM has mainly been used to get low magnification micrographs of the grain structure. A simple method made possible by the optically anisotropic nature of the oxide layer formed on aluminium is used to give grains of different orientations distinct colours. After grinding and mechanical polishing (electro polishing is optional), samples were anodized in a 5% HBF_4 aqueous solution (Barkers reagent) at 20 V for 90 seconds. Under polarized light and with a λ-plate inserted, the grains will typically be coloured in different shades of blue, purple and yellow.

3.2.1 Constituent Particles

Characterization of constituent particles in the commercial purity alloys A1 and A2 was done by SEM and the *back-scattered electron* (BSE) technique. Samples selected from both homogenized and 92.5% deformed material were prepared by grinding and mechanical polishing and imaged with a Hitachi SU6600 VP Schottky FE-SEM in BSE composition mode. Acceleration voltage was 20 kV and the working distance 9 mm. By adjusting brightness and contrast, binary images were captured in the SEM and, hence, no further image processing was necessary. In Feature-mode in Bruker Quantax Esprit 1.9.4. the settings for particle analysis included filling of holes and acceptance of boarder particles. Minimum particle size was four pixels for homogenized samples and two pixels for deformed samples. For each alloy and state, between 1300 and 1600 particles were measured.

3.2.2 Grain Break-Up

The effect of alloy content on grain subdivision during deformation was investigated. RD-ND samples from the cold rolled sheets of all high purity alloys at strain 1.6 and 3.0 were cut and prepared according to standard metallographic sample preparation procedures. Cross sections were selected both at random positions laterally from the edge and from the centre of the sheets. Narrow bands of similar orientation, although separated by HAGBs, are difficult to resolve in anodized samples with LOM. Instead, break-up during deformation was investigated in the SEM by EBSD.

Grain break-up factors were also investigated in RD-ND cross sections from $A2^{hom}_{600}$ and A2 samples. While the deformed samples and undeformed A2 sample were characterized by EBSD, the undeformed $A2^{hom}_{600}$-sample had to be investigated by LOM under polarized light due to a truly coarse grain structure. For SEM characterization it was necessary to electropolish the surface in order to remove the plastically deformed surface layer after mechanical polishing. Electro polishing was done at -30 °C at 20 V for 15 seconds in an ethanol (CH_3CH_2OH) solution of 10% perchloric acid ($HClO_4$). In a Zeiss Ultra 55 FE-SEM equipped with a NORDIF UF-390 EBSD detector, scans over the entire sheet-thickness were made at 20 kV acceleration voltage. In the high purity alloys, 1.2 µm and 0.2 µm step sizes were used for the 1.6 and 3.0 strain cases, respectively. In the commercial alloys, 2.0 µm, 0.2 µm and 0.1 µm step sizes were used in the A2 sample and $A2^{hom}_{600}$ and A2 samples after deformation, respectively. The scans were later post-processed and viewed in EDAX TSL OIM Analysis 6.1 to identify HAGBs. Only boundaries extending over a significant number of subgrains were counted.

The degree of grain break-up taking place during deformation was identified by the grain *break-up factor* (BUF), defined by Equation 3.1. To find the calcu-

lated spacing between HAGBs in the ND-direction $D_{calculated}$, the initial grain size (thickness of columnar grains) D_0 and strain ε were required. The BUF gives the ratio between the necessary spacing between HAGBs prescribed by the degree of plastic deformation and the actual spacing which also incorporates grain subdivision.

$$\frac{D_{calculated}}{D_{measured}} = \frac{D_0/\exp(\varepsilon)}{D_{measured}} \tag{3.1}$$

3.2.3 Vickers Hardness Test

The Vickers hardness test is a simple method used to measure the hardness of a material. The method was here used to follow the softening behaviour during annealing and always with exactly the same settings. A diamond indenter shaped like a pyramid will, when forced into the material, plastically deform the material. The size of the indent depend on the hardness of the material, load, load time and loading speed. It is the sizes of the indent's diagonals which are measured and used to calculate the hardness number, defined as the pressure obtained by dividing the test force with the sloping area of the indent according to Equation 3.2. P_l is the applied load in kilograms and $\overline{d}$ the average length of the diagonals. Because the area is not normal to the force, the pressure is just an empirical value and, in practise, the Vickers hardness number HV is found by inserting the mean diagonal length into Equation 3.2. All measurements were done on a Matsuzawa DVK-1S Vickers hardness tester at RT with a 1 kg load, 15 seconds loading time and 100 µm/s loading speed. Five indents per sample were made in the RD-TD plane after grinding the surface with grit 2400 SiC paper.

$$HV = \frac{1.854P_l}{\overline{d}^2} \tag{3.2}$$

3.2.4 Electrical Conductivity

Electrical conductivity measurements were performed to follow recovery, recrystallization and the degree of precipitation during annealing. In a perfect crystal lattice, accelerated electrons will not interact with the atoms. However, under the influence of an electric field, the electrons in any real lattice will be scattered by imperfections and loose some of their kinetic energy, e.g. observed as power losses through heat. The resistivity ρ is the friction force resulting from this scattering of electrons typically by substitutional and interstitial atoms, vacancies and dislocations, and thermal vibrations like phonons. Close to 0 K, the resistivity is dominated by solute elements and lattice defects. However, phonons are the main reasons for scattering at RT. These two effects are nearly independent of each other and the Matthiesen rule given in Equation 3.3 is

applicable [Tilley, 2008];

$$\rho = \rho_p(T) + \rho_{res}(c_1, ...c_n) \tag{3.3}$$

where ρ is the overall alloy resistivity, $\rho_p(T)$ is the temperature dependent resistivity and $\rho_{res}(c_1, ...c_n)$ is mainly a function of the composition.

The resistivity ρ and conductivity σ are reciprocal values and can be readily measured in materials that are not ferromagnetic, like paramagnetic aluminium. The addition of alloying elements to pure aluminium distorts the crystal lattice more than e.g. strain hardening or precipitation hardening and the resistivity increases almost linearly with increasing solute level [Ólafsson et al., 1996; Polmear, 2006]. In pure aluminium, the resistivity is reported to be 26.5 nΩm by several authors, including Cooper et al. [1974].

Conductivity measurements of the high purity alloys were made with a Sigmascope EX 8 by Fischer. This works by Eddy currents and the method is sensitive to surface imperfections. A surface roughness of less than 10 µm is required for a measuring error smaller than 1%. Therefore, samples were ground with grit 4000 SiC paper. Three measurements per samples were done. It was noted though, that the scatter was smaller than the graduation on the analogue scale, hence no standard deviation was calculated.

For the commercial purity alloys, conductivity data were collected with a different instrument working in the same way, i.e. by Eddy currents. Grinding to grit 4000 with SiC paper was necessary. The Foerster Sigmatest 2.069 is operated by a hand-held probe, which turned out to introduce several factors affecting the accuracy of the conductivity measurements. Getting consistent readings required patience and a careful approach. Because it was less than trivial to make perfect contact between probe and sample, the highest reading that was also reproducible was considered representative of the sample.

In addition to electrical conductivity measurements at room temperature by Foerster Sigmatest 2.069, A1 samples with a particularly high solute level for studies of the effect of interannealing and precipitation were measured by the four point probe method which utilizes the electrical impedance between the probes. The two outer probes carry a current which induce a voltage drop that the two inner probes can sense. The voltage drop is measured and the resistance calculated. Because very little current is carried by the sensing electrodes, impedance contributions from wiring and contact resistances are eliminated making this method more accurate than the Eddy current variant. Resistivity measurements with the four point probe method were made at Hydro R&D Bonn at 293K and 4.2K, referred to in Chapter 5 as the RDB experiments. By plotting the measured resistivity values as resistivity ratios $RR = R_{293K}/R_{4.2K}$, the error introduced by the shape factor is also eliminated.

3.2.5 Subgrain Growth

The EBSD technique is a well-known and recognized method for microstructural characterization with a wide range of applications. One of which, through continuous improvements, has more recently become adequate for subgrain characterization as well. Still, subgrains are not trivial to characterize by EBSD because of the low misorientation across the boundaries. Not all boundaries are necessarily identifiable with the EBSD method and there are several reasons for this. If e.g. the step size is too coarse compared to the subgrain size, the spatial resolution is poor, several patterns are overlapping or pattern precision is bad, a complete boundary map of the subgrain structure may not be possible to attain [Humphreys, 2001].

However, with optimised SEM and acquisition settings and appropriate post processing, reconstructed subgrain maps which give a realistic representation of the true microstructure can be made. When automated, thousands of subgrains can be characterized with respect to size and average boundary misorientation with acceptable accuracy and good statistics [Humphreys, 2004a]. To exemplify the possibilities and limits of fast EBSD, Brough and Humphreys [2010b] used the Vmap-software to characterize EBSD data from an Al-0.1Mg alloy with a spatial resolution of $\sim$50 nm and angular resolution $\sim$1°. Barou et al. [2009], utilizing a unique method combining image processing and standard EBSD software, have done extensive investigations of subgrain boundary mobilities in Al-Mn alloys with a minimum boundary misorientation threshold at 0.7°. The approach to EBSD data analysis taken in this PhD work differs from the two previous examples mainly in that it is not fully automatic. However, similar to the method developed by Barou et al. [2009], image processing is an important step in achieving complete boundary closure of the reconstructed subgrain boundary maps which is necessary for obtaining accurate subgrain size data.

With any kind of characterization using EBSD, the first and most important step is sample preparation. Without high quality diffraction patterns, further processing of the EBSD data is worthless. Hence, ND-RD sections of the annealed samples were mechanically ground and polished, using 1 µm small particles in the final step, before electro polishing in an ethanol (CH_3CH_2OH) electrolyte containing 10% perchloric acid ($HClO_4$). Electro polishing was either done at RT and 30 V for 8 seconds or at -30 °C and 20 V for 15 seconds, both methods gave perfect sample surfaces for EBSD characterization. If scanning directly after electro polishing, plasma cleaning of the sample surface was also necessary to remove remains from the electrolyte which would otherwise be deposited on the sample during scans. Al4N samples annealed at 180 °C were scanned in a Zeiss Ultra 55 FE-SEM with settings as given in Table 3.4. For the other annealing temperatures of Al4N and the Al-0.25Mn and A1 alloys, all scans were made with a Hitachi SU6600 VP Schottky FE-SEM and settings according to

Table 3.4.

Table 3.4: SEM and EBSD settings for characterization of subgrains.

	Zeiss Ultra 55	**Hitachi SU6600 VP**
Acc. voltage [kV]	20	16
Beam current [nA]	∼100	∼200
Magnification	2000	2000
Working distance [mm]	20	26
Tilt angle [°]	70	70
EBSD detector	Nordif UF-390	Nordif UF-1000
Pattern resolution [px]	120x120	120x120
Acquisition speed [fps]	200	600
Step size [nm]	50	50

Both SEMs use an off-line EBSD system in the sense that indexing is not done simultaneous with EBSD pattern acquisition. Instead, using Nordif 1.4.0 software, patterns and acquisition settings were stored in a file which could be indexed subsequently on any computer or laptop running EBSD post-processing software. Here, that meant EDAX TSL OIM Data Collection 5 running a classic Hough transformation with 9×9 convolution mask and 1° theta step size. Further post-processing of the indexed files was done in EDAX TSL OIM Analysis 6.1.

Because characterization of sub-micron subgrains with a boundary misorientation as low as 0.7° is at the limit of what is actually currently possible with the EBSD technique, commercial software does not have a dedicated routine good enough to reconstruct a subgrain map with fully connected subgrain boundaries. The two previously discussed methods were not applicable or available either [Barou et al., 2009; Humphreys, 2004a]. Hence, a novel approach for subgrain characterization satisfying the need for high resolution and complete boundary closure had to be outlined.

The problem at hand was to connect subgrain boundaries in a realistic way. Barou et al. [2009] used *pattern quality* (PQ) data directly in an advanced image processing routine to detect and connect all subgrain boundaries because "PQ gives a faithful image of the deformation structure". Several approaches at utilizing similar data available from the TSL software were tried, using both e.g. currently available image filters and watershed methods. Developing completely new algorithms for image processing was tried as well, although neither approach gave satisfactory results. For a method to be applicable it had to handle a wide range of *image quality* (IQ) or *confidence index* (CI) maps where magnification, resolution, microstructure, brightness etc. were varying. It was soon realized that to develop an adequate algorithm was non-trivial and would

require too much time to develop. Instead, by connecting the boundaries manually using commercially available image software, although admittedly very time-consuming, time spent on one scan would give results immediately.

The resulting process is illustrated graphically in Figure 3.6 step by step. Incomplete subgrain boundary maps (after clean-up), IQ maps and local misorientation maps were exported from TSL and combined into a new grayscale image where all subgrain boundaries were recognizable by eye. By adjusting brightness and contrast, most subgrain boundaries were already black while the missing boundary sections, delineated by the IQ and local orientation map, were drawn in black by hand. Now, by converting this map into a one dimensional matrix with values from 0 to 1 and replacing the original CI values, new "CI" values were created. All pixels belonging to a boundary got then a "CI"-value of zero, which made it possible for the TSL software to easily detect all, unique subgrains. The average orientation of each subgrain was then calculated and assigned to the whole grain.

However, because the boundaries were not necessarily one pixel wide and large areas may be un-indexed, e.g. because of pores or particles in the sample surface, it was essential to make the boundaries impinge for correct grain size calculations and average boundary misorientation calculation. Such routines are built into the TSL software but, although giving a realistic image of the true subgrain structure, the boundaries may deviate somewhat from their true shape and spatial position. After complete dilation, average grain size and average boundary misorientation can be readily measured in TSL. The theoretically smallest subgrains detected using this method have a mean diameter of 0.15 μm and an average boundary misorientation of 0.7°.

From the above described method, orientation dependent average subgrain size and boundary misorientation measurements were done on as-deformed and annealed samples from the Al4N, Al-0.25Mn and A1 alloy. The scans were made on areas with a homogenous microstructure, typically in the centre of bands in the lamellar structure. The bands had an as ideal orientation as possible, were constituted by at least 10 subgrains in the ND direction and did not contain any odd microstructural features. Typically 1–2 scans per uniquely oriented band were made from each samples (representing one annealing time-temperature combination). This resulted in about 3 scans for each unique annealing condition.

In addition, scans of the commercial purity A1 alloy covering regions with several orientations were also made. Scans covering several bands with e.g. Cube, Cu and S oriented regions were made and the average subgrain size and average boundary misorientation calculated. Without considering the orientations or the HAGB regions, these measurements gave the average orientation independent subgrain sizes and misorientations. These scans made it possible to investigate the effect of defects like HAGBs in the crystal lattice on subgrain

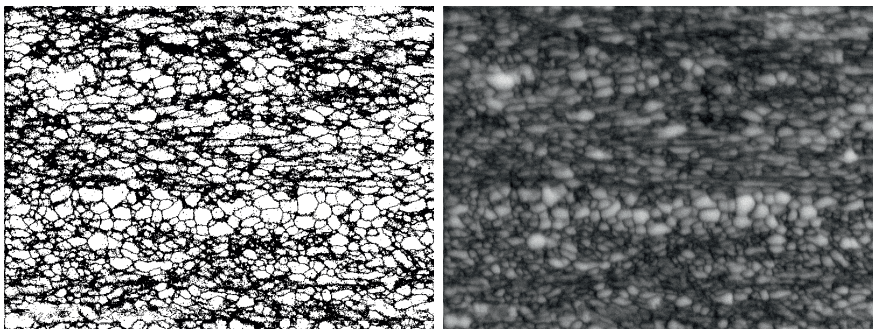

(a) Subgrain boundary map. *(b) IQ map.*

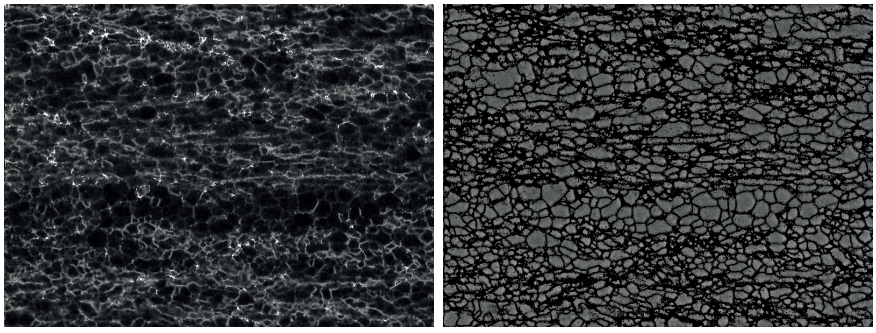

(c) Local misori. spread map. *(d) New CI map.*

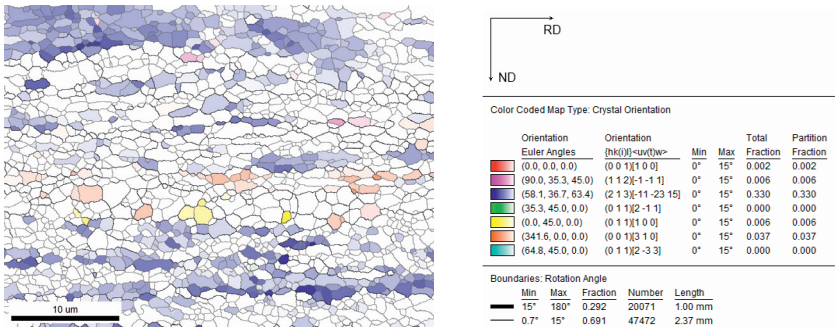

(e) Subgrain orientation map. *(f) Legend.*

Figure 3.6: Graphical representation of the subgrain characterization method. This particular sample is from Al4N annealed for 100 seconds at 220 °C.

growth kinetics. 2–3 scans were made per sample, except for the as-deformed sample where only one successful scan was made due a heavily distorted lattice. When covering several orientation bands which should give realistic numbers for the average values, HAGBs and severely deformed regions could of course not be excluded.

3.2.6 Texture

In addition to hardness measurements, deformed and recrystallized states from both the high purity Al4N and Al-0.25Mn alloys and commercial purity alloys A1 and A2 have been characterized by their texture. Texture plots are useful in that they clearly illustrate the macroscopic grain orientations after a series of complex and highly microstructure-dependent growth processes taking place during recrystallization.

For bulk texture, X-ray goniometers are frequently used because they sample a large volume. The number of individual orientations necessary for statistically valid measurement of the orientation distribution depends, among other parameters, on the crystal symmetry and texture sharpness. According to Engler and Randle [2010], 1000 orientations (i.e. grains) is typically considered a minimum while 10^4 orientations is adequate. Hence, in coarse-grained materials, good statistics may be difficult to achieve.

All the texture measurements performed in this PhD work were done by EBSD and SEM. This method is well suited for analysing microtexture. Bulk measurements are more difficult to obtain because the number of grains within the sampling area is normally several orders of magnitude smaller than with the X-ray goniometer. Fortunately, for Cubic materials, 100 grains will give away the characteristic texture and sturdy measurements are obtained with 500–1000 grains [Engler and Randle, 2010]. For this reason, the EBSD-technique was deemed adequate and able to meet the requirements of the texture experiments in this PhD work. If not otherwise specified, the ODF calculations presented are statistically sound.

Macro texture by EBSD

After recrystallization, the yield strength is relatively low, particularly for the high purity alloys (σ_y<20 MPa), making them susceptible to scratches and deformation during sample preparation. Sample preparation was still done according to standard metallographic methods, i.e. grinding and mechanical polishing, for both high and commercial purity alloys. To prepare the samples for EBSD characterization, the mechanically deformed surface layer was removed by electro polishing at room temperature for 10 seconds at 25 V in a 10% perchloric acid ($HClO_4$) ethanol (CH_3CH_2OH) solution. The actual SEM and EBSD work was carried out in a Hitachi SU6600 VP Schottky FE-SEM prepared

with EBSD equipment supplied by NORDIF. Both 96×96 and 120×120 pattern resolutions were used in combination with a frame rate of 600 fps. 17 kV and 20 kV acceleration voltage were used to collect scans from high and commercial purity alloys, respectively.

EDAX TSL OIM Analysis 6.1 software was used for light clean-up of the scans and to make pole figures and ODFs for presenting the texture measurements. Some light clean-up was always performed (orientation correlation, CI standardization and grain dilation) to reduce noise, though recrystallized structures in aluminium are straightforward to scan — even at the very low magnifications used here, e.g. 30×. For generating ODFs in EDAX TSL OIM Analysis 6.1, a series expansion of spherical harmonic functions with a series rank $L = 21$ was used. A *Dirac delta* representation was used in the series coefficient calculations, leading to negative values which were handled by a Gaussian spread function with a half-width $\omega = 5°$. In addition, orthotropic sample symmetry was applied to the calculations. Hence, the results were plotted in the 90°, three-dimensional Euler space with Bunge notation and 5° resolution in φ_2.

In addition, the EBSD scans of the deformed microstructures of the high purity alloys made for BUF calculations were also used for texture measurements. ODF plots were readily made using the above described method in order to show the bulk texture after deformation, although with sample preparation according to Section 3.2.2.

Temperature sensitivity of Cube component in Al4N

The effect of temperature of Cube texture was investigated in Al4N after recrystallization at three different temperatures. The samples were first cold rolled to strain $\varepsilon = 1.6$ and then recrystallized for 60 seconds at 400 °C in a salt bath in order to achieve some grain refinement. Thereafter the samples were cold rolled to strain $\varepsilon = 1.4$ and annealed at 250, 300 and 450 °C for 10^5, 10^4 and 10 seconds, respectively. The samples were then fully recrystallized and the macro textures were obtained as described previously in this section.

3.2.7 Grain Size

Grain size data for A1 and A2 were obtained from EBSD scans processed in EDAX TSL OIM Analysis 6.1. For details concerning sample preparation and EBSD scanning, see Section 3.2.6. In short, normal metallographic sample preparation finished off with electro polishing at room temperature for 10 seconds at 25 V in a 10% perchloric acid ($HClO_4$) ethanol (CH_3CH_2OH) solution was done before the samples were scanned in a Hitachi SU6600 VP Schottky FE-SEM equipped with NORDIF EBSD equipment. Typical acceleration voltage was 20 kV. Grain diameters were calculated as *equivalent circle diameter*

(ECD) using EDAX TSL OIM Analysis 6.1.

For accurate measurements of the grain size, only true grains should be identified and it is thus important to set a threshold value for the smallest grains included in the measurements. During clean up, some regions of low confidence index may incorrectly be identified as grains, particularly around constituent particles or in heavily deformed samples. Such regions are evident in Figure 3.1 as regions of contrasting orientation located typically in micro-shear bands but can be excluded from the statistics by the minimum grain size option in TSL due to a very small size of typically 1–4 pixels. A minimum of nine pixels (the equivalent grain size is a function of the step size which is adjusted depending on whether the microstructure is deformed or recrystallized) was required for a grain to be recognized by the software. A grain tolerance angle of 5° was also used. Twin plane matching was executed with a 1° tolerance angle; however, twin boundaries in aluminium are rare. Finally, edge-grains were included in the average grain diameter calculations.

3.2.8 Precipitation

Electrical conductivity measurements suggested the solute level of iron, and possibly silicon, in the A1 alloy diminished by some sort of clustering or precipitation of a second phase during annealing. Identification and characterization of precipitates was done by two different methods described in the following. Etching, which is simple, fast and cheap, was done first to confirm the presence of cluster or precipitates. Then, qualitative characterization was done by TEM.

Etching

It is reported in literature that iron as an intermetallics phase is detrimental to the corrosion resistance of aluminium. Electrochemically noble intermetallics typically act as cathodes to the less noble matrix which will dissolve through an anodic reaction in the vicinity of such particles. E.g. Nişancioğlu [1990] found Al_3Fe to particularly give unfavourable corrosion properties when exposed to NaOH, while the addition of Si, resulting in AlFeSi phases, slowed down the reaction kinetics. However, anodic reactions were also occurring on the intermetallics and caused compositional and structural changes. It is not only iron in intermetallics which cause pitting. Segregation of the elements Fe, Cu and Si to cell boundaries in 4N, 5N and 6N all caused pitting in a NaCl-H_2O_2 solution due to reduced cathode overvoltage at the cell-nodes [Bond et al., 1966]. In addition, or as a consequence, the protective oxide layer was notably thinner her, causing a reduced electrical resistance and speeding up of cathodic reaction kinetics.

Whether it is due to the potential differences in the surface or thinning of the oxide layer, iron present in the form of intermetallics or clusters at disloca-

tions has been demonstrated by etching [Bunk, 1965]. Some of the techniques developed to etch dislocations, even in high purity alloys, require the dislocations to be enriched by iron atoms or perhaps pinned by iron clusters [Barber, 1962; Biloni and Bolling, 1965; Jacquet, 1956; Wyon and Marchin, 1955]. Some of the etchants used contain hydrofluoric (HF) acid [Metzger and Levy, 1985; Vandermeer, 1967]. Hence, in order to characterize the precipitation reactions during annealing of A1, samples from as-deformed, fully back-annealed and flash annealed states of both 50% and 92.5% deformed material were etched in a 5% HF-solution for 30 seconds at RT. The etched samples were studied in a Leica MEF4 M light optical microscope at 188× magnification and a Hitachi SU6600 VP Schottky FE-SEM at 4000× magnification.

TEM Characterization

Precipitation during annealing observed by conductivity measurements was confirmed by etching, which revealed etch-pits in annealed and fully soft material. Thus, it was considered feasible to do a qualitative characterization of these precipitates by TEM.

Flat strips in the RD-ND plane were prepared by grinding with SiC paper to 110 μm thickness. 50% and 92.5% deformed samples were both prepared, together with fully soft samples annealed for 10^5 seconds. One sample, deformed 92.5% and annealed for only 10^4 seconds, was unintentionally also prepared and investigated. TEM samples are normally 3 mm wide discs, though the thickness of the deformed material was only 2.25 mm in the ND direction. This was, however, not a problem as the samples, after being punched out from the strips, could still be double jet electro polished without problems in a Struers TenuPol-5 at 20 V with a 1:2 nitric acid (HNO_3) methanol (CH_3OH) solution.

The samples were mounted in a double-tilt holder and investigated at 200 kV in a Jeol JEM-2010 TEM with Gatan Inc. imaging system and EDAX Apollo XLT EDS detector with Team EDS software. The precipitates were imaged in both *bright field* (BF) and *dark field* (DF) and, with a parallel beam, selected area *diffraction patterns* (DP) were also acquired.

Chapter 4

Materials Characterization

In this chapter the starting materials are characterized. Because the focus of this PhD work is on annealing related phenomena, the starting materials are in cold rolled state. The alloys and their particular processing give unique properties which will subsequently be reflected by their different annealing response. The commercial purity alloys are also to a large extent affected by homogenization, which is why results from characterization of both the homogenized and deformed states can be found in the following. For the high purity alloys, neither as-cast nor homogenized states were available for investigations. The results are presented for high and commercial purity alloys separately.

4.1 High Purity Alloys

The high purity alloys are the Al4N alloy and the three binary Al-Mn alloys. In these four alloys, grain break-up and deformation texture were investigated before annealing. The results are presented below.

4.1.1 Grain Break-Up

Since the materials were only available in as-deformed state, the initial grain size and the solute dependence of this is not known. Grain BUFs therefore are calculated based on the HAGB spacing found experimentally in samples deformed to a strain $\varepsilon = 1.6$. In Table 4.1, neither BUFs calculated from RD-ND cross sections at arbitrary distance from the sheet edge nor BUFs calculated from centre sections of the sheets show any correlation with increasing manganese content.

However, when looking at the HAGB spacing measurements for the two strain cases there seems to be a correlation between grain subdivision and alloy content. These are the average distances between HAGBs found at random positions and in the centre of the sheets. At strain $\varepsilon = 1.6$ the HAGB spacing

is similar in the Al4N, Al-0.25Mn and Al-0.5Mn alloys but much smaller in the Al-1.0Mn alloy. With further deformation to a strain $\varepsilon = 3$ all the manganese containing alloys have more or less the same HAGB spacing, while significantly less subdivision has occurred in the high purity alloy, indicating that increasing alloy content promotes grain subdivision.

Table 4.1: Observation of grain subdivision as a result of cold-rolling to strains of $\varepsilon = 1.6$ and $\varepsilon = 3.0$.

	Al4N	**Al-0.25Mn**	**Al-0.5Mn**	**Al-1.0Mn**
$\mathbf{D}_{measured}, \varepsilon = 1.6$ [µm]	189	137	156	75
$\mathbf{D}_{measured}, \varepsilon = 3.0$ [µm]	29	12	16	13
$\mathbf{BUF}_{random}$	1.51	2.34	3.65	1.05
$\mathbf{BUF}_{center}$	1.81	3.39	1.42	1.76

Several bands of typical deformation texture components were usually found within each investigated cross section. Two EBSD scans of the deformation microstructure after 80% and 95% deformation are shown in Figure 4.1 which illustrates the microstructures found. No correlation between alloy and microstructure was observed. The topmost scan from Al4N at strain $\varepsilon = 1.6$ shows e.g. mostly S and Brass oriented bands. There is also one band oriented close to Goss and one transition band with S and ND-rotated Cube components. Two neighbouring Brass bands are separated by a true LAGB and have the same symmetry. The lower scan is from Al-1.0Mn deformed to strain $\varepsilon = 3.0$ and in this case only Cu, S and Brass orientations are observed. However, due to the initially coarse grain structure another cross section would yield a different microstructure, although usually also constituted by several bands of varying size with orientations close to the deformation texture components. This is very different from a fine grained material, where the banded microstructure will be nearly identical in any cross section due more homogenous deformation and the sheer number of bands.

4.1.2 Deformation Texture

Due to the very coarse grained structure after deformation, bulk texture could not be measured with an X-ray texture goniometer. Instead, the ODF shown in Figure 4.2 was created by combining several EBSD scans made in the RD-ND plane, covering the whole thickness. However, these ODFs are not statistically sound — something which would require a very substantial number of cross sections to be scanned. Still, the ODFs give away the characteristic texture and confirm a strong β-fibre in the four alloys, typical for deformed FCC-materials with a high stacking fault energy.

The same peak intensity of ∼19 times random is observed in all but the

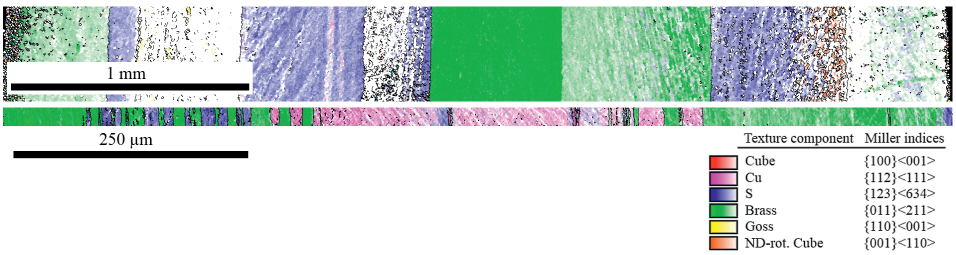

Figure 4.1: Examples of orientations in deformed samples within a 15° spread from the perfect orientations, including HAGBs in black. Uppermost is Al4N deformed to strain $\varepsilon = 1.6$ and below is Al-1.0Mn deformed to strain $\varepsilon = 3.0$.

Al-1.0Mn alloy where the maximum intensity is 39. The Brass, Copper and S components are all easily identified at $\varphi_2 = 0°/90°$, 45° and 65°, respectively, although their strength varies. In Al4N, the Brass and Cu components have similar intensities while S is stronger. The S is also the strongest component in Al-0.25Mn and Al-0.5Mn, while Brass and Cu are less pronounced. What leads to the strong peak intensity in Al-1.0Mn is a very distinct Brass component. The intensity of Cu and S coincides with Al-0.25Mn and Al-0.5Mn and is slightly weaker than in Al4N.

4.2 Commercial Purity Alloys

The commercial purity alloys A1 and A2 contain enough iron and silicon for constituent particles to form during casting. These break up during deformation and influence the softening behaviour, which is why their size and shape have been characterized in addition to grain break-up and deformation texture.

4.2.1 Properties Inherent to Casting and Homogenization

Because the commercial purity alloys A1 and A2 were received in as-cast state they had to be homogenized. Figure 4.3 illustrates the difficulty associated with finding an appropriate temperature for the homogenization treatment of the A2 alloy, which was extremely susceptible to abnormal grain growth. The highest temperature where a 24 hours holding time was possible was 540 °C. Abnormal grain growth of course affect the deformed microstructure, which are also compared in Figure 4.3 for homogenization at 600 °C and 540 °C. From Table 4.2 it is clear how the HAGB spacing is almost one order of magnitude larger after homogenization at 600 °C compared to the 540 °C variant, despite significantly more grain subdivision during deformation taking place in the 600 °C variant.

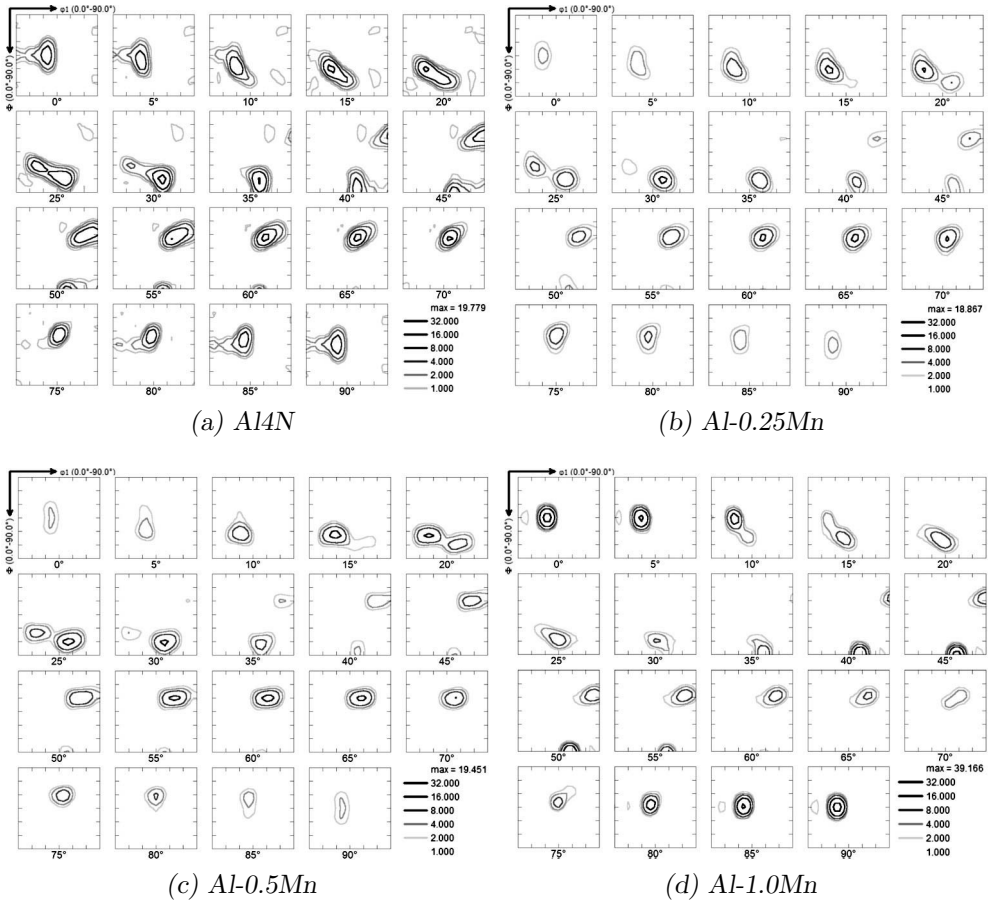

(a) Al4N *(b) Al-0.25Mn*

(c) Al-0.5Mn *(d) Al-1.0Mn*

Figure 4.2: Deformation texture (β-fibre) as measured by EBSD of the different alloys after cold rolling to strain $\varepsilon = 3$.

Table 4.2: Break-up factor calculations after different homogenization treatments of $A2^{hom}_{600}$ and A2.

	600 °C		**540 °C**	
	Measured	Calculated	Measured	Calculated
Hom. HAGB-spacing [mm]	3.1579		0.0789	
Def. 92.5% HAGB-spacing [mm]	0.0164	0.2345	0.0021	0.0059
Break-up factor (BUF)	14.31		2.74	

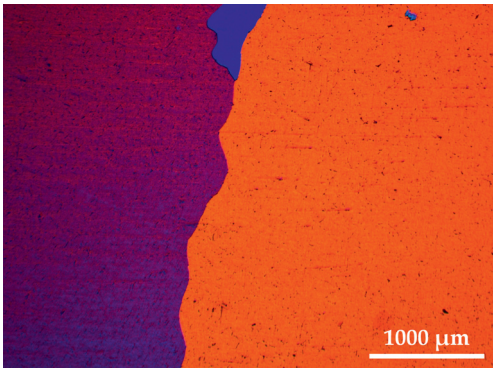

(a) $A2^{hom}_{600}$ as-cast.

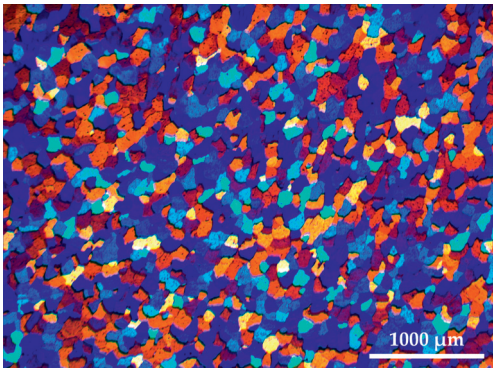

(b) A2 as-cast.

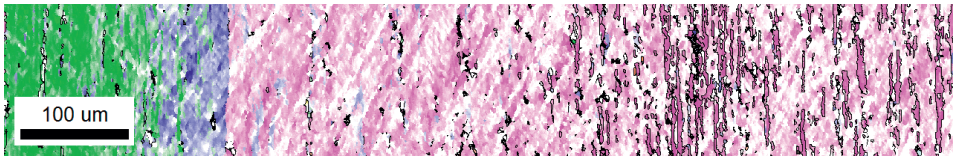

(c) $A2^{hom}_{600}$ deformed 92.5%.

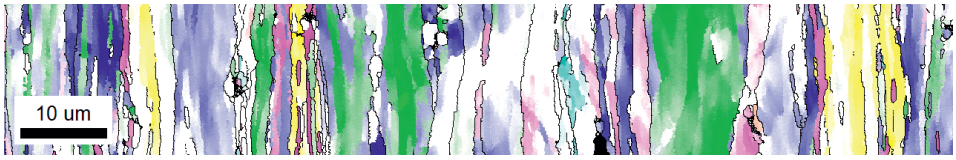

(d) A2 deformed 92.5%.

Figure 4.3: Abnormal grain growth observed during homogenization of alloy A2.

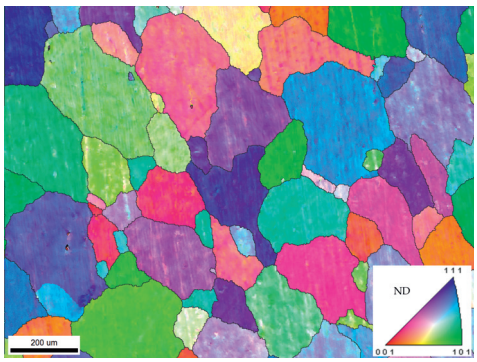

(a) A1

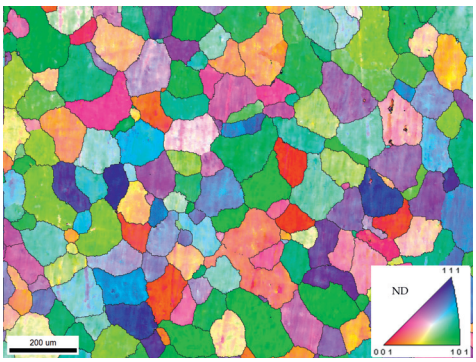

(b) A2

Figure 4.4: Inverse pole figure maps illustrating the microstructure of A1 and A2 after homogenization (540 °C, log-cooling). Black lines represent HAGBs.

When homogenized at 540 °C, there is a large difference in grain size between the two alloys. In the A1 alloy the grains are almost twice as large as the grains in the A2 alloy. Grain size and other properties of the A1 and A2 alloys in as-cast state and after homogenization at 540 °C are listed in Table 4.3. Homogenization leads to an increase in the conductivity of 0.9 and 0.6 m/Ωmm^2 for the A1 and A2 alloys, respectively. Compared to A2, the overall conductivity is 0.8 m/Ωmm^2 larger in A1.

For the constituent particles in the homogenized samples, both the size and density was found to be distributed heterogeneously on the scale of centimetres. However, because the particles break up during deformation, any effect of constituent particles on the softening behaviour is related to their size and distribution after deformation. Hence, the particles were also investigated in the as-deformed state. Binary BSE-images are shown in Figure 4.5 for both homogenized and deformed states. From Table 4.3 it is clear that there is no tangible difference between the constituent particles of the two alloys. Also, break-up is not extensive and only marginally smaller particles were observed after deformation. Slightly more break-up occurs in A1 than in the silicon rich A2. The area fraction is ∼0.65 in both alloys and the average area of particles after deformation is ∼1.8 μm^2 and ∼1.9μm^2, respectively. The equivalent circle diameters are 1.50 μm and 1.57 μm.

Table 4.3: Conductivity, grain size and constituent particles in A1 and A2 in as-cast and homogenized state. Constituent particles were also measured in deformed samples.

		A1	**A2**
Conductivity [m/Ωmm^2]			
As cast		34.5	34.0
Homogenized		35.4	34.6
Grain size [μm]			
Homogenized		134.1	80.5
Constituent particles			
	Particles [#]	1491	1610
	Density [#/μm^2]	0.0030	0.0032
	Average area [μm^2]	2.15	1.99
Homogenized	Area fraction [%]	0.68	0.65
	Particles [#]	1289	1360
	Density [#/μm^2]	0.0034	0.0036
	Average area [μm^2]	1.77	1.93
Deformed (92.5%)	Area fraction [%]	0.63	0.67

In accordance with the few differences observed in Table 4.3, the respective two-dimensional size distributions of constituent particles in A1 and A2 given in Figure 4.6 are nearly identical. There are only a few larger particles and slightly more of the particles between 1 μm and 1.5 μm in the A2 alloy.

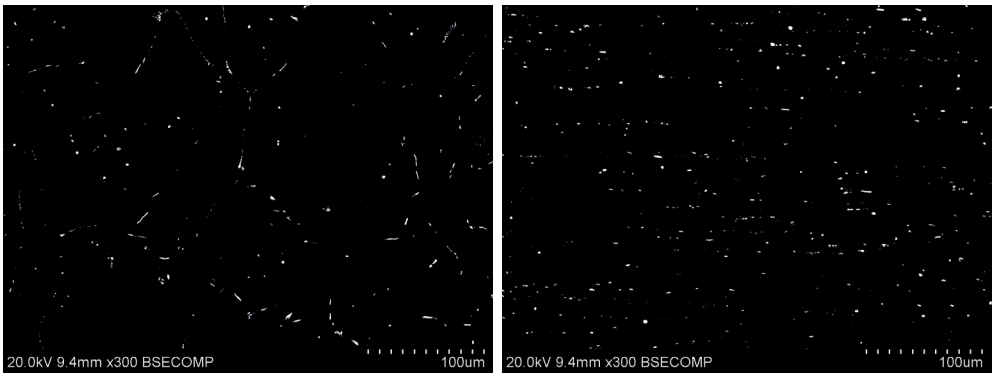

(a) A1, homogenized. *(b) A1 deformed.*

(c) A2, homogenized. *(d) A2, deformed.*

Figure 4.5: Back-scattered electron images of constituent particles in A1 and A2 after homogenization and deformation to strain $\varepsilon = 2.6$.

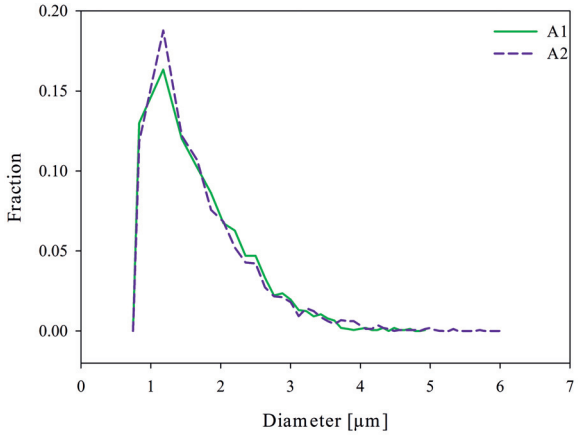

Figure 4.6: 2D size distribution of equivalent circle diameter of constituent particles in A1 and A2 after deformation.

The deformation textures of A1 and A2 after cold rolling to strain $\varepsilon = 2.6$ (92.5% reduction) are shown in Figure 4.7 and Figure 4.8, respectively. The ODFs show a typical β-fibre and all the typical components (Brass, Cu and S) are present in both A1 and A2. However, the peak intensity is slightly stronger in A1 at 21.5 times random, compared to 17.6 times random in A2.

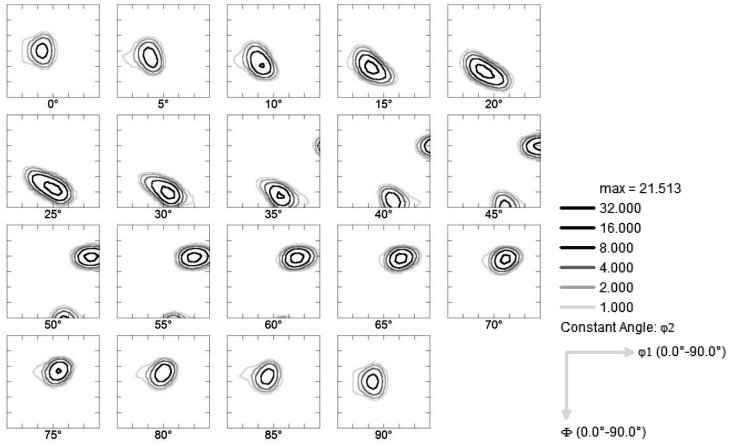

Figure 4.7: ODF constructed from EBSD measurements of A1 sample after cold rolling to strain $\varepsilon = 2.6$ (92.5% reduction).

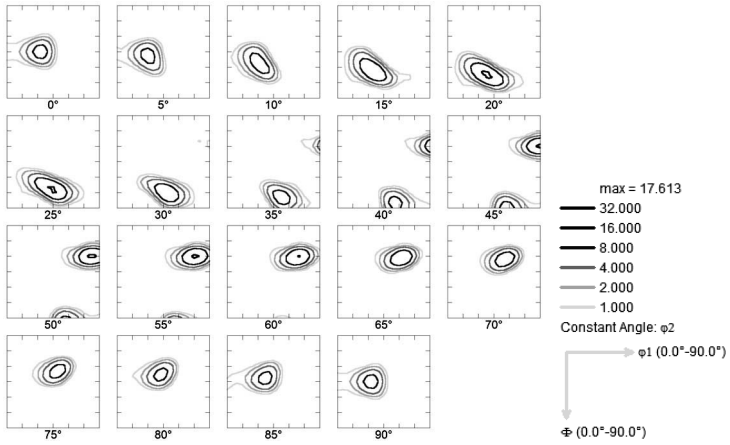

Figure 4.8: ODF constructed from EBSD measurements of A2 sample after cold rolling to strain $\varepsilon = 2.6$ (92.5% reduction).

Chapter 5

Experimental Results

Subgrain growth and recovery kinetics are a function of alloy composition, casting, homogenization, deformation and annealing. The properties of the materials after casting, homogenization and deformation have already been presented, i.e. the starting materials for subsequent annealing. In the following, a complete and detailed description of the softening behaviour is made in accordance with the scope of this PhD work. The results are presented with the layout introduced in the experimental part, starting with the high purity alloys and followed by the commercial purity alloys.

In all plots of either hardness, conductivity, subgrain size or average boundary misorientation, the as-deformed state is equivalent to 10^0 second of annealing since these data are plotted versus a logarithmic time scale. The absolute shortest annealing time experienced by any sample was 2 seconds.

Orientation maps are either presented according to specific texture components as shown in Figure 5.1(a) or as inverse pole figure maps relative to the TD-directed and Figure 5.1(b) if not specified otherwise. The colour schemes are chosen so that they correlate, e.g. pink means Cu and green means Brass, in both inverse pole figure maps and reconstructed subgrain maps. Similar colours have also been used in plots related to the various texture components, both here in the results chapter but also later in the discussion chapter (Chapter 6).

5.1 High Purity Alloys

The high purity alloys were characterized in terms of softening behaviour, subgrain structure evolution during annealing and recrystallization texture.

5.1.1 Annealing Behaviour

The softening curves for the high purity alloys are given in Figure 5.2 and Figure 5.3. Figure 5.3 also show how the electrical conductivity varies during

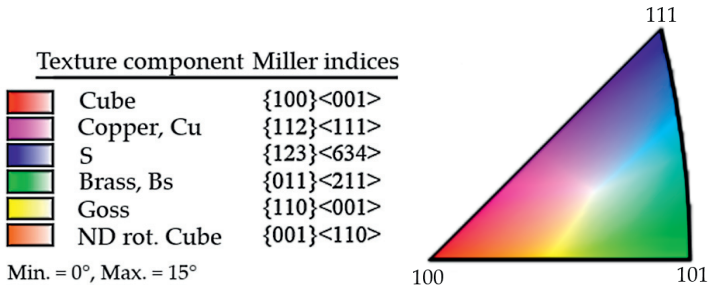

(a) Colour code. *(b) Inverse pole figure.*

Figure 5.1: Colour representations for orientation micrographs used in this work.

annealing in Al-0.5Mn and Al-1.0Mn. The electrical conductivity of Al4N and Al-0.25Mn was 36 m/Ωmm^2 and 28 m/Ωmm^2, respectively, but is not included in the graphs simply because it is constant during the whole annealing process.

In the Al4N material (Figure 5.2(a)), recovery and recrystallization took place simultaneously at 220 °C and above. Below this temperature, extended recovery was observed and accompanied by an increase in hardness after short annealing times. The recrystallization behaviour was very heterogeneous, as exemplified by the two data sets obtained at 220 °C predicting both extended recovery (open triangles) and recovery followed by recrystallization (closed triangles). Similarly, at 240 °C there are two curves which seemingly depict fast recrystallization but on closer inspection the hardness value at 1000 seconds is more appropriate for an extended recovery process. The reason for this behaviour lies partially with the coarse, columnar grain structure after casting resulting in few HAGB that may act as nucleation cites for recrystallization. However, once nucleation actually commence, growth is expected to be very rapid because the low solute content should only have a weak drag-effect on the boundaries. Figure 5.4 shows the microstructures in the RD-TD plane after 10^4 seconds of annealing at 240 °C and the heterogeneous nature of the microstructure is apparent. Due to this somewhat unusual recrystallization behaviour, it was possible to study recovery in bands of certain textures even at 240 °C. During annealing, no precipitation reactions were detected by the electrical conductivity measurements in the Al4N alloy.

The softening behaviour of the Al-0.25Mn material (Figure 5.2(b)) is more consistent compared to Al4N. Above 250 °C, recovery is succeeded by more homogenous recrystallization. Still, at 265 °C and 275 °C, the measurements are not entirely consistent and a higher hardness is sometimes found at the higher temperature after similar annealing times. This is, however, most likely attributed to the coarseness and orientation of the banded structure after defor-

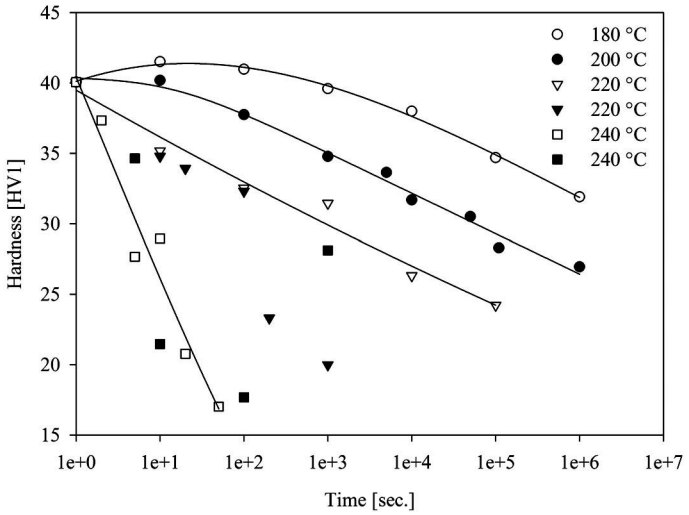

(a) Al4N

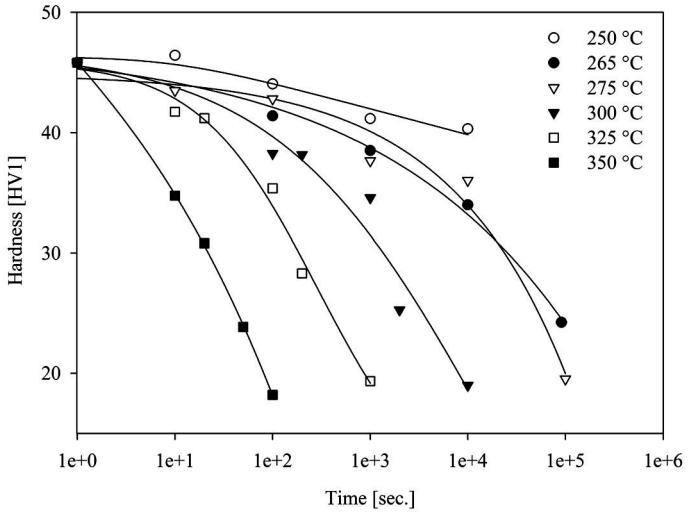

(b) Al-0.25Mn

Figure 5.2: Softening curves of Al4N (a) and Al-0.25Mn (b). Notice both extended recovery and recrystallization at 220 °C and 240 °C for Al4N.

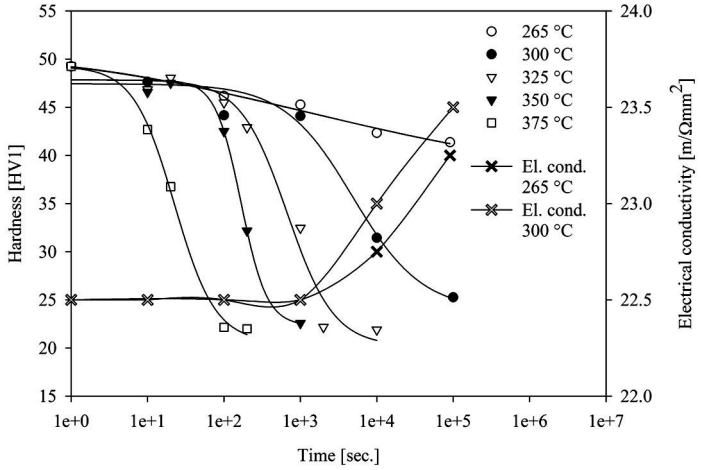

(a) Al-0.5Mn

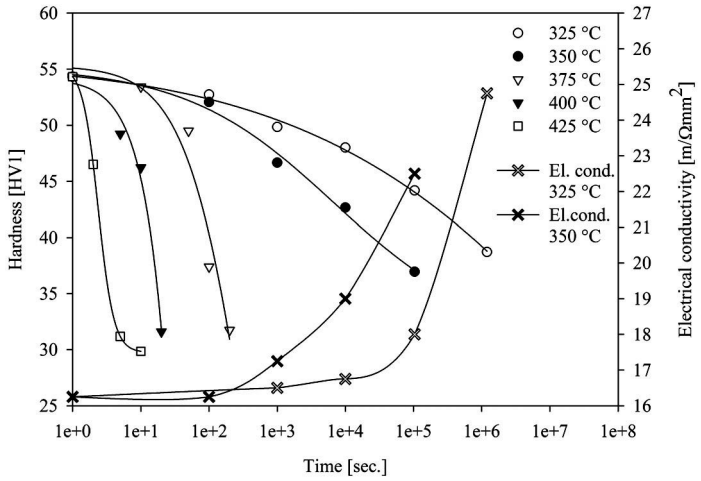

(b) Al-1.0Mn

Figure 5.3: Softening curves and electrical conductivity of Al-0.5Mn (a) and Al-1.0Mn alloys (b).

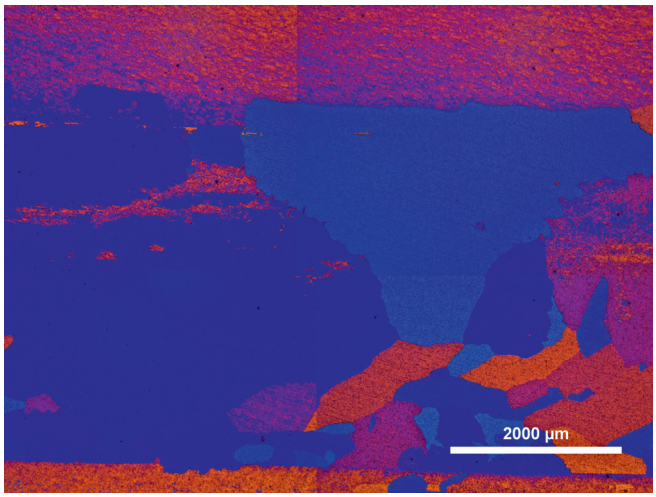

Figure 5.4: Microstructure in the RD-TD plane of Al4N deformed to strain $\varepsilon = 3.0$ and annealed for 10^4 at 240 °C.

mation which gives rise to a heterogeneous microstructure. Recovery is the only softening reaction observed at 250 °C, although annealing was not done beyond 10^4 seconds, and the curve reveals that some initial hardening on annealing is also taking place in this alloy. According to the electrical conductivity measurements, Mn stays in solution throughout the annealing process irrespective of temperature.

In terms of increasing Mn content, recovery and recrystallization was found to be influenced by concurrent precipitation at the two lowest annealing temperatures in Al-0.5Mn and Al-1.0Mn. The electrical conductivity measurements included in Figure 5.3(a) show how the conductivity increases in Al-0.5Mn due to precipitation after 1000 seconds at both 265 °C and 300 °C. Above 300 °C, the alloy is recrystallizing without simultaneous precipitation. From the softening curves of Al-1.0Mn in Figure 5.3, it is even more clear how precipitation of particles slows down the softening kinetics after 100 seconds at 325 °C and 350 °C. While the samples annealed at 350 °C are actually not fully soft after 10^5 seconds, a 25 °C hike in temperature sees the alloy completely recrystallized after 200 seconds. The hardness measurements then clearly show why it is not possible to study the effect of solute on recovery kinetics in the Al-0.5Mn or Al-1.0Mn alloys. Either the temperature is too low for any significant recovery to happen or precipitation will occur at low to intermediate temperatures or the samples are already recrystallized after 1000 seconds.

5.1.2 Subgrain Structure Evolution

A major effort has been made to characterize the recovery kinetics in the various deformation texture components and to some extent the effect of Mn in solid solution. By means of EBSD and a novel characterization method, the subgrain size and average boundary misorientation evolution during isothermal annealing were followed in the Al4N and Al-0.25Mn alloys.

Al4N

The recovery-characteristics of Al4N are shown graphically in Figure 5.5 at four different annealing temperatures. Average subgrain sizes and boundary misorientations in the different texture components of Al4N are also listed in Table 5.1 and Table 5.2, respectively.

The as-deformed microstructures of both Cu and S were found to have a larger subgrain size than after annealing by approximately 0.3 μm. From two as-deformed cross sections, only three areas with Cu and S orientations suitable for subgrain boundary reconstruction were found. They all gave higher subgrain sizes than in any of the six annealed Cu and S oriented subgrain structures investigated. Subgrain sizes of 0.82 μm and 0.93 μm were successfully reconstructed from the as-deformed state in Al-0.25Mn and A1, respectively, proving that the method is capable of handling the as-deformed state. That a smaller average size of subgrains with Cu and S orientation in Al4N was not found is simply a result of stochastic variation caused by the very heterogeneous material, illustrated in Figure 5.6 by two Cu oriented subgrain structures. Hence, in Figure 5.5, the subgrain sizes of Cu and S in as-deformed state were back-extrapolated from data collected at 180 °C where hardly any growth occurs. The misorientation values are the true values measured in as-deformed samples with Cu and S orientations.

It is clear from the graphs in Figure 5.5 that subgrain growth in the deformation textures components Cu, S and Brass is weak. Only in for Cube and Goss oriented subgrains is more than a doubling of the as-deformed size observed. Ignoring the behaviour of Cube and Goss subgrains for a while, there is no abrupt increase or decrease in size for any of the Cu, S or Brass oriented subgrains. The typical growth behaviour of subgrains in the Cu, S and Brass texture components is illustrated in Figure 5.7 which shows reconstructed subgrain maps of subgrains with Copper orientation in as-deformed state and after 10^6 seconds of annealing at 220 °C.

The growth rate in the deformation texture components increases weakly with increasing temperature and there are only marginal differences between the three orientations, particularly Cu and S oriented subgrains behave similarly. Growth of subgrain in Brass is perhaps slightly faster. The average boundary misorientation measurements are sensitive to experimental scatter. Still, the

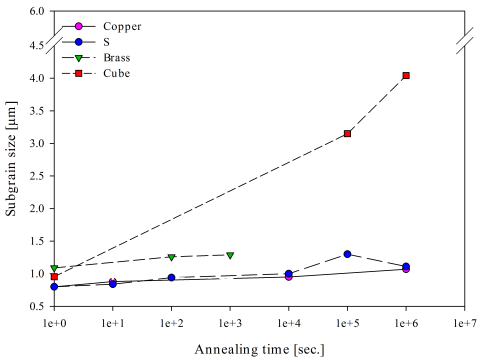

(a) Subgrain sizes Al4N, 180 °C

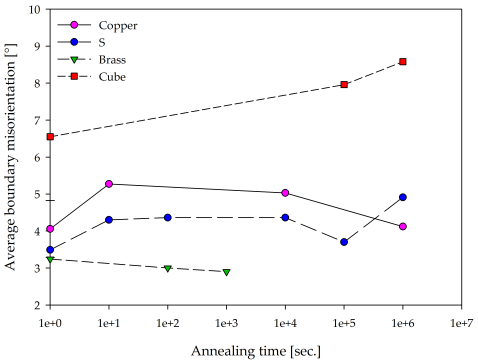

(b) Misorientations Al4N, 180 °C

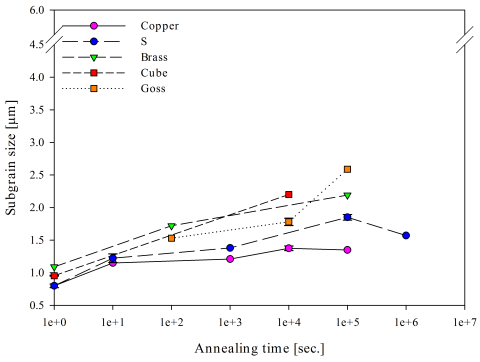

(c) Subgrain sizes Al4N, 200 °C

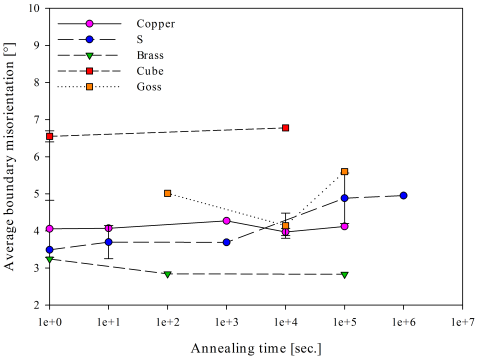

(d) Misorientations Al4N, 200 °C

Figure 5.5: Subgrain growth (left) and evolution of average boundary misorientations (right) during annealing of Al4N at 180 °C ((a) & (b)) and 200 °C ((c) & (d)).

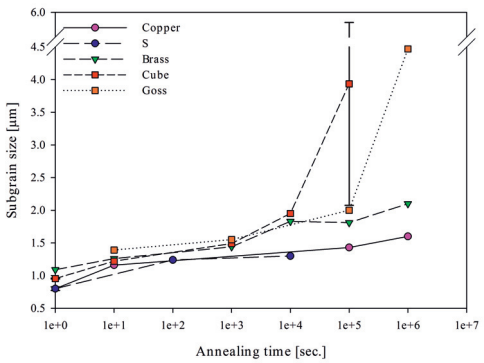

(e) Subgrain sizes Al4N, 220 °C

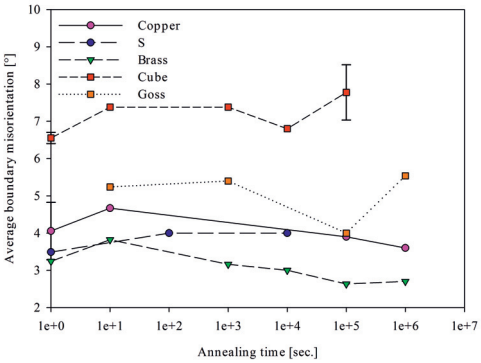

(f) Misorientations Al4N, 220 °C

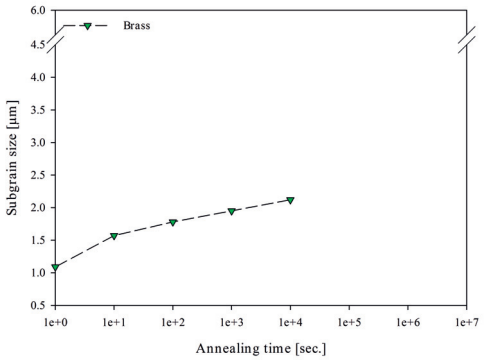

(g) Subgrain sizes Al4N, 240 °C

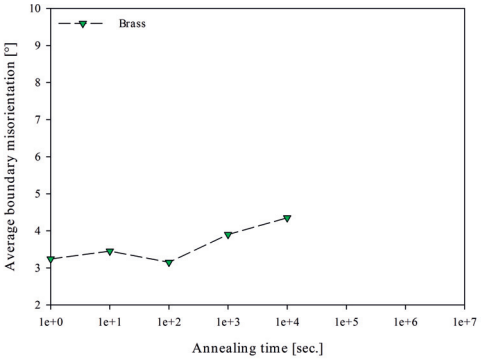

(h) Misorientations Al4N, 240 °C

Figure 5.5: Subgrain growth (left) and evolution of average boundary misorientations (right) during annealing of Al4N at 220 °C ((e) & (f)) and 200 °C ((g) & (h)).

Table 5.1: Orientation dependent subgrain sizes in Al4N after cold rolling to strain $\varepsilon = 3$ and annealing.

Temp. [°C]	Time [s]	Subgrain size [µm]				
		Cu	**S**	**Brass**	**Cube**	**Goss**
as def.	0	0.80	0.80	1.09	0.96	-
180	10^1	0.88	0.84	-	-	-
	10^2	-	0.94	1.26	-	-
	10^3	-	-	1.29	-	-
	10^4	0.95	1.00	-	-	-
	10^5	-	1.30	-	3.15	-
	10^6	1.07	1.11	-	4.04	-
200	10^1	1.15	1.22	-	-	-
	10^2	-	-	1.72	-	1.53
	10^3	1.21	1.38	-	-	-
	10^4	1.38	-	-	2.20	1.78
	10^5	1.35	1.85	2.19	-	2.59
	10^6	-	1.57	-	-	-
220	10^1	1.16	-	1.26	1.22	1.39
	10^2	-	1.24	-	-	-
	10^3	-	-	1.44	1.49	1.55
	10^4	-	1.3	1.83	1.95	-
	10^5	1.43	-	1.81	3.94	2.00
	10^6	1.6	-	2.10	-	4.47
240	10^1	-	-	1.57	-	-
	10^2	-	-	1.78	-	-
	10^3	-	-	1.95	-	-
	10^4	-	-	2.12	-	-

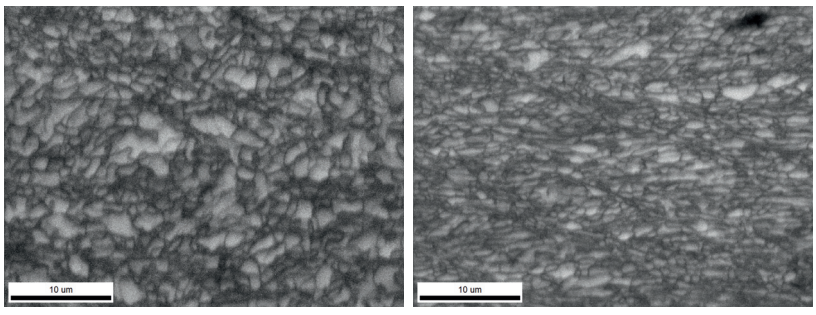

(a) Al4N, as-deformed. *(b) Al4N, 180 °C, 10 s.*

Figure 5.6: Image quality (IQ) maps of subgrain structure of Cu oriented regions in (a) as-deformed and (b) slightly annealed (10 seconds at 180 °C) state.

Table 5.2: Orientation dependent average boundary misorientations in Al4N after cold rolling to strain $\varepsilon = 3$ and annealing.

Temp. [°C]	Time [s]	Misorientation [°]				
		Cu	**S**	**Brass**	**Cube**	**Goss**
as def.	0	4.06	3.49	3.24	6.55	-
180	10^1	5.27	4.3	-	-	-
	10^2	-	4.36	3.00	-	-
	10^3	-	-	2.90	-	-
	10^4	5.03	4.36	-	-	-
	10^5	-	3.70	-	7.96	-
	10^6	4.12	4.91	-	8.58	-
200	10^1	4.07	3.70	-	-	-
	10^2	-	-	2.84	-	5.01
	10^3	4.27	3.69	-	-	-
	10^4	3.97	-	-	6.78	4.14
	10^5	4.12	4.88	2.83	-	5.60
	10^6	-	4.95	-	-	-
220	10^1	4.67	-	3.82	7.38	5.24
	10^2	-	4.00	-	-	-
	10^3	-	-	3.16	7.38	5.40
	10^4	-	4.00	3.00	6.80	-
	10^5	3.90	-	2.63	7.78	4.00
	10^6	3.60	-	2.70	-	5.54
240	10^1	-	-	3.45	-	-
	10^2	-	-	3.15	-	-
	10^3	-	-	3.90	-	-
	10^4	-	-	4.35	-	-

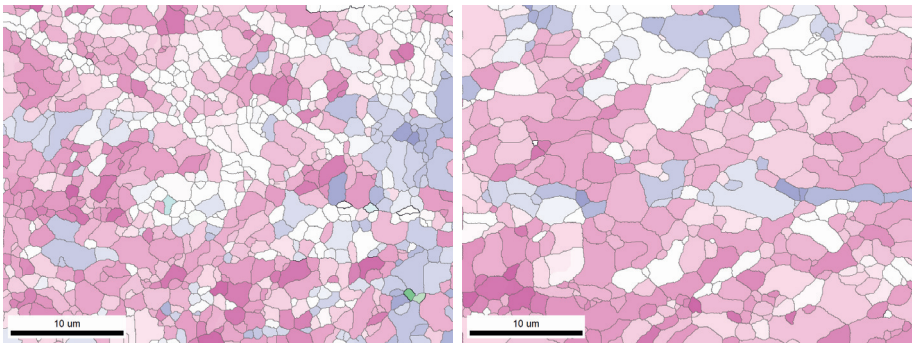

(a) Cu, Al4N, as-deformed. *(b) Cu, Al4N, 220 °C, 10^6 s.*

Figure 5.7: Reconstructed maps of the subgrain structure in Copper regions after deformation (a) and subsequent annealing at 220 °C for 10^6 seconds (b).

evolution is definitely different in Cu and S and Brass. Whereas the misorientations appear to be stable in Cu or possibly increase by ∼1° as in S, a distinct decrease by ∼0.5° is observed for Brass oriented subgrains with annealing. The behaviour is seen at all temperatures except at 240 °C, where only Brass was measured, and the misorientations are clearly increasing.

Increasing misorientations were observed in Cube (∼1–2°). In Goss the increase is less pronounced and the measurements scatter more. Initially, the rate of subgrain growth is comparable to that of Brass. However, after what appears like an incubation time, the growth rate increases rapidly and some grains are able to grow more than others. This is tried illustrated in Figure 5.8 for subgrains with near-Cube orientations. After deformation the subgrain size is uniform but after rapid growth has initiated there seems to be islands of large subgrains with smaller subgrains in between. In the figure, black lines represent HAGBs and grey lines LAGBs.

As opposed to regions with Cu, S or Brass orientation where there typically is less than 1% HAGBs, there are slightly more HAGBs in Goss (1–10%), and many more HAGBs in the near-Cube regions. In e.g. Figure 5.8(a), (b) and (c) there are 58%, 34% and 53% HAGBs, respectively. Even so, and perfectly illustrated by Figure 5.5(e), Goss and Cube both exhibit similar growth behaviour where there is a transition from slow to rapid growth after an incubation time. The transition occurs earlier in Cube than in Goss.

Reconstructed subgrain maps clearly reveal contrasting evolution of the subgrain structures with C/S/Brass and Cube/Goss orientations upon annealing. In Cu/S/Brass, represented by S in Figure 5.9, subgrains grow continuously and have uniform size even after long annealing times. However, for Cube/Goss, illustrated by a near-Cube region in Figure 5.9, what appears to be a bimo-

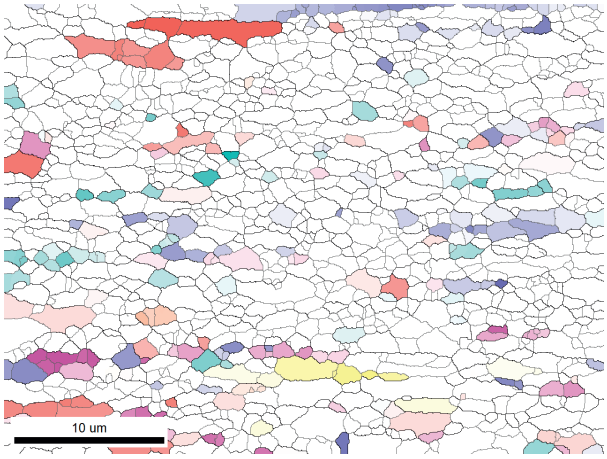

(a) Cube, Al4N, as-deformed.

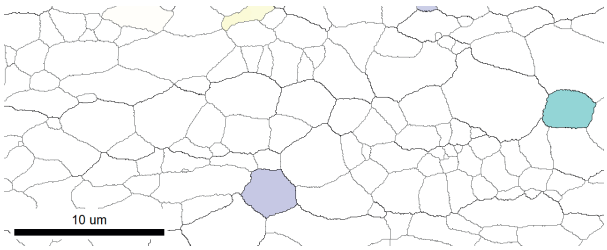

(b) Cube, Al4N, 220 °C, 10^4 s.

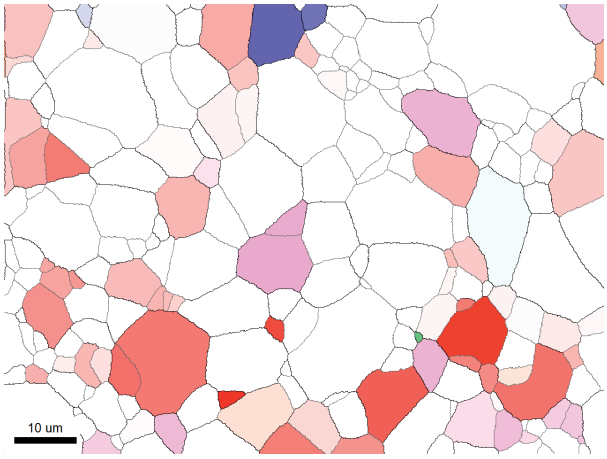

(c) Cube, Al4N, 220 °C, 10^5 s.

Figure 5.8: Reconstructed maps of the subgrain structure in near-Cube regions after deformation (a) and subsequent annealing at 220 °C for 10^4 seconds (b) and 10^5 seconds (c).

dal size distribution (Figure 5.9(c)) develops. After an incubation period, the subgrain structure rapidly evolves by growth of a large selection of subgrains. This discontinuous growth results in a more heterogeneous microstructure (Figure 5.9(d)).

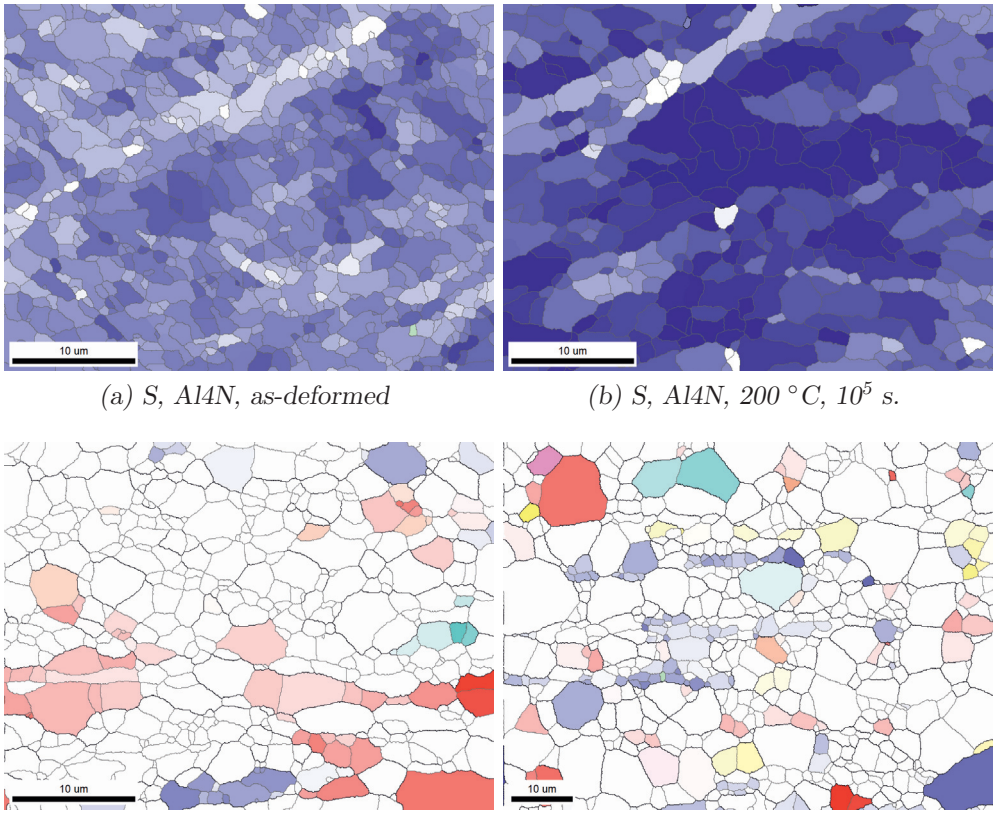

(a) S, Al4N, as-deformed *(b) S, Al4N, 200 °C, 10^5 s.*

(c) Cube, Al4N, 220 °C, 10^3 s. *(d) Cube, Al4N, 220 °C, 10^5 s.*

Figure 5.9: Reconstructed maps of the subgrain structure illustrating continuous growth of S oriented subgrains (a) & (b) and the transition from slow (c) to rapid discontinuous growth of near-Cube oriented subgrains (d).

Discontinuous growth is followed by increasing misorientations in Goss and Cube. Although the average boundary misorientations also increase for subgrains with S orientation, growth is continuous and there is no change in the growth rate. For growth of subgrains with Brass orientation investigated after annealing at 240 °C the misorientations are suddenly also increasing. At lower temperatures the misorientations were consistently decreasing and growth was slow and continuous. At 240 °C it is possible that a transition toward discontinuous growth occurs, although not to the same extent as for Cube oriented

subgrains. Two reconstructed subgrain maps of these microstructures are given in Figure 5.10. In Figure 5.10(a) the subgrains have a more uniform size distribution than in Figure 5.10(b) where a discontinuous growth process could be about to initiate. After further annealing, it was not possible to find unrecrystallized areas large enough for subgrain characterization which could have confirmed whether the growth is truly discontinuous.

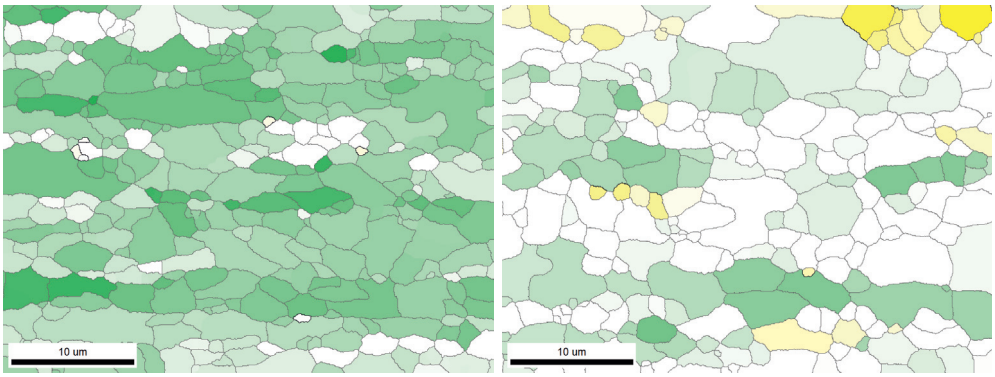

(a) Brass, Al4N, 240 °C, 10^2 s. *(b) Brass, Al4N, 240 °C, 10^4 s.*

Figure 5.10: Reconstructed maps of the subgrain structure revealing a possible transition from continuous to discontinuous growth.

From the subgrain size versus misorientation plots of subgrains with Cube, S and Brass orientations in Figure 5.11 there are clearly major differences already after deformation (note that the vertical scale in the figure is changing and that the average misorientation values are not weighted by the boundary lengths). Subgrains with Cu orientation were found to be similar to S-oriented subgrains but sometimes also have a very low fraction of HAGBs like Brass. For Cube, the majority of the crystallites (grains and subgrains) have an average misorientation larger than 15° and these grains are also significantly larger than most of the subgrains. For this particular scan, 61% of the boundaries have high-angle character. Hence, growth in Cube oriented regions is neither pure subgrain growth nor recrystallization or grain growth. Recrystallization is, by definition, growth by mobile high-angle boundaries. However, as there is clearly a large fraction of low-angle boundaries present here, Cube oriented regions are included in this PhD work.

Due to the challenge of obtaining representative areas, the data for the S oriented subgrains was gathered in a sample annealed for 10 seconds at 180 °C. Besides some possible dislocation annihilation, this microstructure is not significantly different from the as-deformed state. Also in S there are several subgrains with average boundary misorientations larger than 15°. In this case

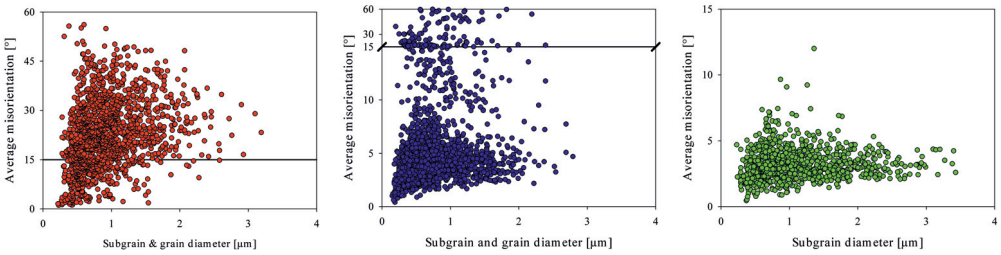

(a) Cube. *(b) S.* *(c) Brass.*

Figure 5.11: Average misorientation plotted against mean equivalent circle diameter for individual subgrains and grains with Cube (a), S (b) and Brass (c) orientations in as-deformed state, after 10 seconds of annealing at 180 °C and in as-deformed state, respectively.

the fraction of HAGBs is 5% but typically the fraction for both S and Cu is closer to 1%. In Brass oriented regions, on the other hand, HAGBs were rarely observed at all, which Figure 5.11 clearly illustrates.

Figure 5.11 shows that there is only a weak correlation between subgrain size and average boundary misorientation. In all texture components, the minimum misorientation increases with increasing subgrain size. Although less pronounced, the minimum subgrain size increases marginally with increasing misorientations. The majority of subgrains with S and Brass orientations have misorientations less than 8° and larger subgrains have a random spread within the size distribution. In fact, most subgrains larger than 1 µm are those with misorientations between 2° and 5°. Cube oriented subgrains, on the other hand, do show a correlation between size and misorientation. Although the subgrains are not larger than in S or Brass, subgrains in Cube oriented regions that are larger than 2 µm all have misorientations in the range 10–45°.

The subgrain growth curves in Figure 5.5 and size and misorientation plots in Figure 5.11 illustrate that growth of subgrains with Cube orientations is very different from growth of subgrains with Brass, Cu and S orientations. The same is most likely true for subgrains with Goss orientation but there are too few observations and they are not considered further. In Figure 5.12, growth of Cube oriented subgrains leads to a shift of the whole size distribution to larger grain sizes and in Figure 5.12(c) there is a bimodal size distribution after 10^3 seconds of annealing. Growth is associated with increasing misorientations at all the different temperatures. In Figure 5.12(b) and Figure 5.12(d) the average boundary misorientations of Cube-subgrains are increasing marginally. The number of boundaries with misorientations less than 3° is decreasing the most. These misorientation plots do not include the many HAGBs that are

evident in Figure 5.11.

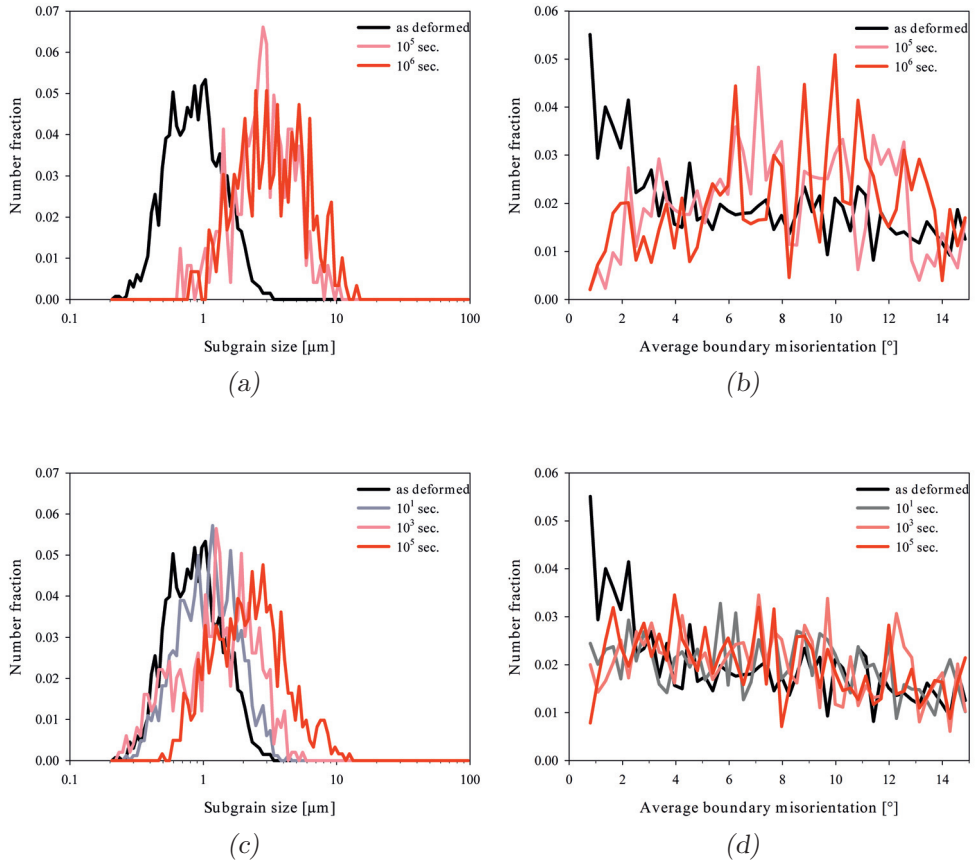

Figure 5.12: Size and average boundary misorientation distributions of Cube oriented subgrains during annealing at 180 °C ((a) & (b)) and 220 °C ((c) & (d)).

That subgrains with Cube orientation behave differently from subgrains with other orientations during annealing is apparent also when comparing Figure 5.12 with Figure 5.13 where size and misorientation distributions of subgrains with Cu, S and Brass orientations is presented. The initial size distributions are rather similar and have the same spread, though in the Cube-distribution the peek has more of a plateau with steep sides than in the Cu, S and Brass distribution. There is of course less growth, something the subgrain size distributions illustrate by not shifting to larger diameters as observed for Cube. Instead, there is a subtle decrease in the amount of the smallest subgrains and consequently an accumulation of subgrain sizes closer to the maximum within the initial spread. The average boundary misorientations showed no change

or only a weak increase with growth. This is confirmed by the marginal changes observed for the misorientation distributions in Figure 5.13. A reduction of the fraction of boundaries with the absolutely smallest misorientations is observed but is hardly significant.

Growth of subgrains with Brass orientation has already been shown to progress either by decreasing or increasing misorientations. In Figure 5.14 it is seen that for low temperatures, where the misorientations were decreasing with annealing, growth results in a clear bimodal size distribution after 10^3 seconds of annealing (light green colour). The decreasing misorientations are also very noticeable in the misorientation distribution plot in Figure 5.14(b) by an increase in the fraction of boundaries with misorientation less than 3°. At 240 °C, subgrain growth progressed very differently from at lower temperatures and in Figure 5.14(c) there is no sign of a bimodal transition period. The misorientations were also increasing as a result of a marginally larger fraction of more misoriented boundaries and a decrease of boundaries with smaller misorientations.

Al-0.25Mn

The subgrain growth behaviour in the Al-0.25Mn alloy, presented in Figure 5.15, was barely any different from in the Al4N alloy. Just a few texture components were observed and annealing was only done at 275 °C. The experimental data from the graphs are also listed in Table 5.3 and Table 5.4. The subgrain sizes after deformation were similar in S and Brass, with 1.16 μm and 1.13 μm respectively. In contrast to what was previously found in Al4N, the size of subgrains with Cube orientation was found to be the smallest and only 0.82 μm. The average boundary misorientations in as-deformed state of Cube and S oriented subgrains were 6.25° and 4.16° respectively, and almost identical to those in the Al4N alloy. The measurement of Brass, on the other hand, differ greatly from all other measurements and is probably not representative for the general misorientations in Brass after deformation.

In terms of subgrain growth, exactly the same observations are made in Al-0.25Mn as in Al4N. Growth is significantly faster for near-Cube oriented subgrains and discontinuous growth is already occurring after 1000 seconds, as shown in Figure 5.16(a). Hence, growth of Cube-subgrains evolves similarly in Al4N and Al-0.25Mn, as does growth of subgrains with Brass orientation. For subgrains with S orientation on the other hand, growth results in a decrease of the average boundary misorientations of ∼0.5°. Still, the microstructure after annealing, pictured in Figure 5.16(b), appears analogous to the one in Al4N, shown in Figure 5.9(b).

The evolution of the misorientations for Brass oriented subgrains is similar to that observed in Al4N at the lowest temperatures. As already mentioned, subgrains with S-orientation somehow become more misoriented with annea-

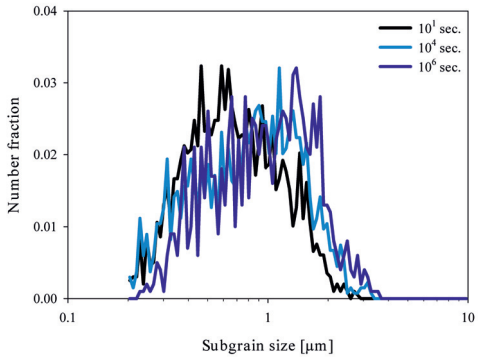

(a) S, Al4N, 180 °C.

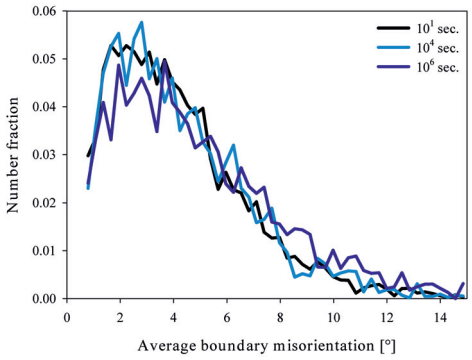

(b) S, Al4N, 180 °C.

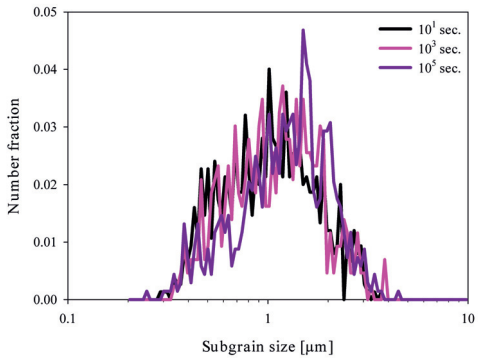

(c) Cu, Al4N, 200 °C.

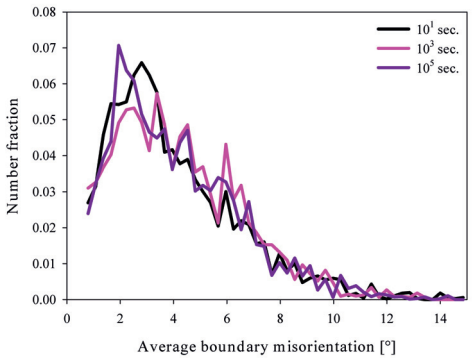

(d) Cu, Al4N, 200 °C.

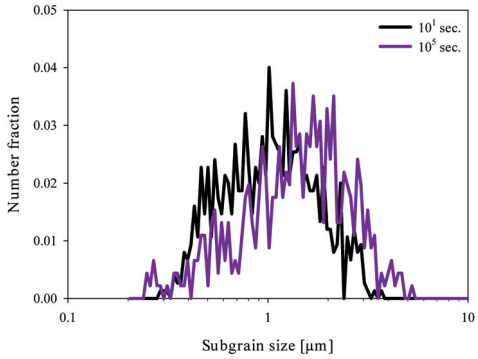

(e) Cu, Al4N, 220 °C.

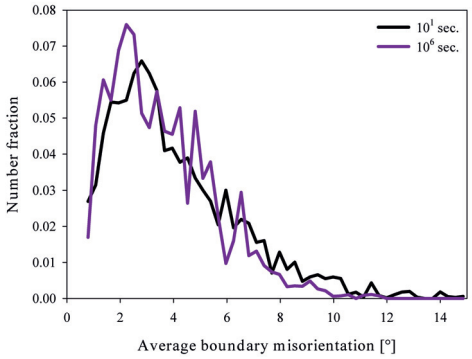

(f) Cu, Al4N, 220 °C.

Figure 5.13: Size and average boundary misorientation distributions of subgrains with Cu, S and Brass orientations.

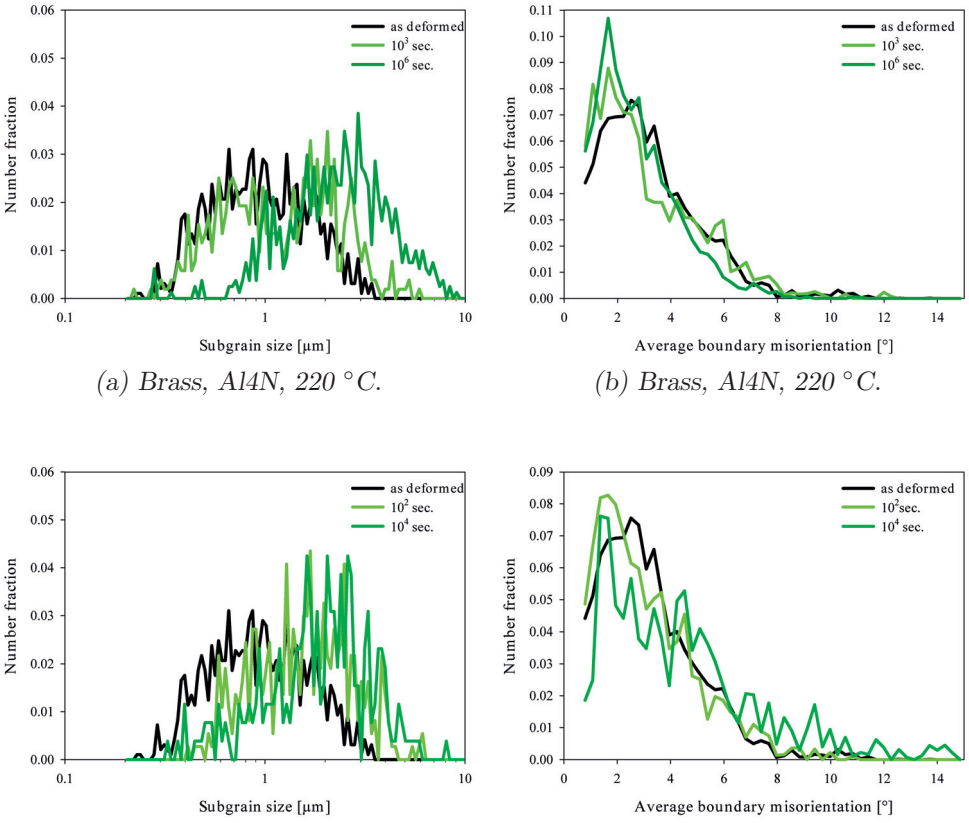

(a) Brass, Al4N, 220 °C. *(b) Brass, Al4N, 220 °C.*

(c) 240 °C. *(d) 240 °C.*

Figure 5.14: Size and average boundary misorientation distributions of subgrains with Cu, S and Brass orientations.

Table 5.3: Orientation dependent subgrain sizes in Al-0.25Mn after cold rolling to strain $\varepsilon = 3$ and annealing.

Temp. [°C]	Time [s]	Subgrain size [µm]		
		S	**Brass**	**Cube**
as def.	0	1.16	1.13	0.82
275	1e^1	1.17	1.33	-
	1e^2	-	1.39	-
	1e^3	1.19	1.60	1.87
	1e^4	-	1.78	-
	1e^5	1.57	-	-

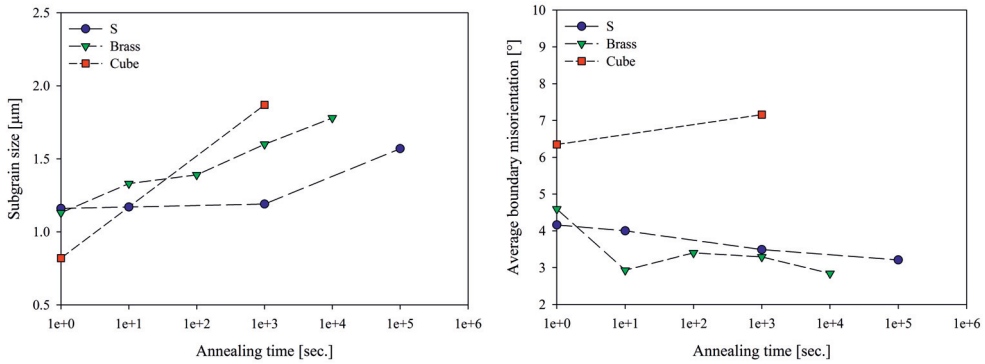

(a) Average subgrain size. *(b) Average boundary misorientations.*

Figure 5.15: Subgrain growth (a) and evolution of average boundary misorientations (b) during annealing of Al-0.25Mn at 275 °C.

Table 5.4: Orientation dependent average boundary misorientations in Al-0.25Mn after cold rolling to strain $\varepsilon = 3$ and annealing.

Temp. [°C]	Time [s]	Misorientation [°]		
		S	**Brass**	**Cube**
as def.	0	4.16	4.59	6.35
275	$1e^1$	4.00	2.93	-
	$1e^2$	-	3.40	-
	$1e^3$	3.49	3.29	7.16
	$1e^4$	-	2.84	-
	$1e^5$	3.21	-	-

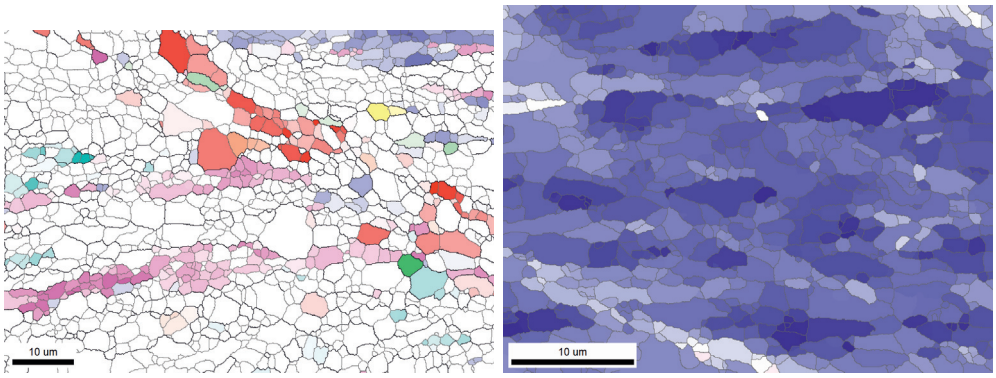

(a) Cube, Al0.25Mn, 275 °C, 10^3 s. *(b) S, Al0.25Mn, 275 °C, 10^3 s.*

Figure 5.16: Reconstructed maps of subgrain-structure revealing discontinuous growth in Cube-region (a) and similar growth of S as seen in Al4N (b).

ling, something which is opposite of what occurred in Al4N. The size and misorientation distributions presented in Figure 5.17 are both interesting. As the subgrains coarsen, only the largest subgrains appear to be growing. A growth behaviour very different from that of S-oriented subgrains in Al4N shown in e.g. Figure 5.13(a). Hence, it is likely that the size distribution could become bimodal upon further growth. The fraction boundaries with misorientations larger than 10° diminishes and instead the misorientations below 3° become more frequent, as was also seen for Brass in Al4N when there was a bimodal distribution at 240 °C.

5.1.3 Recrystallization

Nucleation of recrystallization and the final recrystallization texture was characterized in both the Al4N alloy and the Al-0.25Mn alloy. The resulting textures were very different and particularly the Al4N alloy exhibited some interesting recrystallization behaviour.

Al4N

Nucleation of recrystallization in Al4N was investigated by EBSD scans over the whole sample thickness in the RD-ND plane from samples annealed at 220 °C. The resulting inverse pole figure maps after different annealing times are given in Figure 5.18 (each figure is a composite of two scans) and confirmed that the nature of the materials also caused very heterogeneous nucleation of recrystallization. E.g. the fraction recrystallized in the sample annealed for 100 seconds is, according to the EBSD scans, larger than at any other annealing

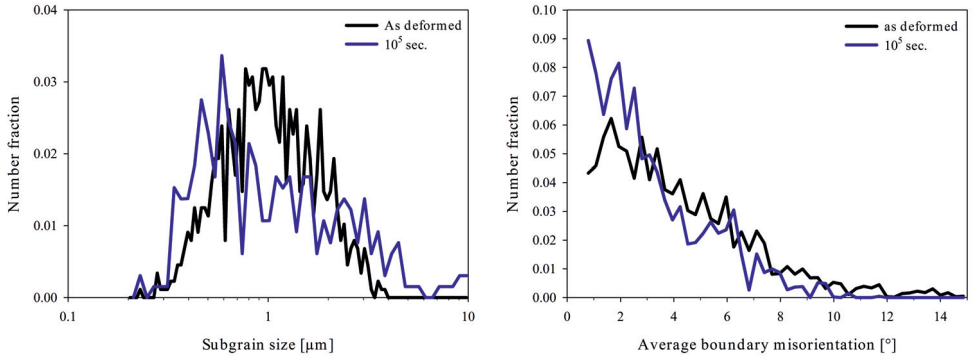

(a) Size distribution. *(b) Misorientation distribution.*

Figure 5.17: Size (a) and average boundary misorientation (b) distributions of subgrains with S orientation in Al-0.25Mn during annealing at 275 °C.

temperature. Although the fraction recrystallized is large, the number of recrystallized grains is small which makes it difficult to be precise about the origin of nucleation. Looking at the recrystallized grains at the other temperatures, the recrystallized grains are mostly associated with HAGBs and nucleation by the SIBM mechanism seems likely.

Some of the recrystallized grains have an orientation close to Cu, S or Brass and several are heavily rotated, often in the direction of Cube around a <111>-axis. A few grains have an orientation close to ND-rotated Cube, but not a single grain was found to have an ideal Cube orientation. In fact, hardly any of the recrystallized grains have any of the orientations typical of recrystallization textures (Cube, R, P, BR). In bands which are oriented close to Cube, several crystallites have the Cube orientation and they are much large than subgrains in bands of other orientations. However, in one of these Cube-bands there are also several crystallites with Cu-orientation, one of which has become a recrystallized grain.

The Al4N samples annealed at 220 °C did not become fully recrystallized (see Figure 5.2(a)) and the recrystallization texture was instead attempted characterized in samples annealed at 240 °C. However, the grain structure was very coarse and only a few EBSD scans were made. Some information of the global texture is provided by Figure 5.19, although only a handful of grains are shown. The orientations of the recrystallized grains at 240 °C were mainly scattered about the deformation texture orientations like the recrystallized grains at 220 °C and grains with typical recrystallization orientations were generally missing.

Not even at 240 °C did the samples become fully recrystallized and new

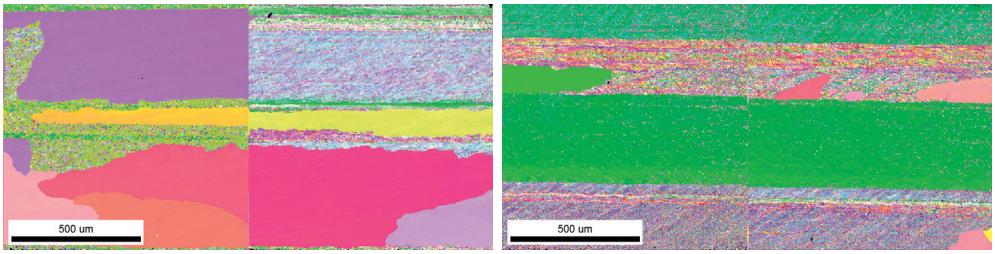

(a) Al4N, 220 °C, 10^2 s. (b) Al4N, 220 °C, 10^3 s.

(c) Al4N, 220 °C, 10^4 s. (d) Al4N, 220 °C, 10^5 s.

Figure 5.18: Inverse pole figure maps of recrystallized grains in Al4N after increasing time of annealing at 220 °C in otherwise layered deformation structure.

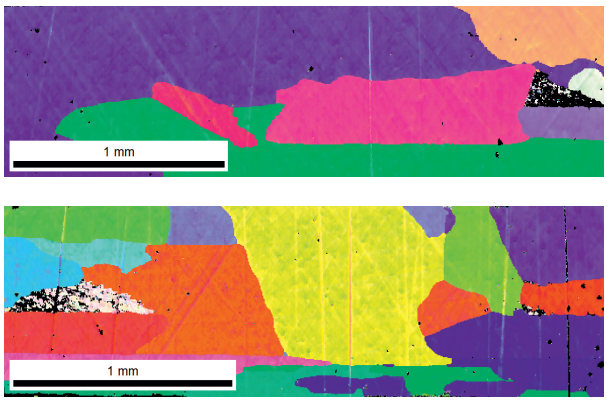

Figure 5.19: Inverse pole figure maps of almost fully recrystallized microstructure in Al4N after annealing at 240 °C for 10^5 seconds.

samples had to be annealed at 350 °C. Figure 5.20 shows how both the grain sizes and orientations now differ significantly from the recrystallized microstructures after annealing at lower temperatures shown in Figure 5.18 and Figure 5.19. Also, with the more fine-grained microstructure, a better description of the bulk texture can be obtained by plotting the ODFs as done in Figure 5.21. The ODF plotted after annealing at 240 °C in Figure 5.21(a) is not recognizable as anything typical texture and only a few components can be identified. However, at higher temperature, i.e. 350 °C, the ODF in Figure 5.21(b) reveals a texture with a strong Cube component typical for recrystallization. The Cube component is slightly RD-rotated and in addition there is an R component and a weak P component.

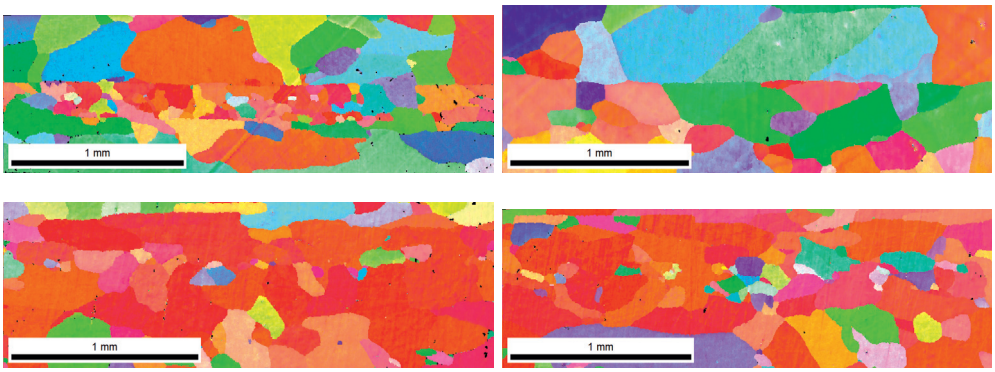

Figure 5.20: Inverse pole figure maps of fully recrystallized microstructure in Al4N after annealing at 350 °C for 10 seconds.

Because some of the peak intensities in the ODF are not immediately recognisable in the annealed samples at 240 °C, the 111-pole figures for high and low temperature annealing are illustrated together with the corresponding pole figures of the as-deformed state in Figure 5.22. It is clearly seen that there are recrystallized grains in samples annealed at 240 °C with normal recrystallization texture orientations like Cube. There are also some grains with orientations close to the Cu, S and Brass. At 350 °C the recrystallization texture is dominated by Cube but also has a weak R component.

A more detailed comparison of the orientations of the recrystallized grains is given in Figure 5.23 where the orientation of each recrystallized grain is plotted with pole diameters proportional to the grain size. Several of the grains at 350 °C have an orientation close to the R recrystallization texture component and these are among the largest grains. Most of the recrystallized grains with a Cube orientation are relatively small.

The effect of temperature on recrystallization texture in Al4N was confirmed in samples cold rolled to a lower strain with a finer grain size (achieved by

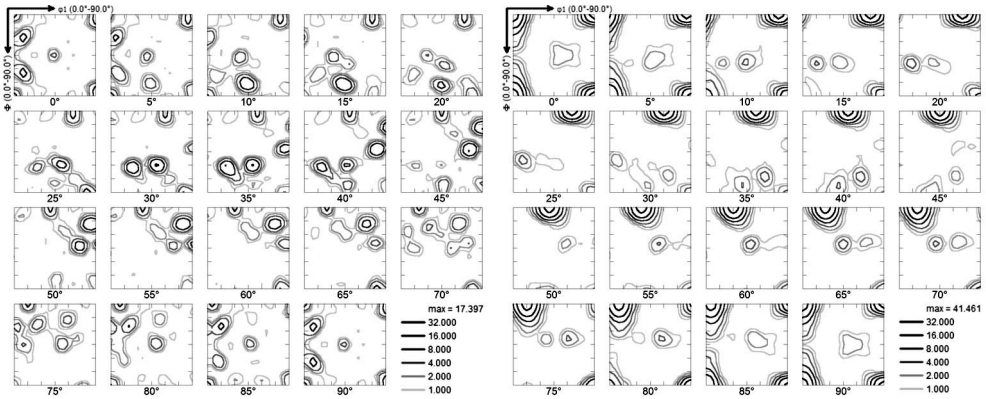

(a) Al4N, 240 °C, 10^5s. *(b) Al4N, 350 °C, 10 s.*

Figure 5.21: ODFs of Al4N recrystallized at low and high temperature.

interannealing). As Figure 5.24 shows, the Cube texture component increases significantly in strength with increasing annealing temperature. After annealing to fully recrystallized state at 250 °C there are a few signs of a near Cube texture component while after flash annealing to recrystallized state at 450 °C the major texture component is Cube and it is rather strong.

Al-0.25Mn

The addition of 0.25 wt.% Mn to the high purity alloy had a noticeable effect on the recrystallization texture and recrystallized grain size. Two composite EBSD scans from Al-0.25Mn annealed at low and high temperature are shown in Figure 5.25. The sample in Figure 5.25(a), annealed at 275 °C for 10^5 seconds, is nearly 100% recrystallized. However, the few unrecrystallized areas are easily excluded (due to low CI) from the ODF calculations presented in Figure 5.26. The grain size, measuring 32 μm and 41 μm for annealing at 275 °C and 400 °C, respectively, is significantly smaller than in the Al4N alloy.

On the other hand, both textures are very similar to the texture observed in the Al4N after high temperature recrystallization. It is mainly constituted by a strong Cube component that is RD rotated in the direction of Goss. Other texture components are also present. Localized near the surface are some regions with orientations that appear blue or purple in the inverse pole figure maps in Figure 5.25, particularly in the sample annealed at 400 °C. After annealing at 275 °C, the surface component is the retained rolling texture component, R, while at 400 degree C the component is not well defined but some 15° rotated away from the deformation texture components Cu.

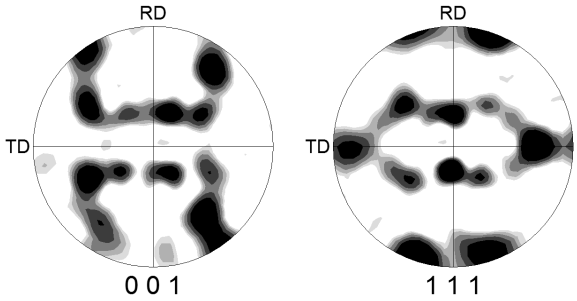

(a) Al4N, as-deformed.

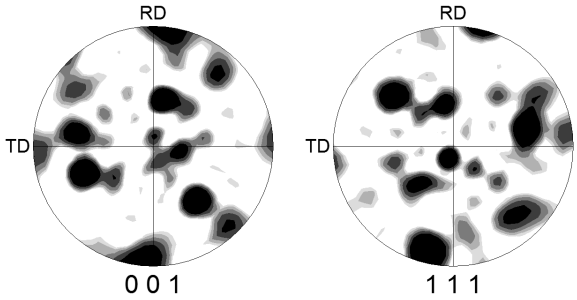

(b) Al4N, 240 °C, 10^5 s.

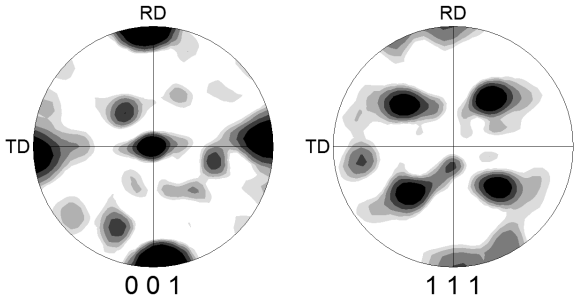

(c) Al4N, 350 °C, 10 s.

Figure 5.22: 111-pole figures of Al4N in as-deformed state (a), after 10^5 seconds of annealing at 240 °C (a) and 10 seconds annealing at 350 °C.

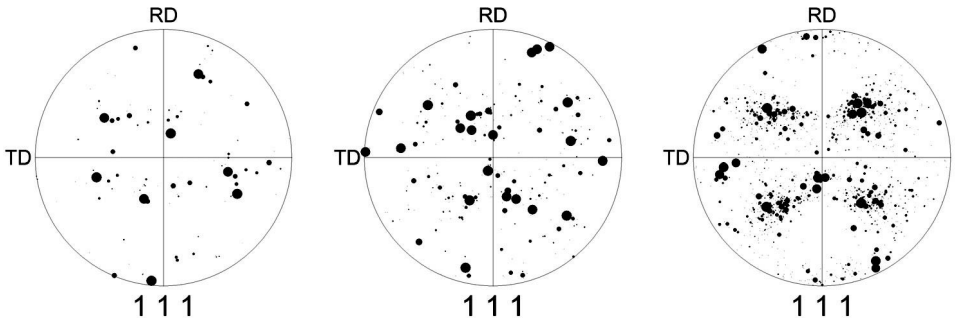

(a) Al4N, 220 °C. (b) Al4N, 240 °C. (c) Al4N, 350 °C.

Figure 5.23: 111-pole figures of recrystallized grains after annealing at different temperatures. The size of the poles is correlated with the size of the grains.

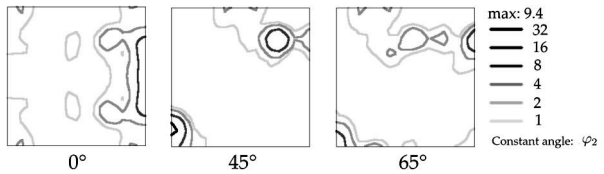

(a) 250 °C, 10^5 s.

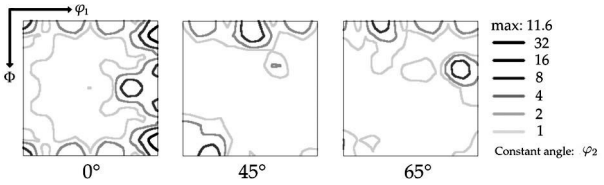

(b) 300 °C, 10^4 s.

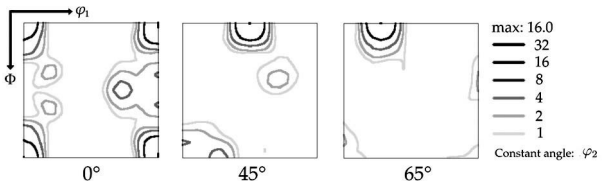

(c) 450 °C, 10 s.

Figure 5.24: The effect of recrystallization temperature on the Cube texture component in Al4N interannealed to give finer grain size and then cold rolled to strain $\varepsilon = 1.4$.

(a) Al-0.25Mn, 275 °C, 10^5s.

(b) Al-0.25Mn, 400 °C, 10 s.

Figure 5.25: Inverse pole figure maps of Al-0.25Mn after low and high temperature recrystallization.

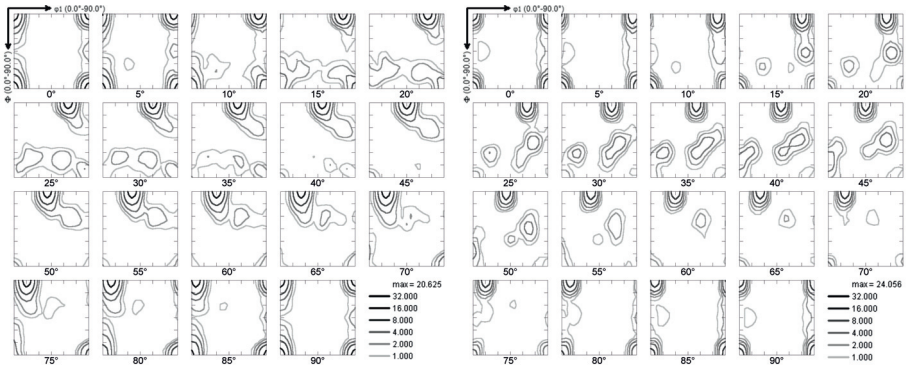

(a) Al-0.25Mn, 275 °C, 10^5s. (b) Al-0.25Mn, 400 °C, 10 s.

Figure 5.26: ODFs of Al-0.25Mn after low and high temperature recrystallization.

5.2 Commercial Purity Alloys

The softening behaviour was also investigated in the commercial purity alloys containing iron and silicon with a particular focus on subgrain growth and average boundary misorientation evolution during annealing of the A1 alloy. In addition, results from a detailed study on the effect of interannealing on the softening behaviour with an emphasis on Fe in solution versus Fe-precipitates are presented.

5.2.1 Softening Behaviour

Parts of the softening characterization of A1 and A2 after deformation were carried out by Sande [2012] and are included in Figure 5.27 with black colour. These samples were homogenized at 600 °C for 24 hours before cooling to 450 °C. Only the softening behaviour at 250 °C, indicated by red curves, was investigated by the present author. The materials for the new softening curves differ from the previous ones in that the highest temperature during homogenization was only 540 °C. The absolute hardness values shifted and are roughly 2–4 HV lower. However, the softening kinetics and conductivity at 250 °C exhibit behaviour which is a very reasonable evolution from that at higher temperatures, i.e. the effect of homogenization temperature is minimal. On the other hand, the conductivity of A2 in as-deformed state is notably different and 0.4 units higher when measured by the present author.

Comparing A1 with A2, the A2 alloy is significantly harder after deformation while the difference in fully soft state is only marginal. The relative softening kinetics are comparable at low temperature, but at temperatures higher than 300 °C the A2 alloy is an order of magnitude faster than A1. Concurrent precipitation is a likely explanation for this behaviour, as the difference in hardness evolution seems to be related to the two types of conductivity evolution. For A2, above 300 °C the conductivity reaches a plateau level after 100 seconds. At 300 °C and below, the conductivity continues to increase with increasing annealing time. Thus, it seems very likely that at 350 and 325 °C there is no concurrent precipitation while at lower temperatures precipitation and softening processes are occurring simultaneously. A similar behaviour in A1 cannot be ruled out but is less pronounced.

Because the samples annealed at 250 °C were not fully softened after 10^5 seconds of annealing, a recrystallization texture comparison between A1 and A2 was done with new samples annealed for 100 seconds at 350 °C. In Figure 5.28 and Figure 5.29 the respective textures of A1 and A2 are presented in terms of ODFs. Like the deformation textures, the recrystallization textures are rather similar and the A1 peak intensity is again a bit stronger. The Brass component is nearly gone, while both Cu and S components are still present. The S component is particularly strong in A1. Of new components, the Goss component is

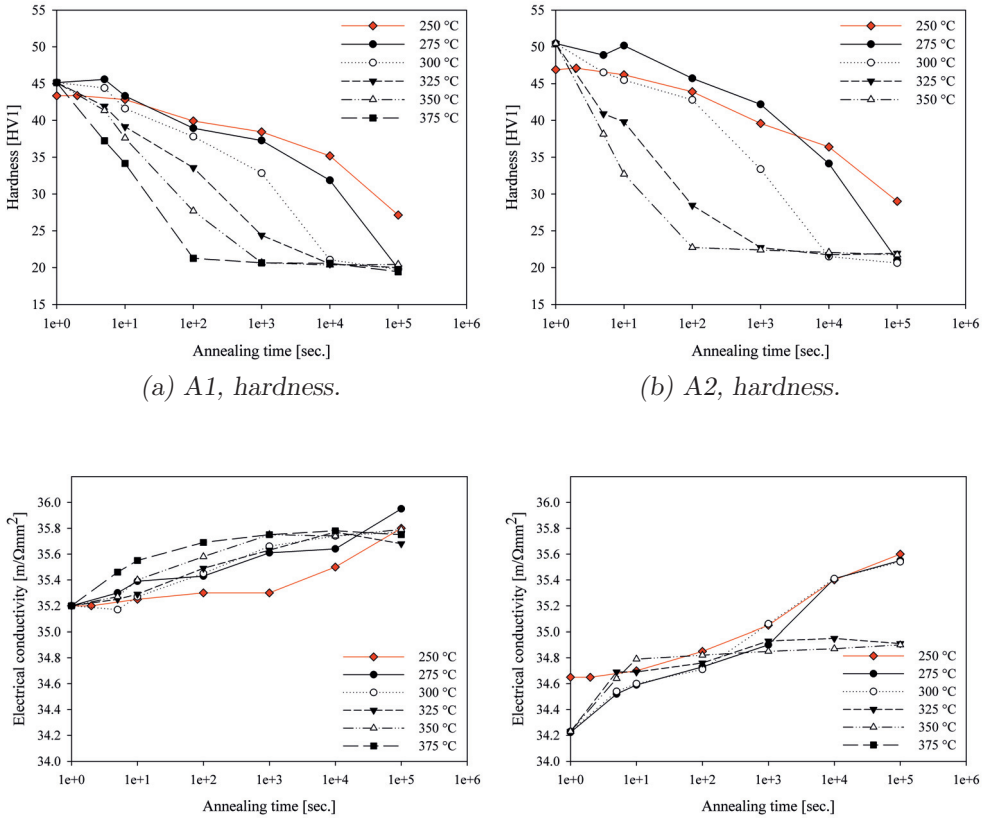

(a) A1, hardness. (b) A2, hardness.

(c) A1, conductivity. (d) A2, conductivity.

Figure 5.27: Softening behaviour of A1 and A2 alloys during annealing at various temperatures post cold rolling to strain $\varepsilon = 2.6$, illustrated by the evolution in hardness and electrical conductivity. Black curves were measured by Sande [2012] on samples homogenized at 600 °C, while red curves are from samples homogenized at 540 °C with measurements performed by the present author.

relatively strong in both alloys, while Cube is relatively weak in A1 and almost invisible in A2.

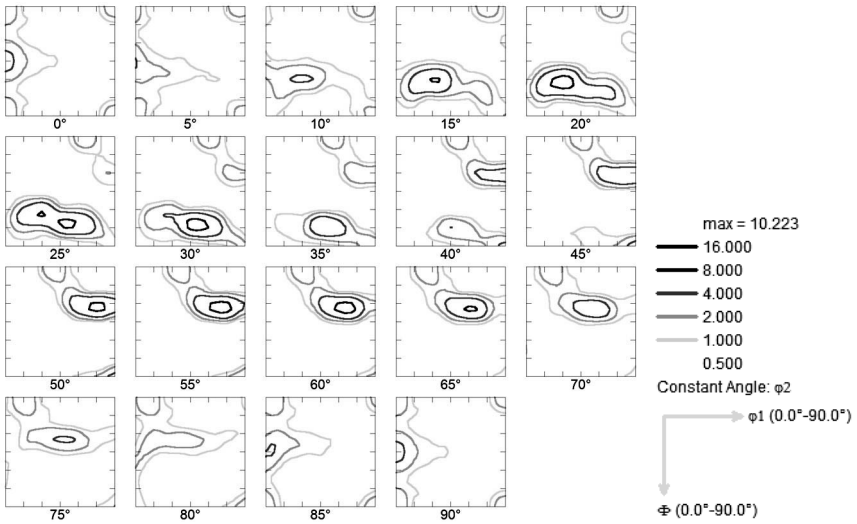

Figure 5.28: ODF constructed from EBSD measurements of A1 sample after recrystallization at 350 °C for 1000 seconds.

The grain size after recrystallization was found to be similar in the two alloys and is given in Table 5.5. Surprisingly, deformation leads to a marginal increase in the A2-conductivity, which is opposite from the weak and expected decrease of 0.2 m/Ωmm^2 which is seen in A1. The conductivity after recrystallization is for A1 0.6 m/Ωmm^2 larger than for A2, which is a smaller difference than was observed after homogenization. More interestingly, the conductivity of A1 is significantly lower than what Sande [2012] found in Figure 5.27(c). After 1000 seconds at 350 °C, Sande [2012] found a conductivity of 35.75 m/Ωmm^2 for the A1 alloy, which is 0.25 units higher than the current measurement. For A2 compared with Figure 5.27(d), however, the two investigations coincide well.

5.2.2 Subgrain Structure Evolution

The growth of subgrains and the evolution of average boundary misorientations were given special attention similar to the investigations done on orientation dependent subgrain growth in the high purity alloys Al4N and Al-0.25Mn. Due to a much finer grain size after casting in the commercial purity A1 alloy, it was more challenging to find adequate areas for orientation dependent subgrain characterization. In Figure 5.30, some typical areas which are more than 10 subgrains wide and have near ideal orientations illustrate the microstructures in various texture components after different annealing times at 250 °C. In all

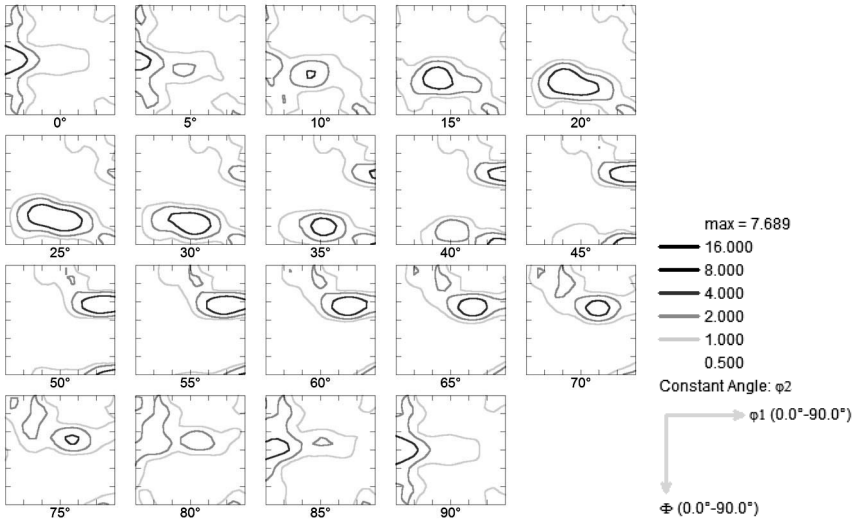

Figure 5.29: ODFs constructed from EBSD measurements of A2 sample after recrystallization at 350 °C for 1000 seconds.

Table 5.5: Conductivity, grain size and maximum texture intensity of the different materials after processing.

	A1	**A2**
Conductivity [m/Ωmm^2]		
Initial state	35.40	34.58
As-deformed (92.5%)	35.20	34.65
Def. 92.5% & rex. 350 °C, 10^3 s	35.50	34.90
Grain size [μm]		
Initial state	134.1	80.5
Def. 92.5% & rex. 350 °C, 10^3 s	21.0	22.0
Texture [f_{max}]		
As-deformed (92.5%)	21.5	17.6
Def. 92.5% & rex. 350 °C, 10^3 s	10.2	7.7

the reconstructed maps there are elements of other orientations in addition to the main one and also some HAGBs.

In addition to the orientation dependent investigations, subgrain growth and boundary misorientations were studied without considering the local orientations by making random scans with "mixed orientations". Figure 5.31 presents two such reconstructed subgrain maps which contain several bands of different orientations. After deformation, as shown in Figure 5.31(a), the microstructure consists of a few bands with ideal orientations, some transition bands and is quite heterogeneous. There are several bands which are only a few subgrains wide, in fact there is a Cu oriented band measuring only one subgrain in width. Figure 5.31(b) shows the annealed state and there seems to be a tendency for subgrains in the vicinity of high-angle boundaries separating differently oriented bands to be larger than subgrains in the centre of bands.

The results from both orientation dependent and orientation independent investigations are presented graphically in Figure 5.32 and in Table 5.6 and Table 5.7. As seen in Figure 5.32(a), after deformation subgrains with Cu orientation measuring 1.14 μm were found to have the smallest size, closely followed by S and Cube oriented subgrains. Brass subgrains were significantly larger at 1.41 μm. However, within the first 10 seconds of annealing the grain sizes varies a lot — much more than can be attributed to actual growth. This clearly shows the heterogeneity of the microstructure after deformation. Still, there is a growth trend for all orientations except Cube which always have subgrains around 1.25 μm. A distinction cannot be made of the growth rates observed in Cu, S and Brass; it is equally slow for subgrains with all three orientations.

In Figure 5.32(b) the misorientations are also seen to scatter, probably as a result of the heterogeneous microstructure. Brass oriented subgrains have the lowest initial misorientation of 4°, while subgrains with Cu and S orientations are nearly identical at around 4.5°. The misorientations increase similarly for Cu and S oriented subgrains and the increase is weaker than for subgrains with Brass orientation. The misorientations of Cube oriented subgrains are 2° larger than for Cu and S oriented subgrains after deformation, though it cannot be concluded whether the misorientations are increasing or decreasing with annealing. From Figure 5.30 it appears as if there could be larger misorientations in this commercial purity alloy as compared to the high purity alloys due to less ideal orientations for the various microstructures. Indeed, Table 5.7 and Figure 5.32(b) confirm slightly larger misorientations in the A1 samples.

Looking at the orientation independent data (averaged over several reconstructed subgrain maps) presented in Figure 5.32(c) and Figure 5.32(d), the results appear to scatter less with annealing time but the error bars clearly show that microstructural variations are not avoided by scanning over several orientations. The average subgrain growth rate is stronger than any of the growth

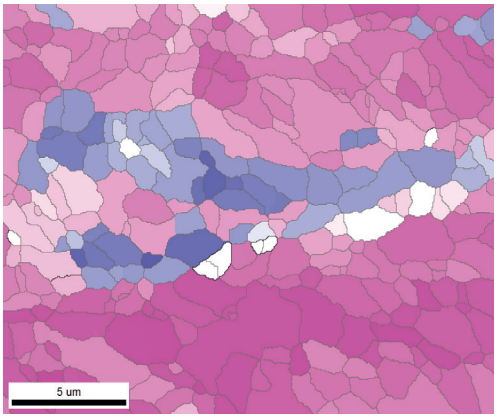

(a) Cu in as-deformed state.

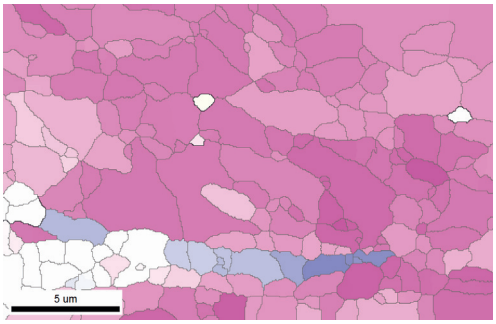

(b) Cu after 2 sec. annealing.

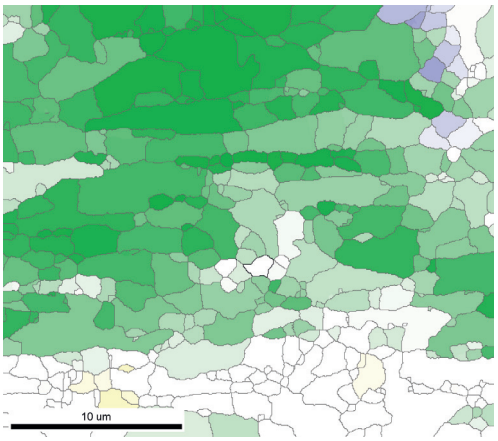

(c) Brass after 10 sec. annealing.

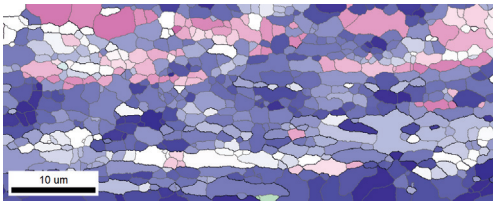

(d) S after 10^4 sec. annealing.

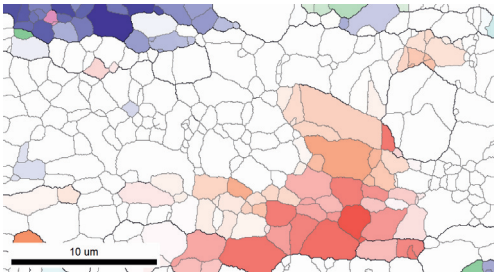

(e) Cube after 10^4 sec. annealing.

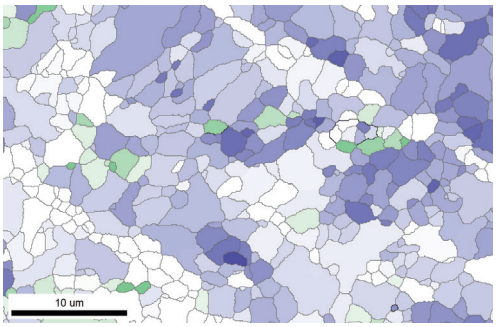

(f) S after 10^5 sec. annealing.

Figure 5.30: Examples of reconstructed subgrain structures with various orientations in A1 after annealing at 250 °C. RD is parallel with the horizontal direction.

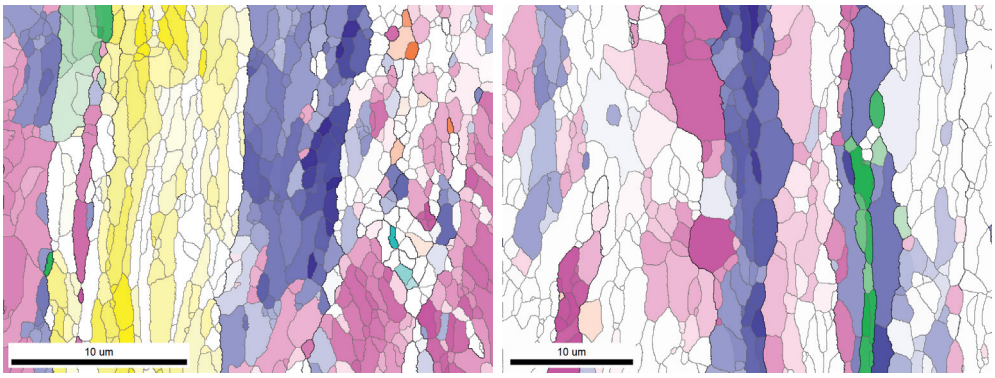

(a) As deformed state. *(b) After 10^5 sec. annealing.*

Figure 5.31: Examples of reconstructed subgrain structures with mixed orientations in A1 after annealing at 250 °C. RD is parallel with the vertical direction.

rates observed for individual orientations and the subgrain size increases from 0.93 µm to 1.52 µm. Average boundary misorientations are decreasing marginally from 5.5° to 5°.

Table 5.6: Subgrain sizes in A1 after cold rolling to $\varepsilon = 2.6$ and annealing at 250 °C.

Temp. [°C]	Time [s]	Subgrain size [µm]				
		Cu	**S**	**Brass**	**Cube**	**Average**
as-def.	0	1.14	1.07	1.41	1.22	0.93
250	2	1.13	1.40	1.49	-	0.94
	10^1	1.02	1.11	1.18	-	1.11
	10^2	1.15	1.43	1.28	1.28	1.15
	10^3	1.19	-	-	-	1.34
	10^4	1.47	1.48	1.61	1.26	1.44
	10^5	1.39	1.56	1.44	-	1.52

The size and misorientation distributions in Figure 5.33 provide additional information about the subgrain growth. For orientation dependent subgrain growth, the subgrain size distributions and average boundary misorientation distributions from Cu and Brass orientations are presented. Subgrains with S orientation have very similar distributions as the Cu oriented subgrains. On the other hand, for Cube oriented subgrains there are limited data and they are therefore not presented. For Brass oriented subgrains, the as-deformed subgrain size is rather large and, hence, the size distributions in Figure 5.33(c) are almost identical with similar spread and only marginally more of the largest subgrains after 10^4 seconds of annealing. The data for the Cu oriented subgrains are rather

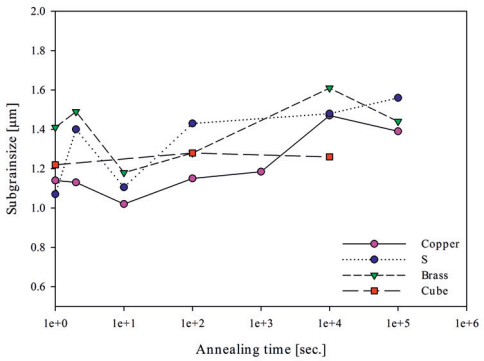

(a) *Orientation dependent subgrain diameter.*

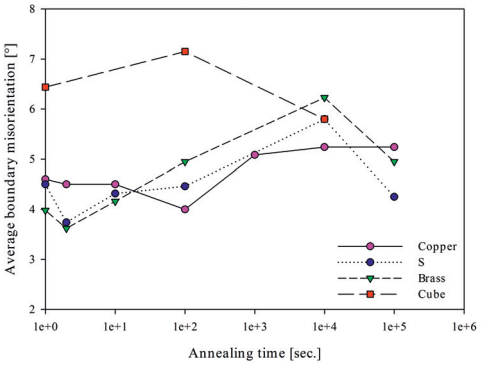

(b) *Orientation dependent average boundary misorientation.*

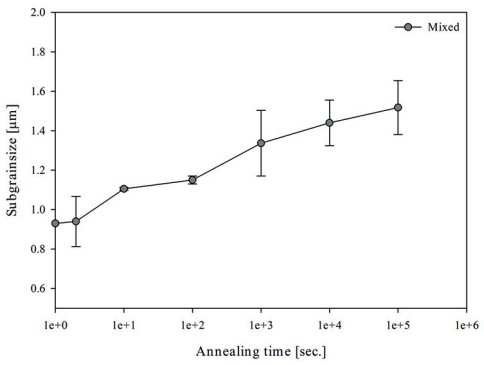

(c) *Orientation independent subgrain diameter.*

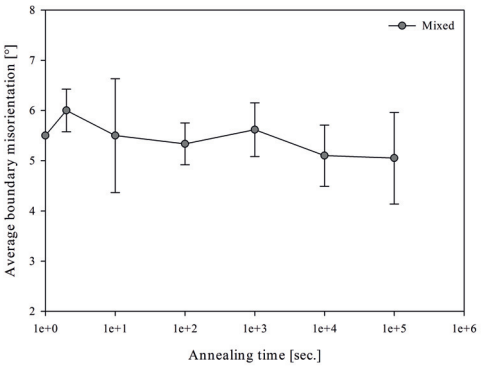

(d) *Orientation independent average boundary misorientation.*

Figure 5.32: Evolution of subgrain size and average boundary misorientation in specific orientations and bulk (mixed orientations) during annealing of A1 at 250 °C after (ε = 2.6).

Table 5.7: Boundary misorientations in A1 after cold rolling to $\varepsilon = 2.6$ and annealing at 250 °C.

Temp. [°C]	Time [s]	Misorientation [°]				
		Cu	**S**	**Brass**	**Cube**	**Average**
as-def.	0	4.60	4.50	3.98	6.44	5.50
250	2	4.50	3.74	3.62	-	6.00
	10^1	4.50	4.32	4.16	-	5.50
	10^2	4.00	4.46	4.95	7.15	5.33
	10^3	5.09	-	-	-	5.62
	10^4	5.24	5.80	6.23	5.80	5.10
	10^5	5.24	4.25	4.95	-	5.05

consistent during annealing and subgrain growth is accompanied by a weak increase of the boundary misorientations. In Figure 5.33(a), subgrain growth leads to fewer small and more large subgrains without significantly exceeding the initial size range.

In terms of average boundary misorientations, very little is happening in the Cu-case (Figure 5.33(b)). The most notable change is a decrease for the absolutely smallest misorientations. Similar behaviour was found for S oriented subgrains. Subgrains with Brass orientation also became more misoriented, although the increase is particularly large after 10^4 seconds of annealing shown in Figure 5.33(d). The amount of LAGBs with misorientations less than 4° is significantly reduced compared to as-deformed state and balanced by an increase of LAGBs with larger misorientations. After 10^5 seconds of annealing, the misorientations are smaller again and the distribution is similar to the initial one, as observed for Cu and S oriented subgrains in Figure 5.33(b).

For the mixed orientations, the changes with growth are more obvious. Stronger growth is observed in Figure 5.34(a), resulting in a shift of the peak to larger subgrains sizes while still retaining the smallest subgrains initially present even after 10^5 seconds of annealing. In the earliest stages of annealing, the size distribution has a distinct tail toward larger subgrain sizes. This shape of the curve is mirrored after 10^5 seconds of annealing and the tail is now stretching toward the smallest subgrain sizes. The two intermediate size distributions are showing signs of a bimodal distribution with two peaks around 0.5 µm and 1.5 µm, respectively.

Figure 5.34(b) shows how the misorientations become more centred around 3°, i.e. both misorientations below 1° and above 7° are decreasing. This is also occurring without a change in the fraction HAGB, which is varying between 7 and 30% independent of annealing time. Even if the fraction of HAGBs is sometimes low also in as-deformed state, the smallest fraction is in fact observed after 10^5 seconds of annealing.

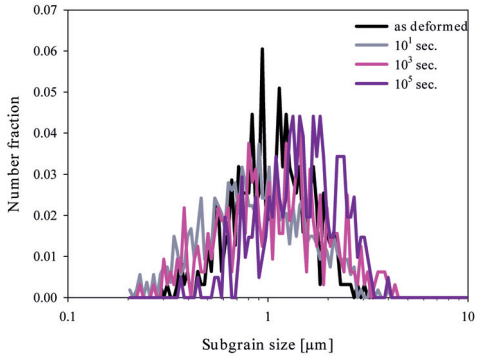

(a) *Cu, A1, 250 °C.*

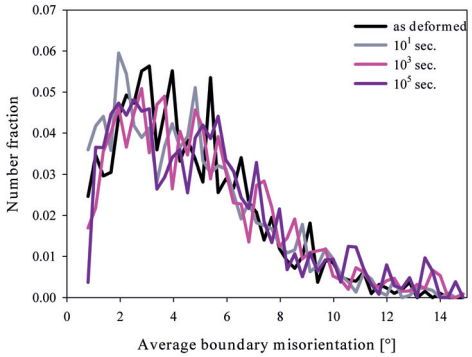

(b) *Cu, A1, 250 °C.*

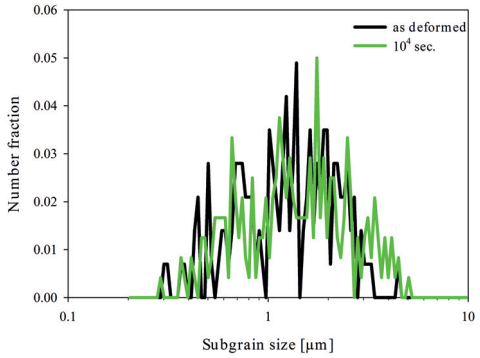

(c) *Brass, A1, 250 °C.*

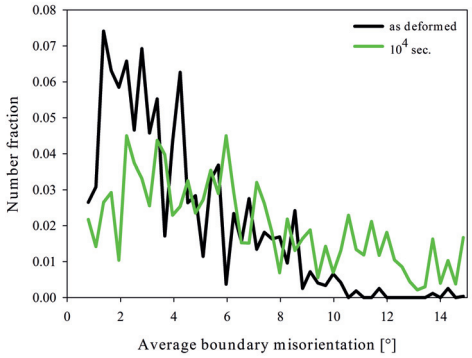

(d) *Brass, A1, 250 °C.*

Figure 5.33: Size and average boundary misorientation distributions of subgrains with deformation texture orientations Cu and Brass texture in A1.

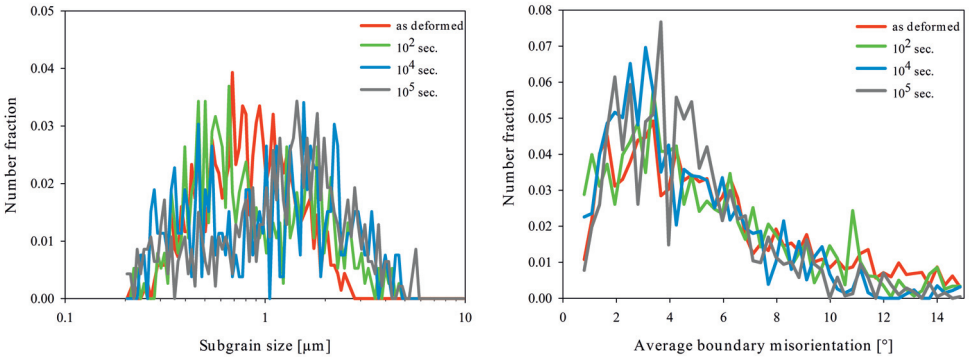

(a) Mix, A1, 250 °C. *(b) Mix, A1, 250 °C.*

Figure 5.34: Size and average boundary misorientation distributions of subgrains with mixed orientations (orientation independent) in A1.

5.2.3 Softening Kinetics Following Interannealing

The effect of intermediate annealing was investigated in the A1 alloy. After homogenization at 540 °C (quenched), 50% deformation and back-annealing at 300 °C for 10^5 seconds, the microstructure pictured in Figure 5.35 had a near random texture and grain size of 29.2 µm. Figure 5.36 reveals the complete ODF with a peak intensity of 2.5 times random. This is the starting material for another deformation and annealing process. Both 50 and 92.5% deformed variants of the interannealed materials were annealed at various temperatures. A comparison with samples from the A1 alloy without interannealing is presented in Table 5.8.

Similar to the A1 alloy without interannealing, softening was followed and characterized by hardness and conductivity measurements. The results are illustrated graphically in Figure 5.37. The 50% deformed samples directly annealed at 300 °C show a strong initial hardening on annealing before the material becomes softer. After 10 seconds of annealing the conductivity begins to increase from 35.2 m/Ωmm^2 and settles before the material is fully soft after 10^4 seconds at 35.6 m/Ωmm^2. For the material already annealed once, then deformed again and annealed, both the hardness and conductivity are higher after deformation than in the homogenized and deformed material. Hardening on annealing is not observed and the hardness falls off rapidly during annealing. Actually, the material is almost fully soft after only 10^3 seconds. After the material is recrystallized, conductivity continuous to increase to 35.75 m/Ωmm^2, which is higher than the directly annealed material.

The samples deformed 92.5% are harder by about 8 HV for as-deformed

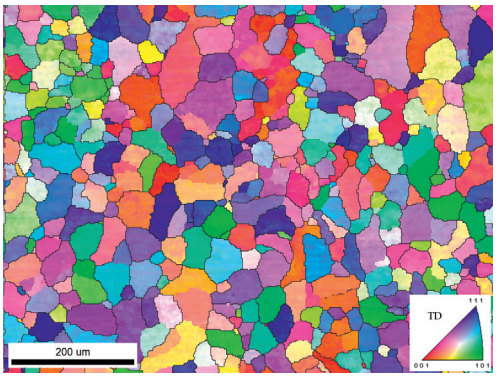

Figure 5.35: Inverse pole figure maps illustrating the microstructure after inter-annealing (50% deformation followed by 10^5 seconds at 300 °C). Black boundaries have high-angle character.

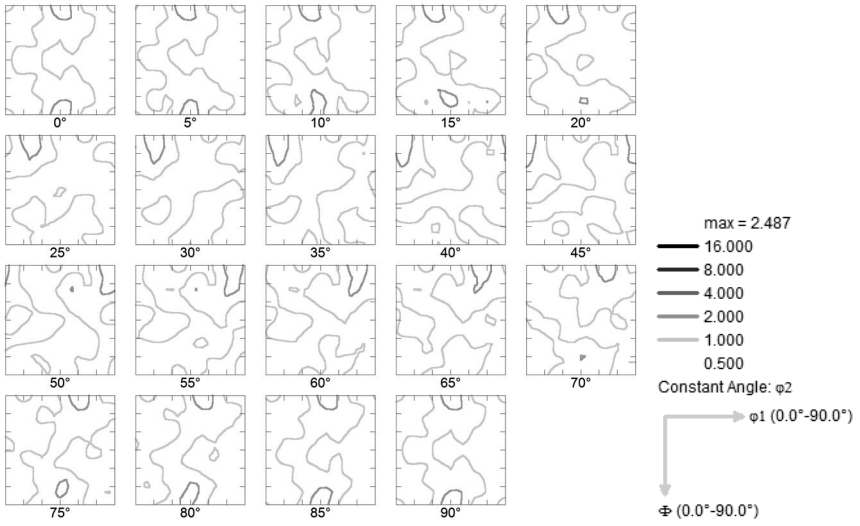

(a) A1 def. 50 %, 10^5s/300 °C. *(b) Legend.*

Figure 5.36: Near random texture of A1 sample deformed 50 % and annealed to fully soft condition at 300 °C for 10^5 seconds.

Table 5.8: Conductivity, grain size and maximum intensity of the different materials after processing.

	A1	$\mathbf{A1}^{\mathbf{rex}}_{300}$
Conductivity [m/Ωmm^2]		
Initial state	35.40	35.60
As deformed (50%)	35.20	35.50
As deformed (92.5%)	35.20	35.20
Def. (50%) & rex (300 °C, 10^5 s)	35.60	35.75
Def. (92.5%) & rex (250 °C, 10^5 s)	35.80	35.60
Def. (92.5%) & rex (350 °C, 10^3 s)	35.50	35.50
Grain size [µm]		
Initial state	134.1	29.2
Def. (50%) & rex (300 °C, 10^5 s)	29.2	-
Def. (92.5%) & rex (350 °C, 10^3 s)	21.0	24.5
Texture [f_{max}]		
Initial state	-	2.5
Def. (92.5%) & rex (350 °C, 10^3 s)	10.2	8.1

condition compared to the 50% deformed samples, both in the directly deformed sample and sample deformed after interannealing. The conductivity, on the other hand, is unaffected by more deformation in the directly deformed materials. The interannealed variant has the same conductivity and the conductivity does not increase by interannealing after 92.5% deformation, which it does after 50% deformation. To compensate for the increased stored energy, annealing was done at a lower temperature of 250 °C. In the 92.5% deformed samples, hardening on annealing did not occur and softening was very slow. Only the interannealed material becomes fully soft after 10^5 seconds of annealing. The conductivity of the directly deformed sample increased to 35.8 m/Ωmm^2 — the highest conductivity measured in any of the A1 samples. The effect of interannealing is also in the 92.5% deformed case seen to increase the as-deformed hardness and give faster softening kinetics, although perhaps not as pronounced as in the 50% deformed case. A difference in conductivity introduced by interannealing is not observed until after 100 seconds when the material starts to recrystallize, which occurs at an earlier stage in the interannealed material. Before the material is fully recrystallized, the conductivity settles at 35.6 m/Ωmm^2 and does not increase further.

It is also interesting to look at the recrystallization texture of the interannealed material after recrystallization at 350 °C for 1000 seconds. Compared to A1 presented in Figure 5.28, the ODF given in Figure 5.38 also show the presence of a strong Cube component. The maximum peak intensity is weaker than for A1 without interannealing and both the R and S texture components are also weaker. The Cu peak is shifted about -5° in the φ_1 direction, a weak

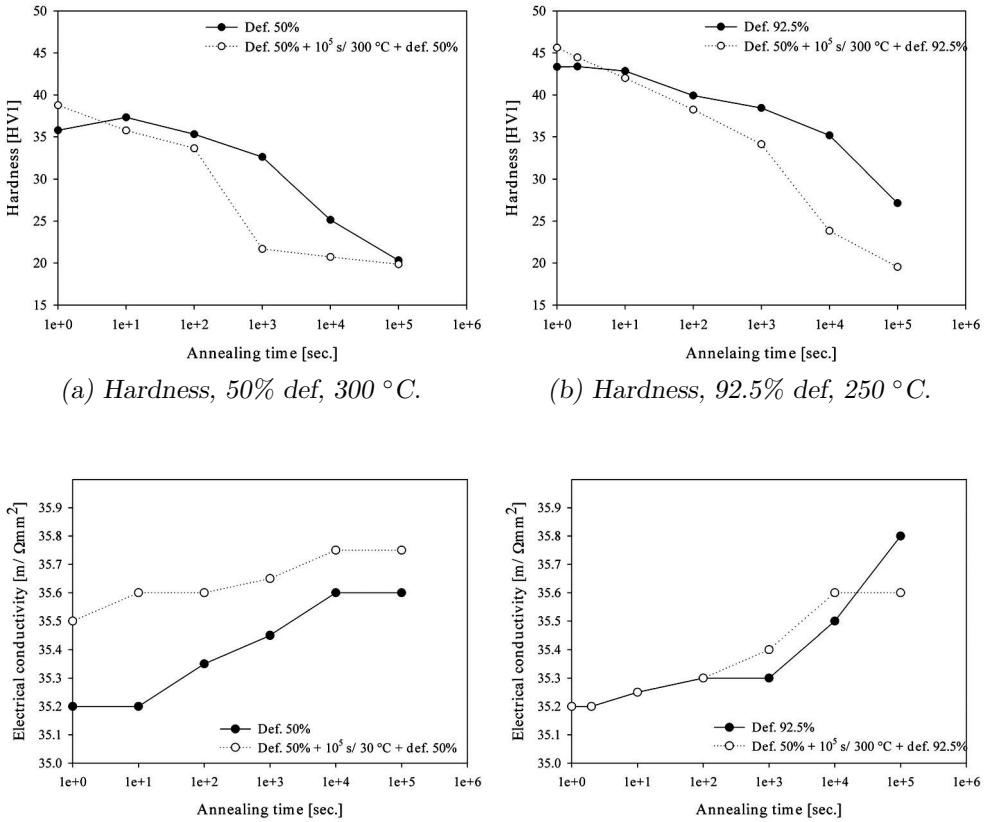

(a) Hardness, 50% def, 300 °C. *(b) Hardness, 92.5% def, 250 °C.*

(c) Conductivity, 50% def, 300 °C. *(d) Conductivity, 92.5% def, 250 °C.*

Figure 5.37: Effect of interannealing (50% deformation followed by 10^5 seconds at 300 °C) on softening kinetics and conductivity for A1 after deformation. The 50% and 92.5% deformed samples were annealed at 300 °C and 250 °C, respectively.

P component is present and the Goss components is significantly weaker in the interannealed sample compared to the directly deformed and recrystallized sample.

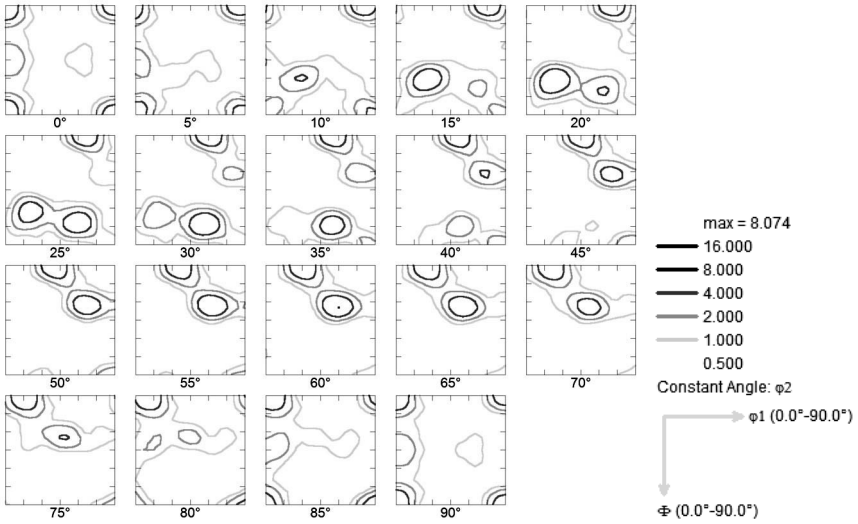

Figure 5.38: ODF constructed from EBSD measurements of interannealed and 92.5% deformed sample after recrystallization at 350 °C for 1000 seconds.

5.2.4 Concurrent Precipitation of Fe in A1

The level of iron in solid solution was increased drastically compared to the A1 material discussed so far by homogenizing at 620 °C followed by quenching. Many of the same experiments were repeated with the intention to clearly show the effect of iron in solid solution and interannealing on the final softening behaviour. In addition to conductivity and hardness measurements describing the softening behaviour, independent conductivity measurements were done by Hydro R&D Bonn (RDB-experiments), as well as extensive texture investigations and qualitative particle characterization (particle type identification). A complete as possible picture is given in the following.

Vickers hardness and conductivity measurements following softening of 50% and 92.5% deformed samples annealed at 320 °C and 300 °C, respectively, are presented in Figure 5.39. The 50% deformed samples in Figure 5.39(a) and Figure 5.39(c) show a very distinct behaviour that is related to their processing history. The directly quenched and deformed samples show no sign of hardening on annealing (although apparent in the previous case with less solute) and after a prolonged period of recovery the material quickly recrystallizes. The conductivity, on the other hand, increases more gradually from 34.4 m/Ωmm^2

and reaches a peak value of 35.6 m/Ωmm^2. When the 50% deformed material is back-annealed and deformed again before final annealing, a more typical softening behaviour is seen where recovery is gradually followed by recrystallization. The hardness after deformation is also ∼3 HV larger and the conductivity is significantly higher for the 50% deformed material with a previous interannealing. Thus, the conductivity increase much less (from 35.35 m/Ωmm^2 to 35.6 m/Ωmm^2) and reaches a plateau even before recrystallization is complete. Deforming the material 92.5% before interannealing raises the initial hardness further by another 1.5 HV and speeds up the softening kinetics even more. The effect on conductivity is a general hike in the conductivity by 0.25 m/Ωmm^2.

The 92.5% deformed material without interannealing behaves in much the same way as the 50% deformed material, although the transition from recovery to recrystallization is smoother at this strain level and temperature. The conductivity increases continuously to 35.9 m/Ωmm^2, a higher level than for any of the 50% deformed variants. Interannealing results in significantly faster softening and recrystallization takes place almost immediately. Unlike in the 50% deformed case, the as-deformed hardness remains unchanged at 44 HV after interannealing and deformation. The conductivity behaves similarly to what is observed in the 50% deformed material, starting at 35.3 m/Ωmm^2 and rapidly increasing to 35.8 m/Ωmm^2 at the same time as recrystallization is completed.

Additionally, the conductivity was measured in as-cast, homogenized and flash-annealed samples and the 92.5% deformed sample back-annealed at 320 °C. The results are listed in Table 5.9.

Table 5.9: Conductivity of A1 samples other than those shown in annealing curves. Units in [m/Ωmm^2].

	Sigmatest 2.069	**Four point (RDB)**
As cast	34.9	35.01
Homogenized	34.7	34.36
50% def. 500 °C/10 s	34.6	-
92.5% def. 500 °C/10s	35	-
A1 92.5 320/100000s	35.8	-

As mentioned, in addition to the in-house experiments, the conductivity was also measured at Hydro R&D Bonn by a more accurate method. These results are referred to as the RDB experiments and are plotted in red and compared to the already presented results, in grey, in Figure 5.40. At 293K, i.e. 20 °C, all the RDB measurements show a lower conductivity than the in-house measurements. The relative conductivities between the materials processed differently are also different from the measurements done in-house. The trends are however similar. In as-deformed state the conductivity increases with interannealing, and the increase is even larger with more deformation before final annealing. For the materials deformed 50%, the increase is not as large as in the in-house

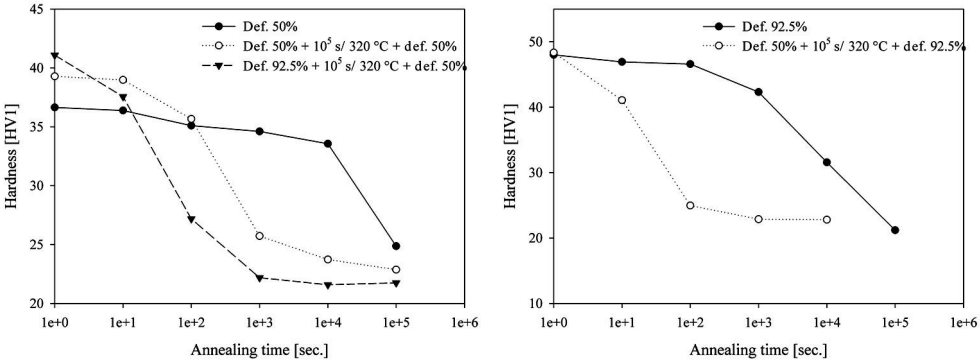

(a) $\varepsilon = 0.7$, $T = 320\,^{\circ}C$. (b) $\varepsilon = 2.6$, $T = 300\,^{\circ}C$.

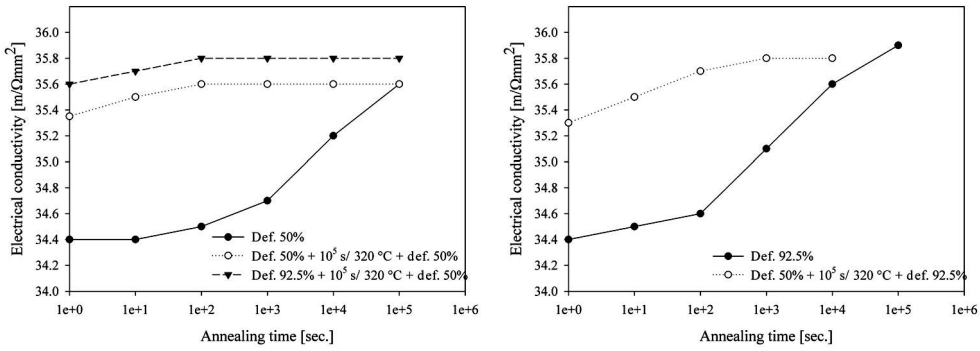

(c) $\varepsilon = 0.7$, $T = 320\,^{\circ}C$. (d) $\varepsilon = 2.6$, $T = 300\,^{\circ}C$.

Figure 5.39: Softening behaviour of A1 after homogenization at 620 °C, characterized by Vickers hardness and electrical conductivity measurements at RT.

experiments when deformed only 50% before annealing. Also, when only 50% deformation is applied the final conductivity is independent of interannealing. However, introducing more deformation (92.5%) before interannealing gives a much higher conductivity both in as-deformed and fully recrystallized state, more so in the RDB experiments than in the in-house experiments. For the materials deformed 92.5% the increase in conductivity is not as extensive as the in-house observations suggest. However, also the RDB experiments indicate that the conductive after a second annealing process is actually slightly lower than the directly back annealed material deformed 92.5%.

The resistivity ratios (RR), eliminating errors caused by the shape factor, show a better resemblance with the in-house measurements. The ratios between the differently processed materials follow the evolution pictured by the original (grey) measurements closely and give a more realistic behaviour than the measurements at 293K. Yet, a discrepancy is found in the interannealed and 50% deformed materials where the degree of deformation before interannealing does not affect the conductivity much during the second annealing. In the 92.5% deformed material, the effect of interannealing on conductivity in full back-annealed state is only a marginal increase from the resistivity ratio measurements.

Texture

The results from the texture investigations are presented in terms of ODFs. To begin with, the deformation textures after 50% and 92.5% deformation are presented in Figure 5.41 and Figure 5.42. Although the peak intensity is actually higher in the 50% deformed sample than in the 92.5% deformed samples, the β-fibre deformation texture has not yet developed in the 50% deformed samples. In the 92.5% deformed sample, on the other hand, the typical Brass, Cu and S texture components are all present.

Flash annealing at 500 °C for 10 seconds of the 50% deformed sample resulted in a very weak texture with signs of an ND-rotated Cube component as shown in Figure 5.43. The 92.5% deformed and flash annealed sample also has a relatively weak texture with a maximum intensity of 6.6 but the texture still resembles a recrystallization texture. In the ODF in Figure 5.44 both weak Cube and Goss components are seen in addition to the deformation texture components Cu and S.

By back-annealing more slowly, i.e. for 10^5 seconds at 320 °C, the texture of both the 50% and 92.5% deformed material becomes slightly stronger. The weak texture of the 50% deformed material presented in Figure 5.45 shows only indications of some components near the Brass and S orientations. In the 92.5% deformed case, presented in Figure 5.46, the Cu and S components are almost gone and replaced by Cube and Goss texture components that are even stronger than those found after flash-annealing. Both components are

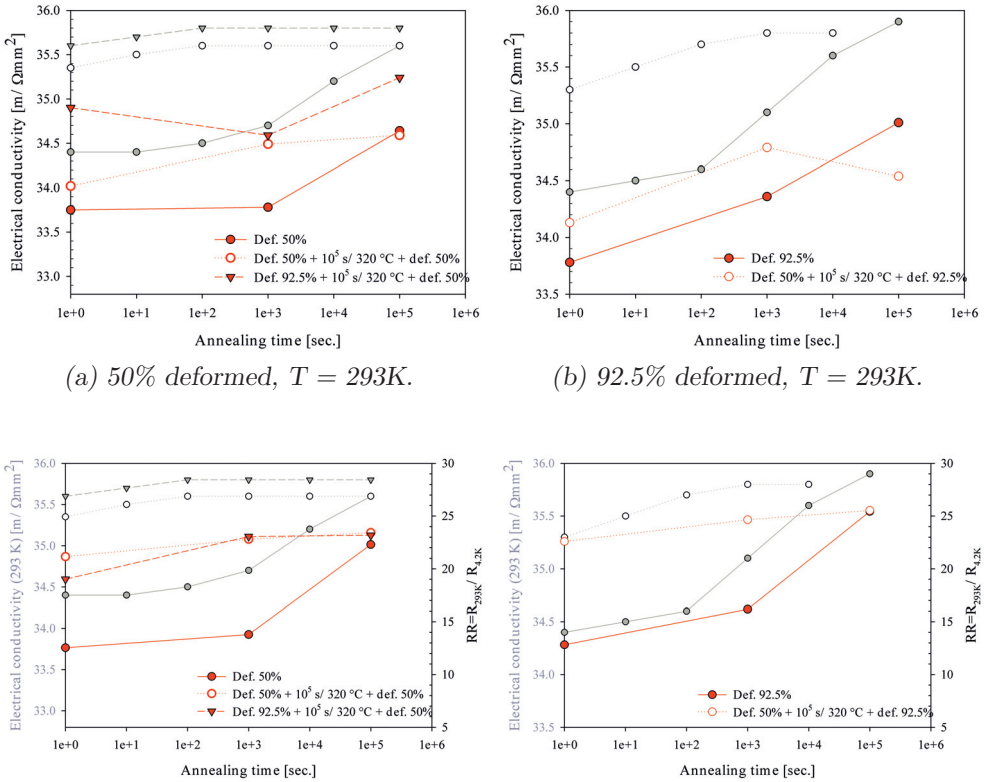

(a) *50% deformed, T = 293K.*

(b) *92.5% deformed, T = 293K.*

(c) *50% deformed, resistivity ratio.*

(d) *92.5% deformed, resistivity ratio.*

Figure 5.40: Conductivity of the different states of the A1 alloy homogenized at 620 °C during annealing with and without prior intermediate annealing. Measurements drawn in red colour were performed at Hydro R&D Bonn at 4.2 and 293K. The in-house data from Figure 5.39 are reproduced in grey for comparison.

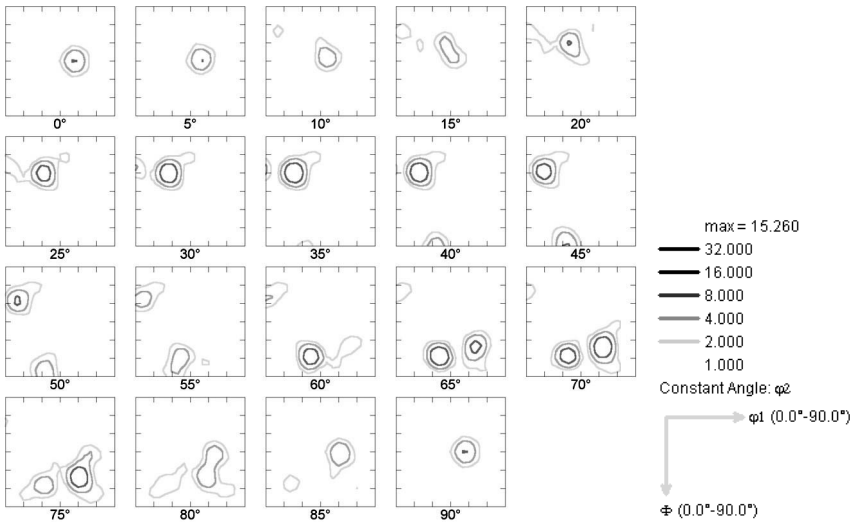

Figure 5.41: ODF of 50% deformed A1-sample after homogenization at 620 °C.

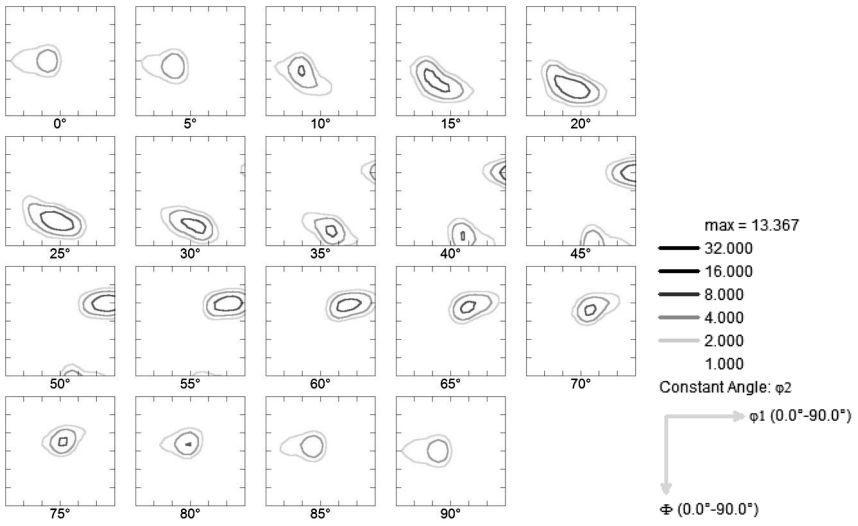

Figure 5.42: ODF of 92.5% deformed A1-sample after homogenization at 620 °C.

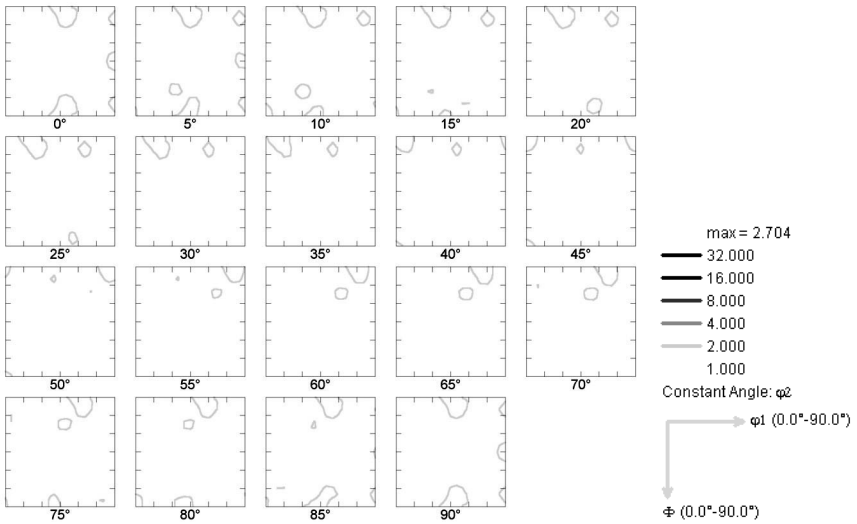

Figure 5.43: ODFs of 50% deformed A1-sample after flash-annealing at 500 °C for 10 seconds.

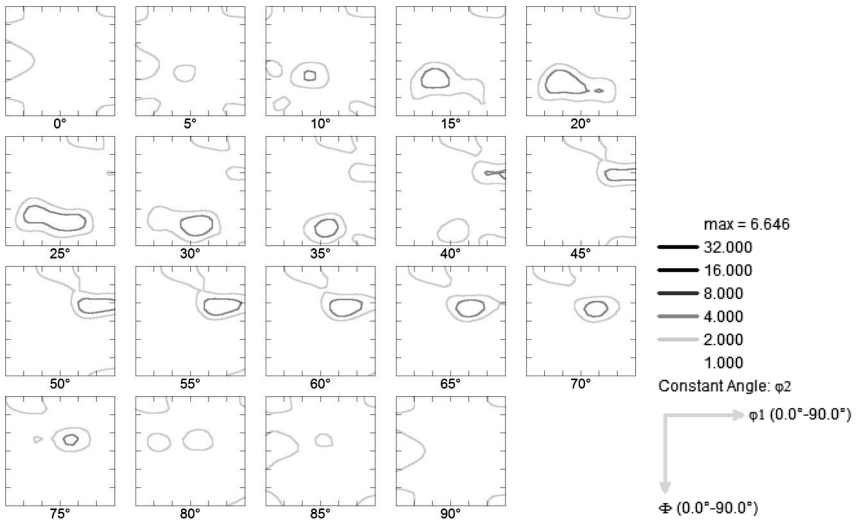

Figure 5.44: ODF of 92.5% deformed A1-sample after flash-annealing at 500 °C for 10 seconds.

significantly scattered in RD.

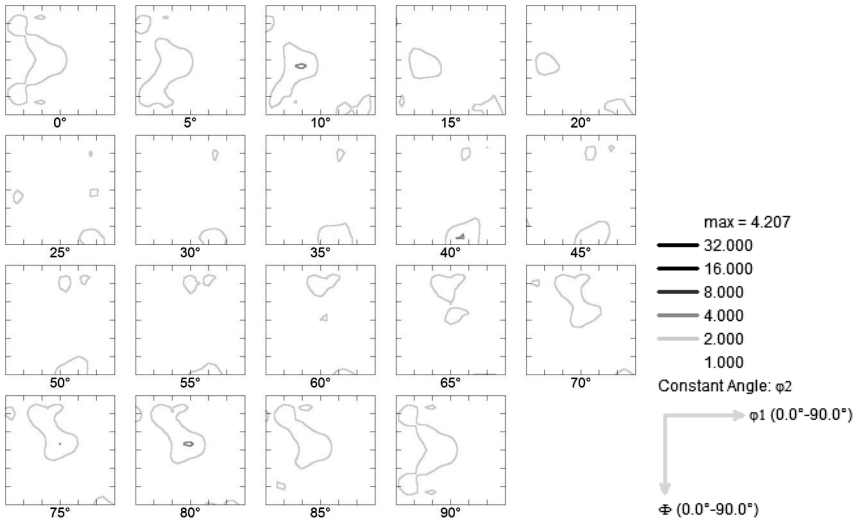

Figure 5.45: ODF of 50% deformed A1-sample after slow back-annealing (10^5 s/320 °C).

After interannealing, subsequent deformation lead to three more material variants. The first one, the 50% deformed, interannealed and again 50% deformed samples in Figure 5.47, has a peak intensity of 9 and a typical deformation texture, although with some scatter around Brass, Cu and S. Further deformation to 92.5%, as shown in Figure 5.48, gave a strong deformation texture which is well-defined. The samples deformed 92.5% before interannealing, and then subsequently deformed 50% exhibited a somewhat different texture compared to the two previous ones. The ODF in Figure 5.49 shows a weaker texture compared to the two other deformation textures but has a relatively strong Goss component and also a very weak Cube component.

When these deformed samples were annealed at low temperature (300 and 320 °C) one more time, profoundly different textures were observed. The sample which was deformed 50% twice, with intermediate annealing in between, is clearly seen from Figure 5.50 to have a near random texture. When the final deformation was instead 92.5%, the ODF in Figure 5.51 is not at all random but have distinct Cube and TD-rotated Cube texture components, although the peak intensity was somewhat low at 10.4. The intensity of the 92.5% deformed, interannealed and 50% deformed sample in Figure 5.52 is lower but also far from random at 7.8. This latter ODF also displays a texture with a distinct Cube component in addition to a Goss component.

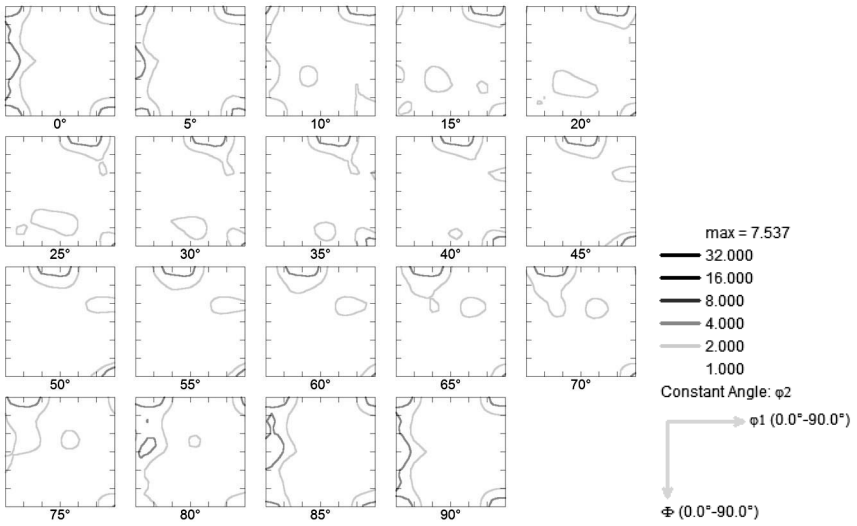

Figure 5.46: ODF of 92.5% deformed A1-sample after slow back-annealing (10^5 s/300 °C).

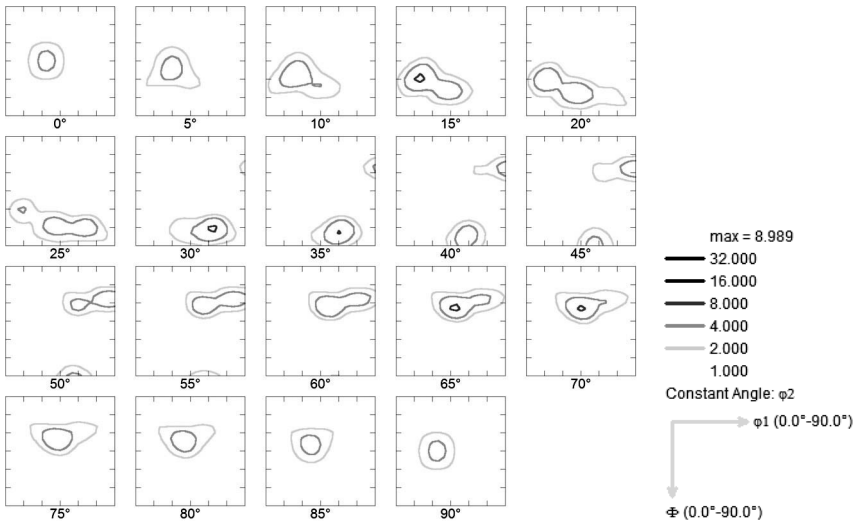

Figure 5.47: ODF of as-deformed A1-sample after 50% deformation, complete back-annealing and 50% deformation (50% + b.a. + 50%).

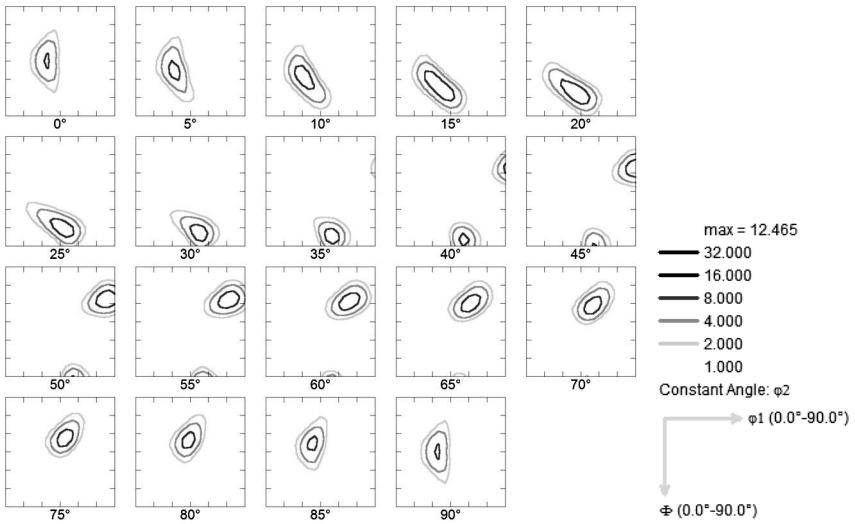

Figure 5.48: ODF of as-deformed A1-sample after 50% deformation, complete back-annealing and 92.5% deformation (50% + b.a. + 92.5%).

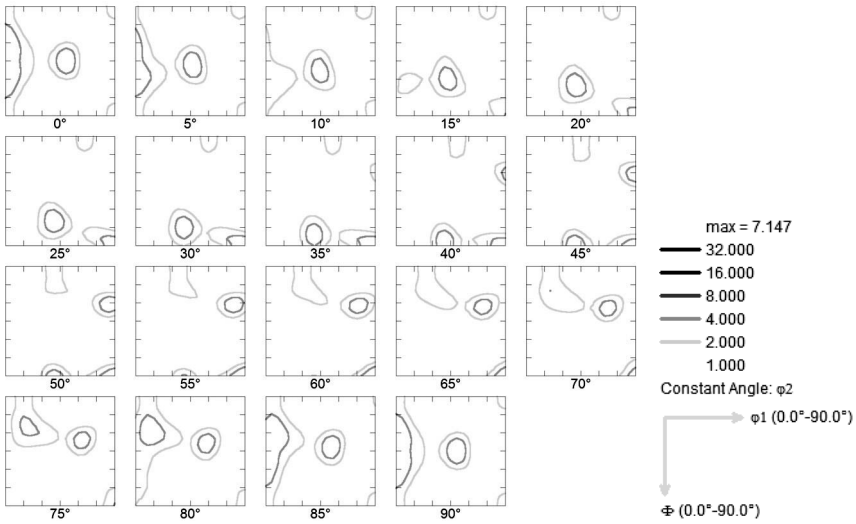

Figure 5.49: ODF of as-deformed A1-sample after 92.5% deformation, complete back-annealing and 50% deformation (92.5% + b.a. + 50%).

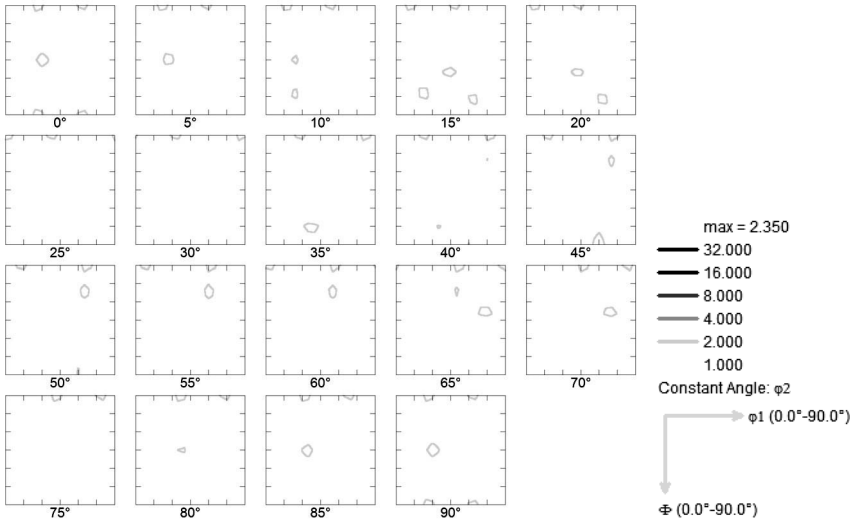

Figure 5.50: ODF of backannealed A1-sample after 50% deformation followed by intermediate annealing and a second deformation of 50% (50% + b.a. + 50%, 10^5 s/320 °C).

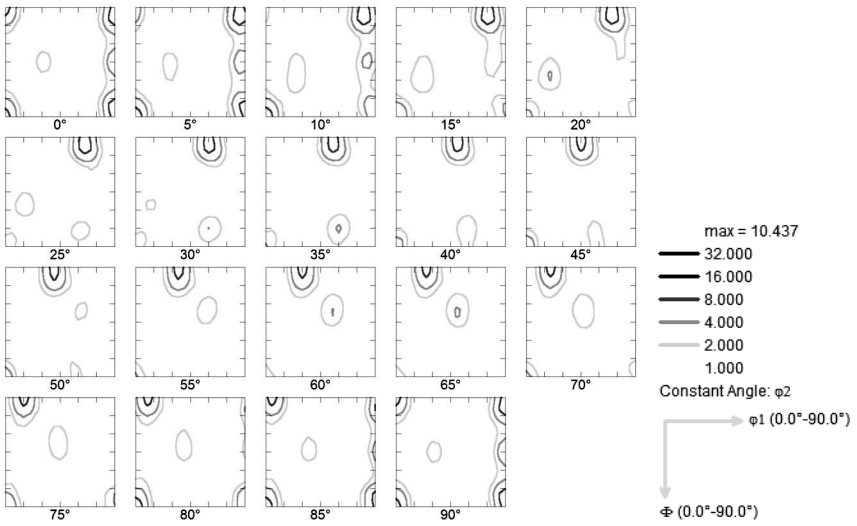

Figure 5.51: ODF of backannealed A1-sample after 50% deformation followed by intermediate annealing and a second deformation of 92.5% (50% + b.a. + 92.5%, 10^5 s/300 °C).

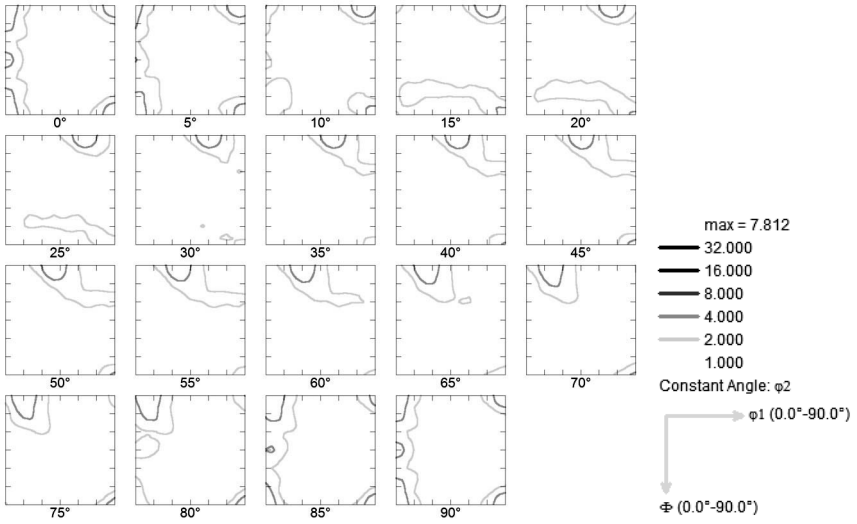

Figure 5.52: ODF of backannealed A1-sample after 92.5% deformation followed by intermediate annealing and a second deformation of 50% (92.5% def. + b.a. + 50%, 10^5 s/320 °C).

Precipitates

The light optical micrographs in Figure 5.53 clearly reveal the presence of a second phase precipitating during annealing. In the as-deformed state, shown in Figure 5.53(a) and Figure 5.53(b), only the constituent particles are causing pits when the sample surface is etched by 5% HF. The relief on the surface caused by etching makes the deformation structure recognizable and even some of the micro-shear bands are easily identified. After back-annealing at low temperature, Figure 5.53(c) and Figure 5.53(d) show that the relief of micro-shear bands and HAGBs observed after deformation are completely gone and replaced by a relief of the recrystallized grain structure. However, in place of the deformation relief are now strings of sub-micron pits following what appear to be old HAGBs, dense dislocation walls, microbands or perhaps S-bands. Whatever caused the pits to form, it seemingly has a strong link to the deformed microstructure. The same observation is not as apparent in the flash annealed samples in Figure 5.53(e) and Figure 5.53(f). This is mainly because these latter micrographs instead try to highlight the relationship between pits and HAGBs of recrystallized grains. Even if pits and boundaries are coinciding, the frequency of pits in the grain interior is higher. It is, however, very clear, particularly in Figure 5.53(f), that there is an interaction between what causes the pits and the grain boundary.

Because the pits were relatively small and had to be imaged at the highest magnification in the optical microscope, new micrographs shown in Figure 5.54

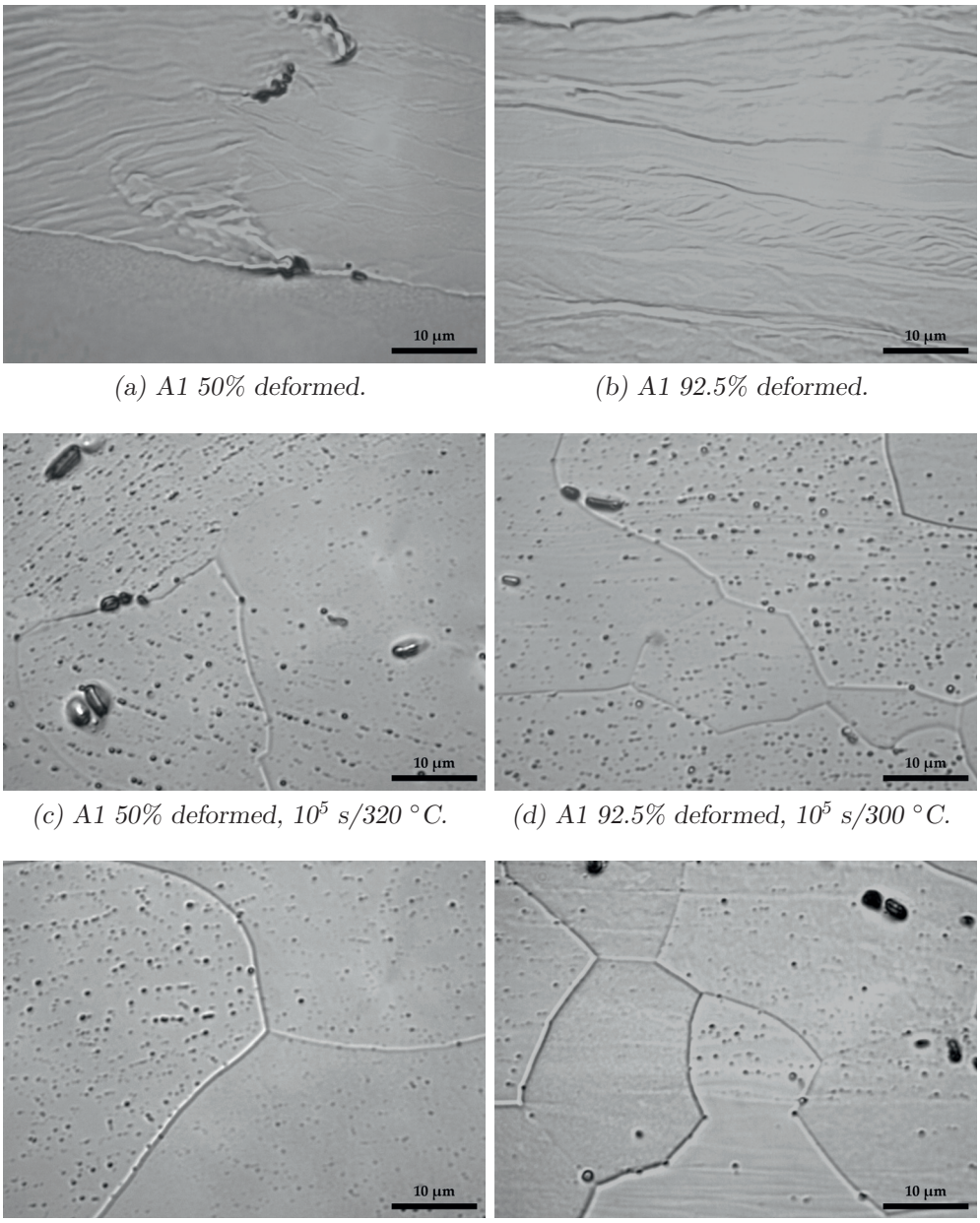

(a) A1 50% deformed. *(b) A1 92.5% deformed.*

(c) A1 50% deformed, 10^5 s/320 °C. *(d) A1 92.5% deformed, 10^5 s/300 °C.*

(e) A1 50% deformed, 10^2 s/450 °C. *(f) A1 92.5% deformed, 10 s/500 °C.*

Figure 5.53: Light optical micrographs of deformed and back-annealed A1 samples etched in 5% hydrofluoric acid (HF) for 30 seconds.

were taken of exactly the same samples in SEM. However, apart from demonstrating the crystallographic dependence of pit propagation, the pictures mainly confirmed what was already observed in Figure 5.53. The relief structure was perhaps even more apparent due to better depth resolution and finer details were more clearly visible. Still, in as-deformed state no pits were formed, except for extremely large ones arising from constituent particles. The long strings of pits were also now frequently observed in the slowly annealed samples. The strings of pits in the 50% deformed material which was at an angle to RD and extending through several recrystallized grains were also observed in the SEM.

Due to better resolution of SEM over LOM, more pitting at the boundaries of recrystallized grains was observed in the flash annealed samples. Both in the case of the 50% and 92.5% deformed samples, some areas had a significantly higher fraction of pits at the recrystallized grain boundaries than in the grain interior. Figure 5.54(e) shows the surrounding area of a triple-junction in the 50% deformed sample where there are almost no pits in the grain interior and several pits near or at the high-angle boundaries. Nevertheless, pit formation in the interior of grains was frequent in other areas and pits at grain boundaries as shown in the 92.5% deformed samples of Figure 5.54(f) seems to be caused by a combination of an energetically favourable process and statistical coincidence.

The size of the pits was typically in the range 0.2–0.5 μm but pits with a diameter larger than 1 μm were also observed. However, there were no signs of any particles within the pits.

TEM investigations of both 50% and 92.5% deformed samples annealed for 10^4 and 10^5 seconds revealed the existence of two different types of precipitates, none of which were observed in as-deformed samples which were free from particles (constituent particles are of course present in the deformed material but were not observed in any of the TEM samples). Hence, both precipitates were formed during the annealing process. The precipitates are pictured by bright field imaging in Figure 5.55(a). The small, round particles labelled “1” were often grouped together in stringers but were also found one by one. The near circular shape measured from a few nano meter in diameter and up to about 200 nm. The EDS-spectrum of this particle is shown in Figure 5.55(b) and labelled “1”. The red peaks belong to the particle spectrum, while the blue peaks are superimposed and from the α-Al matrix. The circular particles clearly contain only one element in addition to aluminium, namely iron.

The larger of the two types of particles observed, labelled “2” in Figure 5.55, was usually elongated in one direction where it measured several hundred nanometres. In the width direction they were usually 20–50 nm. These precipitates were observed less frequently than the circular particles. In Figure 5.55(b) the EDS spectrum is illustrated and, as opposed to the smaller, circular particles which only contained iron, these larger particles also contained some silicon in addition to iron. The oxygen peak was seen to vary significantly, however this

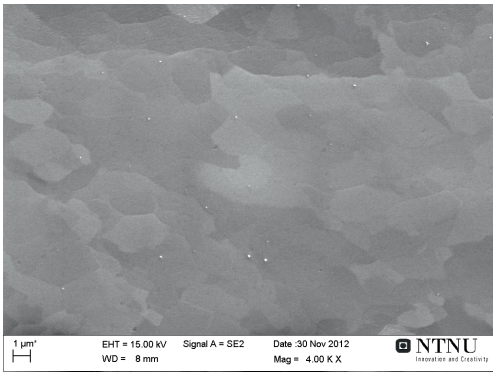

(a) A1 50% deformed.

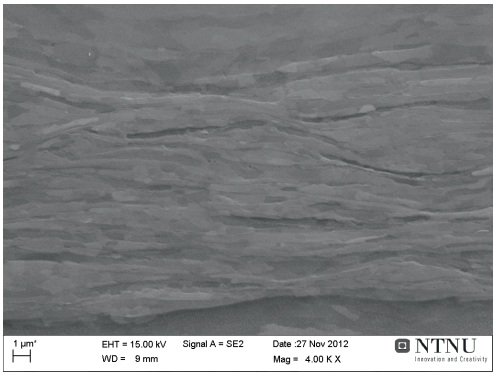

(b) A1 92.5% deformed.

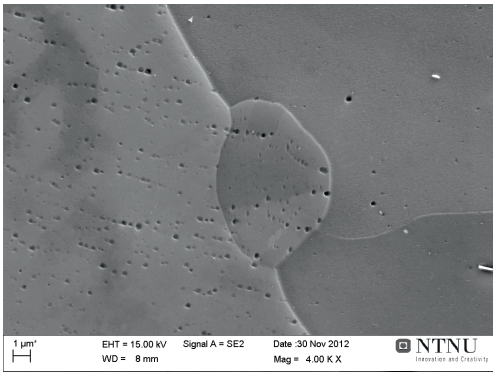

(c) A1 50% deformed, 10^5 s/320 °C.

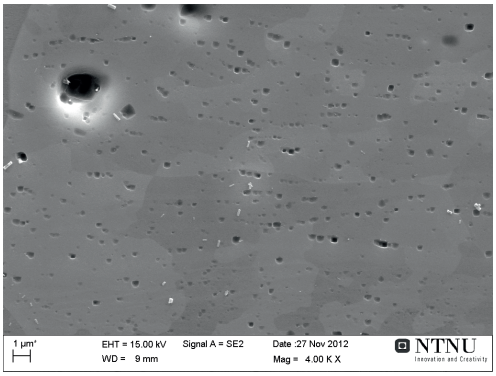

(d) A1 92.5% deformed, 10^5 s/300 °C.

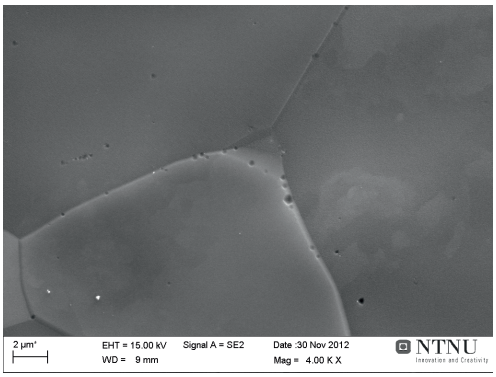

(e) A1 50% deformed, 10^2 s/450 °C.

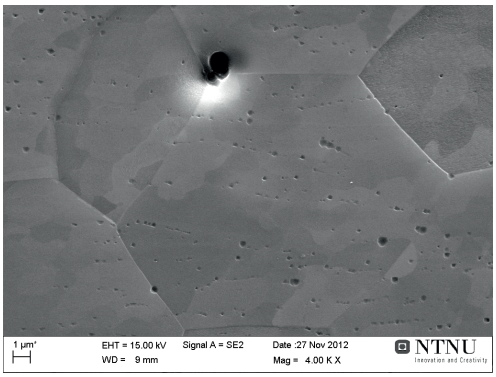

(f) A1 92.5% deformed, 10 s/500 °C.

Figure 5.54: SEM images of deformed and back-annealed A1 samples etched in 5% hydrofluoric acid (HF) for 30 seconds.

aspect can be ignored as it is of no importance for identifying the particles.

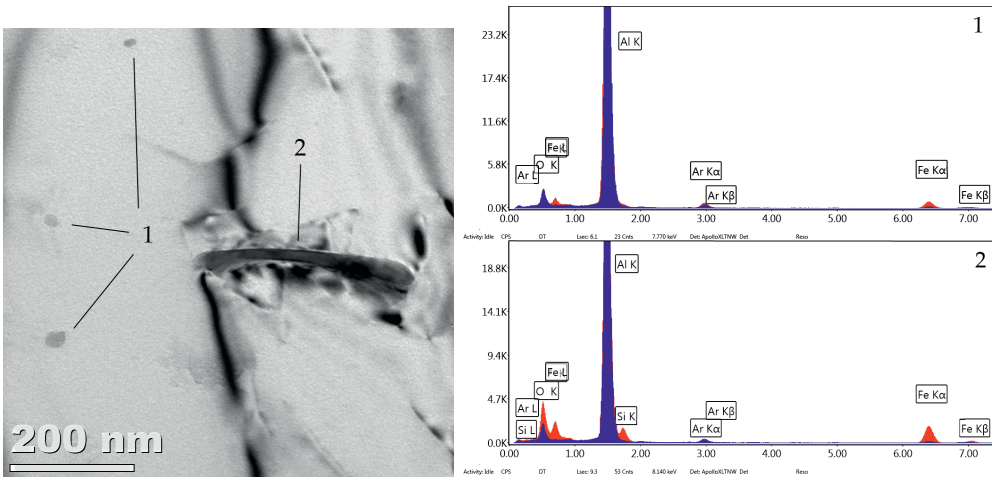

(a) TEM, BF. *(b) Spectrum, EDS.*

Figure 5.55: Two different kinds of particles were observed, independent of the degree of deformation, in samples with the A1 composition annealed for 10^4 & 10^5 seconds at 300–320 °C. The EDS spectrum from the α-Al matrix is coloured blue and the particle spectrums are red.

From both types of precipitates several diffraction patterns were indexed in order to identify the phases. Figure 5.56(a) shows an example of one of the circular, iron-containing particles with its diffraction pattern. To the right in Figure 5.56(b) the pattern is indexed using the lattice parameters belonging to monoclinic Al_3Fe with $a_0 = 15.49$ Å, $b_0 = 8.083$ Å, $c_0 = 12.48$ Å and $\beta = 107.6°$ [Black, 1955]. Similarly, in Figure 5.56(c) an example of one of the iron-silicon-containing particles and its diffraction pattern is imaged. Next to it in Figure 5.56(d) the pattern has been index with the following lattice parameters $a_0 = b_0 = 12.30$ Å, $c_0 = 26.20$ Å and $\gamma = 120°$ belonging to the hexagonal α_h-AlFeSi phase [Mondolfo, 1976].

To sum up, during annealing there are two phases which are formed, independent of the degree of deformation. The smallest one is circular and often observed several together on a string as illustrated by the bright field and dark field micrographs in Figure 5.57(a) and Figure 5.57(b), respectively, and contain aluminium in combination with iron. From the diffraction patterns the phase was recognized as Al_3Fe. The bright field image in Figure 5.57(c) and dark field image in Figure 5.57(d) show the other type of particles found in the samples, which were both larger and more elongated. They contain both iron and silicon and formed, together with aluminium, the hexagonal α_h-AlFeSi phase which was less frequent than Al_3Fe.

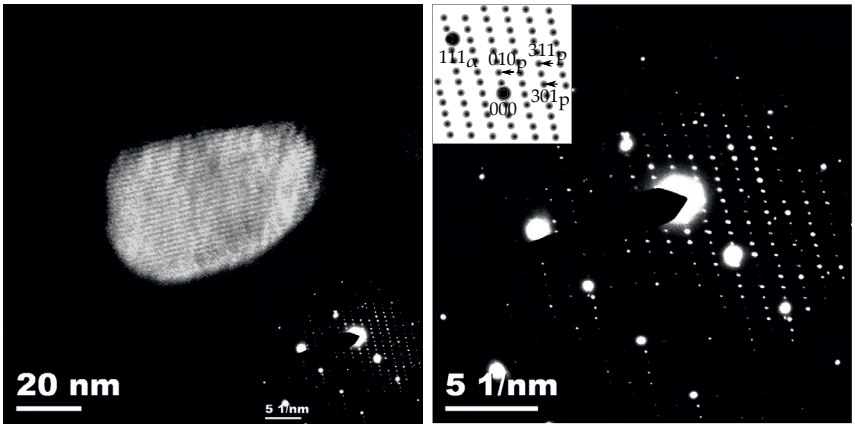

(a) Al_3Fe, DF. *(b) Al_3Fe, DP.*

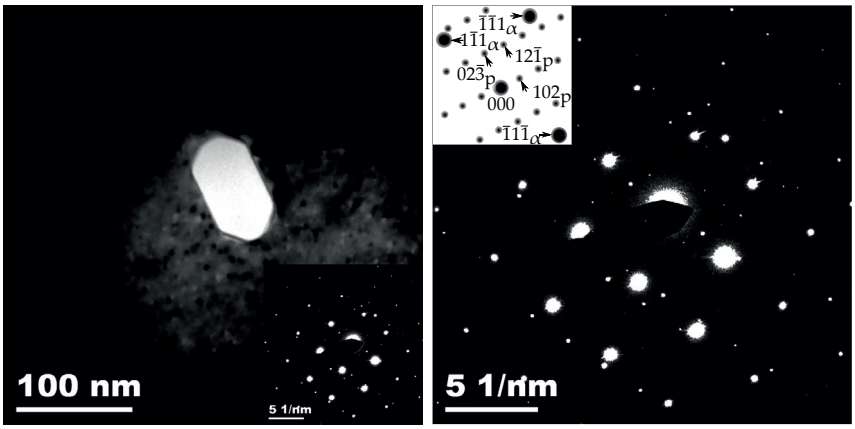

(c) α_h-AlFeSi, DF. *(d) α_h-AlFeSi, DP.*

Figure 5.56: TEM dark field images and diffraction patterns of Al_3Fe and α_h-AlFeSi observed in A1 samples. This particular Al_3Fe particle was observed in a 92.5% deformed sample annealed for 10^4 seconds at 300 °C and the α_h-AlFeSi was observed in a 50% deformed sample annealed for 10^5 at 320 °C.

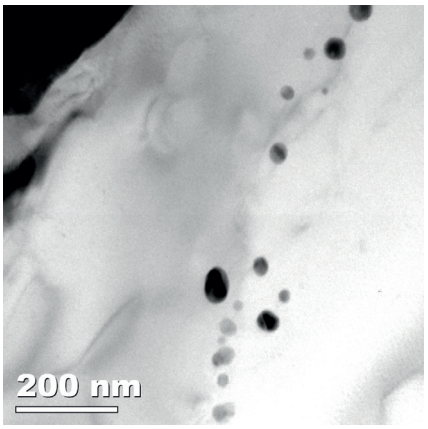

(a) Al_3Fe, BF.

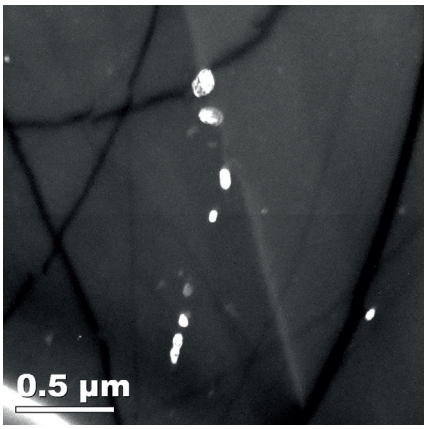

(b) Al_3Fe, DF.

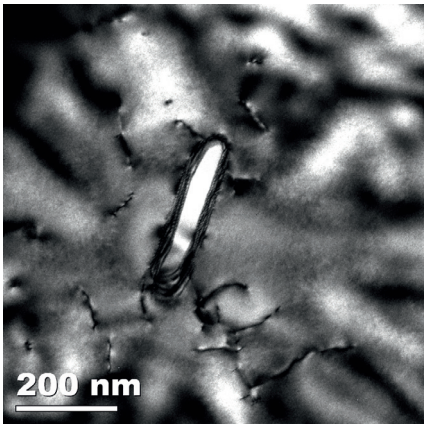

(c) α_h-AlFeSi, BF.

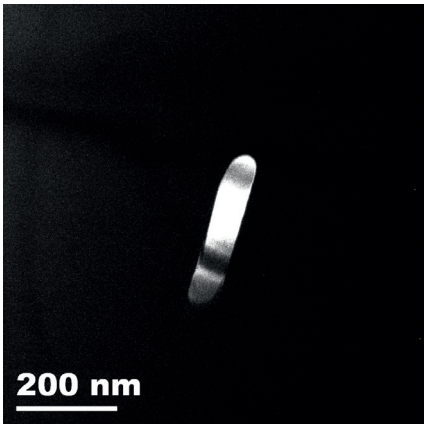

(d) α_h-AlFeSi, DF.

Figure 5.57: TEM images of Al_3Fe and α_h-AlFeSi which were observed in both 50% and 92.5% deformed A1 samples annealed for 10^4 & 10^5 seconds at 300–320 °C.

Chapter 6

Discussion

Initially it is noted that the discussion chapter will have a somewhat different structure as compared to the results chapter. Rather than distinguishing between the high and commercial purity alloys, the different phenomena are discussed in light of the two alloy systems. The present chapter consist of three major sections which initially summarize the main findings and the main issues to be considered in the subsequent more detailed discussion. When necessary, a short summary of the following discussion is first given also for some of the subsections.

In the first section, aspects which were presented in Chapter 4, like phenomena occurring during homogenization and deformation, are discussed. This part also considers and discusses the mechanical softening during annealing. Then follows an in-depth discussion of recovery by subgrain growth and nucleation of recrystallization, included a section on validation of the characterisation method. The third and final part discusses interannealing and particularly the effect of iron on the microstructure during and after annealing is discussed.

6.1 Overview & Bulk Properties

When investigating particular properties of a material, it is common to also do more general investigation simply to confirm that the initial and expected properties of the material before any further processing. Sometimes unexpected properties might be revealed that are either important for the later investigations or in themselves interesting. While characterizing the starting materials and mechanical softening behaviour, several such interesting aspects will be addressed in the following, although of minor relevance to the main objectives of this PhD work. The A2 alloy was found sensitive to the homogenization soaking temperature with respect to abnormal grain growth. In both A1 and A2, but particularly in A2 due to more Si, there are probably fine dispersoids which dissolve upon annealing and cause unpinning of certain boundaries. In

combination with a much larger driving force for grain growth in the A2 alloy than in the A1 alloy, this is believed to cause abnormal grain growth in A2. The amount of grain break-up during deformation was found most likely not to be directly influenced by the variations in alloy composition but rather indirectly by the effect of alloying on reducing the grain size after solidification. The textures after deformation were found to be typical pure metal textures with a strong β-fibre. Upon annealing, a weak hardening was observed initially that was less trivial to understand but has been linked to a stronger resistance against deformation of a well recovered subgrain structure compared to one which has a more cellular structure of tangle dislocation.

6.1.1 Abnormal Grain Growth in A2

During homogenization of the A2 alloy at 600 °C, abnormal grain growth occurred and the homogenization temperature had to be lowered to 540 °C in order to achieve a homogenous grain size on the micro meter level. The transition from normal to abnormal grain size was very abrupt and at 560 °C similarly large grains as at 600 °C were present.

The mechanism behind abnormal grain growth has been debated. However, in bulk materials, two mechanisms are generally accepted; non-uniform boundary mobilities and unpinning of certain boundaries due to dissolution of second-phase particles [Holm et al., 2003]. Because both A1 and A2 were homogenized with a casting texture but only A2 exhibited abnormal grain growth at $T > 540$ °C, an explanation by non-uniform boundary mobility would necessitate a difference in the distribution of boundaries in A1 and A2 which is unlikely. There are, on the other hand, many more grain boundaries in A2 compared to A1 as the grain size measurements in Table 4.3 indicate. Hence, the driving pressure for grain growth during homogenization is much larger in A2 and may explain why abnormal grain growth takes place in this alloy and not occurring in A1.

The A2 alloy contains more silicon than A1 and Si is indeed known to enhance precipitation of iron containing particles, thus making subsequent dissolution of second-phase particles a plausible mechanism [Ito et al., 1982; Miki and Warlimont, 1968]. The transition is also very abrupt and temperature sensitive, which further supports the assumption that dissolution of second-phase particles is the cause of abnormal growth in A2 [Beck et al., 1948]. After casting, the microstructure is not in equilibrium and it is possible that fine dispersoids form during heating (50 °C/h) up to 600 °C. Sampath et al. [1996] followed the evolution of second-phase AlFeSi particles and the solute level in an AA1050 alloy of similar composition to A2 during homogenization with a heating rate of 75 °C/h up to 605 °C. Below 490 °C dispersoids formed readily, leading to a decrease in the solute content. However, above 490 °C, dissolution of these newly formed dispersoid occurred rapidly and the dispersoids were almost gone

when the soaking temperature was reached.

During heating, eventual dispersoids forming in A2 exert a Zener pinning force that is present at all boundaries. However, subsequent dissolution of the same dispersoids at higher temperature is probably not homogeneous and may cause some grain assemblies to grow freely during the final stages of heating and early stages of the soaking period [Straumal et al., 1997]. Thus, in combination with a strong driving force for grain growth, abnormal growth of some grains is possible.

6.1.2 Deformed Microstructure

The as-deformed state of the high purity alloys and A2 were characterized with respect to grain break-up during deformation, while the deformation texture was investigated in all alloys. A discussion of the results presented in Chapter 4 follows.

Grain Break-Up

According to Table 4.1 and Table 4.2 the high purity, binary and commercial purity alloys all experience significant break-up, although there is no apparent alloy dependency. Nevertheless, the evolution of the spacing $D_{measured}$ between HAGBs varies with alloy composition at both strain levels. After 80% deformation, i.e. $\varepsilon = 1.6$, the spacing is significantly smaller in the Al-1.0Mn alloys, while Al4N, Al-0.25Mn and Al-0.5Mn all show a larger spacing. With increasing deformation to strain $\varepsilon = 3$, the spacing decreases and is very similar in the Mn-containing alloys but about twice as large in Al4N. According to Humphreys et al. [1999], grain subdivision is affected by material through the stacking fault energy γ_{SFE}, grain orientation, orientation relationship with neighbouring grains, strain, deformation mode and initial grain size and shape. It is noted that in the present PhD work grain break-up only refers to the number of new high-angle boundaries generated during subdivision relative to the initial number.

Significant break-up is usually expected during deformation, particularly in coarse grained materials. In addition to strain, the initial grain size is one of the main parameters that is confirmed to have an effect on break-up [Forbord, 1999; Lee et al., 1993; Ryen, 2003; Sæter, 1997]. A fine initial grain size gives more homogenous deformation and less break-up, as clearly demonstrated in Table 4.2 where there is a large difference in the break-up factors of the two A2 samples. Apart from having a very different initial grain size, there is presumably a difference in the solute level and fraction dispersoids in $A2^{hom}_{600}$ and A2. Figure 5.27(d) indicates that there is more in solid solution in $A2^{hom}_{600}$ than in A2 after deformation, although not enough to change the softening behaviour significantly in Figure 5.27(c). Differences in microchemistry and

effects of solute through γ_{SFE} have only a secondary effect compared to initial grain size [Hughes and Hansen, 1995; Lee et al., 1993]. E.g. Ryen [2003] has shown that grain break-up is not affected by the solute content in aluminium alloys containing Mg while a coarser initial grain structure leads to more break-up, as illustrated in Figure 6.1. In addition to grain size, the texture and orientation of the different grains may also have a strong influence on grain break-up [Hughes and Hansen, 1995; Lee et al., 1993]. During e.g. rolling, more HAGBs are created in the unstable deformation texture components Cube and Goss as compared to the stable components Cu, S and Brass [Hughes and Hansen, 1997]. For $A2^{hom}_{600}$ the texture, or rather the orientation of the few grains present after homogenization, is influencing grain break-up but because the grains size is so much smaller in A2, texture-differences between $A2^{hom}_{600}$ and A2 are less important.

Unfortunately, there is no available data on the initial grain size of the Al4N or Al-Mn alloys studied in this work. They were cast without grain refiner and, thus, the grain size is coarse but most likely finer with increasing alloy content [Easton and StJohn, 1999; Lee et al., 2000; Maxwell and Hellawell, 1975]. From Figure 4.2, the very strong and sharp texture of Al-1.0Mn indicates a much finer initial grain size than in the other alloys [Hansen et al., 1985]. Al-0.25Mn and Al-0.5Mn, on the other hand, have weaker, very similar textures and probably similar initial grain size, while Al4N in addition to a similarly strong deformation texture as Al-0.25Mn and Al-0.5Mn also have elements of other texture components thus indicating a slightly more coarse grained structure. At a strain of $\varepsilon = 1.6$, the HAGB spacing data indicate a consecutively decreasing break-up from Al4N through to Al-1.0Mn.

At a strain of $\varepsilon = 3$, saturation seems to have occurred to the Mn-containing alloys. Hughes [1995] has observed temporary saturation of the BUF followed by a decrease upon further deformation. Whether Al4N is still not saturated or the HAGBs spacing is increasing in accordance with Hughes [1995], thus explaining the large HAGB spacing value, is not obvious. Although the coarser grain structure of Al4N suggests the first explanation. All the alloys should display an initially similar texture after casting and homogenization, though Al4N (and $A2^{hom}_{600}$) could be affected somewhat by orientation dependent grain break-up due to a very coarse grain structure. However, it must be concluded that the main cause for the HAGB spacing and break-up factors observed here is directly linked to the initial grain size, in accordance with general experience.

Deformation Texture

The deformation texture is mainly determined by the stacking fault energy γ_{SFE}, which again is determined by the atomic bonding strength. Other important parameters are related to process parameters (identical in our case), second phase particles, extensive solute hardening (which causes shear banding

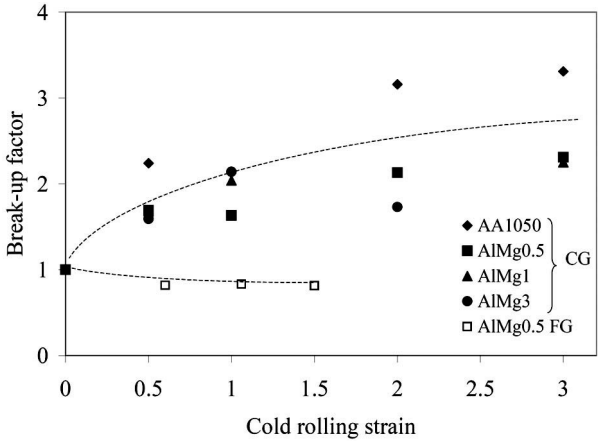

Figure 6.1: Grain break-up factors of different solute levels and grain sizes (coarse grain, CG, and fine grained, FG) as a function of strain. Ryen [2003]

and leads to a reduction of the Cu component and a strengthening of the Brass and Goss components) [Humphreys and Hatherly, 2004]. All the alloys, from the high purity Al4N to the commercial purity alloy A2, show a strong deformation texture after rolling to strains ε ranging from 2.6 to 3.0. Neither a manganese addition of 1.0 wt.% nor low levels of iron or silicon affect the stacking fault energy γ_{SFE} notably with respect to the texture development and all alloys exhibit a typical pure metal deformation texture with a strong β-fibre.

After deformation and break-up the microstructures typically consist of alternating bands of the deformation texture components Cu, S and Brass, although a few transition bands and Cube bands were also observed. In a different study on cold-rolled high purity aluminium directionally solidified and consisting of coarse, columnar grains, the deformed structure was made up of alternating Cu omponents ($\pm$) separated by sharp transition bands [Hjelen et al., 1991]. In the broad Cu band of Al-1.0Mn in Figure 4.1, actually two very narrow Cu oriented bands are seen and their symmetries are different from their surroundings. However, on either side the symmetry is identical and thus this is not similar to what was observed by Hjelen et al. [1991].

6.1.3 Softening Behaviour

Besides the relatively slow recovery kinetics of A1 (and A2) which is addressed in more detail later, the softening behaviour for all alloys is as expected with consistent behaviour at the various temperatures. It is noted, although not further investigated, that the softening kinetics of A2 are independent of the initial grain size. As already discussed, the two different homogenization

temperatures of 540 and 600 °C resulted in very different grain sizes. Even if significant break-up is occurring in the coarse grained $A2^{hom}_{600}$ material, the HAGB spacing after deformation is still about eight times larger than in A2. HAGBs act as dislocation sinks and are highly mobile features which normally are expected to enhance both recovery and recrystallization through e.g. SIBM as described in Section 2.2. Faster softening kinetics is for example demonstrated by Kwieciǹski and Wyrzykowski [1989] in high purity aluminium. Apparently, the number of HAGBs is not particularly important for the recovery and recrystallization kinetics of the commercial purity alloy A2.

One interesting feature is observed when looking at the softening curves of Al4N and possibly Al-0.25Mn, A1 and A2. The hardness increases marginally for short annealing times at the lowest annealing temperatures, i.e. there is hardening on annealing. Such behaviour is described in literature and often associated with clustering or precipitation. In Al-0.25Mn, A1 and A2 the effect is not very pronounced, except for the 50% deformed A1 condition in Figure 5.37(a), and in the case of A1 and A2 can be linked to clustering or precipitation. However, no hardening on annealing is observed after increasing the solid solution level in A1 through homogenization at 620 °C and quenching.

The standard deviation of the hardness measurements of A1 are less than 1 HV and usually about 0.4 HV, while the contribution from hardening on annealing caused by clustering in an AA1050 alloy was according to Ryen et al. [2006] approximately 1 HV. Therefore, it could be difficult to capture this effect in the A1 alloy which contains less solute. After equal channel angular pressing, hardening on annealing in an AA1050 alloy is more pronounced [Bowen, 2008]. Neither Sæter [1997] nor Furu [1992] observed hardening on annealing in their commercial purity alloys, though additions of Mn to the AA1070 alloy of Sæter [1997] resulted in increasing strength within the first 1000 seconds of annealing. Both Si and Mn enhance precipitation of iron-rich phases in commercial purity alloys and Birol [2008] has found precipitation to cause hardening on annealing in an Al-Mn-Fe-Si alloy as well. The A1 alloy contains, in addition to Fe, some Si that could help form precipitates during annealing. In Figure 5.39(a) it is shown how deformation enhances precipitation. It is thus strange why hardening on annealing is observed for the 50% deformed sample and not the 92.5% deformed variant, where more precipitation is happening, if clustering or precipitation causes the hardening effect.

For Al4N, presented in Figure 5.2(a), hardening on annealing is more evident than for any of the other alloys. Figure 6.2(a) shows the evolution of the hardness for the first 100 seconds of annealing in a second, independent set of measurements. As opposed to what is usually referred to in the literature, hardening on annealing in the Al4N case cannot be related to precipitation as the total alloy content is less than 100 ppm. In severely deformed materials, typically ARB (accumulative roll bonding) or ECAP (equal channel angular

pressing), hardening on annealing is frequently observed in high purity materials as well and explained by a dislocation source limitation due to closely spaced HAGBs acting as dislocation sinks [Huang et al., 2006]. However, since there are very few HAGBs in Al4N as compared to severely deformed materials, the number of sinks is not sufficient to expect an impact on dislocation sources by this mechanism.

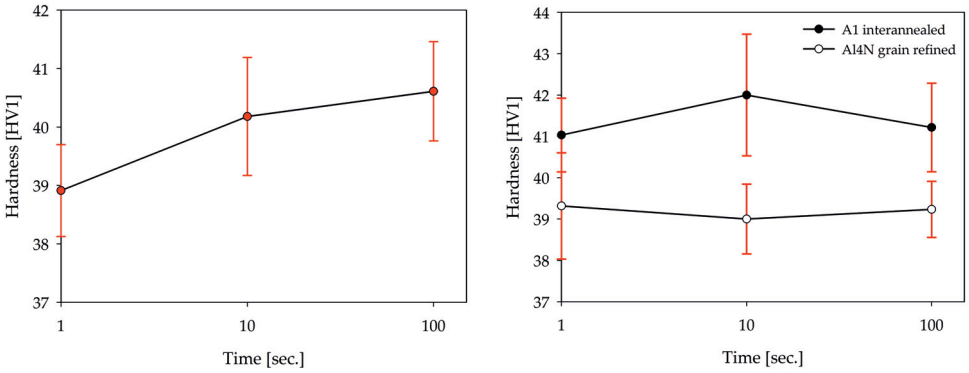

Figure 6.2: Hardening on annealing at 180 °C in Al4N cold rolled to strain $\varepsilon = 3.0$ (a). Hardening on annealing is plausible during annealing at 150 °C of interannealed A1 (deformed 92.5%, fully softened at 320 °C and deformed 50%) but not observed in Al4N (deformed and recrystallized to give finer grain size) deformed 80% (b).

Looking to creep literature, it is quite common to read about how recovery processes lead to a stronger material in the sense of lower creep rates. Clauer et al. [1970] observed a decreasing creep rate with increasing creep strain in single crystal molybdenum and suggested this behaviour to be related to climb of isolated edge dislocations in the subgrains and edge dislocations in the subboundaries. This decreasing creep rate was interpreted by Amin et al. [1970] as "strengthening due to dispersal of entanglements by dislocation climb". Alden [1977] described the phenomenon from a recovery perspective in his creep experiments on 99.99% pure Pb. Fully cellular structures have a lower recovery rate than non-cellular structures, thus a cellular structure is stronger than a non-cellular one because the strain rate is lower at constant stress. Rather vaguely, Alden [1977] explains the behaviour of the different structures by the indirect effect of the dislocation density and distribution on thermally activated structural changes to the recovery rate.

When translating this mechanism to apply for hardening on annealing, it can only be expected to operate for relatively short annealing times and low temperatures since creep tests are generally performed at a temperature much

lower than typical annealing temperatures. Because the hardness change comes about as a transition from a non-cellular to cellular structure, it should be promoted by low to medium rolling strains, i.e. strain $\varepsilon < 2$, to ensure that there are free or tangled dislocations that can be absorbed by the subgrain boundaries. Absorption of dislocations by HAGBs is what causes hardening on annealing in ECAP-materials and sub-boundaries may thus cause a similar but weaker effect in more lightly deformed materials. Hence, in A1 after most solute has precipitated during an intermediate annealing step and another 50% deformation, hardening on annealing by this mechanism should be expected. Why the recovery strengthening is so strong in Al4N after a strain of $\varepsilon = 3$ could be because of the very coarse, initial microstructure making dynamic recovery more difficult than in a more fine grained material. From Figure 6.2(b) there is some strength gained in interannealed and 50% cold rolled A1 by 10 seconds of annealing at 150 °C, though the results scatter and the effect is weak. However, in Al4N after grain refinement by interannealing and 80% deformation, there is no evidence of any hardening during annealing at 150 °C. Both alloys were however stored at room temperature for quite some time, the A1 alloy for almost a year and the Al4N for more than one year. Room temperature recovery might thus explain why so little hardening is observed.

This form of hardening on annealing seems sensitive to processing conditions and, besides creep experiments, there is little evidence for such a mechanism in the literature. The only experimental evidence for this mechanism operation during recovery-annealing of aluminium is by Perryman [1954] from micro-hardness tests on super-purity aluminium. Generally the hardness of unusually large subgrains, 10–30 μm in diameter, within a normal subgrain structure was lower than in the surrounding, smaller subgrains. However, for 20% deformed samples, the strength of coarse subgrains was increasing by several units during annealing at 375 °C. For samples cold worked to larger deformations, hardening was not observed. Although an interesting and plausible explanation for the hardening observed in Al4N, more work is required to determine the actual mechanism involved.

6.2 Recovery by Subgrain Growth

Recovery processes are important industrially for controlling the mechanical properties during thermomechanical processing, in particular subgrain growth. The subgrains which form during heavy cold rolling, coarsens when the materials is heated. How to characterize the evolution of the subgrain structure, how it progresses and what parameters are important for controlling the growth kinetics are discussed in the following. The transition from recovery to recrystallization, i.e. nucleation of recrystallization is also briefly discussed. A quick summary of the discussion is given next.

The microstructural evolution during annealing was characterized by a novel method, which was validated by TEM and found adequate. General subgrain growth as characterized by orientation independent EBSD scans showed that subgrain growth was enhanced near HAGBs separating differently oriented bands, while random HAGBs within bands of homogenous orientation were only important for the growth kinetics when consisting a major fraction of all boundaries as in Cube and possibly Goss oriented regions. During orientation independent growth, the subgrain size distributions became temporarily bimodal due to more growth near the interface of bands in the lamellar rolling structure rather than in the centre of the bands. This caused the average boundary misorientations to decrease marginally, although the actual boundary misorientations were most likely increasing slightly.

When there are strong orientation gradients the misorientations should increase, which the orientation dependent subgrain growth data confirmed. For e.g. Cube oriented subgrains there was a misorientation advantage related to growth and the size distribution became temporarily bimodal. However, for Cu, S and Brass oriented subgrains when the misorientations were increasing there was no particular growth advantage, growth was homogenous and the size distributions uniform. On the other hand, when the misorientations were decreasing, which was only observed in Brass and S oriented regions with very weak orientation gradients, there was no orientation advantage but a possible size advantage reflected by temporary bimodal size distributions developing with subgrain growth.

While orientation gradients seemed to greatly influence the subgrain growth behaviour, individual subgrain boundary misorientations only became important during the final stages of recovery, i.e. nucleation of recrystallization. Most nuclei in the Al4N alloy were misoriented subgrains from the edge of the orientation spread or even more misoriented about a $\langle 111 \rangle$-axis. The recrystallization front usually had a 25–45°$\langle 111 \rangle$ orientation relationship with the deformed microstructure. Nucleation and growth by exactly 40° $\langle 111 \rangle$-rotated boundaries typical for growth of Cube and R oriented nuclei was not significant at low temperatures but became preferable at higher temperatures. This behaviour is explained by a solute drag effect from particularly iron impurities in the Al4N alloy.

6.2.1 Validation of EBSD Subgrain Characterization Method

Subgrain growth has been characterized with respect to size and average boundary misorientations using EBSD. Alternatively, in traditional TEM characterization less than 100 subgrains are within the field of view and all misorientation calculations have to be done by comparing individual diffraction patterns. However, recently an equivalent method to EBSD in SEM has be-

come available for TEM grain and subgrain characterization. The NanoMEGAS ASTAR system makes orientation mapping in TEM possible with statistics more comparable to EBSD and with significantly better spatial resolution. For the EBSD scans made in this PhD work, the minimum misorientation angle was 0.7° with a minimum equivalent circle diameter of 0.15 µm. The number of subgrains detected per scan was usually between 500 and 1500. Though in some cases, primarily for Cube oriented regions, it was difficult to find representative areas and scans with fewer subgrains were made.

In total, approximately 400 EBSD scans were made where about 150 yielded fully reconstructed subgrain maps. The regions scanned were selected in order to make "bulk" observations of the microstructural evolution within the different texture components during annealing. However, even careful selection of areas sometimes resulted in unwanted microstructures. These were usually unique microstructures like highly misoriented regions of supposedly stable orientations or regions experiencing unusual amounts of shear, as the fully reconstructed subgrain maps in Figure 6.3 exemplifies. In Figure 6.3(a), a scan made in Al4N after 10^5 seconds of annealing at 180 °C shows Cu/S oriented subgrains with extraordinarily large misorientations and 23% HAGB. Figure 6.3(b), on the other hand, is from A1 after annealing for 10 seconds at 250 °C and shows both several orientation bands and small subgrains within an area to the left which is distinctly different from its surroundings. Hence, not all maps qualified for size and misorientation calculations.

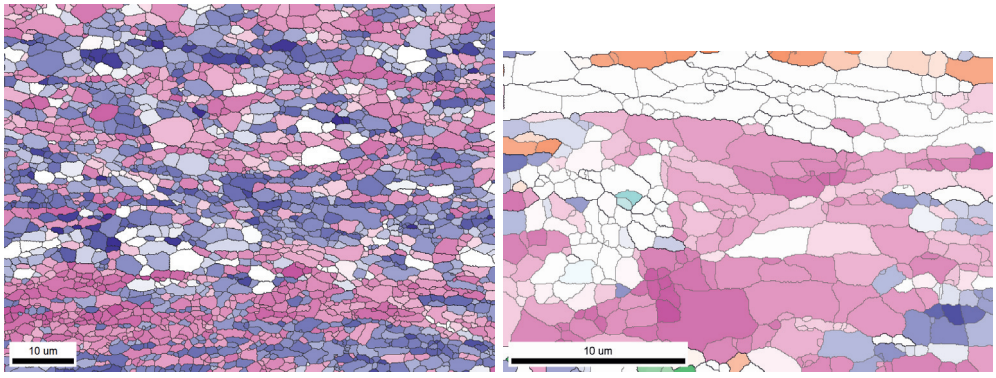

(a) Al4N *(b) A1*

Figure 6.3: Examples of unusual microstructures excluded from size and misorientation measurements.

Due to the heterogeneous nature of the samples, although an effort has been made to minimise the effect, the scatter of the size and average boundary misorientation data clearly show how unlike the microstructure of similar texture components may be even after deformation. This was particularly true

for the commercial purity alloy A1 and the annealing only magnified the heterogeneity as Figure 6.4 illustrates. These orientation maps were not intended for subgrain characterization and, hence, have been cleaned-up using EDAX TSL OIM Analysis 6.1 only. It is obvious how subgrain boundaries (grey) are incomplete and unable to define the individual subgrains. Thus, a method for subgrain reconstruction is required.

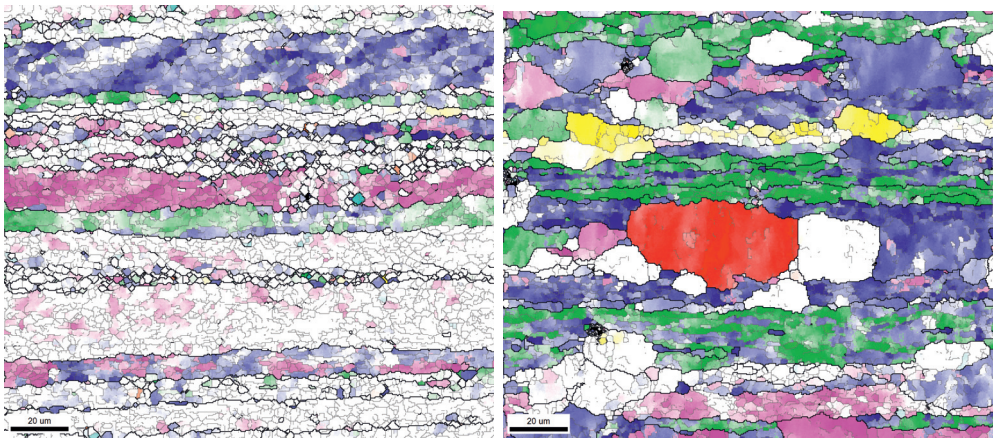

(a) As-deformed. *(b) Annealed 10^5 sec. at 250 °C.*

Figure 6.4: Typical microstructure of cold rolled A1 sample after deformation and annealing with a heterogenous character to some extent.

The biggest challenges associated with EBSD characterization of subgrains is expected to be in the as-deformed samples because of the relatively high density of dislocations which have a negative effect of the quality of the diffraction patterns. With annealing, dislocations are annihilated and the boundaries become sharper which benefits the EBSD method. Regions with Cube orientation after cold rolling typically have a substructure of rather equiaxed subgrains with a low density of internal dislocations and sharp, often high-angle boundaries — ideal for EBSD characterization. The opposite is true for Brass regions which have a high fraction of low-angle boundaries with misorientations of typically 3-4° [Albou et al., 2011; Humphreys and Bate, 2007; Xing et al., 2006]. This makes Brass more challenging to characterize by the EBSD method.

However, with a method for sampling of areas likely to represent bulk behaviour and despite the scatter still observed resulting from unlike microstructures, although similarly oriented, the resulting grain sizes and misorientations observed in the present PhD work compare well to TEM investigations and literature as discussed in the following.

Table 6.1 compares mean intercept count measurements parallel to RD and ND and converted to equivalent circle diameters by assuming rectangular sub-

grains from reconstructed subgrain maps (EBSD), IQ maps and *secondary electron* (SE) images. SE images are sensitive to surface properties (i.e. oxide layer, contamination, etc.) and BSE images (channelling contrast) are usually preferred but since images were taken while the samples was tilted, the BSE detector was not inserted simultaneously and would in any case not have a high detection level due to the 70° tilt angle. Except for scan "05" in Table 6.1, the measurements compare well. Due to the surface sensitive nature of the SE images, the size measurements probably underestimate the subgrain sizes somewhat.

Table 6.1: EBSD measurements of subgrain sizes done on reconstructed subgrain maps of cold rolled material to strain $\varepsilon = 2.6$ compared to mean lineal intercept counts measurements on image quality (IQ) maps and secondary electron images (SE). All sizes are given as equivalent circle diameters.

Sample	**Scan**	**Orientation**	**EBSD**	**IQ**	**SE**
A1 asdef	05	Cube	1.22	1.54	0.83
A1 asdef	07	Cu	1.14	1.18	1.07
A1 asdef	09	Brass	1.41	1.70	1.27

An example showing an SE image and an IQ map of the same area is given in Figure 6.5, together with a map constructed from both IQ and the local orientation spread. Intelligibly, to assume rectangular grains when converting mean lineal intercept counts into equivalent circle diameters is a fair approximation. From Figure 6.5 it is evident how contrasts may occur in the SE image, e.g. diagonally from upper left corner to lower right corner, that clearly are not related to the microstructure. Similarly, the IQ map does not reveal all the boundaries and size measurements based on such images probably overestimated the actual size. Hence, the size data obtained from reconstructed subgrain maps, which from Table 6.1 are found to be in between the IQ and SE measurements, are believed to be reliable.

Figure 6.5(c) also shows that there are several small regions which appear to have well defined interfaces to their surroundings but during the reconstruction process (Section 3.2.5) are removed and will not be considered in the calculations. This is mainly a problem in the as-deformed state and close to triple junctions etc. This causes some bias toward larger subgrain sizes, hence, the minimum subgrain size of 0.15 μm is applied. Still, rather good correlation is achieved with size measurements done in TEM on A1 samples in as-deformed state. Unfortunately, only orientation independent, i.e. mixed orientations, subgrain size data are available from the TEM investigations. Similar to the SE and IQ images, subgrain sizes from the TEM images were measured using mean lineal intercept counts in ND and RD, respectively. Rectangular subgrains were assumed and the area calculated from which the equivalent circle diameter was obtained.

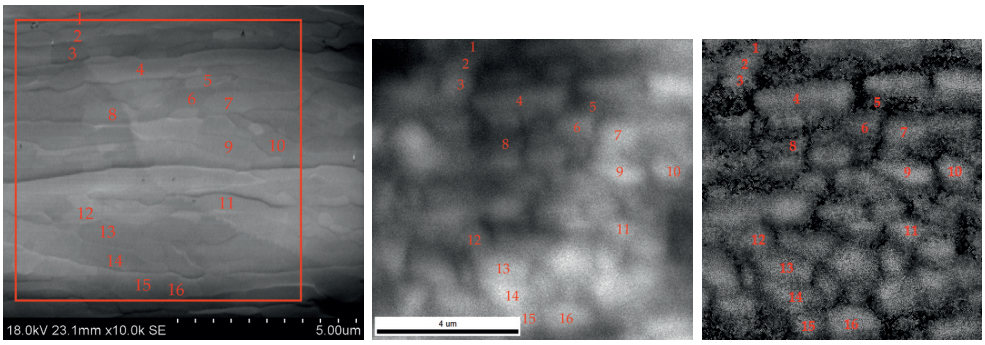

(a) SE *(b) IQ* *(c) IQ + ori.*

Figure 6.5: Comparison of visible details in the same area using different imaging modes. From left to right are SE image, IQ map and IQ combined with local orientation spread map (IQ+ori.).

Again, from looking at Figure 6.6 the assumption of rectangular subgrains is acceptable. More than 200 subgrains were measured randomly from several TEM samples, mainly from composite images like the one in Figure 6.6(a). The average subgrain size from these measurements is given in Table 6.2 where a comparison with the average subgrain size calculated from all the orientation dependent (o.d.) scans and all the orientation independent (o.i.) scans from A1 in as-deformed state is made. In addition, average subgrain size from the as-deformed and 10 seconds annealed samples at 180 °C of orientation dependent (o.d.) scans are also included. The average subgrain size as measured by TEM is significantly smaller than the ones measured by EBSD.

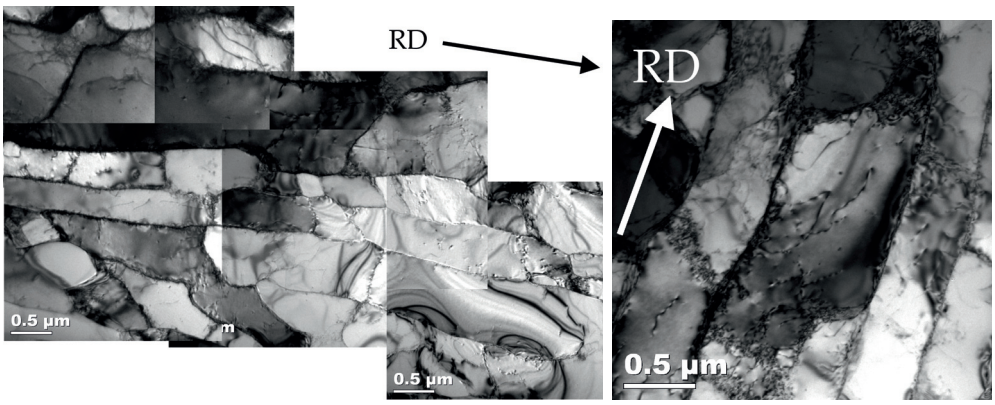

(a) *(b)*

Figure 6.6: TEM micrographs of A1 sample in as-deformed state ($\varepsilon = 2.6$).

Table 6.2: Comparison of average subgrain size measurements from reconstructed subgrain maps (EBSD) with TEM measurements of samples in as-deformed state after cold rolling.

Method	**Alloy**	**Strain**	**Subgrain size** [μm]
TEM	A1 (o.i.)	$\varepsilon = 2.6$	0.73
EBSD	A1 (o.d.)	$\varepsilon = 2.6$	1.20
EBSD	A1 (o.i.)	$\varepsilon = 2.6$	0.93
EBSD	Al4N (o.d.)	$\varepsilon = 3.0$	1.03

Although the spatial resolution of EBSD is clearly not as good as TEM, the discrepancy between the two methods is quantified in Table 6.2. In an early work by Schuh and Heimendahl [1974] on 99.98% pure aluminium cold rolled up to 99% deformation, the subgrain size saturated at about 0.85 μm after 80% deformation. Other TEM investigations on comparable materials have often found smaller average subgrain sizes. Using a threshold of 100 nm, corresponding to a misorientation limit of 0.1–0.2°, Sandström et al. [1978] studied subgrain sizes in Al-1% Mn and pure aluminium of 4N quality. They found average subgrain size in 80% cold rolled Al-1% Mn to be ∼0.45 μm and roughly 0.7 μm in the 80% cold rolled 4N aluminium. Xing et al. [2006] observed subgrain sizes similar to the A1 alloy, i.e. 0.93 μm, in an AA1200 alloy (99.1% pure). After 86.4% ($\varepsilon = 2$) cold rolling and treating the boundary spacing data to a similar analysis as in this PhD work, an equivalent circle diameter of 0.78 μm resulted. TEM subgrain size measurements were compared to EBSD measurements during annealing of cold rolled commercial purity aluminium by Furu et al. [1995] and found to be rather similar but usually slightly smaller. On the other hand, TEM measurements by the same authors of an aluminium alloy containing 0.29 wt.% Fe and 0.12 wt.% Si deformed 86.4% ($\varepsilon = 2$) and 95% ($\varepsilon = 3$) resulted in, by the same analysis as above, much smaller equivalent circle diameters of 0.60 μm and 0.48 μm, respectively. At a strain $\varepsilon = 3$, Sæter [1997] also observed similarly small subgrains (ECD = 0.45 μm) in an AA1070 alloy. These subgrain diameters are among the smallest reported in literature and significantly smaller than found in this PhD work. Still, the subgrain diameters found by TEM here are still reasonable and are generally in accordance with literature.

In terms of EBSD observations of subgrain sizes in as-deformed state in literature, one frequently comes across studies by F. J. Humphreys & co-workers. In aluminium single crystals containing 0.05 % Si and cold deformed 70%, the initial subgrain size was 0.9 μm when a minimum size of ∼0.2 μm was applied [Huang and Humphreys, 2000]. In an earlier work on nearly the same material and state, the diameter of small subgrains was quoted to be 1.5 μm, though

the results are probably less accurate due to poorer SEM and EBSD equipment [Ferry and Humphreys, 1996]. In aluminium containing 1.3 wt.% Mn, cold rolled 90% and with a 0.2 μm detection limit, the ECD analysis gives an average subgrain size of 1.0 μm [Somerday and Humphreys, 2003a]. While in Somerday and Humphreys [2003b], a follow up paper on a leaner alloy version with only 0.3 wt.% Mn also deformed 90%, both 0.75 μm subgrains in a band with several texture components and 2 μm subgrains in a Goss oriented band were seen. After grain refinement of this material, an average subgrain size of 2.5 μm was observed. However, characterization of subgrain sizes after deformation is challenging and e.g. Sukhopar et al. [2012] only reports subgrain sizes of an AA8079L alloy after cold rolling and annealing for 2 seconds at 280 °C and 5 seconds at 320 °C. Then the subgrain sizes were approximately 0.82 and 0.78 μm.

A summary of as-deformed subgrain size data from the literature at large cold rolling strains in various Al alloys is given in Table 6.3. The results are organized by characterization method, TEM or EBSD, and as a reference the subgrain size evolution with strain as measured by TEM by Schuh and Heimendahl [1974] is reproduced in Figure 6.7. Sjølstad [2003] found the as-deformed subgrain size to be, when converted to ECD, 0.58 μm in an AA3103 alloy. With decreasing content of dissolved Mn, Tangen [2004] found the initial subgrain size to decrease from 0.58 μm in Al-0.85 wt.%Mn to 0.45 μm in Al-0.3 wt.%Mn. As shown in Table 6.3, the results of Sjølstad [2003] and Tangen [2004] are the smallest ones measured by EBSD in any material and also small when compared to TEM measurements. This could be a result of the inherent orientation noise of the EBSD method which can introduce artificial subgrain boundaries which, due to their vastness, may significantly affect subgrain size measurements [Schwartz et al., 2009]. Actually, Godfrey [2011] states that caution should be exercised when interpreting published subgrain data unless handling of small "grains" is discussed explicitly! According to [Schwartz et al., 2000], as a general rule, EBSD subgrain sizes are typically a factor 2 larger than TEM subgrain sizes. When Tangen [2004] made a comparison between EBSD and TEM, the difference was much smaller at 0.46 μm versus 0.39 μm, respectively. This gives a ratio of ∼1.2 which is also in better agreement with Table 6.3 and a factor 2 difference in subgrain size between TEM and EBSD seems large.

Despite the difficulty of characterizing as-deformed state by EBSD, the method is still preferred by several authors. Like Cao et al. [2009] for example, who studied an AA1200 alloy deformed 86.4% by cold rolling reported a subgrain size of 0.74 μm which is actually smaller than the TEM findings by Xing et al. [2006] of the same alloy and strain. Barou et al. [2009] made a careful investigation of 79% cold rolled aluminium with 0.1 and 0.3 wt.% Mn additions and found average subgrain sizes to be 0.93 μm and 0.95 μm, respectively. Although there is some scatter and the alloys and conditions are not exactly the

Table 6.3: Subgrain sizes measured by TEM and EBSD of heavily cold deformed aluminium before annealing as reported in literature (all values are given as ECD).

	Alloy	**Strain**	**Subgrain size** [μm]
TEM			
Schuh and Heimendahl [1974]	Al99.98%	$\varepsilon = 3.0$	0.85
Sandström et al. [1978]	Al-1Mn	$\varepsilon = 1.9$	0.45
Sandström et al. [1978]	Al-4N	$\varepsilon = 1.9$	0.70
Xing et al. [2006]	AA1200	$\varepsilon = 2.0$	0.78
Furu et al. [1995]	Al-0.29Fe-0.12Si	$\varepsilon = 2.0$	0.60
Furu et al. [1995]	Al-0.29Fe-0.12Si	$\varepsilon = 3.0$	0.48
Sæter [1997]	AA1070	$\varepsilon = 2.6$	0.45
EBSD			
Sjølstad [2003]	AA3103	$\varepsilon = 3.0$	0.58
Tangen [2004]	AA3103	$\varepsilon = 3.0$	0.45
Huang and Humphreys [2000]	Al-0.05Si	$\varepsilon = 1.2$	0.90
Somerday and Humphreys [2003a]	Al-1.3Mn	$\varepsilon = 2.3$	1.00
Somerday and Humphreys [2003b]	Al-0.3Mn	$\varepsilon = 2.3$	0.75–2.00
Somerday and Humphreys [2003b]	Al-0.3Mn (g.r.)	$\varepsilon = 2.3$	2.50
Cao et al. [2009]	AA1200	$\varepsilon = 2.0$	0.74
Cao et al. [2009]	AA1200	$\varepsilon = 4.0$	0.47
Sukhopar et al. [2012]	AA8079L	$\varepsilon = 1.2$	0.78–0.82
Barou et al. [2009]	Al-0.1Mn	$\varepsilon = 1.6$	0.93
Barou et al. [2009]	Al-0.3Mn	$\varepsilon = 1.6$	0.95

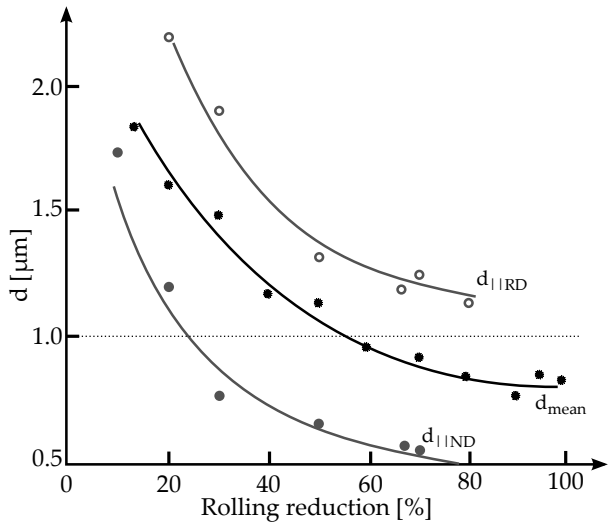

Figure 6.7: Evolution of subgrain size diameter with strain as measured by TEM in 99.98% pure aluminium. After [Schuh and Heimendahl, 1974]

same, the EBSD method does not have as good spatial resolution as TEM and generally produce larger subgrain size values. These findings from literature are similar to the observations made here and presented in Table 6.2. The average subgrain size of A1 with mixed orientations, i.e. orientation independent, is comparable to the subgrain sizes from studies on similar materials by the EBSD technique.

Perhaps more interesting is the difference between orientation independent and dependent subgrain size measurements. In the latter case the size is considerably larger, which means there must be smaller subgrains closer to HAGBs separating differently oriented bands and narrow bands only a few subgrains in thickness. Somerday and Humphreys [2003b] observed the same in their cold deformed aluminium alloy, while in hot deformed material Humphreys [2004b] found slightly larger subgrain sizes at HAGBs possibly resulting from faster recovery kinetics here due to a larger mean misorientation. Liu and Zhai [2011] actually found smaller subgrain sizes but larger boundary misorientations and orientation gradients near grain boundaries and triple junctions in hot deformed AA3104 aluminium. The subgrain size of hot deformed materials depends on dynamic recovery, though the larger misorientations suggests that HAGB regions accommodate more slip, perhaps on other slip systems, than the interior regions, which would result in a finer and more misoriented substructure, i.e. more stored energy.

Accurate subgrain size data would not be possible if the angular resolution was too low to actually detect the smallest subgrain boundaries. In this

PhD work, a minimum boundary misorientation of 0.7° could be applied due to the good quality of patterns achieved by the high current density of the SEM equipment. A threshold value of 2° is often reported in the literature, though according to Humphreys [2001] the EBSD characterization method should have an angular resolution of 0.5–1.5° depending on the sample and SEM/EBSD equipment and even lower resolution may be achieved by carefully comparing individual diffraction patterns [Bate et al., 2005]. A significant fraction of the boundaries in deformed metals has a misorientation in the range 0.5–3.0°. Hence, the threshold value of 0.7° used for the subgrain characterization done in this PhD work should be adequate to capture most subgrain boundaries while not introducing false boundaries resulting from orientation noise [Humphreys and Hatherly, 2004]. The misorientation distribution is expected to converge to zero intensity for 0° misorientation, which was indeed observed for most of the misorientation distributions plotted in Chapter 5 [Humphreys, 2001].

To summarize, the EBSD-generated and reconstructed subgrain maps, from which the subgrain size and misorientation date presented in this PhD work are calculated, are indeed able to provide reliable data on subgrain growth characteristics.

6.2.2 Subgrain Growth and Evolution of Average Boundary Misorientation during Annealing

The main focus of this PhD work has been on characterizing orientation dependent subgrain growth by sampling of areas with an ideal orientation and homogenous microstructure. In order to obtain the actual, overall subgrain growth behaviour and capture the effect of heterogeneities like transition bands and HAGBs, random scans with a variety of texture components in the A1 alloy were also investigated. Similar scans independent of the orientations could not be made in the Al4N alloy because the layered structure was very coarse and the investigated cross sections usually contained only a few bands of different orientation.

Orientation Independent Subgrain Growth

Subgrain growth is found to be more rapid when studied in orientation independent scans than in orientation dependent scans, although the overall growth is still relatively weak. In the A1 alloy, as opposed to the Al4N and Al-0.25Mn alloys, concurrent precipitation is occurring but the recovery and subgrain growth rates do not seem particularly affected. However, the size distribution does develop a strong bimodal character upon annealing for 10^2–10^4 seconds. Rather than being a result of concurrent precipitation (a bimodal distribution was not observed for orientation dependent growth), the bimodal

size distributions seems to be a result of favourable growth condition for a large fraction of subgrains. These subgrains do not have a particularly large size and are not the most misoriented, although growth for subgrains with misorientations less than 3.5° is marginal. Above 3.5° the growth rate seems independent of the average boundary misorientation.

As already mentioned, the smallest average subgrain size after deformation and the most rapid growth was observed in the orientation independent scans. After short annealing times, neighbouring subgrains to HAGBs separating differently oriented bands are larger than subgrains in the centre of bands due to a higher stored energy close to HAGBs [Liu and Zhai, 2011]. Strong orientation gradients at the HAGBs yield favourable conditions for recovery, particularly at HAGBs separating bands with orientations close to the rolling texture components and bands with other orientations [Engler et al., 1996b; Xing et al., 2006]. This, in addition to giving rise to highly mobile HAGBs, leads to the formation of recrystallization nuclei by SIBM [Humphreys, 2004c]. Thus, the presence of HAGBs and high stored energy regions is probably why more recovery by subgrain growth is observed in the orientation independent annealing experiment (Figure 5.32(c)) compared to any of the orientation dependent cases (Figure 5.32(a)). However, as seen from the literature-data gathered in Figure 6.8, when compared to subgrain growth during annealing at various temperatures characterized in similar materials at large strains, growth of subgrains with mixed orientations in A1 correspond well with some investigations and less so with other. There is clearly a lot of experimental variation.

Several of the curves in Figure 6.8 are obtained at significantly higher temperatures than the 250 °C annealing temperature of A1. Increasing the temperature further would rapidly lead to significant recrystallization in A1 as recrystallization is already quite prominent after 10^5 seconds as illustrated by Figure 6.4(b). Although the as-deformed subgrain size is comparable to what has been reported in literature, the growth curve for the A1 alloy at 250 °C is somewhat shifted to slightly higher subgrain sizes after annealing compared to the other results. Starting from the same as-deformed subgrain size as Barou et al. [2009] and Huang and Humphreys [2000], it is the initial growth rate of subgrains in A1 which is larger and comparable to Barou et al. [2009] and Sandström et al. [1978]. However, both Furu et al. [1995] and Sæter [1997] measured significantly smaller subgrain sizes and ditto larger growth rates. Together with the data gathered by Huang and Humphreys [2000], which capture subgrain growth by a factor 5, are unique in this context.

In A1, it is important to remember that the solute concentration is not stable during annealing and concurrent precipitation is taking place. This may change the rate controlling mechanism for growth from solute drag to Zener drag with time. However, no abrupt or even continuous change of the growth

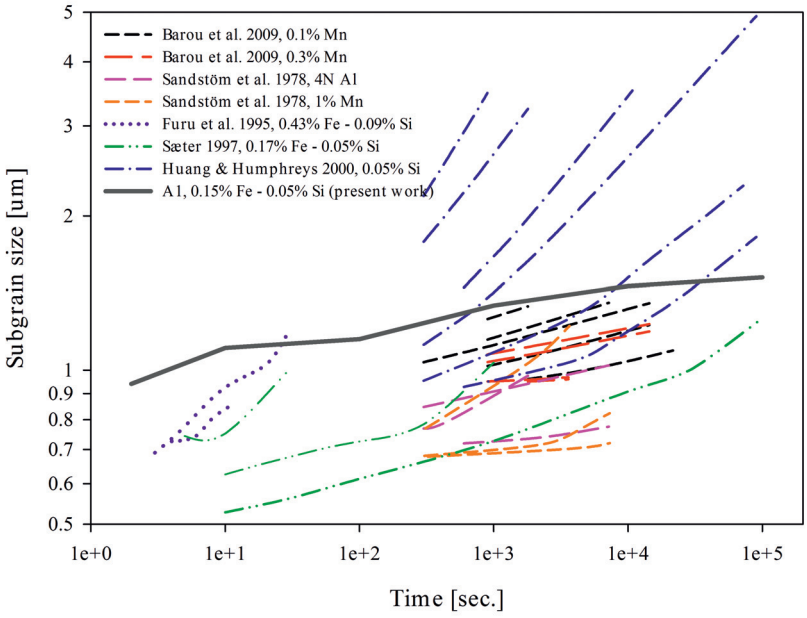

Figure 6.8: Comparison of subgrain growth in A1 (fully-drawn, grey line) during annealing at 250 °C with other relevant subgrain growth data from the literature at various temperatures. The data from Furu et al. [1995] and Sæter [1997] are converted to ECD.

rate in the log-log plot of Figure 6.8 or log-normal plots in Figure 5.32 is detected. Both effects are thermally activated but to what extent is difficult to predict as single solute atoms migrate to dislocations and sub-boundaries where they accumulate and eventually precipitate, thus making accurate experiments difficult to perform. A better understanding of the interplay between solute, precipitates and sub-boundaries would probably require investigations by atom-probe tomography.

In the data presented in Figure 6.8, concurrent precipitation is occurring in the materials investigated by both Furu et al. [1995] and Sæter [1997]. If thermal activation of sub-boundaries away from the precipitates is easier than thermal activation of solute at the respective temperature, similar abrupt changes in the growth curves could be expected, as is observed in the case of Sæter [1997]. In the A1 samples studied here, even flash-annealing for 10 seconds result in some precipitation along the deformation structure and the rapid growth observed by Sæter [1997] at the highest temperature and by Furu et al. [1995] could be, at least partially, explained by precipitation. Of course, thermal activation of solute also becomes easier as the temperature increases and there are no theoretical considerations of any solute effects at high temperatures. This is purely a speculation from the author's side, stemming from observations made at high temperature in this PhD work and is further discussed later on.

Figure 5.34(a) gives a graphical presentation of the subgrain size distribution evolution. After 10^5 seconds of annealing at 250 °C the peak at low values and tail toward larger sizes observed after deformation is mirrored about a vertical axis to give a peak for large values and a tail toward the lower sizes. This change came about through a slightly bimodal transition period at intermediate annealing times. The bimodal distribution indicates that a considerable amount of subgrains experience favourable growth conditions and is not similar to discontinuous subgrain growth. Still, the growth process is clearly not homogenous and continuous and there seems to be a size advantage for large subgrains. However, the large fraction of fast growing subgrains cannot be accounted for by only extraordinarily large subgrains and Gundlach et al. [2004] has shown by 3DXRD that size alone is not implicit with faster growth.

Huang and Humphreys [2000] observed a situation where general, slow and continuous growth in combination with rapid growth of a few remarkably large subgrains was occurring and lead to a bimodal size distribution. The large subgrains were found to be more misoriented than their neighbours, suggesting a misorientation advantage for growth. In Equation 2.12 the relationship between mobility and average boundary misorientation is expressed. The mobility is a function of the misorientations and it is well known that larger mobilities are observed with increasing misorientation [Huang and Humphreys, 2000].

However, when looking at a plot of average boundary misorientation versus subgrain size as in Figure 6.9, a misorientation advantage is only observed to a

limited extent. The graph also include "subgrains" with misorientations larger than 15° because a subgrain with a high-angle boundary on one side is here still considered a subgrain although the average misorientation is significantly larger. A large fraction of the "subgrains" are actually proper grains with only high-angle boundaries also, and the term crystallite is used when referring to both subgrains and grains as one. Whether the crystallites are subgrains or grains is less important in this context as growth is uniformly distributed along the misorientation axis. Statistical influence is of course difficult to interpret in such a plot but does not seem at all significant. Taking into account the number of crystallites with the different misorientations, the number of crystallites larger than 3 μm is independent of the misorientation as Figure 6.10 illustrates. Hence, a large average boundary misorientation is clearly not a requirement for subgrain growth. Only for the smallest misorientations is growth negligible and above ∼3.5° growth seems to be frequent and fast irrespective of misorientation.

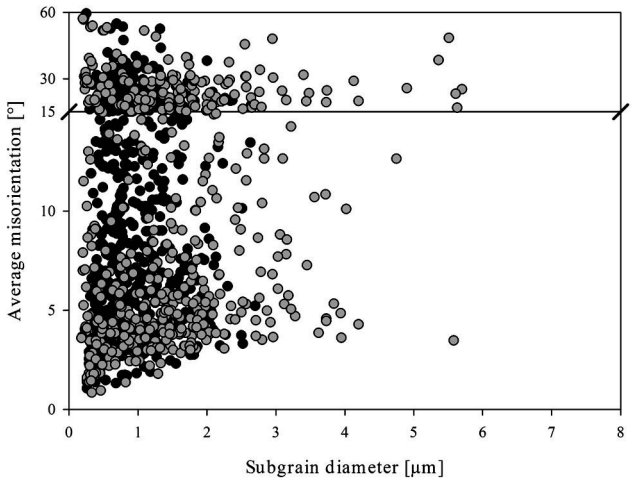

Figure 6.9: Average misorientation of individual subgrains and grains plotted against mean equivalent circle diameter for subgrains in A1 with several orientations after deformation (black circles) and after 10^5 seconds annealing at 250 °C (grey circles).

From this analysis, homogenous growth is occurring for a substantial number of crystallites which is independent of the misorientations when larger than a critical value of ∼3.5°. Below this level, there is still a significant fraction of subgrains that do not appear to grow at all. In addition, there are extremely small subgrains present which have large misorientations, even after annealing. However, the majority of these are probably larger in reality but appear small in the measurements due to sectioning of the sample for 2D analysis.

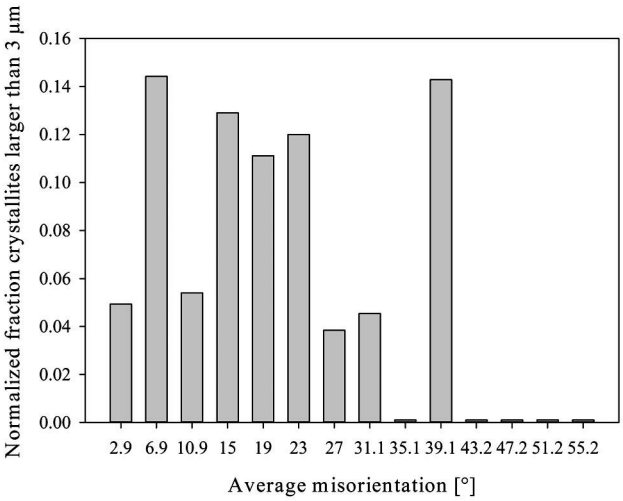

Figure 6.10: Fraction crystallites larger than 3 µm as a function of misorientation after annealing for 10^5 seconds at 250 °C and normalized with respect to the total number of crystallites within each bin.

Orientation Independent Boundary Misorientation Evolution

The orientation independent measurements of subgrains reveal a relatively large average boundary misorientation after deformation. Upon annealing and subgrain growth the misorientations were seemingly decreasing, which is atypical for subgrain growth in the presence of orientation gradients as found here. The size distributions revealed that growth was heterogeneous and orientation gradients, usually strongest near HAGBs, give higher growth rates. Subgrains that have boundaries with average or large misorientations (>3.5°) are coarsening faster than less misoriented subgrains and it is likely that the misorientations are actually increasing. The average misorientation still gives the impression that the misorientations are decreasing, which is interpreted as a result of less growth of subgrains with the smallest misorientations that are typically found in the centre of orientation bands where there are weak orientation gradients and also low boundary misorientations.

In polycrystalline materials, the reported subgrain boundary misorientations for heavily cold rolled aluminium with lean alloy compositions are usually around 4° or slightly larger. This is similar to the 5.5° found for the A1 alloy with mixed orientations here and presented in Table 6.4 together with some relevant average boundary misorientation after cold rolling from literature. Similar to the subgrain sizes, the average misorientations vary some from one author to the other. In Table 6.4, the largest misorientations are those of the

A1 alloy. As already discussed, the reconstructed subgrain maps give a credible representation of the true microstructure and to a great extent eliminate the effect of small pixel-size, artificial subgrains which can be difficult to avoid by other methods. Except for the investigation by Barou et al. [2009] who used a similar approach and a 0.7° threshold as applied in this PhD work, the other non-TEM measurements used a minimum misorientation of 1.5°. TEM has again better angular resolution and compared to TEM, early EBSD measurements also have a tendency to underestimate the boundary misorientation due to noise [Ryen, 2003]. In Table 6.4, however, the TEM results by Sæter [1997] and [Furu et al., 1995] are the smallest ones.

In the orientation independent EBSD scans of A1 in this PhD work, HAGB regions were definitely frequent. The EBSD scans are large and cover an area of ∼500–1000 μm^2. To what extent similarly large scans were made by the other authors is of course not known, although smaller areas are probably investigated, particularly by TEM investigations, and could be biased e.g. by avoiding high-angle grain boundary regions.

Table 6.4: Average misorientation of contiguous subgrains in similar materials after cold rolling measured by EBSD and TEM.

Authors	Alloy	Strain	Misori. [°]
EBSD			
This PhD work	A1	$\varepsilon = 2.6$	5.5
Somerday and Humphreys [2003b]	Al-0.3Mn	$\varepsilon = 2.3$	∼5
Barou et al. [2009]	Al-0.1Mn	$\varepsilon = 1.6$	4.6
Tangen [2004]	AA3103	$\varepsilon = 3.0$	∼4.4
Sjølstad [2003]	AA3103	$\varepsilon = 3.0$	∼4.3
TEM			
Ryen [2003]	AA1050	$\varepsilon = 2.0$	∼4.6
Sæter [1997]	AA1070	$\varepsilon = 2.6$	∼3.3
Furu et al. [1995]	Al-0.29Fe-0.12Si	$\varepsilon = 3.0$	∼3.0

The decreasing average boundary misorientations found for subgrain growth in orientation independent microstructures are illustrated in Figure 5.32(d). Although the decrease was rather weak with relatively large scatter, a clear trend is shown by Figure 6.11(a) when the misorientations are plotted against the average subgrain size. In terms of available literature, most misorientation evolution data is orientation dependent and will be discussed later in this chapter. However, at nearly the same strain and annealing temperature, Furu et al. [1995] observed an increase from 3° to 7°, while Sæter [1997] found an increase from 3.3° to 4.5°. In this PhD work a weak decrease from 5.5° to 5° is observed.

Apparently, the above discussed decreasing misorientations contradicts the literature and theory by Humphreys and Hatherly [2004]. The A1 alloy is highly polycrystalline with an average grain size of 134.1 μm before deformation and

obviously there are both short and long range orientation gradients present after deformation and annealing, as illustrated by Figure 6.11(b). According to Humphreys and Hatherly [2004], the misorientations should increase during annealing and subgrain growth of a sample with orientation gradients, i.e. as reported by Furu et al. [1995] and Sæter [1997]. Only when there are no orientation gradients can the misorientation decrease, which has been shown both by vertex model computer simulations and experimentally in single crystals of Goss orientation [Huang and Humphreys, 2000; Humphreys and Hatherly, 2004].

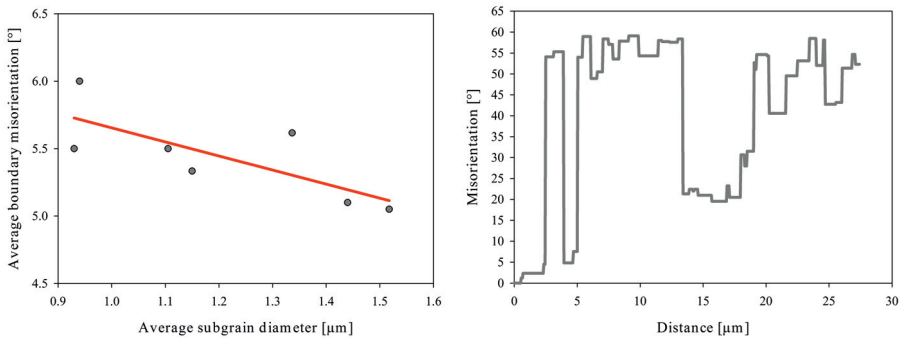

Figure 6.11: (a) Average boundary misorientation versus average subgrain size in A1 when subgrain growth is followed independently of orientation. (b) Misorientation profile for A1 samples after 10^5 seconds of annealing at 250 °C.

However, by a careful consideration of the EBSD scans covering several bands of various orientations and the enhanced recovery in such HAGB regions, the orientation independent misorientation values reported for A1 might be somewhat misleading. From Figure 5.34(b) the decreasing misorientations are seen to be an effect of an increase in the fraction of boundaries in the range 1.5–6°. It has been verified that the decrease in misorientation is not due to accumulation of dislocations for subgrain boundaries with misorientations close to 15° which then after annealing will be classified as HAGBs and not included. Figure 6.9 indicates that for subgrains with the smallest misorientations (<3.5°) there is very little growth. Hence, if there are regions with small subgrains and low misorientations that do not change size noticeably during annealing and more misoriented subgrains which grow faster at a similar rate, the total length of boundaries with misorientations larger than 3.5° decreases. This heterogeneous growth behaviour caused by HAGB regions is explained by two exaggerated, schematic microstructures in Figure 6.12. Several of these regions were included in the EBSD scans on purpose in order to obtain the orienta-

tion independent subgrain growth and misorientation evolution data (which is more true to the overall subgrain growth behaviour). Although the actual microstructural evolution of course appears more subtle, a coarsening close to HAGB regions separating bands of different orientations is evident.

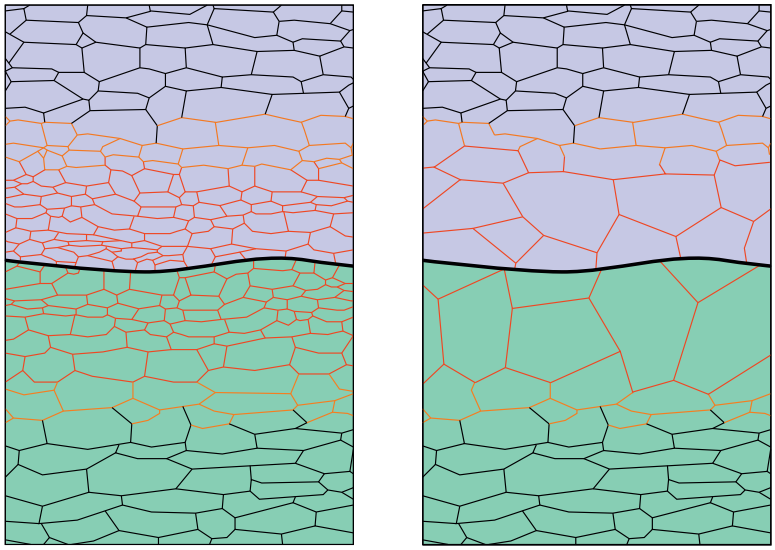

(a) As-deformed. *(b) Annealed.*

Figure 6.12: Schematic illustration of microstructure of HAGB (thick, black line) regions constituted by bands with different orientations (purple and green). The thin sub-boundaries of low misorientation are black and closer to the HAGB they become more misoriented as demonstrated by the transition to red colour. The as-deformed state is illustrated in (a) and subgrain coarsening is more rapid close to the HAGB, leading to a coarser structure here after annealing as shown in (b).

As previously discussed, subgrains near such HAGB regions have a finer subgrain size initially and are more misoriented than subgrains located further away from the boundary, as indicated by the colour of the sub-boundaries in Figure 6.12. During annealing, the small and more misoriented subgrains (red boundaries) grow faster than those located at a distance to the boundary, as the orientation independent and dependent growth curves in Figure 5.32 attest. Thus, what is perceived as a decrease of the mean misorientation of the sub-boundaries is an effect of coarsening of boundaries with misorientation larger than 3.5° (Figure 6.9) reducing the number, and total length, of these boundaries. Figure 6.9 and Figure 5.34(b) show the subgrain and sub-boundary misorientations, respectively, and in Figure 5.34(b) it is seen that particularly the total length of boundaries with misorientation larger than 6° which decreases. It is also mentioned in Section 2.2.1 how it is more likely that coarsening by

subgrain rotation and coalescence will occur near HAGBs, which if operating leads to larger individual boundary misorientations.

In these orientation independent scans, the fraction HAGBs can be anything from 10% to 50% but does not change notably with annealing. After 10 and 10^5 seconds of annealing both high and low HAGB-fractions are observed. Figure 6.13 compares two scans from A1 after 10^5 seconds of annealing with 20% and 50% HAGBs. With many HAGBs present the subgrain size is in fact 50% larger while the average subgrain boundary misorientations are only 10% larger, clearly confirming the significance of HAGB regions in relations to faster recovery kinetics.

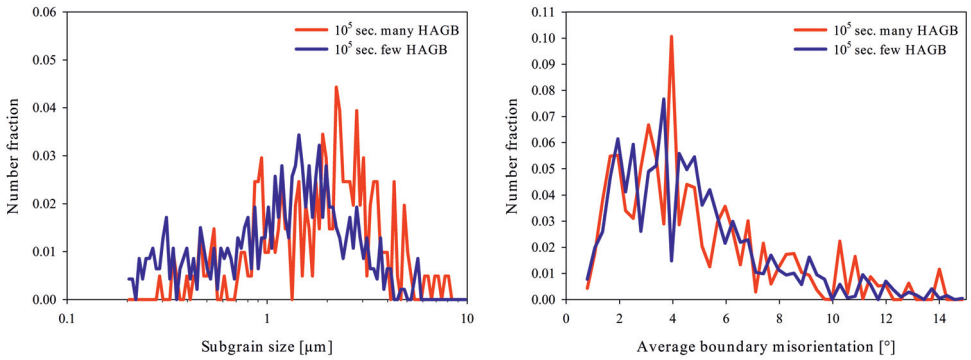

(a) (b)

Figure 6.13: Comparison of size (a) and average boundary misorientation (b) distributions of subgrains with mixed orientations and with different fraction HAGBs in the A1 alloy. For the red curve there are 50% HAGBs while for the blue curve only 20% of the boundaries have HAGB character.

Orientation Dependent Boundary Misorientation Evolution

Moving on to the orientation dependent boundary misorientation evolutions during annealing, a weak alloy dependence of the boundary misorientations was found and possibly related to micro-shear bands. Upon annealing, it is not clear from experimental work in literature how the misorientations should evolve. In this work it is found that the misorientation evolution is orientation dependent, most likely because the size of the orientation gradients created during deformation differs systematically in the various orientations. For subgrains with Cube, Goss and to some extent Cu orientations, the misorientations are increasing. In Brass and S, depending on the size of the orientation gradients, both increasing and decreasing misorientations were observed. Hence, for large

and small orientation gradients, respectively, subgrain growth appears to occur by two different mechanisms. The effect of orientation gradients on boundary misorientations during growth is described in literature but the picture seems to be more complicated. Rather than simply being present, it looks like the orientation gradients need to have a certain size for misorientations to increase. Because the boundary misorientations are responding differently to annealing depending on the orientation gradients, the subgrain growth mechanism also is sensitive to orientation gradients.

The boundary misorientations are alloy dependent for subgrains with deformation texture orientations. In the commercial purity alloy A1 the subgrains are misoriented about 1° more than in the high purity Al4N alloy, despite being deformed only 92.5% and not 95% as the Al4N alloy. In the Al-0.25Mn alloy, the misorientations are not as large as in A1 but slightly larger than in Al4N. The misorientation of subgrains with Cube orientation is not affected by the solute content. Figure 6.14 illustrates the solute and orientation dependence of the misorientations. In the case of Brass oriented subgrains, the data acquired during early stages of annealing in Al-0.25Mn are larger than in Al4N, but the as-deformed data point is clearly an outlier and therefore not a contradiction to the above statements.

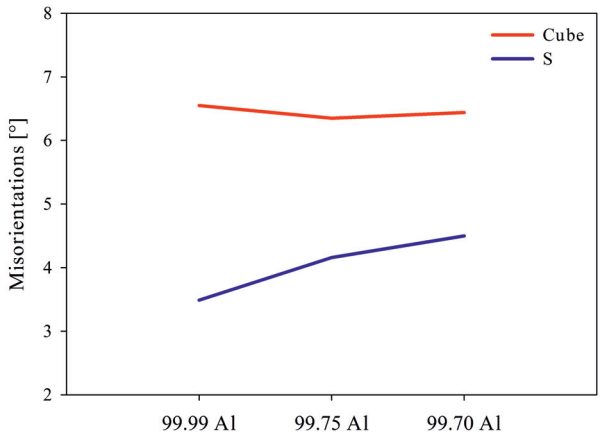

Figure 6.14: Simple graph of alloy or solute dependence of boundary misorientations in Cube and S orientations. From left to right are the Al4N, Al.0.25Mn and A1 alloy, respectively.

Literature data, presented e.g. in Table 6.4, do not give a definite answer to the alloy dependency of boundary misorientations. In aluminium with 0.5, 1.0 and 3.0 wt.% Mg, Ryen [2003] observed rising misorientations with alloy

additions. At $\varepsilon = 2$ only a week increase was found while increasing the strain to $\varepsilon = 3$ resulted in misorientations of about 6° in the high alloy case, an increase from ∼3.7° in the low alloy case. Increasing shear band formation with increasing solute levels of Mg was found by Ryen [2003] and in Chapter 2 it is described how shear bands accumulate a lot of deformation, leading to larger than average boundary misorientations. However, none of the alloys investigates here are prone to shear banding and only micro-shear bands were observed. However, also micro-shear bands accommodate more slip and subgrains in such regions are thus slightly more misoriented from their surroundings, indicating that micro-shear bands are also promoted by increasing alloy content and cause the increase in subgrain misorientation with alloy content after deformation observed in this PhD work.

The boundary misorientations in A1 after deformation were found to increase from Brass, through S and Cu, to Cube oriented subgrains. Table 6.5 lists some orientation dependent misorientation data from other relevant investigations. In addition, Brough and Humphreys [2010a] found subgrains with rolling texture orientations (Cu, S and Brass) to be disoriented by 3.9° and those with Cube orientation to be disoriented 4.8°. These were measured in an Al-0.1Mg alloy after hot deformation and actually stayed constant during the whole annealing process. While most measurements are relatively consistent, there is still some unsystematic scatter which is independent of whether characterization was done using EBSD or TEM. In Table 6.5, the misorientations of the deformation texture components are generally very similar but decreases from Cu to S to Brass. The opposite trend and unusually low misorientations for Cu is found by Humphreys [2004b]. Bardal et al. [1995] on the other hand, found rather low values for Cube which is not found in any other literature. Also atypical are the results by Albou et al. [2011], where high misorientations for both S and Goss were observed. Generally, the largest misorientations are found in Cube, while both large and intermediate misorientations are found for Goss. Unfortunately, sufficient Goss areas were not observed in any of the as-deformed samples in the present work.

As seen from Table 6.5, the orientation dependent misorientations found in this PhD work after deformation are in good agreement with the general picture. In all the three alloys Al4N, Al-0.25Mn and A1, subgrains with Brass orientations have the least amount of misorientation, closely followed by S and the Cu. Cube subgrains are significantly more disoriented. How the misorientations vary between differently oriented subgrain structures will be further discussed in terms of the observed subgrain growth rates in the different texture components.

For the orientation dependent misorientation evolution in A1, there is some scatter but the trend seems to be a weak increase in all the deformation texture components Brass, Cu and S. Recovery of Cube oriented regions in A1

Table 6.5: Average misorientation of contiguous subgrains within different texture components in similar materials.
**The results from Godfrey et al. [2001] (low strain, ε=1.5) and Albou et al. [2011] are average pixel–by–pixel misorientations from EBSD scans.*
***Reproduced values from Xing et al. [2006] is the mean from GNBs and IDBs balanced by the aspect ratio which is 3.*

	Alloy	Misorientation [°]				
		Cu	**S**	**Brass**	**Cube**	**Goss**
Cold deformed						
This PhD work	Al4N	4.06	3.49	3.24	6.55	-
This PhD work	Al-0.25Mn	-	4.16	-	6.35	-
This PhD work	A1	4.60	4.50	3.98	6.44	-
Hurley and Humphreys [2003]	Al-0.1Mg	2.80	2.55	2.25	-	2.45
Godfrey et al. [2001]*	Al4N	3.3	∼3	1.6	-	-
Albou et al. [2011]*	Al-0.1Mn	-	7.8	3.7	-	8.5
Xing et al. [2006]**	AA1200	3.6	3.1	-	5.0	-
Hot deformed						
Humphreys [2004b]	AA5182	1.93	4.19	4.55	6.63	2.59
Bardal et al. [1995]	AA3004	4.8	4.4	3.9	4.0	4.1

is generally very fast and nucleation of recrystallization occurs after short annealing times, which is most likely why the results for Cube oriented subgrains show decreasing misorientations because only special regions experiencing very slow recovery are investigated. Thus, these Cube regions are a compromise to show how Cube oriented subgrains are different form subgrains with other orientations without actually giving a good description of Cube regions in general. However, in both Al4N and Al-0.25Mn, more representative data for Cube oriented subgrains were collected and the average boundary misorientations were increasing somewhat.

From the ODFs of Al4N, Al-0.25Mn and A1 after annealing at temperatures similar to the subgrain growth experiments, Figure 5.21(a), Figure 5.25(a) and Figure 5.46, respectively, the Cube texture component becomes more prominent than was the case in as-deformed state of the respective alloys (Figure 4.2(a), Figure 4.2(b) and Figure 4.7). Thus, the highly misoriented Cube-subgrains provide recrystallization nuclei which consume regions with other orientations during recrystallization; i.e. growth is occurring in a constant and steep orientation gradient. In Figure 5.12(b) and, particularly, Figure 5.12(d), where the misorientation distributions for growth of Cube oriented subgrains in Al4N are plotted, the reason for increasing misorientations is clearly a rapid boundary sharpening or decrease of those boundaries with misorientations smaller than ∼3°. This is perfectly in accordance with the theory presented in Section 2.2.1 which states that growth in an orientation gradient results in increasing misorientations and is driven by a reduction of the total stored energy.

Scatter makes characterization of the misorientation evolutions challenging, which to some extent must be limited to analysing trends. However, the variations in misorientations are mostly less than 2° and often closer to 1°. Cu, S and Goss oriented subgrains in Al4N and Al-0.25Mn have the most variation. The misorientations of subgrains with Cu orientation sometimes increases marginally by a reduction of the boundaries with the absolutely smallest misorientations, as e.g. Figure 5.33(b) illustrates. Similarly, subgrains with Cu orientation becomes slightly more disoriented in Al4N at 180 °C and 200 °C. Then, at 220 °C the misorientations are decreasing slightly. The change is subtle and probably caused by fluctuations resulting from the heterogeneous microstructure after deformation. The misorientation distributions reveal similar characteristics as for increasing misorientations in Cu, i.e. some of the boundaries with the smallest misorientations diminish as seen in Figure 5.13(d). Because the increase is very weak and the misorientation distributions look otherwise very similar, the change from increasing to decreasing misorientations does not suggest a change in the growth mechanism.

A special case is found for S oriented subgrains. In A1 and at all temperatures in Al4N the trend is that subgrains with S orientation, and similar to Cu, become marginally more disoriented during annealing. Not so in Al-0.25Mn, where the consequence of coarsening during annealing is a consistent decrease of the average boundary misorientations. When comparing the misorientation distribution evolutions, particularly for misorientations less than 3°, in Figure 5.17(b) to e.g. S or Cu in Al4N and A1, the contrasting behaviour for very low-angle boundaries is distinct. In Al4N at 180 °C, S-subgrains behave like Cu-subgrains and the fraction boundaries with the lowest misorientations is reduced while no significant change is occurring for more misoriented boundaries. In Al-0.25Mn, a higher fraction of boundaries with misorientation less than 3° is seen and reaches a maximum value at the detection limit of 0.7°, suggesting a different growth mechanism than when the misorientations are increasing.

In both Al-0.25Mn and Al4N the subgrains with Brass orientation respond to annealing in exactly the same way as S-subgrains in Al-0.25Mn. Except for at 240 °C in Al4N where the misorientations are consistently decreasing with subgrain coarsening. The misorientations in Figure 5.14(b) also show a markedly higher fraction of boundaries with misorientations lower than 3° after annealing. Brass has initially less misoriented subgrains which are also larger on average than subgrains with any other orientations. Although subgrain growth is slightly faster than in S or Cu, recrystallization nuclei are struggling to nucleate in bands with Brass orientation. Brass is e.g. found to remain in recovered state while the majority of the sample is recrystallized and this behaviour is attributed to the low number of slip systems active during deformation, resulting in a low stored energy and discussed in more detail later.

Slow recrystallization of Brass is well-known and described in the literature by e.g. Rajmohan and Szpunar [1999] and Alvi et al. [2008]. Interestingly, at 240 °C the recovery or growth mechanism of Brass is different and associated with increasing misorientations, similar to the evolution of the misorientations as observed for Brass in A1 and S in Al4N and A1. It appears as if growth of subgrains with both Brass and S orientations is occurring by two different mechanisms.

According to Humphreys and Hatherly [2004], what decides the misorientation evolution is the presence of local orientation gradients as already discussed. Though, in similar Goss oriented single crystals having allegedly no orientation gradients Humphreys & co-workers have made contradicting findings. Decreasing misorientations were seen by Huang and Humphreys [2000] from 3.7° to 2.9°. However, in an earlier paper on the same single crystal material, at only a slightly larger strain (75% vs. 70% plane strain compression in a channel die), Ferry and Humphreys [1996] actually found increasing misorientations from 2.3° after deformation to 3.5° after annealing for 235 hours at 300 °C. It is clearly stated in Huang and Humphreys [2000] how the two materials displayed similar annealing response since neither had any orientation gradients, though the contrasting behaviour of the mean boundary misorientations is not mentioned. Still, by plotting some randomly selected orientation profiles from S and Brass, as in Figure 6.15, the theory of Humphreys and Hatherly [2004] seems to hold. Where increasing misorientations are found (S in Al4N & Brass at 240 °C in Al4N) the gradients are larger than when the misorientations are decreasing (S in Al-0.25Mn & Brass at 220 °C in Al4N). A rough estimate from Figure 6.15 of the critical orientation gradient indicates a value of $\sim 0.5^\circ/\mu m$.

For Brass oriented subgrains the transition from decreasing to increasing misorientations could also possibly be temperature dependent. At a temperature where recrystallization occurs immediately, Brass does not recrystallize and it is possible to detect increasing misorientations with subgrain growth. At 275 °C in Al-0.25Mn, recovery is slower than at 220 °C but faster than at 180 °C in Al4N. 275 °C is the temperature at which subgrains with S orientation are portraying decreasing misorientations, which based on the observations made in Al4N should possibly have occurred at a higher temperature where recrystallization takes place earlier. The misorientation increase in Brass at 240 °C and decrease in S at 275 °C is very consistent, although it is hard to rule out the effect of sampling. Without in-situ experiments it cannot be ruled out that the change from increasing to decreasing misorientation, although consistent, is caused by sampling areas with very different deformation history, but it is unlikely. As Figure 6.15(b) illustrates, there are significant orientation gradients in the Brass regions annealed at 240 °C, also at shorter annealing times. A plausible temperature dependence must be ruled out in favour of an explanation by orientation gradients. The heterogeneous deformation history within

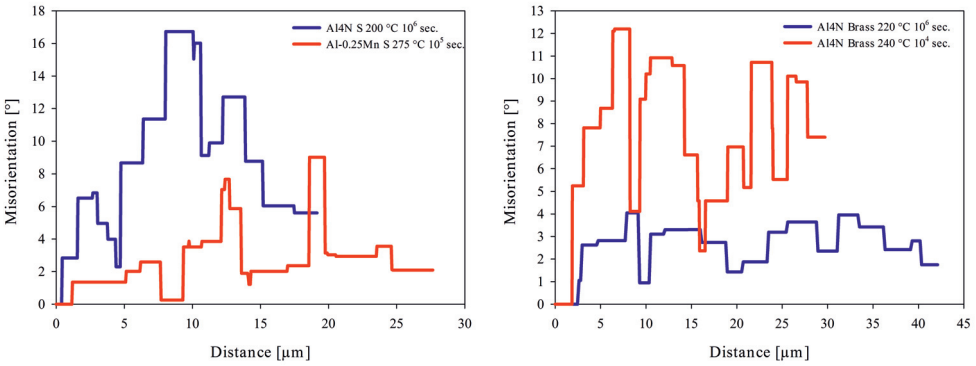

(a) S. *(b) Brass.*

Figure 6.15: Characteristic orientation profiles in subgrain structures with S and Brass orientations resulting in different evolution of subgrain misorientations during coarsening.

the samples leads to Brass regions also with significant orientation gradients and S regions with low orientation gradients.

In literature there is little research on the effect of annealing on the disorientation of contiguous subgrains with specific orientations. In addition to Humphreys & co-workers who, as already described, have mainly studied the Goss orientations, Albou et al. [2011] have investigated channel die compressed single crystals of Brass, Goss and S orientations in an alloy containing 0.1% Mn. They did not measure the mean misorientation between contiguous subgrains but the misorientation between random pixel pairs. In Brass, extremely low orientation gradients were observed and the non-correlated disorientations remained nearly unchanged after 10 minutes of annealing at 320 °C. On the other hand, in both Goss and S there were large orientation gradients ($>0.5^\circ/\mu m$), but both smaller and larger misorientations resulted after annealing. In Goss the change was from 8.5° to 6.8° and in S from 7.8° to 8.2°. In channel die compressed pure aluminium, Godfrey et al. [2001] noticed decreasing misorientations in S, a weak decrease also in Cu but an increase in Brass. Larger misorientations in Brass after annealing was also found by Benum [1995], who also found subgrains with Cube, S, Goss and random orientations to also become more disoriented. Cu-subgrains were the only ones which got less misoriented. Thus, literature does not give a consistent description of the evolution of misorientations with annealing in the various texture components. A correlation between the size of orientation gradients and the misorientation evolution (increase/decrease) is also absent.

Nevertheless, the experimental evidence of this PhD work shows that the

theory for misorientation evolution in deformed polycrystalline material, which always will have orientation gradients and ergo increasing misorientations during annealing, is inadequate as both decreasing and increasing misorientations are found here. It seems that not only the presence of but also the size of the orientation gradients is important for the preferred recovery and subgrains growth mechanism. Recovery and subgrain growth is indeed complex and a major challenge is to get good enough statistics in order to describe the different growth behaviours well.

The evolution of the misorientation distributions as a result of annealing reveal that subgrain coarsening is occurring by at least two different mechanisms in this PhD work. Based on the orientation dependent investigations of A1, subgrains of all orientations experience increasing misorientations with annealing, suggesting that the orientation independent decrease was in fact due to a decrease of the total length of sub-boundaries with large misorientations. The individual boundary misorientations are, for the most part and in all likelihood, increasing. Similar misorientation distributions to the orientation independent ones were not seen in any of the subgrain structures of uniform orientation. Boundaries with misorientations larger than 4° changed little and differences were mainly confined to less misoriented boundaries. These could become dominating if the orientation gradient was lower than $\sim 0.5^{\circ}/\mu m$, leading to decreasing misorientations with annealing. For larger gradients, some sharpening of the absolutely least misoriented boundaries and growth of more misoriented subgrains at the expense of less misoriented ones. At the same time the boundaries are probably becoming more misoriented, contributing to the observed increasing boundary misorientations.

Orientation Dependent Subgrain Growth

No particular alloy dependency of subgrain growth was revealed. Recovery by subgrain growth is however highly orientation dependent. There is a positive correlation between the stored energy and recovery kinetics and orientation gradients, respectively. However, an even stronger correlation is found between the orientation gradients and the recovery kinetics. For those orientations where there are large orientation gradients after deformation, subgrain growth is also fast. This is the case for Cube and Goss oriented structures, where high-angle boundaries are more mobile and the subgrains become more misoriented upon growth. For subgrains with Cu, S and Brass orientations, the coarsening kinetics are nearly independent of the size of the orientation gradients and also the fraction of HAGBs. Instead there is a change in the growth mechanism when the orientation gradients are about $0.5^{\circ}/\mu m$, as discussed in the previous section. Above this critical value growth is homogenous and the misorientations are increasing during annealing. Below this value, subgrain growth results in a temporal period where the size distribution is bimodal, possibly due to a size

advantage and the misorientations are decreasing.

Because the measurements in this PhD work are not done in-situ but on different samples annealed for various times, care must be taken when analysing the growth results. As already mentioned, elongated bands of similar orientation in a polycrystalline material may have a very different deformation history. When e.g. most of the sample is recrystallized and only a few deformed bands remain, these do not necessarily represent the typical growth behaviour of bands with similar orientations present in a different sample annealed for shorter times. This is the primary cause for the scatter observed with annealing time of the subgrain sizes and average boundary misorientations.

Judging by the three alloys studied here, orientation dependent subgrain growth does not seem to be particularly affected by the different solute elements or levels. Similar growth behaviour was observed in both high and commercial purity alloys. Not even concurrent precipitation and the significant decrease of the solute level in A1 seem to influence subgrain growth notably. On the other hand, it should be emphasized that although Al4N is high purity, there is iron in solution after deformation. A few ppm dissolved iron in high purity aluminium alloys has been shown to slow down recovery kinetics drastically [Marshall and Ricks, 1993; Masing et al., 1956]. The iron atoms are redistributed during annealing to dislocations and sub-boundaries, resulting in a strong solute drag force [Bond et al., 1966; Vandermeer, 1967; Wyon and Marchin, 1955]. It was attempted to investigate the effect of different solute concentrations of iron on the texture in Al4N but the results were not reproducible. In Al-0.25Mn, no precipitation was detected and Mn is assumed to be completely dissolved. In A1, on the other hand, interannealing experiments have shown that even after concurrent precipitation during the first annealing step, there is still solute present in the fully soft condition. Thus, all samples are affected by solute drag to some extent, although this aspect was not studied any further. Still, drastically different solute levels have no apparent effect on the subgrain growth mechanism, although the kinetics and the whole softening process, including recrystallization and texture as discussed later, are affected by solute.

Subgrains with Cube orientation, and to some extent Goss orientation, exhibit quite unique growth behaviour. Cube oriented subgrains were always found to be rather disoriented and equiaxed after deformation and half of the boundaries would normally be of high-angle character, resulting in large average boundary misorientations and orientation gradients as Figure 6.16 illustrates for the Al4N alloy. Interestingly, the rate of subgrain growth follows the degree of orientation gradients found in the differently oriented bands. Although not very apparent in the early stages, growth of Cube and Goss oriented subgrains is faster than for subgrains with deformation texture orientations. A transition to rapid growth was only observed for Cube and Goss oriented subgrains and

occurred earlier in Cube than Goss. Looking at Figure 6.16, the order in which the orientation gradients are decreasing is from Cu to S to Brass but does not match the growth rates perfectly. The growth rate of subgrains with Brass orientation is slightly faster than for subgrains with Cu and S orientation when the misorientations are decreasing, despite weaker orientation gradients. Goss show distinctly larger orientation gradients while in Cube the largest orientation gradients are found, in good agreement with the particularly rapid growth kinetics and also the early onset of this. After annealing, the orientation gradients are seen to increase in Goss, Cu and S while in Brass they remain on a somewhat similar level — as also the evolution of the boundary misorientations indicate. Thus, the orientation gradients and the growth kinetics are strongly correlated, as well as the evolution of the misorientations with annealing.

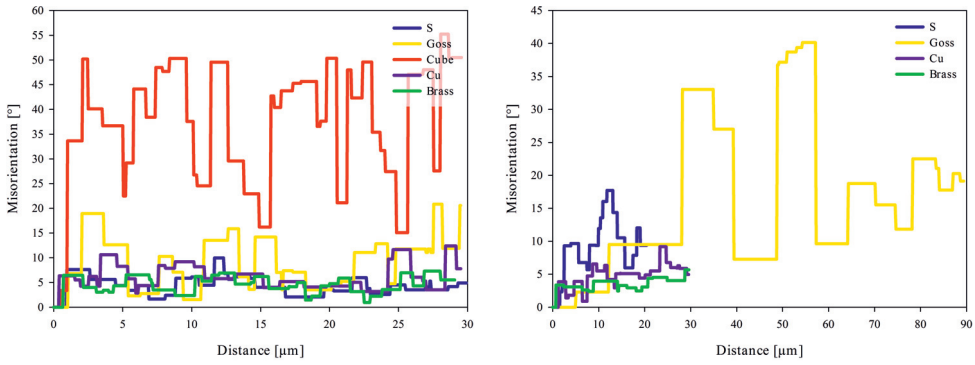

(a) As-deformed.

(b) Annealed at an elevated temperature for more than 24h.

Figure 6.16: Misorientation gradients of various texture components from Al4N parallel to ND in the investigated RD-ND sections in as-deformed and annealed state.

There are two important factors referred to in literature that are believed to control the rate of subgrain coarsening; one is the stored energy and the other is the boundary mobility. According to Equation 2.12, the boundary mobility is a function of the boundary misorientation and increases with increasing misorientation. Bardal et al. [1995] did a detailed TEM study of subgrain sizes, misorientations, dislocation densities and stored energies in an AA3004 containing 1% Mg and 1% Mn which was deformed 86.4% ($\varepsilon = 2$) in plane strain compression at 350 °C. The results for different texture components and the average values are presented in Table 6.6. Since these results were obtained in a hot worked material, some dynamic recovery has already occurred and the subgrain sizes are also larger than in as-deformed cold rolled state, which could be why the results also differ both quantitatively and qualitatively from

the observation made in this thesis. However, these results represent a very complete set of data for differently oriented subgrains. Bardal et al. [1995] observed rapid growth and recrystallization of Cube subgrains. Cube bands are frequently found next to bands of S orientation, ensuring that growth of low energy Cube grains into high energy S oriented regions is favourable due to the $40°\langle 111\rangle$ orientation relationship.

The reason for the low stored energy in Cube observed by Bardal et al. [1995] is mainly due to a larger average subgrain size after deformation. Similar behaviour is reported by Brough and Humphreys [2010a] in hot deformed Al-0.1Mg where Cube subgrains were significantly larger than those with Cu, S or Brass orientations and Cube subgrains also grew faster. After recrystallization, Cube was the dominating texture component. That subgrains with Cube orientation were initially larger than subgrains with deformation texture orientations was interpreted as a growth advantage of Cube oriented subgrains. Cube-subgrains are thus potent recrystallization nuclei that can grow at the expense of particularly S oriented regions as confirmed by Humphreys [2004b] and Alvi et al. [2008]. That Cube regions have the least amount of stored energy and S regions have the largest was also observed by Vatne [1995].

Table 6.6: Orientation dependent subgrain size (ECD), misorientation, dislocation density and calculated stored energy from Bardal et al. [1995] measured by TEM in hot worked AA3004.

	$\boldsymbol{\delta}$ [µm]	$\boldsymbol{\omega}$ [°]	$\boldsymbol{\rho}$ [$\mathbf{10^{13}}$ $\mathbf{m/m^3}$]	**E** [$\mathbf{10^5}$ $\mathbf{J/m^3}$]
Cube	1.07	4.0	3.6	4.50±0.30
Cu	0.98	4.8	3.6	5.34±0.27
Bs	0.86	3.9	3.3	5.39±0.30
Goss	0.83	4.1	-	-
S	0.79	4.4	2.7	5.76±0.32
Average	0.90	4.3	3.2	5.25

The picture is different in cold deformed materials. The driving pressures for recovery and subgrain growth observed in this PhD work are given in Table 6.7, together with some results from literature. According to Equation 2.10, a good estimate for the driving force is obtained through the misorientations and subgrain sizes. By dividing Equation 2.10 with the total boundary area per unit volume and assuming that the sub-boundary energy γ_{SB} follows the Read-Schockley relation, thus being independent of subgrain size r, a driving pressure is obtained which is proportional to the sub-boundary energy and inversely proportional to the subgrain size $P_D = \gamma_{SB}/r$. Hence, the driving pressure for the three alloys investigated here can be calculated and are presented in Table 6.7.

A few investigations of stored energy in cold deformed materials and various texture components are reported in literature. Godfrey et al. [2001] studied

single crystal 4N aluminium deformed 78% in a channel die. Rajmohan and Szpunar [1999] investigated an AA3104 alloy cold rolled to 88% reduction while Takata et al. [2007] investigated a 99.9% pure alloy experiencing industrial thermomechanical processing finished off by a cold rolling step. Their results from these investigations are summarized in Table 6.7. The results by Godfrey et al. [2001] and Rajmohan and Szpunar [1999] correlate reasonably well with this PhD work. That is, more rapid recovery of Cube regions, as well as Goss regions, than in any of the regions with deformation texture orientations (Cu, S, Brass). The driving pressures in Table 6.7 partially explain this behaviour. In Al4N at 240 °C Brass was the only orientation in which subgrain growth was possible to characterize since most other regions were recrystallized — indicating very low stored energy, something which the low driving pressure in Brass indeed confirms. However, the rate of recovery and the stored energy are not perfectly correlated. The growth rates in Cu and S is e.g. similarly slow as in Brass but cannot be explained only by the driving pressure which are very different, suggesting that growth of subgrains with Brass orientation occurs by a different mechanism than Cu/S. The high driving pressure for recovery in Cube after cold deformation also explain the lager subgrain size and low stored energy for Cube oriented regions in hot deformed materials, like those of Table 6.6, since they are experiencing dynamic recovery.

Table 6.7: Stored energy after cold deformation of various orientations in aluminium alloys, both from literature and from the three alloys investigated here using Equation 2.10. The value for Brass in Al-0.25Mn was obtained using data from the sample annealed for 10 seconds.

	Stored energy				
	Cu	**S**	**Brass**	**Cube**	**Goss**
This PhD work, Al4N [$\times 10^5$ J/m^3]	2.5	2.3	1.6	2.7	-
This PhD work, Al-0.25Mn [$\times 10^5$ J/m^3]	-	1.8	1.3	3.1	-
This PhD work, A1 [$\times 10^5$ J/m^3]	1.9	2.0	1.4	2.1	-
Godfrey et al. [2001] [$\times 10^5$ J/m^3]	5.2	5.2	3.4	-	-
Takata et al. [2007] [$\times 10^5$ J/m^3]	1.7	1.5	1.6	0.8	-
Rajmohan and Szpunar [1999] [J/mol]	8.2	4.7	3.2	13.6	1.9

The driving pressure is greatly influenced by the initial subgrain size after deformation and Table 6.8 compares data found in this PhD work with subgrain sizes found in similar materials from literature. First of all, the data compare very well to each other. Unfortunately, there is no data on Cube oriented subgrains. Sukhopar et al. [2012] did investigate subgrain sizes after 2 seconds of annealing at 280 °C in an AA8079L alloy after 70% cold rolling but found only small variations between Cube, S, Cu and Brass, which were all around 0.8 µm. In this PhD work, growth of Cube and Goss oriented subgrains has many similarities. From Table 6.5, both Cube and Goss are found to have large

misorientations and in Table 6.8 both Cube and Goss oriented subgrains are among the smallest ones, illustrating that a higher stored energy after deformation is important for the rapid recovery observed for subgrains with these two orientations.

Table 6.8: Orientation dependent subgrain sizes after cold deformation as found in this PhD work and selected literature on comparable aluminium alloys at large strains.

	Alloy	Subgrain size [μm]				
		Cu	**S**	**Brass**	**Cube**	**Goss**
This PhD work	Al4N	0.80	0.80	1.09	0.96	-
This PhD work	Al-0.25Mn	-	1.16	1.33	0.82	-
This PhD work	A1	1.14	1.07	1.41	1.22	-
Barou et al. [2009]	Al-0.1Mn	0.97	0.96	-	-	1.02
Barou et al. [2009]	Al-0.3Mn	0.94	0.99	-	-	0.90
Hurley and Humphreys [2003]	Al-0.1Mg	0.75	0.75	0.70	-	0.67

The recovery rates of Cube, and to some extent Goss, oriented subgrain structures found in this PhD work are indeed rapid compared to differently oriented subgrains, as seen from Figure 5.5(a), Figure 5.5(c), Figure 5.5(e), Figure 5.15(a) and Figure 5.32(a). There is also evidence for this in literature. Sukhopar et al. [2012] found more rapid coarsening of subgrains with Cube orientation than those with Cu, S and Brass orientations, which all three had similar kinetics. Also Barou et al. [2009] found slow subgrain growth in the deformation texture components S and Cu, while in Goss growth was significantly faster. Albou et al. [2011] saw much faster subgrain coarsening in Goss oriented single crystals after channel die deformation, as compared to e.g. in Brass oriented single crystals. However, the fraction residual hardness decreased almost as fast in S as it did in Goss. To begin with, recovery was related to dislocation annihilation, possibly in combination with annihilation of dislocation walls with dipole character, and thus not particularly influenced by orientation. Because the initial driving force was considered to be similar in the three cases, the different recovery rates were attributed to the local orientation gradients and their influence on dislocation or dislocation boundary mobilities.

The observations made by Albou et al. [2011] are in good agreement with what happens here in the Al4N, Al-0.25Mn and A1 alloys during recovery annealing. An effect of the orientation gradients is expected but to be more prominent in the later stages of subgrain growth, which in the case of Goss should result in an even faster recovery rate [Albou et al., 2013]. The presence of steep but short-range orientation gradients in Cube and Goss regions studied in this PhD work has a strong influence on the recovery kinetics and seems to determine the incubation time for rapid subgrain growth to occur (continuous recrystallization). Sukhopar et al. [2012] confirms the existence of an incubation time for nucleation of recrystallization in Cube, one that is much shorter

than in Cu, S or Brass. In this PhD work, subgrain growth rates during the incubation time, approximately the first ∼100 seconds of annealing, are less influenced by lattice orientation than the incubation time itself, which is in good agreement with Sukhopar et al. [2012].

While discussing the evolution of the boundary misorientations, the degree of orientation gradients in the microstructure after deformation was found to be of great importance, dictating whether the misorientations would increase or decrease during annealing. The stored energy and, hence, the subgrain growth kinetics are also closely related to the degree of orientation gradients in the various texture components as illustrated in Figure 6.16. The unique deformation history of similarly oriented subgrain microstructures greatly influences the orientation gradients and alters the recovery kinetics and sometimes the mechanism. A comparison e.g. between two scans of Cube orientations after 10^5 seconds annealing at 220 °C is made in Figure 6.17 and the average grain size is very different in the two scans. Even better examples are found in other orientations where the growth mechanism also changes and will be discussed later.

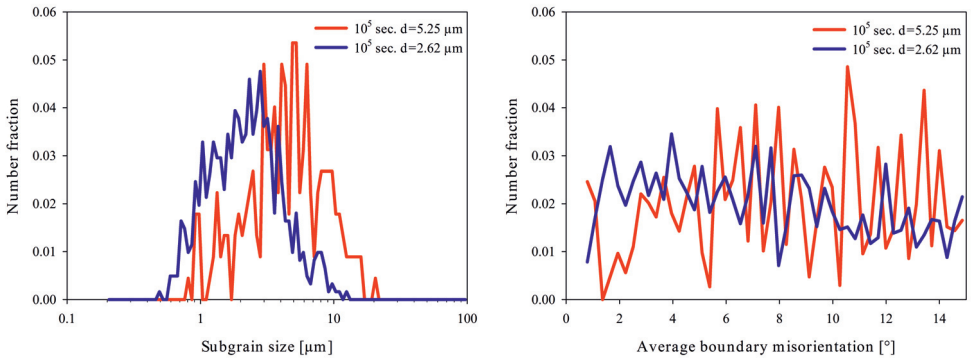

(a) Size distribution. *(b) Misorientation distribution.*

Figure 6.17: Comparison of size and average boundary misorientation distributions for Cube oriented subgrains after annealing at 200 °C for 10^5 seconds with average subgrain sizes of d=2.62 µm and d=5.25 µm.

Coarsening of Cube oriented subgrains occurs in two steps. Growth is initially slow but becomes much faster after an incubation time in which a bimodal size distribution develops as seen in Figure 5.12. This could be the result of a size advantage, i.e. that fast recovery leads to some large Cube-subgrains with an overcritical size which grow faster than smaller ones. However, Figure 6.18 also shows how a clear correlation between misorientation and growth is present in Cube regions. There are some similarities with discontinuous subgrain growth

as described by Huang and Humphreys [2000] although the requirement for a lack of orientation gradients is hardly fulfilled. However, in a similar way to discontinuous growth, it appears as if initially more misoriented crystallites only need minor alterations during the incubation time to become disoriented by more than 15° and thereby grow faster than less misoriented subgrains. Hence, there is an obvious misorientation advantage related to growth, just as Huang et al. [2000] found for growth in an orientation gradient with increasing misorientations in similar material. From the as-deformed state illustrated in Figure 5.11(a), the largest subgrains are also highly misoriented and Cube-subgrain growth is thus a result of selective growth caused by a combination of large size and large misorientation. Looking more closely at Figure 6.17(b) and Figure 6.18, the true subgrains, i.e. those subgrains with misorientations smaller than 15°, are more misoriented in the "large subgrain size"-case, an indication of larger orientation gradients, and these subgrains have also grown more than the true subgrains in the "small subgrain size"-case.

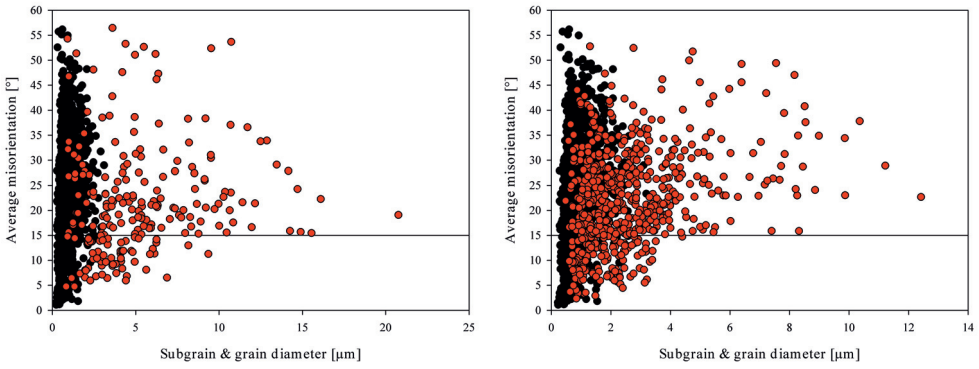

(a) d=5.25 µm *(b) d=2.62 µm*

Figure 6.18: Average misorientation of individual grains plotted against mean equivalent circle diameter for Cube (red) oriented subgrains and grains after 10^5 seconds annealing at 220 °C. Black dots are superimposed from Figure 5.11(a) for comparison with the as-deformed state.

Turning attention to the deformation texture components Cu, S and Brass, growth is generally weak and less than a factor 2. The first case discussed here is the most frequently observed, i.e growth in a large orientation gradient accompanied by increasing misorientations. As shown in Figure 6.19, the majority of subgrains with deformation texture orientations are less than 2 µm in diameter with misorientations smaller than 8°. Compared to the as-deformed state illustrated in Figure 5.11(b), the most obvious difference after annealing is particularly a shift to larger subgrain sizes for subgrains with misorientations

between 2–10°. As opposed to the orientation independent growth and growth of Cube-oriented subgrains, HAGBs do not enhance growth significantly for subgrains with Cu, S or Brass orientations. Growth is very homogenous and there is no sign of a bimodal size distribution for Cu or S (for Brass oriented subgrains, when the misorientations were decreasing with growth, growth was very much bimodal during a transition period which will be discussed later). The largest subgrains after annealing are those close to the mean average boundary misorientation and neither a size nor a misorientation advantage is apparent.

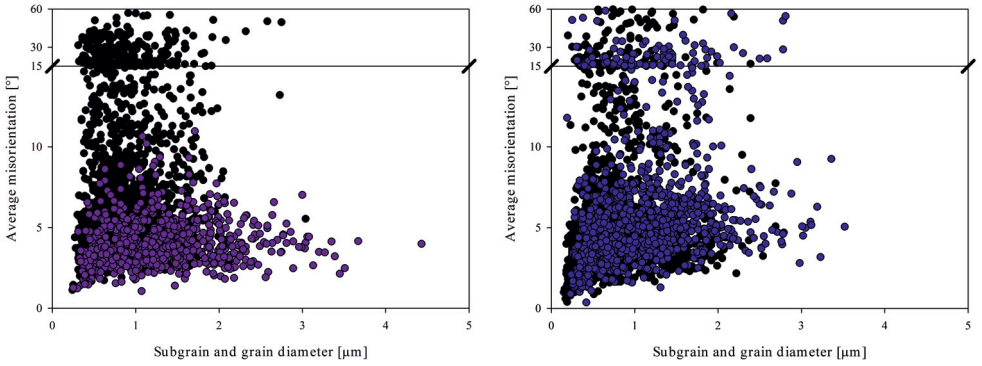

(a) Cu. *(b) S.*

Figure 6.19: Average misorientation of individual grains plotted against mean equivalent circle diameter for S (blue) and Cu (purple) oriented subgrains and grain after 10^6 seconds annealing at 180 °C and 10^5 seconds annealing at 200 °C, respectively. Black dots are superimposed for comparison with the as-deformed state.

That HAGBs have little impact on the growth kinetics is obvious in Figure 6.20. Two different regions with completely different fraction HAGBs, one has five times as many as the other, are compared with respect to both size and misorientation distribution after annealing. Both show near identical distributions after 10^5 seconds annealing at 250 °C. The subgrain size is only 16% larger in the high fraction HAGB case. Despite the large difference in HAGB fraction, Figure 6.21 shows that there is clearly no misorientation advantage during growth and, interestingly, the misorientation gradients in the two cases are similar. Because subgrain growth is complex the orientation gradients alone will not suffice to explain why similar growth kinetics are observed irrespective of the HAGB fraction, but it is yet another indication that they play a major role for the recovery mechanisms.

It is possible that growth of subgrains with Brass orientation is marginally faster when the orientation gradients are very low and the misorientations are

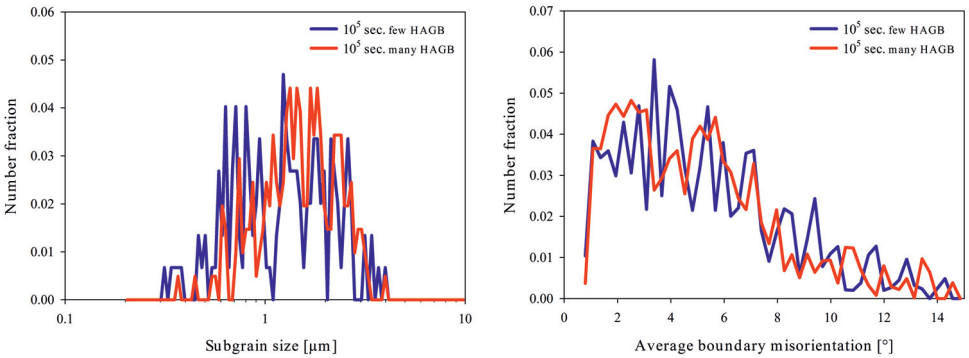

Figure 6.20: Comparison of size (a) and average boundary misorientation (b) distributions of subgrains with Cu orientation in A1 after annealing for 10^5 seconds at 250 °C. The average subgrain size of one is 16% larger and has 5 times as many high-angle grain boundaries.

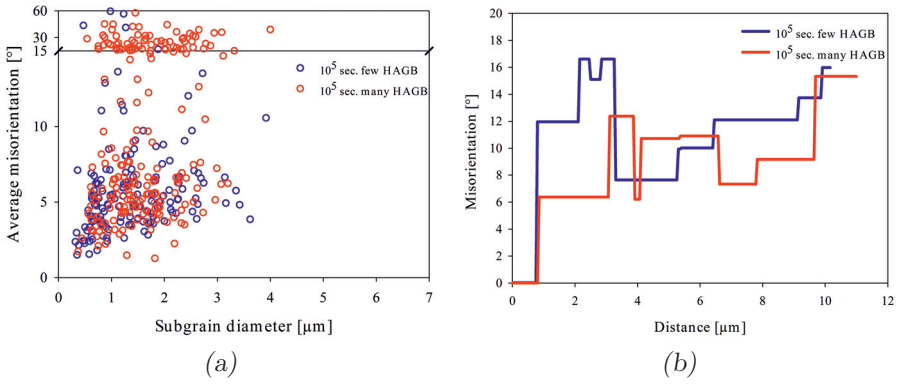

Figure 6.21: Size versus misorientation plot (a) and orientation gradients (b) parallel with ND in ND-RD sections from A1 samples with Cu-oriented subgrains annealed for 10^5 at 250 °C where the average subgrain size of one is only 16% larger but has 5 times as many high-angle grain boundaries.

decreasing. Still, the growth kinetics during early stages of subgrain growth are mostly unaffected by the orientation gradients which mainly influence the growth mechanism and whether the misorientations are increasing or decreasing. Brass and S oriented bands exhibiting growth by both increasing and decreasing misorientations depending on the size of the orientation gradient. When the gradients are larger and smaller than $0.5^\circ/\mu m$ the misorientations are increasing and decreasing, respectively. In the respective microstructures, the degree of coarsening and the size distribution after long annealing times are closely related — even if the misorientation distributions are very different as shown in Figure 6.22. That the mechanism for growth is different in the two cases is evident also when looking at Figure 6.23. Whereas in the sample annealed at 240 °C a definite misorientation and size advantage is missing and growth is, as previously discussed, homogenous, growth of subgrains with Brass orientation annealed at 220 °C goes through a period with a bimodal size distribution as illustrated in Figure 5.14(a). Since growth is hardly affected by the misorientations, the bimodal size distribution, seen to develop during annealing when the orientation gradients are less than $0.5^\circ/\mu m$, is believed to result from more rapid growth of subgrains with a size larger than some critical value of ∼1 µm. During discontinuous subgrain growth, a bimodal size distribution also develops. Growth by this mechanism occurs when the misorientations are extremely low and the microstructure is homogenous. However, the rapidly growing subgrains have a misorientation advantage which was non-excising for the largest S or Brass oriented subgrains after annealing in this PhD work [Huang and Humphreys, 2000].

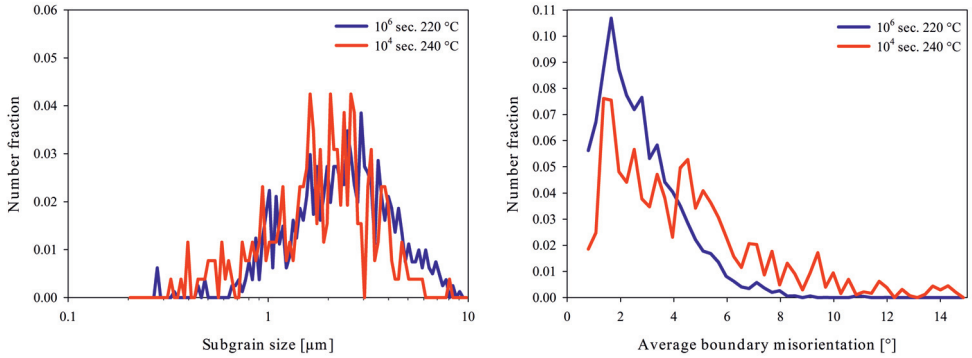

Figure 6.22: Comparison of subgrain size (a) and average boundary misorientation (b) distribution of subgrains with Brass orientation exhibiting decreasing and increasing average boundary misorientations with growth at 220 and 240 °C, respectively.

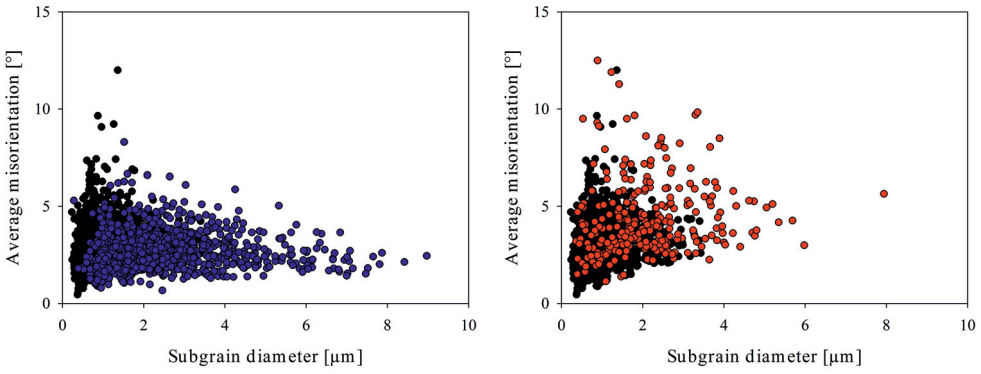

(a) 220 °C. *(b) 240 °C.*

Figure 6.23: Average boundary misorientation of individual Brass oriented subgrains plotted against mean equivalent circle diameter after 10^6 seconds annealing at 220 °C (a) and 10^4 seconds annealing at 240 °C (b). Black points are from Figure 5.11(b).

For Brass in Al4N at 180, 200, 220 °C and for S in Al-0.25Mn, the sub-boundary misorientations were consistently decreasing during annealing. It is interpreted as an actual decrease and not related to sampling of areas with very different deformation history. For S in A1 after 10^5 seconds of annealing, on the other hand, this is exactly what has happened, causing the abrupt decrease in misorientation found in Figure 5.32(b). Despite different growth mechanisms and average boundary misorientations, the subgrain size distributions in Figure 6.24 are unaffected and the growth kinetics are similar in the two cases as the steady growth in Figure 5.32(b) illustrates. What is not apparent from the misorientation distributions in Figure 6.24 but clearly seen in Figure 6.25 is how big the difference in fraction HAGBs is after 10^4 and 10^5 seconds of annealing. Similarly to when the misorientations are increasing, the presence of HABGs does not speed up the growth kinetics. Actually, if ignoring the very steep gradients caused by HAGBs in Figure 6.26, the two different growth mechanism observed can be explained by the orientation gradients. E.g. in the high HAGB case (10^4 seconds of annealing), the orientation gradients are larger than $0.5°/\mu m$ and the misorientations are increasing and vice versa.

It is interesting to find such consistent result with respect to the orientation gradients which lead directly back to the local deformation history of each banded structure. In recent work by Majumdar et al. [2012] on deformed single crystal aluminium with Brass and Goss orientation, vertex model simulations of Brass with low misorientations and weak orientation gradients resulted in very little growth. In Goss, an alternating ± ND-rotated, banded structure, as found experimentally, was applied and gave periodic and abrupt orientation

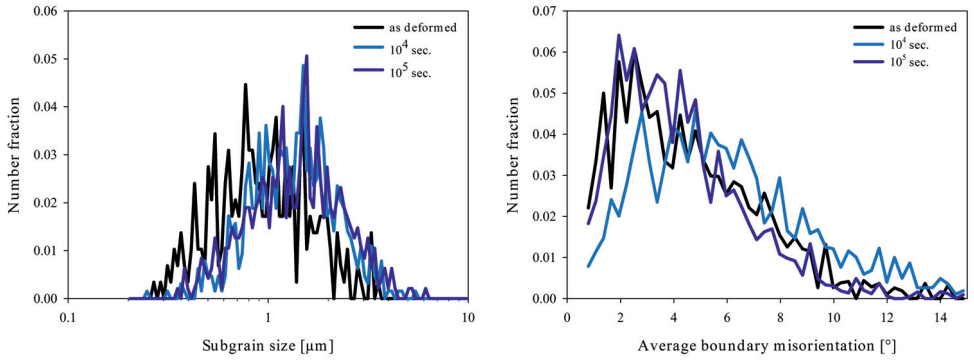

(a) (b)

Figure 6.24: Size (a) and average boundary misorientation (b) distributions for subgrain of S orientation in A1.

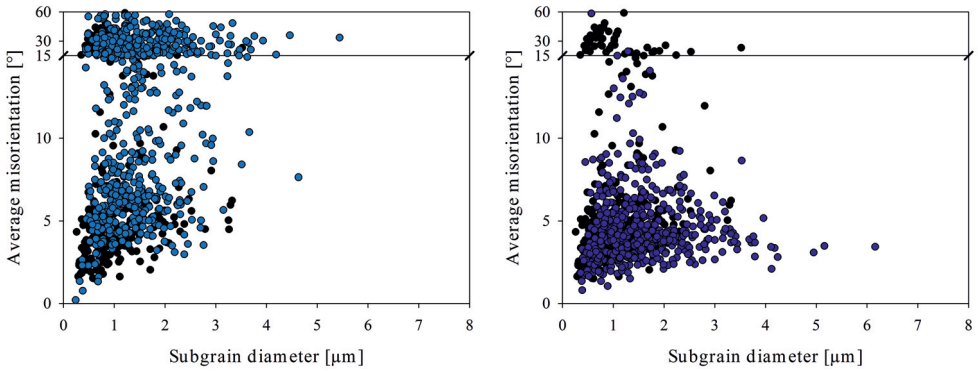

(a) (b)

Figure 6.25: Average misorientation of subgrains plotted against equivalent circle diameter for S orientated subgrains in A1 after 10^4 (a) and 10^5 (b) seconds of annealing at 250 °C.

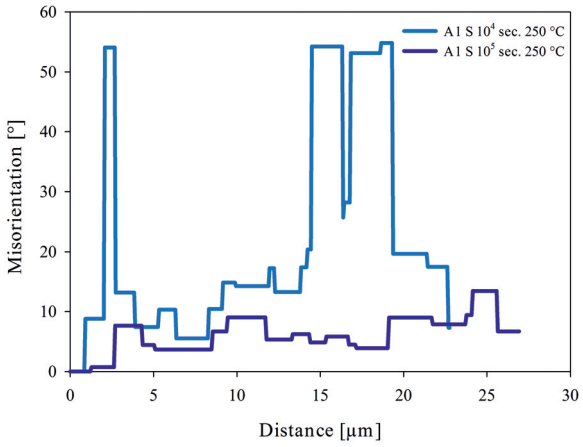

Figure 6.26: Misorientation gradients parallel with ND in ND-RD sections from A1 samples with S-oriented subgrains annealed for 10^4 and 10^5 seconds at 250 °C.

gradients. Simulations of this structure revealed strong growth at the interface of the ±-rotated microstructures and only weak growth in the centre of each band. In this PhD work, both Cube and Goss were present in rather narrow bands but a similar ±-structure is not detected. Similar structures have been observed in Cu and S, although the different bands were separated by HAGBs and experienced early recrystallization.

6.2.3 Nucleation of Recrystallization

The recrystallization texture of Al4N was sensitive to the recrystallization temperature. At high temperature the Cube texture was strong, but as the temperature decreased components of the deformation texture became much more prominent. Because recovery of Cube subgrains is fast, there are many potential nuclei also at low temperature. However, growth of highly misoriented subgrains with other orientations is faster. Slow migration of the special $40°\langle 111\rangle$ Cube-boundaries due to clustering or precipitation of dissolved iron seems to be the most likely explanation. At higher temperature where iron is in solution, the activation energy for boundary migration is higher for more random boundaries than for special Σ7 Cube boundaries. Recrystallization nuclei were typically subgrains with an orientation at the extreme of the orientation spread, while some were even more misoriented by a $\langle 111\rangle$-rotation of 10–40° from their parent bands. Both types of nuclei had a $25–45°\langle 111\rangle$ orientation relationship with the region into which they were growing, indicating that the boundaries have some of the special Σ7 character but are less perfect and have

a more open structure than for Cube oriented subgrains growing into S regions.

To predicted what are nuclei and if they will become recrystallized grains is notoriously difficult. The degree of internal misorientations is a common tool for distinguishing between recrystallized grains and the deformation structure. If e.g the recrystallization and deformation textures are desired from a partially recrystallized sample, computer software can readily distinguish between the two types of microstructures by the *grain orientation spread* (GOS). The technique has been applied somewhat successfully to also detect viable recrystallization nuclei by Wang et al. [2012] and Helbert et al. [2012]. In these works, most recrystallized grains which grow large have a GOS value of less than 2°. However, there are several nuclei both with GOS <2° and surrounded by mobile HAGBs that do not grow. Even a very few nuclei with a high GOS value (thus not really nuclei but simply subgrains) actually grow into recrystallized grains with a low GOS value, something which from an Gibbs Free energy point of view is not favourable. On the other hand, Sabin et al. [2003] have observed that several of the nuclei can have average interior grain misorientations of up to 6°, which is much more than fully recrystallized grains which typically have internal misorientations of less 2°. Thus, the earliest stage of recrystallization was deemed too uncertain with respect to what actually become recrystallized grains and "nuclei" were studied at a later stage in the recrystallization process.

Attempts to predict the most viable nuclei from GOS measurements were abandoned in this PhD work, even if it was found that most recrystallized grains do have a low GOS value. The measurements still did not give reliable predictions about which nuclei actually grew to large, recrystallized grains. Only a weak correlation was found in the Al4N alloy at low annealing temperatures.

Although there are numerous publications about subgrain growth and nucleation of recrystallization by subgrain coalescence, it is according the Humphreys and Hatherly [2004] questionable whether such a mechanism is at all important or even taking place during recovery of normal subgrain structures at low temperatures. Hence, growth of nuclei is generally assumed to take place by classical boundary migration of individual subgrains present in the deformed microstructure that has a growth advantage. Characterization of subgrain growth in Al4N showed that Cube oriented subgrain regions recovered fastest and that after a short incubation time, very rapid subgrain growth occurred. However, other potent nuclei have far better growth conditions, resulting in discontinuous recrystallization with hardly any Cube grains after recrystallization at temperatures below 250 °C. From Figure 5.18, most recrystallized grains appear to have nucleated at transition bands or HAGBs separating both wide and narrow bands of different orientations. This picture is consistent with the subgrain growth data, as discontinuous growth of subgrains with Brass, Cu or S orientations in a similar way as Cube and Goss oriented grains was not

observed for the investigated annealing times and temperatures.

Before discussing nucleation of recrystallization in Al4N, a few comments on the texture of Al-0.25Mn are made. The textures were relatively similar after high and low temperature annealing. However, both Figure 5.25 and the ODFs in Figure 5.26 show the presence of other components in addition to the prevalent Cube, particularly close to the surface. The through-thickness variation of the deformation texture is determined by draught and lubrication, as it is the additional shear deformation near the surface that gives rise to a different texture than in the bulk [Engler et al., 2000]. The shear texture mainly constitutes of ND-rotated Cube and the $\{111\}\langle 112\rangle$ and $\{111\}\langle 011\rangle$ BCC rolling texture components. Little is known about how these shear textures affect the recrystallization texture, although Choi and Lee [1997] have presented an ODF of fully recrystallized Al99.99. However, neither the high nor the low temperature recrystallization textures of Al-0.25Mn share any of the components found by Choi and Lee [1997]. The recrystallization texture by Truszkowski et al. [1980] in a through-thickness study of an AA1050 alloy is weak and difficult to interpret. Hence, why the retained rolling texture components R in the sample annealed at 275 °C manifests itself near the surface is not understood, although it is a common recrystallization texture component typically found after extended recovery [Engler, 1999]. Even more curious is the unknown texture component in the high temperature case, though it could be nucleated from within the spread of the shear texture component $\{111\}\langle 011\rangle$ as it is rotated not far away from this one. Hence, it is noted that there is a strong through-thickness texture variation after recrystallization for the Al-0.25Mn alloy and that the near-surface texture is temperature dependent.

None of the high purity Al4N textures were notably affected by surface conditions. Of course, at low temperature only a couple of grains are found in the thickness direction and any grains nucleating at the surfaces would impinge near the centre. However, Figure 5.18 shows that recrystallization primarily nucleates in the centre of the sheet. With increasing temperature, more nuclei have been activated at similar annealing times. Thus, the recrystallized grain structure becomes finer and gets a rather different texture. In high purity alloys with low iron contents like the Al4N alloy, a strong Cube component is expected [Hirsch and Lücke, 1985; Suzuki et al., 1985]. In fact, according to literature, in alloys containing less than 30 ppm iron the volume fraction of Cube has been reported to be higher than 80% regardless of temperature [Ito et al., 1983a]. The Cube texture component is indeed strong in the samples recrystallized at 350 °C as shown in Figure 5.21(b). There is also a P component present, although neither shear bands nor large secondary particles, from which P is assumed to nucleate, are abundant in the microstructure. Any previous evidence of the P texture component in high purity alloys could unfortunately not be found in literature and further investigations of the origin of this component was not

possible within the time frame of this PhD work.

Compared to annealing at 350 °C, the Cube component in Al4N is much weaker after recrystallization at lower temperatures (220 and 240 °C) and only a few recrystallized grains have a near Cube orientation. Even though an ODF of the sample annealed at 240 °C is presented in Figure 5.21(a), it only gives an indication of the texture due to very poor statistics. However, by looking at the inverse pole figures in Figure 5.18 and Figure 5.19 the volume fraction of recrystallized Cube regions (in red colour) is low and much lower than the predicted 80%. From Siebel [1966] it appears that the Cube component, as measured by the earing tendency in 99.98% pure aluminium, decreases with temperature which is also observed by Akef and Driver [1993] on 99.993% pure aluminium. A high purity alloy containing 100 ppm Fe was processed in order to achieve a fine grain structure, i.e. by interannealing, by Rogers and Roberts [1974] and the actual solute level before final cold rolling was probably low and maybe as low as 1 ppm. Isothermal annealing at 500 °C resulted in a very strong Cube component. When a slow, initial heating rate up to 500 °C was applied, the Cube component was accompanied by a relatively strong R component as well. The observations were explained by a reduced driving force for Cube nucleation due to some recovery, slower boundary migration of Cube-grain boundaries and formation of mainly other nuclei in the deformation structure because of the low temperature. The current subgrain investigations show, to the contrary, that there are numerous Cube nuclei present but that growth is actually slower, as found by Rogers and Roberts [1974], than for those very few nuclei with near-rolling texture orientations. So the Cube nuclei are there, albeit they are not as viable at low temperature as at high temperature or the migration of the special $40°\langle 111\rangle$-rotated boundaries is impeded at low temperatures.

A transition from discontinuous (typical) to continuous recrystallization in high purity aluminium has been observed by Li and Saimoto [1998] that inevitably caused a change in the recrystallization texture. From a strong Cube texture, the texture of the continuously recrystallized structure had a strong resemblance to the deformation texture. With decreasing solute content of iron, Li and Saimoto [1998] describes how, at about 1 ppm Fe in solid solution, recrystallization changes from discontinuous to continuous — still with a relatively strong Cube texture component. However, at even lower solute levels of Fe, the Cube component of the recrystallization texture becomes weaker as the activation energy for unpinning of random boundaries decreases. Eventually, the solute effect will diminish and the activation energy for boundary migration is inherently lower in open, random boundaries than the Cube boundaries which usually have a compact $\Sigma 7$ boundary. Thus the resulting texture from continuous recrystallization at extremely high purity (Fe(ss)<0.1 ppm) will not have a strong Cube component.

In Al4N, recrystallization occurs discontinuously rather than continuously and with only 5 ppm Fe in the composition, precipitation may seem unlikely. However, according to Saimoto and Jin [2007] the solubility limit of iron at 230 °C is 0.014 ppm and Engler and Huh [1999] have actually confirmed Fe-precipitates in an alloy containing 28 ppm Fe. Thus, it is possible that precipitation during annealing at 220 and 240 °C, resulting in a drop in the solute level from 5 to about 0.014 ppm, causes the strong retained deformation texture found in Al4N after annealing. In other words, the texture is controlled by oriented nucleation at low temperature and at high temperature, with all iron in solution, oriented growth prevails to give a strong Cube component. The strong RD rotation of Cube, believed to be caused by oriented nucleation at transition bands, will be discussed more in Section 6.3 [Dillamore and Katoh, 1974; Rixen et al., 1975].

Thus, the texture at low temperature annealing is apparently controlled by oriented nucleation because the activation energy for migration of random boundaries is similar to or even lower than the activation energy for Cube-grains with their $\Sigma 7$ boundaries and $40°\langle 111\rangle$-rotation to S. On several occasions it is observed how these grains with non-Cube orientations are even growing into and consuming Cube oriented areas. In Figure 5.18 there are three recrystallized grains with a 10–29° $\langle 100\rangle$-rotation from their parent Brass bands, seven 10–40° $\langle 111\rangle$-rotated recrystallized grains originating from Cu, S or rotated Cube bands and two where no correlation can be found. Nucleation from within or at the edge of the orientation spread of different texture components after deformation is a well-documented nucleation mechanism for recrystallization. Lücke [1974] stresses the importance of the $40°\langle 111\rangle$-rotation for the formation of the recrystallization texture components but notes that in polycrystalline FCC materials a compromised orientation with a basis in the $40°\langle 111\rangle$-rotation is also formed. According to a detailed study on 99.993% pure aluminium single crystals by Godfrey et al. [2001], nucleation in Cu took place along the micro-shear bands and were together with nuclei in S scattered about 25° from the ideal deformation texture components. Also in S a larger misorientation and a weak $\langle 111\rangle$-rotation relationship was sometimes observed, in agreement with Danh et al. [1980]. The $\langle 111\rangle$-rotation relationship of a typical recrystallized grains and its surrounding deformed microstructure is exemplified in Figure 6.27 and appears to be the preferred nucleation mechanism of in the Al4N alloy [Paul et al., 2005].

The orientation relationship between nuclei and the deformation microstructure has been studied in detail by Sabin et al. [2003]. They found two different types of viable recrystallization nuclei. One type was from within the orientation spread of the deformed region and only a few degrees misoriented. The second type was much more misoriented, but always by a rotation about the $\langle 111\rangle$ axis of one of the deformation texture components. The rotations varied

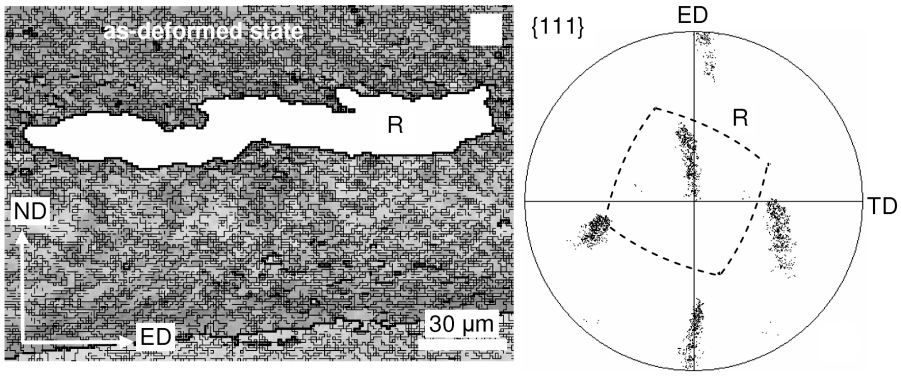

Figure 6.27: ⟨111⟩-rotation relationship between recrystallized grain R and the deformed microstructure. [Paul et al., 2005]

between 10° and 50°, although 30–40° rotations were most frequent. When no alignment of the dislocations with the slip planes was predicted for the parent grains, the first type of nuclei formed. If dislocation alignment with slip planes occurred, the second type of nuclei was anticipated. In FCC metals, most recrystallized grains forming with a misorientation larger than the orientation spread are typically rotated about the ⟨111⟩ axis, i.e. the normal to the most active slip plane [Akef et al., 1991; Hjelen et al., 1991; Sabin et al., 2003]. For those nuclei found in homogenous microstructures without transition bands or shear bands, the orientations are usually within the orientation spread of the parent region [Engler et al., 1996a; Stanford et al., 2003]. The more rotated nuclei associated with deformation heterogeneities like transition bands, are frequently rotated about a ⟨111⟩ axis but also ⟨112⟩ and ⟨100⟩ rotations are observed [Akef and Driver, 1993; Paul and Driver, 2004; Paul et al., 2005]. In this PhD work, Brass which develops a very homogeneous deformation structure have nuclei that are misoriented by about 10° around a ⟨100⟩ axis. They nucleate at the interface of transition-free Brass grains where the neighbouring grain is a transition band. Nuclei present in S or Cu oriented regions, on the other hand, are more frequently rotated by a much larger angle about one of the ⟨111⟩ poles. Most parent grains for nuclei with Cu/S-orientations have large misorientations, either because they are transition bands or have a significant number of micro-shear bands. Hence, nucleation of recrystallization observed in the present PhD work is very much in accordance with the literature.

The EBSD scans in which the subgrains were characterised were selected from the centre of wide bands where the microstructure was homogenous and very narrow bands or transition bands were avoided. Hence, subgrain growth in those regions where the most potent nuclei gradually appear were not investigated in Al4N. The orientation independent scans of A1 revealed more

rapid subgrain growth in HAGB regions and it appears that orientation gradients influence the incubation time for rapid subgrain growth to occur. A certain amount of time is necessary for a growing nucleus to accumulate enough misorientation to become more than 15° rotated from its surroundings and thus possess highly mobile HAGBs necessary for growth. From the 16 or so nuclei in Figure 5.18, 10 grains have a 25–45°⟨111⟩-rotation relationship with the deformation structure (with deformation texture orientations) into which they are growing. Three have only a 10° rotation relationship, while for another three no relationship was found. From literature, the 40°⟨111⟩ boundary is known to have a particularly high velocity [Huang and Humphreys, 2012]. Thus, when recovery and subgrain growth processes in HAGB regions are faster than in bulk, the initially most misoriented subgrains will first attain a high-angle character for its boundaries and also find itself in a position where growth into a neighbouring band is particularly fast due to a near 40°⟨111⟩ boundary. Such boundaries have from the strong Cube texture in Al4N been found to be very mobile at high recrystallization temperatures, i.e. 350 °C. However, at low temperatures, and similar to the observations by Lücke [1974], a compromised relationship with a basis in 40°⟨111⟩ is more favourable. The orientation relationship found during recrystallization with respect to nucleation and growth is exemplified for a Brass nucleus in Figure 6.28 and the mechanism is akin to SIBM. This particular case is also favourable in terms of minimization of the stored energy, since according to Table 6.7 the stored energy of a Brass oriented subgrain structure is much lower than that of a Cube oriented one.

6.3 The Effect of Interannealing on Recovery Kinetics

Iron is almost always present in any aluminium alloy and usually as an impurity element. In high and commercial purity alloys the concentration of iron is typically so large that iron has a strong influence on the material properties because it is a slow diffusing element that has a low solubility in aluminium and forms a number of intermetallic compounds. Therefore, it is very important to know how iron behaves during thermomechanical processing and what the consequences are for e.g. softening kinetics and texture. In this PhD work, interannealing of the A1 alloy cause dissolved iron to precipitate as Al_3Fe and some α-AlFeSi, thus speeding up the recovery kinetics in subsequent annealing processes after deformation. Precipitation took mainly place on the deformation structure and a collection of solute by a sweeping action of the recrystallization front was not prevalent. With regard to the texture evolution during recrystallization, interannealing had a great effect and caused a much stronger Cube recrystallization texture component when applied before final back-annealing. The change from a strong solute drag situation to a weak solute and Zener drag

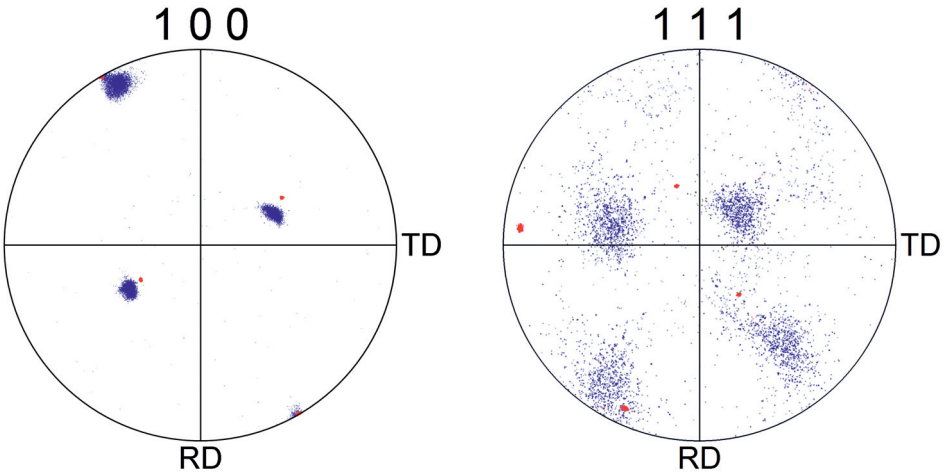

(a) Nucleation. *(b) Growth.*

Figure 6.28: The Brass grain in Figure 5.18(b) originated from the periphery (red) of the orientation spread of the deformed microstructure (blue) (a). It is located at the grain boundary between a Brass and a transition band (blue) where the orientation relationship is close to 40°⟨111⟩ (b).

(low density of precipitates) situation by precipitation of iron was the main factor influencing the texture. The additional deformation and annealing step in itself had only a secondary effect on texture. For high solute contents of iron, a decrease of the solute level is believed to promote migration of the special Σ7 boundaries by which the recrystallization front of Cube is typically growing. However, at very low level of dissolved iron (<1 ppm) there are indications that a further reduction of the solute level will promote growth of recrystallization nuclei which have more random boundaries that inherently are more mobile than special boundaries.

The softening kinetics of A1 represented by hardness values in Figure 5.27(a) reveal a sluggish softening behaviour. A comparison with a similar alloy in Figure 6.29 clearly show how significantly faster recovery and recrystallization kinetics can be achieved at an even lower temperature [Sæter, 1997]. The A1 and AA1070 alloy have nearly the same chemical composition and are 99.73 wt.% pure, the main difference being 0.02 wt.% more Fe and Si in AA1070 than in A1. The homogenization treatments were also similar and cold rolling were done to exactly the same level of strain ($\varepsilon = 2.6$). However, before final cold rolling, the AA1070 alloys of Sæter [1997] had been cold rolled with interpass and final recrystallization annealing at Pechiney in France. Thus, it is believed

that the AA1070 alloy has a much finer grain size before final cold rolling than the A1 alloy. The grain size could possibly be an explanation to the slower softening kinetics of the A1 alloy due to less HAGBs available for grain boundary nucleation here compared to in the AA1070.

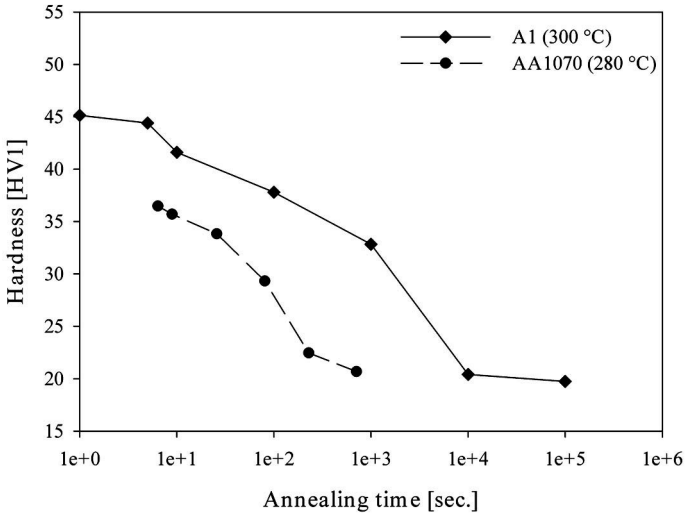

Figure 6.29: Comparison of softening kinetics between A1 and an AA1070 alloy with near identical composition. Despite the higher annealing temperature of A1, the kinetics are slower by almost a factor 10^2. [Sæter, 1997]

To allow for more nucleation sites, the grain size of A1 was successfully reduced from 134 µm to 38 µm through intermediate annealing for 100 seconds at 450 °C. Comparing the new microstructure in Figure 6.30 to the one after homogenization in Figure 4.4(a), a decrease in grain size is obviously achieved. After deforming to strain $\varepsilon = 2.6$ again, the softening kinetics during annealing at 300 °C were, however, not altered and still similarly sluggish. In Figure 6.31 the relevant softening curves of fine and coarse grained material follow each other closely. Figure 5.27(b) illustrate how HAGBs hardly influence the overall softening kinetics. The black curves are from samples homogenized at 600 °C, while the sample represented by the red curve was homogenized at 540 °C. Although shifted slightly, the kinetics are comparable when taking into account the temperature difference even if the HAGB spacing given in Table 4.2 is very different. Nucleation by strain induced boundary migration (SIBM) is known to be more important for hot deformation at low strains and these results indicate that either SIBM is not an important mechanism for recrystallization for heavily cold rolled commercial purity aluminium or that there are sufficient nucleation sites in all the samples [Humphreys and Hatherly, 2004].

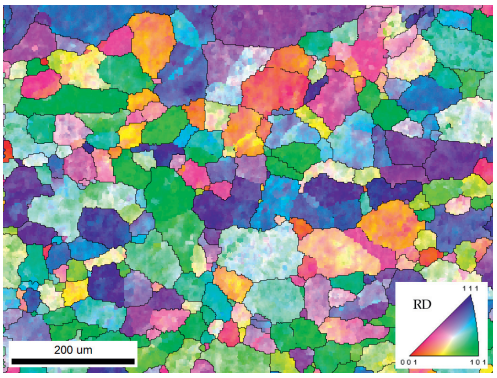

Figure 6.30: Inverse pole figure maps illustrating the microstructure of $A1^{rex}_{450}$. Black boundaries are high-angle grain boundaries.

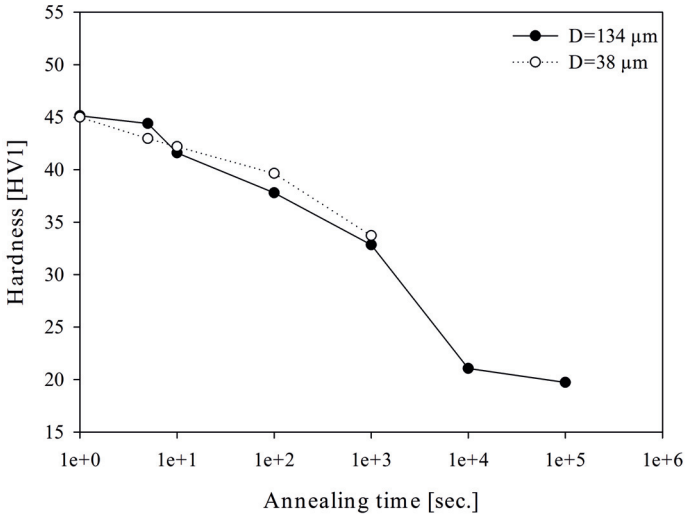

Figure 6.31: Flash-annealed sample (100 s, 450 /degree S) with reduced grain size from 134.1 to 38.2 µm before deformation exhibit similarly slow softening kinetics at 300 °C as coarse grained A1.

6.3.1 Precipitation

By lowering the interannealing temperature, causing the materials to experience more recovery before recrystallizing, the softening progressed much faster upon a second deformation and annealing process. Figure 5.37 shows how the kinetics are faster in both 50% and 92.5% deformed materials. The conductivity, particularly of the 50% deformed material, is increased, clearly indicating clustering or precipitation. Since 50% and 92.5% deformed samples had similar conductivity before intermediate annealing after deformation, it is expected that the two interannealed samples also should exhibit the same conductivity after deformation. Why this is not the case and the reason for the discrepancy is not known, but the two values were reproducible.

According to Thermo-Calc (COST 507 dataset) calculations, about 0.003 wt.% Fe should be in solid solution by holding the samples a 450 °C during homogenization. Thus, there is some room for precipitation after the homogenization process at 540 °C and log-cooling (in Figure 3.4) during subsequent annealing at a lower temperature. Redistribution of iron atoms to heterogeneities like grain boundary triple junctions is observed in 5N aluminium containing 2 ppm iron [Bond et al., 1966]. However, confirmation of cluster formation/precipitation is only found in alloys containing more than 5 ppm iron [Kubota et al., 2001; Metzger and Levy, 1985; Suzuki et al., 1985]. For the A1 alloy in this PhD work, the solute level at 300 °C should be only 0.7 ppm Fe and about 30 ppm Fe is expected to precipitate during interannealing — in agreement with the observed conductivity increase in Figure 5.37(c).

In order to highlight the effects of interannealing, the homogenization temperature of A1 was raised to 620 °C and the samples quenched to "freeze" in as much iron in solution as possible. During subsequent annealing at 300 °C the potential for precipitation is roughly 300 ppm according to Thermo-Calc (COST 507 dataset) calculations. Comparing the electrical conductivity measurements of the samples homogenized at 540 °C and 620 °C in Table 5.8 and Table 5.9, respectively, the higher homogenization temperature caused the conductivity to drop from 35.4 $^{m}/_{\Omega mm^2}$ to 34.7 $^{m}/_{\Omega mm^2}$. By the more accurate four point method, the conductivity was actually measured to be even lower at 34.36 $^{m}/_{\Omega mm^2}$.

It is also clear from Figure 5.39 and Figure 5.40 that the desired effect of a higher initial solute level was achieved. The consequence of interannealing is much more pronounced with the new homogenization process for both the 50% and 92.5% deformed samples. Now, as opposed to in the 540 °C-case, similarly interannealed samples also have nearly the same electrical conductivity after 50% and 92.5% deformation. During direct back-annealing, the conductivity rises to similar levels as those of the samples annealed at a 540 °C. However, after interannealing the conductivity remains the same for the samples deformed 50% prior to annealing as those directly deformed and annealed, a behaviour not

observed in the lower solute case after homogenization at 540 °C. When deforming 92.5% before the intermediate annealing step, the conductivity rises even more and slightly higher than the level seen in the samples deformed 50% before annealing. Because lattice diffusion of iron is extremely slow with an activation energy $Q_{lattice} \simeq 214$ Jmol^{-1}, Metzger and Levy [1985] have suggested that diffusion is only possible through pipe diffusion along dislocations, sub-boundaries and grain boundaries [Du et al., 2003]. Thus, the larger conductivity observed after 92.5% deformation is attributed to more dislocations, dense dislocation walls and subgrain boundaries ($Q_{grainboundary} \simeq 0.6Q_{lattice}$) than in the 50% deformed samples.

Without deformation, Figure 2.25 shows how there is hardly any precipitates compared to a deformed sample [Kubota et al., 2001]. In the present PhD work the effect of the sub-structure on precipitation is evident not only from the hardness and conductivity curves but also from micrographs. Figure 5.53 and Figure 5.54 reveal how the deformation structure is a key factor in the precipitation kinetics. The distribution of etch pits, caused by precipitates, replicates the deformation structure after complete recrystallization, to some extent even in flash-annealed samples. The micrographs also reveal that the density of precipitates is in this case too low to actually exert a Zener drag strong enough to stabilize the microstructure as was reported by Hasenclever [2006], as only a few boundaries are notably pinned by precipitates and the fraction of pits in the matrix and at boundaries is very similar.

Figure 6.32 shows examples of more precipitates at the boundaries in flash-annealed samples and Zener drag pinning. However, the picture is far from as clear as Vandermeer [1967] observed, who did not find precipitates in the centre of recrystallized grains. The mechanism for precipitation was by Vandermeer [1967] described as a sweeping action by migration of grain boundaries. Only when the boundary slowed down did precipitation occur and precipitates could only be found in the grain interior when precipitated at a dislocation left behind by the recrystallization front. In the present work, in the A1 alloy it seems more likely that precipitation occurs before recrystallization is taking place because of the low annealing temperature. Also in the flash-annealed samples this is possible, although solute in some areas is also swept up by moving grain boundaries. The recrystallization front could of course also collect solute which would diffuse laterally (along the boundaries) and precipitate at the boundary where it meets heterogeneities in the deformed microstructure like dislocations, sub-boundaries and old grain boundaries. This would explain the deformation structure pattern revealed by pits also in the slowly annealed samples, though the precipitation mechanism was not further investigated.

When diffusion is assisted by the dislocation network, sub-boundaries and grain boundaries, the equilibrium level of Fe <1 ppm in solution at 300 °C, as predicted by Thermo-Calc (COST 507 dataset), might be reached during annea-

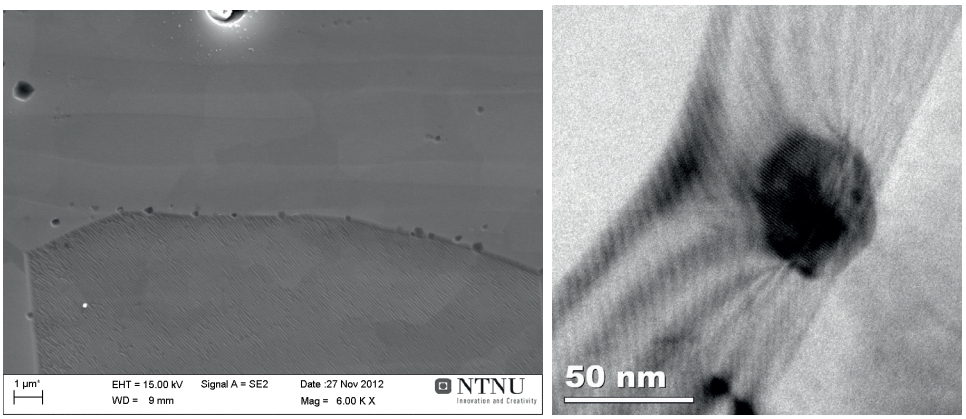

(a) *(b)*

Figure 6.32: Examples of more precipitation (etch pits) at HAGBs in flash annealed samples (a) and how some boundaries are clearly pinned by precipitates (b).

ling. The conductivity curves actually seem to saturate around 35.8 $^{m}/_{\Omega mm^2}$. Subtracting the effect of deformation at around 0.2 $^{m}/_{\Omega mm^2}$, the increase in conductivity due to precipitation during annealing is about 1.2 $^{m}/_{\Omega mm^2}$. In Equation 3.3, the pre-factor for Fe is 0.036 $^{m}/_{\Omega mm^2 wt.\%}$ and that for Si is 0.0068 $^{m}/_{\Omega mm^2 wt.\%}$. The solubility of Si is also less sensitive to temperature than that of Fe, so it is fair to assume that changes in the electrical conductivities are due to variations in the solute level of Fe only. By this reasoning, the electrical conductivity measurements in Figure 5.39 equate to precipitation of ∼300 ppm Fe, i.e. the fully annealed state is close to the equilibrium in terms of solute content of Fe. This is in good agreement with the literature, where the largest amount of precipitation in a high purity alloy containing 50 ppm Fe was observed at 310 °C [Kubota et al., 2001]. Above 400 °C the precipitates are reported to dissolve and below 200 °C diffusion will of course be much slower making precipitation more difficult [Marshall et al., 1991].

Very slow kinetics are found for the directly deformed and annealed samples with the high level of quenched in solute iron after homogenization at 640 °C, as expected for commercial or high purity alloys where dissolved iron is known to slow down the softening kinetics [Marshall and Ricks, 1993; Marshall et al., 1991; Masing et al., 1956]. Correspondingly, the effect of interannealing is stronger and causes softening kinetics that are faster by a factor 10^3 than for directly deformed and annealed samples. For the 50% deformed case, increased conductivity, i.e. precipitation, has a strengthening effect on the as-deformed state. From the micrographs the density of precipitates is roughly 0.9 μm^{-2}. Thus, a strengthening contribution from the precipitates is plausible but very small

due to the relatively low density of precipitates. However, because the effect is most notable in the 50% deformed case, the largest strengthening contribution is most likely a Hall-Petch effect from decreased grain size after interannealing. After 92.5% deformation, the microstructure becomes more homogenous irrespective of the initial grain size due to an increase in the break-up factor with strain [Ryen, 2003; Sjølstad, 2003].

In the literature, it is generally agreed upon that dissolved iron slows down the softening kinetics and deformation followed by annealing around 300 °C causes strong precipitation which speeds up the kinetics noticeably. However, there is more uncertainty on the microscopic level as to what phases are actually precipitating and how. There are two phases precipitating in A1 during annealing, namely Al_3Fe and α_h-AlFeSi. According to Thermo-Calc calculations, only α-AlFeSi and β-AlFeSi should be stable at 300 °C. In literature, on the other hand, Al_6Fe, Al_3Fe and α-AlFeSi are the only phases reported. Al_3Fe is sometimes more precisely referred to as $Al_{13}Fe_4$ [Mondolfo, 1976; Skjerpe, 1987]. Al_6Fe is a metastable precursor to the stable Al_3Fe phase and has been observed by Suzuki et al. [1985], Stickels and Bush [1971], Yamamoto et al. [2004] and Ito et al. [1982] in both deformed and undeformed materials. Stickels and Bush [1971] observed Al_6Fe to be reverted to Al_3Fe only in undeformed samples, while Yamamoto et al. [2004] found deformation to enhance precipitation of Al_6Fe. The alloys in which Al_6Fe was observed are mainly high purity alloys with Fe addition and Miki and Warlimont [1968] found 0.05 wt % Si to significantly improve the nucleation rate of Al_3Fe. The A1 alloy actually contains 0.05 wt % Si and of all the non-Si containing precipitates only the stable phase Al_3Fe was observed (Al_6Fe is usually needle-shaped, Al_3Fe is spherical), suggesting that Si is indeed helping the formation of Al_3Fe. Whenever Al_3Fe is precipitating it occurs heterogeneously, though according to Yamamoto et al. [2004] deformation does not accelerate the rate of precipitation. The rate of precipitation has not been investigated in this PhD work, but it is clear that deformation promotes precipitation and that more deformation enhanced the degree of precipitation. The α-AlFeSi phase is, of course, only reported in alloys containing Si and to co-exist with Al_6Fe and Al_3Fe by Ito et al. [1982], although there are few observations of it in the literature.

6.3.2 Texture

Because the microstructure after 50% deformation is heterogeneous, the texture is not well-defined and hardly useful for materials characterization. In addition, most of the textures of the 50% deformed samples are close to random. Hence, mainly textures of the 92.5% samples will be considered in the following. With interannealing, the texture of A1 after recrystallization at 350 °C becomes slightly weaker but gains a stronger Cube component as shown in Figure 6.33. The R texture component is still strong and only marginally weaker in the

interannealed variant in Figure 5.38.

The texture after recrystallization is influenced by the deformation texture which again to some extent also depends on the texture before deformation. After casting and homogenization, the texture is expected to be random and Figure 5.35 shows that the texture after intermediate annealing is also very close to random. The effect of the deformation texture can be demonstrated by comparing the recrystallization texture of A1 and A2 after annealing at 350 °C in Figure 5.28 and Figure 5.29, respectively. The deformation textures in A1 and A2 share the same components but the texture is stronger in A1. This causes an overall stronger recrystallization texture with a weaker RD-rotated Cube component, a stronger Cube component and slightly stronger R texture components in A1. Besides the stronger deformation texture in the A1 alloy and more silicon in the A2 alloy, the two alloys are very similar. The R texture component is promoted by dissolved iron as documented by e.g. Ito et al. [1983a] and it could be slightly more constituent particles in A2 due to more Si which enhance formation of iron-rich phases. Such iron rich phases can cause PSN which generally leads to a randomization of the texture. However, in Table 4.3 the amount of constituent particles is very similar in the two alloys and thus it is assumed that the solute level of iron is also nearly the same, indicating that the deformation texture is the major parameter influencing the recrystallization texture.

The deformation texture is only a secondary factor for the resulting recrystallization texture of A1 material with and without interannealing. Figure 5.42 and Figure 5.48 show that the interannealing process only has a minor effect on the deformation texture after a reduction of 92.5%. We know that 92.5% deformation and back-annealing result in a very low solute level of iron. After another 50% deformation, recrystallization during subsequent annealing is not affected much by concurrent precipitation. Therefore we can see by comparing the 92.5% deformed and back-annealed texture in Figure 5.46 with the 92.5% deformed, back-annealed, 50% deformed and back-annealed texture in Figure 5.52 that interannealing in itself only has a week effect on the final recrystallization texture. The deformation texture components become slightly weaker and the Goss texture component sharpens a little. Hence, texture variations observed in A1 are caused by the interplay of solute drag, precipitation and recrystallization and e.g. the strong Cube component observed in Figure 6.33 after recrystallization of the interannealed material is an effect of iron present as precipitates rather than in solution during recrystallization.

The texture after slow annealing at 300 °C has a much stronger Cube component than flash annealing at 500 °C, as seen in Figure 5.46 and Figure 5.44 respectively. The texture originates from a similar deformation microstructure and the differences can only be attributed to the temperature difference and its effect on the microstructure. Since in Table 5.9 the conductivity of the flash

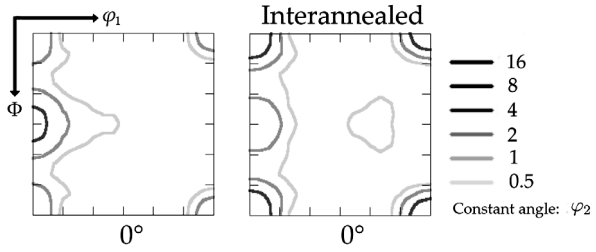

Figure 6.33: Effect of interannealing on Cube texture component in A1 deformed 92.5% and annealed at 350 °C for 1000 seconds.

annealed sample increases only marginally by precipitation, recrystallization is hardly affected by concurrent precipitation and thermal activation of solute at 500 °C is assumed to render the solute drag effect negligible. The sample annealed at 300 °C, on the other hand, is influenced both by solute drag and a possible Zener drag due to concurrent precipitation. Looking at Figure 5.39 for the 92.5% deformed case, the largest structural change occurs after 10^3 seconds causing a 0.2 $^{m}/_{\Omega mm^2}$ hike in the conductivity. Still, a significant amount of solute is precipitated after the onset of recrystallization, i.e. solute drag influences both the nucleation and growth phase of recrystallization.

Technically, both solute and precipitates could cause the strong Cube texture. Cube texture is e.g. reported to prevail in a Zener drag situation [Humphreys and Hatherly, 2004]. On the contrary, Ito et al. [1983a] also found Cube to be inhibited by precipitates. Engler et al. [1996b] found Cube oriented nuclei to have a size advantage and therefore be less sensitive to Zener pinning. In A1, Cube subgrains had a slight size advantage over S and Cu subgrains but not Brass subgrains. And in any case the area fraction of precipitates is very low (0.9 μm^{-2}). Thus, Zener drag is minimal and it is assumed that dissolved iron has the strongest influence on the texture. Also, in the micrographs of recrystallized samples, Zener pinning of grain boundaries is not extensive.

The texture after 50% deformation and annealing at 320 °C in Figure 5.45 is very weak and has no Cube component. The Cube component only appears when the material is deformed to 92.5%. Because 50% deformation and back-anneling does not promote formation of Cube and only marginally affect the texture, the strengthening of Cube in Figure 6.34 by interannealing is due to less iron in solution. From Figure 5.39, it is evident that the second annealing sequence is not as affected by solute and concurrent precipitation as the directly back-annealed samples where most iron precipitates. Thus, there is clear experimental evidence from both Figure 6.33 and Figure 6.34 that a reduction of the solute content of iron promotes a stronger Cube component after recrystallization.

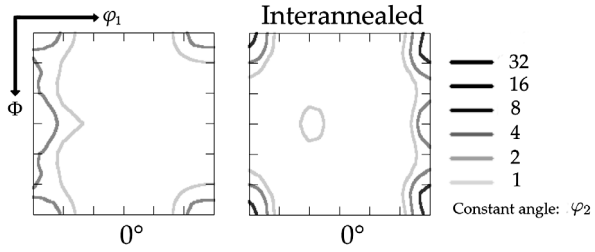

Figure 6.34: Effect of interannealing on Cube texture component in A1 deformed 92.5% and annealed at 300 °C for 10^5 seconds.

Whenever the Cube texture component is weak as a result of a high content of dissolved iron, the R texture is often dominant [Humphreys and Hatherly, 2004; Ito et al., 1976, 1983a; Suzuki et al., 1985]. While the strength of the Cube component is influenced by interannealing in the A1 alloy, the R texture component is generally weak and is only affected marginally. However, that a reduction of the solute content of iron in high and commercial purity alloys leads to a strengthening of the Cube texture component is strongly supported in literature as discussed in Section 2.5. Humphreys and Hatherly [2004], Marshall et al. [1991], Ito et al. [1983a], Bunk [1965], Rogers and Roberts [1974] and Suzuki et al. [1985] have all found increasing levels of iron in solution of high or commercial purity alloys to inhibit the formation of the Cube texture component during recrystallization. According to Ito et al. [1976], the Cube component is more strongly impeded during the nucleation stage than the growth stage.

A graphical presentation of the different recrystallization regimes in commercial purity alloys is given by Ito et al. [1983a] and reproduced in Figure 6.35. The shaded area for minimum Cube volume fraction (<5%) represent a matrix with a combination of precipitates and iron in solid solution. Dissolution of precipitates is occurring above this region and less precipitation is occurring below. That is why at high temperatures, where everything is in solution, increasing alloy concentration leads to a weaker Cube. At low temperature, increasing iron content reduces the mean diffusion path for the slow diffusing iron atoms and enhances precipitation, thus leading to a stronger Cube component.

Ekström et al. [1990] also found similar effects of dissolved Fe but observed a strong Cube texture in an alloy with a high level of dissolved Fe as well. They questioned whether the observations were due to very slow heating rates or an effect of constituent particles. In high purity aluminium, Li and Saimoto [1998] also found somewhat contradicting results where Cube was promoted by solute levels of Fe greater than 1 ppm (though an upper limit was not given). The investigated alloy had initially 90 ppm Fe with less than 1 ppm assumed to be

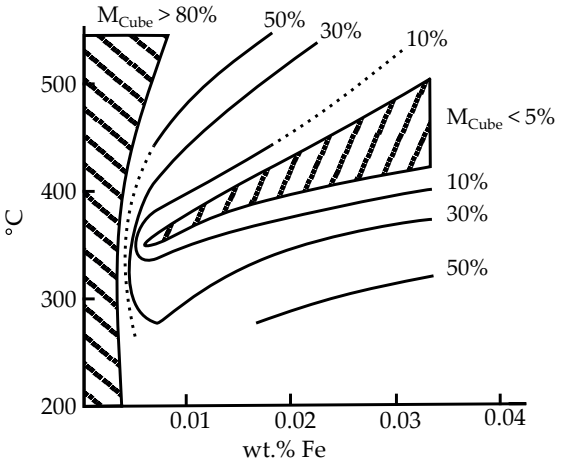

Figure 6.35: Volume fraction of Cube component as a function of temperature and Fe-content. After [Ito et al., 1983a]

in solution. Below 0.1 ppm, the retained rolling texture R was prominent.

A short summary of the solute content of iron and the effect on the Cube texture component in A1 and also Al4N is due before the final discussion is made. A strengthening of the Cube texture component is achieved when adding iron because precipitation becomes easier. Similarly, in the A1 alloy, when interannealing is done to promote precipitation the volume fraction of Cube after recrystallization increases. Before the first annealing step, the A1 alloy contains several hundred ppm Fe in solid solution and the recrystallization texture has a weak Cube texture component after recrystallization. Precipitation during this first annealing step leads to a strengthening of the Cube component after the second annealing step — but only until the solute level reaches about 1 ppm. Below this level and with a further reduction of the solute Fe content the Cube component intensity becomes weaker again because of the inherently more mobile random boundaries. The recrystallization behaviour at very low solute concentrations is challenging to investigate because characterization of clustering or early stage precipitation phenomena is experimentally difficult.

The intensity of some important texture components after interannealing of Al4N at various temperatures is given in Figure 6.36(a). Although neither the R texture component nor the β-fibre are strong in Al4N, it has already been discussed in Section 6.2.3 how the texture at low temperature is closely related to the deformation texture and nucleated in a similar manner as the R component is known to do. On the other hand, at high temperature a strong Cube texture appears. In light of the investigations by Li and Saimoto [1998], precipitation of iron rich particles to give an extremely low solute level of Fe in this high purity alloy is a possible explanation for the decreasing Cube texture

component with decreasing temperature. During annealing at 350 °C of the Al4N alloy deformed to strain $\varepsilon = 3$ there is very little time for precipitation and thermal activation of solute atoms can be rate limiting for boundary migration. It can be assumed that most of the 5 ppm iron is in complete solution and the texture presented in Figure 5.21(b) has a strong Cube component. Figure 6.36(b) shows that a lowering of the solute content through precipitation in A1 leads to a much stronger Cube texture. For interannealed A1 the solute level of iron is similar to that of Al4N when annealed at 350°C, i.e. about 1 ppm as previously discussed. After annealing at similar temperatures, the Cube component is the major texture component in both alloys (a direct comparison of the peak intensities cannot be made due to very different number of grains included in the ODF calculations).

Figure 6.36(b) also show the Cube component and β-fibre of the sample flash-annealed at 500 °C. At such a high temperature as 500 °C, no solute drag effect is expected as thermal activation is easy [Hersent et al., 2013]. In A1, there is still some iron left in solid solution (equilibrium at 0.17 ppm according to Saimoto and Jin [2007]) after interannealing, 92.5% cold rolling and a second annealing process as the temperature was 320 and 300 °C, respectively. That is, a solute drag effect is still present as opposed to during flash annealing where ideally there should be none. During flash annealing there is of course a low temperature period where solute drag is active because the heating rate is not infinite, which is probably why some Cube nuclei are still recrystallizing [Furu, 1992]. However, the major texture components after annealing at 500 °C are Cu and S although the overall texture shown in Figure 5.44 is relatively weak. The mobility of the special $\Sigma 7$ boundaries which give Cube nuclei a growth advantage is caused by a solute pinning of other random boundaries [Porter and Easterling, 2004]. Thus, initially, under light solute drag conditions, Cube boundaries have a growth advantage. As the temperature increases and thermal activation becomes simples, random boundaries, which are also abundant, are able to grow faster. In this sense, flash annealing can be viewed as a case more similar to the <1 ppm-regime in the work of Li and Saimoto [1998] resulting in a strong retained rolling texture.

An alternative explanation for the weak Cube component after flash annealing implies a solute drag effect also at high temperature. From Figure 5.39 and Table 5.9 it can be deduced that only 1/3 of the dissolved Fe in A1 is precipitated during flash-annealing at 500 °C compared to slow annealing at 300 °C. Thus, there is much dissolved Fe present during flash-annealing. It is described in the previous how solute pins the deformation structure during annealing and give rise to the R texture component [Humphreys and Hatherly, 2004; Ito et al., 1976, 1983a; Suzuki et al., 1985]. In Al4N the solute level is maximum 5 ppm, while in A1 the solute content after deformation is 60 times larger at ∼300 ppm. In Figure 6.36, the β-fibre is also much stronger in A1 than Al4N,

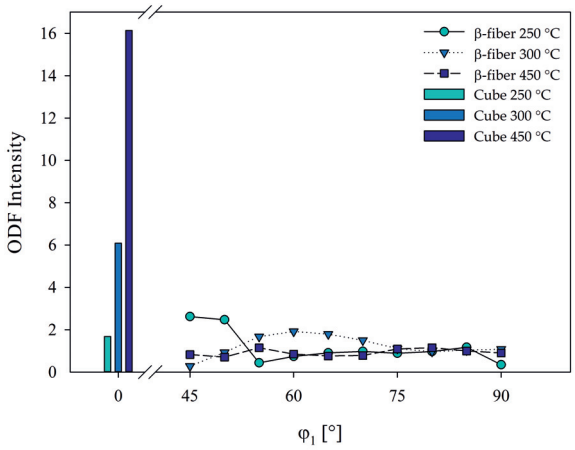

(a) Al4N

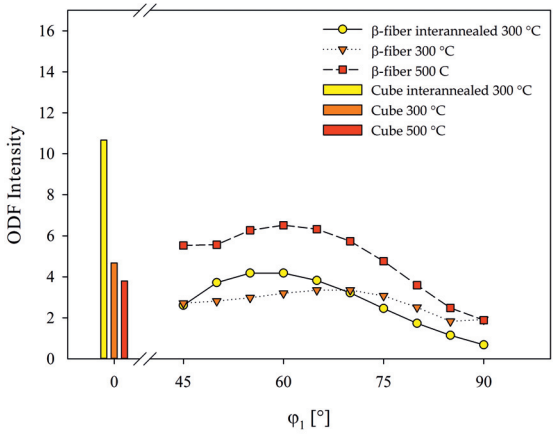

(b) A1

Figure 6.36: The effect of temperature on ODF intensity of β-fibre and Cube texture component in Al4N (a) and the effect of temperature and solute content of Fe on ODF intensity of β-fibre and Cube in A1 (b).

particularly after annealing at 500 °C. At 300 °C the effect of interannealing and a substantially lower solute content influence the β-fibre only marginally, though a considerable amount of precipitation is also occurring before recrystallization during the first annealing. The deformation in itself could also be responsible for the small variations seen in the texture of interannealed and non-interannealed samples as a secondary factor. The β-fibre plots therefore indicate a strong pinning of the deformation structure resulting in a strong R texture, even at high temperature where solute drag should not be operating from a thermal activation point of view. If solute drag, perhaps controversially, is actually effective also at high temperature it could explain why a decreasing Cube component with increasing temperature is observed by Benum [1995], Ito et al. [1976] and others, and why the Cube component is not affected by the temperature in Al-0.25Mn where no precipitation occurs and the solute level is similar at 275 °C and 400 °C.

Another less obvious difference between many of the ODFs presented from the Al4N, Al-0.25Mn and A1 alloys with and without interannealing is an RD rotation of the Cube component, and sometimes even a strong Goss component is evident. The RD-rotated Cube component arises from preferred nucleation at transition bands in copper oriented deformation bands [Dillamore and Katoh, 1974; Rixen et al., 1975]. Also Engler et al. [1996b] suggests that the RD-rotated Cube component originate from oriented nucleation and most notably at low temperatures as oriented growth gives a sharper Cube texture component at high temperatures. At the same time, continuous recrystallization is also promoted by low annealing temperatures and both an RD-rotated Cube component and a Goss component were observed by Hirsch and Lücke [1985] at 280 °C but not at 360 °C or above. The Goss component does not have a $\langle 111 \rangle$ growth advantage but is usually a result of oriented nucleation from transition bands [Hjelen et al., 1991]. There are several transition bands in the alloys studied in this PhD work after deformation, although a strong correlation between the RD-rotated Cube and Goss components with temperature is not found here.

The recrystallized microstructure typically forms by a combination of oriented growth and oriented nucleation. From literature, oriented nucleation generally influences texture more during continuous recrystallization while oriented growth is more important during discontinuous recrystallization. For the alloys studied here, recrystallization is best described as discontinuous. According to Hirsch and Lücke [1985], a strong and isotropic scattering of a recrystallization texture several degree away from S, i.e. R, is evidence of discontinuous recrystallization. Remember, R also has a growth advantage similar to Cube due to a $40°\langle 111 \rangle$ orientation relationship with S [Hirsch and Lücke, 1986]. A weaker scattering around S indicate continuous recrystallization and the exact position of R can then be used to distinguish between these two recrystallization

mechanism [Engler, 1999].

Low temperature annealing of Al-0.25Mn results in both an RD-rotated Cube and a distinct R component away from S, suggesting that oriented nucleation but also discontinuous recrystallization are important mechanisms. In Al-0.25Mn, manganese is expected to be in solution and there is no evidence of precipitation. However, at the same annealing temperature, precipitation of iron in A1 by interannealing strongly reduces the Goss and RD-rotated Cube components, in addition to transform the S component in the high solute case to an R in the low solute case after interannealing. For the most part, recrystallization in A1 is discontinuous. Still, in the high solute case without interannealing, continuous recrystallization sustains the S texture component but oriented nucleation of rotated Cube and Goss components are prevailing in the resulting texture. Not only do dissolved iron atoms prevent growth selection of Cube but also of the R component found after discontinuous recrystallization, both with a $40°\langle 111\rangle$ type relationship. It is interesting to note how solute appears to affect the texture after flash annealing even at 500 °C where a strong S component is present in unison with a less strong R component. After recrystallization of Al-0.25Mn at 400 °C the retarding effect of solute on boundary mobility diminishes but there is still an RD rotation of the Cube component. Also in the high purity Al4N annealed at 350 °C the ODF in Figure 5.21(b) reveals that there is a strong RD-rotation of the Cube component. It has been speculated earlier in Section 6.2 whether clustering or precipitation is also occurring in the Al4N alloy. It could be that the 5 ppm iron, which do not have time to precipitate at 350 °C, are responsible for the strong rotation of Cube.

Chapter 7

Conclusions

The present PhD work has been concerned with experimental investigations of recovery, recrystallization and related annealing phenomena in the high and commercial purity alloys Al4N, Al-0.25Mn and A1. It clearly shows that the subgrain growth behaviour is complex, diverse and challenging to characterize. To predict the softening behaviour, a detailed qualitative and quantitative description of the deformation structure is absolutely necessary as well as how the microchemistry evolves during thermo-mechanical processing. For development of robust and complete softening models applicable to a wide range of alloy systems in the future, a detailed quantitative description of several phenomenon as well as their interactions is required. However, this is still only a long-term goal, nevertheless where the present PhD work has provided some pieces on the way, e.g. it has clearly identified the local orientation gradient as an important factor to understand subgrain growth. The main conclusions from this PhD work can be summarized as follows:

1. Subgrain growth can be successfully characterized by reconstructed subgrain maps from EBSD scans without using dedicated software.

2. Variations in the microchemistry influence the subgrain growth kinetics but the experimental evidence suggests that the same growth mechanisms operate in all three alloy systems.

3. In the early stages, subgrain growth rates in lamellar bands of Cu, S, Brass, Goss and Cube orientations are similar and only weakly correlated with the average boundary misorientations. For Cube and Goss oriented subgrains, which are the most misoriented, the growth rates are slightly faster than for Cu and S. However, despite the lowest amount of misorientations detected, growth of Brass oriented subgrains was marginally stronger than for Cu and S oriented subgrains.

4. Both the growth mechanisms and the kinetics were greatly influenced

by the size of local orientation gradients. For gradients smaller than $\sim 0.5^\circ/\mu m$, the average boundary misorientation evolution during annealing was decreasing in both high purity alloys. For larger orientation gradients the average boundary misorientations were increasing with coarsening during annealing. The evolution of the boundary misorientations and the rate of subgrain growth were not correlated.

5. The orientation dependent subgrain growth investigations revealed three distinct growth behaviours that correlate with the local orientation gradients.

   For the largest orientation gradients as found in Cube and Goss oriented subgrain structures, growth changes from initially slow and continuous to rapid and more discontinuous after an incubation period. Growth results in a temporary bimodal size distribution due to the growth of a large number of subgrains with a definite misorientation advantage and causes the average boundary misorientations to increase.

   For subgrain structures with Cu, S and Brass orientations and orientation gradients larger than $\sim 0.5^\circ/\mu m$, growth during annealing is homogenous with a uniform size distribution and increasing average boundary misorientations during annealing.

   In S and Brass oriented subgrain structures with orientation gradients smaller than $\sim 0.5^\circ/\mu m$, growth results in a temporary bimodal size distribution, possibly due to a size advantage of large subgrains, and decreasing average boundary misorientations.

6. Subgrain growth, investigated independently of orientations in the commercial purity A1 alloy only, is faster than when orientation dependent, indicating faster kinetics near HAGBs separating differently oriented lamellar bands. The average boundary misorientations are decreasing with annealing because only subgrains with an average misorientation larger than 3.5° experience significant coarsening. Thus, the total boundary length of more misoriented boundaries decreases while the individual boundary misorientations most likely increase, as in all the orientation dependent investigations of the same alloy.

7. Recrystallization in the high purity Al4N alloy at low annealing temperatures occurs typically at HAGBs by nuclei oriented at or slightly beyond the edge of the orientation spread of their parent grains. Their orientation relationship to the neighbouring grains into which they are growing is a compromise $40^\circ\langle 111\rangle$ rotation. With increasing temperature, the texture becomes more dominated by the Cube component.

8. Iron in solid solution leads to significantly slower softening kinetics for

the commercial purity A1 alloy. By cold rolling to large strains and inter-annealing at 300 °C the solute content is reduced significantly by precipitation of mainly Al_3Fe and some α_h-AlFeSi phases. Doing so speeds up the softening kinetics by a factor close to 10^3 and causes a considerable strengthening of the Cube component in the recrystallized texture.

Chapter 8

Future Work

This PhD work has shown that the annealing phenomena taking place in high and commercial purity aluminium alloys are very complex. It is essential to relate the static properties of the deformed microstructure to the boundary mobilities, precipitation kinetics, nucleation mechanism etc. in order to describe the dynamic annealing behaviours. In this respect there are several aspects that are interesting for further investigations.

- During the very early stages of annealing, hardening was observed in some of the materials studied in this PhD work. For a dedicated investigation, tensile tests should be carried out in order to quantify the effect properly. Both a high purity alloy and commercial purity alloys with varying solute levels could be interesting to investigate. They should be deformed to at least two different strain levels where the microstructure would consist of mostly tangled dislocations and a well-defined subgrain structure, respectively. This way, it could be identified whether the strengthening is caused by rearrangements of dislocations, by dislocation-solute interactions or dislocation-subgrain interactions. Depending of the results, careful TEM characterization of the annealing response of the microstructure and possibly atom-probe tomography to help identify clustering phenomena should be considered to get an understanding of the exact strengthening mechanism.

- In this PhD work a working method for subgrain characterization is presented and an overview of the subgrain growth behaviour of all the alloys has been established. Further investigations should focus on the subgrain growth behaviour of the Al4N, Al-0.25Mn alloys or other directionally solidified materials. By cold rolling coarse, columnar grained materials with the grains aligned with RD, near identical microstructure can be found for a significant distance along RD. RD-ND cross sections from the same width of the sheets could be annealed for various times. Hence, it

would be possible to follow the evolution of a certain microstructure during annealing and the average subgrain boundary mobilities of the typical deformation texture components could be calculated accurately. The mobilities could be related to solute effects for the various orientations and strain levels by a Taylor factor analysis or calculations of the stored energy directly from the EBSD data [Choi and Jin, 2004]. This approach is a good alternative to in-situ experiments where the growth mechanism and kinetics can be influenced by the free surface, particularly after sample preparation like electropolishing or ion milling. Through such an analysis, the growth mechanisms could be described theoretically and simulations validated against accurate experimental data, thus establishing a more robust softening model with respect to microchemistry.

- Precipitation in the commercial purity alloy A1 was intimately linked with the microstructure after deformation. Despite the very low diffusion coefficient of iron, significant precipitation is even possible within 10 seconds of flash annealing. The exact precipitation mechanism is not known and would be fascinating to understand. Is it a sweeping action of dislocations or subgrain boundaries with lateral diffusion? Is it occurring at the recrystallization front? This could initially be done relatively simple by following the precipitation kinetics by etching in combination with EBSD to identify the involved heterogeneities where precipitation is occurring, e.g. typical boundary misorientations or perhaps CSL boundaries. In a later stage, the evolution of the solute concentration at dislocations and subgrain boundaries could be followed by atom-probe tomography. In addition, the A1 (AA1050) alloy is a good model alloys because of its sensitivity to the solid solution concentration of iron. This could be utilized in careful investigations of the interaction between solute and different boundaries with respect to the mobility during recrystallization, e.g. the $40°\langle 111\rangle$-boundaries versus less perfectly oriented boundaries.

Bibliography

Abtahi, S., Sjølstad, K., Marthinsen, K., and Nes, E. Modelling subgrain growth during annealing of deformed aluminium alloys. In *Recrystallization and Grain Growth, Proceeding of the First Joint International Conference*, pages 251–256, 2001.

Achani, D., Lademo, O.-G., Engler, O., and Hopperstad, O. G. Evaluation of constitutive models for textured aluminium alloys using plane-strain tension and shear tests. *International Journal of Material Forming*, 4(2):227–241, 2011.

Akef, A. and Driver, J. H. Recrystallization nucleation mechanisms in high purity aluminium single crystals after plane strain compression. *Materials Science Forum*, 113–115:103–108, 1993.

Akef, A., Fortunier, R., Driver, J. H., and Watanabe, T. Recrystallization of high symmetry aluminium single crystals after plane strain compression. *Textures and Microstructures*, 14–18:617–622, 1991.

Albou, A., Borbely, A., Maurice, C., and Driver, J. H. Orientation-dependent recovery in strongly deformed Al-0.1% Mn crystals. *Philosophical Magazine*, 91(31):3981–4000, 2011.

Albou, A., Borbely, A., Maurice, C., and Driver, J. H. Orientation dependent recovery in strongly deformed Al-0.1%Mn crystals. *Materials Science Forum*, 753:225–230, 2013.

Alden, T. H. Strain hardening and recovery in lead during primary creep. *Metallurgical Transactions A*, 8(12):1857–1862, 1977.

Alvi, M. H., Cheong, S. W., Suni, J. P., Weiland, H., and Rollet, A. D. Cube texture in hot-rolled aluminum alloy 1050 (AA1050) — nucleation and growth behaviour. *Acta Materialia*, 56:3098–3108, 2008.

Amin, K. E., Mukherjee, A. K., and Dorn, J. E. A universal law for high-temperature diffusion controlled transient creep. *Journal of the Mechanics and Physics of Solids*, 18(6):413–426, 1970.

Argon, A. S. *Strengthening mechanisms in crystal plasticity*, pages 136–153. Oxford University Press, Oxford, 2007.

Barber, D. J. A new etchant for revealing defect structures in aluminium. *Philosophical Magazine*, 7(83):1925–1932, 1962.

Bardal, A., Lindseth, I., Vatne, H. E., and Nes, E. Dislocation densities, subgrain sizes and sub-boundary misorientations within the different texture components of hot-deformed AlMgMn. In *Proceeding of the 16th Risø International Symposium on Material Science*, pages 261–266, 1995.

Barou, F., Guillotin, A., Maurice, C., Feppon, J.-M., and Driver, J. H. Boundary mobilities during recovery and recrystallization of binary Al-Mn alloys. *Materials Science Forum*, 558–559:53–59, 2007.

Barou, F., Maurice, C., Feppon, J.-M., and Driver, J. H. Sub-grain boundary mobilities during recovery of binary Al-Mn alloys. *International Journal of Materials Research*, 100(4):516–521, 2009.

Barou, F., Maurice, C., Feppon, J.-M., and Driver, J. H. Sub-boundary mobilities during recovery of binary Al-Mn alloys. *Materials Science Forum*, 715–716:725–731, 2012.

Bate, P. S., Knutsen, R. D., Brough, I., and Humphreys, F. J. The characterization of low-angle boundaries by EBSD. *Journal of Microscopy*, 220(1): 36–46, 2005.

Bay, B., Hansen, N., Hughes, D. A., and Kuhlmann-Wilsdorf, D. Evolution of f.c.c. deformation structures in polyslip. *Acta Metallurgica et Materialia*, 40 (2):205–219, 1992a.

Bay, B., Hansen, N., and Kuhlmann-Wilsdorf, D. Microstructural evolution in rolled aluminium. *Materials Science and Engineering: A*, 158(2):139–146, 1992b.

Beck, P. A. Notes on work hardening and recovery. *Acta Metallurgica*, 1(4): 422–425, 1953.

Beck, P. A. and Sperry, P. R. Strain induced grain boundary migration in high purity aluminum. *Journal of Applied Physics*, 21(2):150–152, 1950.

Beck, P. A., Kremer, J. C., Demer, L. J., and Holzworth, M. L. Grain growth in high-purity aluminum and in an aluminum-magnesium alloy. *Transactions of the American Institute of Mining Engineers*, 175:372–400, 1948.

Benum, S. *Twin roll casting of AlFeSi aluminium alloys: cold rolling and annealing*. PhD thesis, The Norwegian Institute of Technology, Trondheim, 1995.

Biloni, H. and Bolling, G. F. A simple etching technique that reveals dislocations and copper segregation in aluminum. *Canadian Metallurgical Quarterly*, 4(3):177–180, 1965.

Birol, Y. Recrystallization of a supersaturated Al-Mn alloy. *Scripta Materialia*, 59:611–614, 2008.

Bjørge, R., Nakashima, P. N. H., Marioara, C. D., Andersen, S. J., Muddle, B. C., Etheridge, J., and Holmestad, R. Precipitates in an Al–Mg–Ge alloy studied by aberration–corrected scanning transmission electron microscopy. *Acta Materialia*, 59(15):6103–6109, 2011.

Black, P. J. The structure of $FeAl_3$. I. *Acta Crystallographica*, 8(1):43–48, 1955.

Bond, A. P., Bolling, G. F., Domian, H. A., and Biloni, H. Microsegregation and the tendency for pitting corrosion in high-purity aluminum. *Journal of The Electrochemical Society*, 113(8):773–778, 1966.

Bowen, J. R. Strength and structure in commercial purity aluminium after large strain. *Materials Science and Engineering: A*, 483–484:231–234, 2008.

Brough, I. and Humphreys, F. J. Evaluation and application of a fast EBSD detector. *Materials Science and Technology*, 26(6):636–639, 2010a.

Brough, I. and Humphreys, F. J. Evaluation and application of a fast EBSD detector. *Materials Science and Technology*, 26(6):636–639, 2010b.

Bunge, H. J. *Texture analysis in materials science: mathematical methods*. Butterworths, Oxford, 1982.

Bunk, W. Beeinflussung der Aluminiumtexture durch Legieren. *Zeitschrift für Metallkunde*, 56(10):645–653, 1965.

Cao, W. Q., Godfrey, A., Hansen, N., and Liu, Q. Annealing behaviour of nanostructured aluminum produced by cold rolling to ultrahigh strains. *Metallurgical and Materials Transactions A*, 40A:204–214, 2009.

Choi, C.-H. and Lee, D. N. Evolution of recrystallization texture from aluminum sheet cold rolled under unlubricated condition. *Metallurgical and Materials Transactions A*, 28(11):2217–2222, 1997.

Choi, S.-H. and Jin, Y.-S. Evaluation of stored energy in cold-rolled steels from EBSD data. *Materials Science and Engineering: A*, 371(1–2):149–159, 2004.

Clauer, A. H., Wilcox, B. A., and Hirth, J. P. Dislocation substructure induced by creep in molybdenum single crystals. *Acta Metallurgica*, 18(3):381–397, 1970.

Cooper, J. R., Vučić, Z., and Babić, E. The thermoelectric power of AlMn alloys. *Journal of Physics F: Metal Physics*, 4(3):1489–1500, 1974.

Crussard, C., Aubertin, F., Faoul, B., and Wyon, G. Polygonization in strongly deformed metals. *Progress in Metal Physics*, 2:193–202, 1950.

Daaland, O. and Nes, E. Origin of cube texture during hot rolling of commercial Al-Mn-Mg alloys. *Acta Materialia*, 44(4):1389–1411, 1996.

Danh, N. C., Murakami, T., and Takahashi, T. Recrystallization Textures in Single Crystal of Al-1Rolled to (123)(412). *Transactions of the Japan Institute of Metals*, 21(7):401–408, 1980.

Davies, R. K., Randle, V., and Marshall, G. J. Continuous recrystallization - related phenomena in a commercial Al-Fe-Si alloy. *Acta Materialia*, 46(17): 6021–6032, 1998.

Dillamore, I. L. and Katoh, H. The mechanisms of recrystallization in cubic metals with particular reference to their orientation-dependence. *Metal Science*, 8(1):73–83, 1974.

Doherty, R. D. and Cahn, R. W. Nucleation of new grains in recrystallization of cold-worked metals. *Journal of the Less Common Metals*, 28(2):279–296, 1972.

Driver, J. H., Maurice, C., Barou, F., and Lens, A. Boundary mobilities in binary Al-Mn alloys. *Materials Science Forum*, 519–521:1597–1604, 2006.

Du, Y., Chang, Y. A., Huang, B., Gong, W., Jin, Z., Xu, H., Yuan, Z., Liu, Y., He, Y., and Xie, F.-Y. Diffusion coefficients of some solutes in fcc and liquid Al: critical evaluation and correlation. *Materials Science and Engineering: A*, 363:140–151, 2003.

Easton, M. and StJohn, D. Grain refinement of aluminum alloys: Part I. the nucleant and solute paradigms—a review of the literature. *Metallurgical and Materials Transactions A*, 30(6):1613–1623, 1999.

Ekström, H.-E., Hutchinson, W. B., and Oscarsson, A. The influence of iron on textures and earing in aluminium sheet. *Key Engineering Materials*, 44–45: 188–210, 1990.

Ekström, H.-E., Mishin, O. V., and Östensson, L. Analysis of softening behaviour of AA 1200 alloys using gallium enhanced microscopy. *Materials Forum*, 28:252–257, 2004.

Ekström, H.-E., Mishin, O. V., Östensson, L., and Hagström, J. Softening of an AA3103 alloy analysed using gallium enhanced microscopy. *Material Science Forum*, 519–521:1591–596, 2006.

Engler, O. On the origin of the R orientation in the recrystallization textures of aluminum alloys. *Metallurgical and Materials Transactions A*, 30:1517–1527, 1999.

Engler, O. and Huh, M.-Y. Evolution of the cube texture in high purity aluminum capacitor foils by continuous recrystallization and subsequent grain growth. *Materials Science and Engineering: A*, 271(1–2):371–381, 1999.

Engler, O. and Randle, V. *Introduction to Texture Analysis: Macrotexture, Microtexture, and Orientation Mapping*, pages 270–275. CRC Press, Boca Raton, 2010. Second Edition.

Engler, O., Escher, C., and Gottstein, G. Single grain orientation measurements applied to the formation and growth of recrystallization nuclei. *Textures and Microstructures*, 26–27:337–359, 1996a.

Engler, O, Vatne, H. E., and Nes, E. The roles of oriented nucleation and oriented growth on recrystallization textures in commercial purity aluminium. *Materials Science and Engineering: A*, 205(1–2):187–198, 1996b.

Engler, O, Yang, P., and Kong, X. W. On the formation of recrystallization textures in binary Al–1.3% Mn investigated by means of local texture analysis. *Acta Materialia*, 44(8):3349–3369, 1996c.

Engler, O., Tomé, C. N., and Huh, M.-Y. A study of through-thickness texture gradients in rolled sheets. *Metallurgical and Materials Transactions A*, 31(9): 2299–2315, 2000.

Exell, S. F. and Warrington, D. H. Sub-grain Boundary Migration in Aluminium. *Philosophical Magazine*, 26(5):1121–1136, 1972.

Ferry, M. and Humphreys, F. J. Discontinuous subgrain growth in deformed and annealed {110}<001>aluminium single crystals. *Acta Materialia*, 44(4): 1293–1308, 1996.

Forbord, B. *Annealing behaviour of twin roll cast aluminium alloys*. PhD thesis, The Norwegian University of Science and Technology, Trondheim, 1999.

Friedel, J. *Dislocations*. Pergamon Press, Oxford, 1964.

Furu, T. *Modelling of recrystallization applied to commercial aluminium alloys*. PhD thesis, The Norwegian Institute of Technology, Trondheim, 1992.

Furu, T., Ørsund, R., and Nes, E. Subgrain growth in heavily deformed aluminium - experimental investigation and modelling treatment. *Acta Metallurgica et Materialia*, 43(6):2209–2232, 1995.

Gandin, Ch.-A. From constrained to unconstrained growth during directional solidification. *Acta Materialia*, 48(10):2483–25001, 2000.

Godfrey, A. SEM-EBSD characterisation of deformed microstructures. 11th international summer school – Aluminium alloy technology, 2011.

Godfrey, A., Jensen, D. J., and Hansen, N. Recrystallisation of channel die deformed single crystals of typical rolling orientations. *Acta Materialia*, 49 (13):2429–2440, 2001.

Grewen, J. and Heimendahl, M. v. Gefüge, Textur and Zipfelbildung von Al99,5 in Abhängigkeit von der Verformung. *Zeitschrift für Metallkunde*, 59(3):205–212, 1968.

Gundlach, C., Pantleon, W., Lauridsen, E. M., Margulies, L., Doherty, R. D., and Poulsen, H. F. Direct observation of subgrain evolution during recovery of cold-rolled aluminium. *Scripta Materialia*, 50:477–481, 2004.

Hansen, N. and Huang, X. Microstructure and flow stress of polycrystals and single crystals. *Acta Materialia*, 46(5):1827–1836, 1997.

Hansen, N., Bay, B., Juul Jensen, D., and Leffers, T. The evolution of deformation microstructures and local orientations. In *Proceeding of the* 7^{th} *International Conference on the Strength of Metals and Alloys*, pages 317–322, 1985.

Hasenclever, J. Recovery and recrystallization behaviour of AlMn1 - alloys. *Materials Science Forum*, 396–402:527–532, 2002.

Hasenclever, J. The important role of dissolved elements (Mn, Fe) in the process of rolled products and their effects on final properties. *Materials Science Forum*, 519–521:1447–1452, 2006.

Heidenreich, R. D. Electron Microscope and Diffraction Study of Metal Crystal Textures by Means of Thin Sections. *Journal of Applied Physics*, 20(10):993–1010, 1949.

Heidenreich, R. D. Electron Transmission Through Thin Metal Sections with Application to Self-Recovery in Cold Worked Aluminum. *Bell System Technical Journal*, 30(4):867–887, 1951.

Helbert, A.-L., Wang, W., Brisset, F., Baudin, T., and Penelle, R. In situ EBSD investigation of recrystallization in a partially annealed and cold-rolled aluminum alloy of commercial purity. *Advanced Engineering Materials*, 14 (1–2):39–44, 2012.

Hersent, E., Marthinsen, K., and Nes, E. The effect of solute atoms on grain boundary migration: a solute pinning approach. *Metallurgical and Materials Transactions A*, 44(7):3364–3375, 2013.

Hirsch, J. and Lücke, K. The application of quantitative texture analysis for investigating continuous and discontinuous recrystallization processes of Al-0.01 Fe. *Acta Metallurgica*, 33(10):1927–1938, 1985.

Hirsch, J. and Lücke, K. Investigation of the rolling and recrystallization behaviour of aluminium with the help of texture analysis. In *Proceeding of the 1st Risø International Conference in Aluminum Alloys*, pages 1725–1740, 1986.

Hjelen, J., Örsund, R., and Nes, E. On the origin of recrystallization textures in aluminium. *Acta Metallurgica et Materialia*, 39(7):1377–1404, 1991.

Holm, E. A., Miodownik, M. A., and Rollett, A. D. On abnormal subgrain growth and the origin of recrystallization nuclei. *Acta Materialia*, 51:2701–2716, 2003.

Holm, K. and Hornbogen, E. Annealing of supersaturated and deformed Al-0.042 wt% Fe solid solutions. *Journal of Materials Science*, 5:655–662, 1970.

Hood, G. M. and Schultz, R. J. The diffusion of manganese in aluminium. *Philosophical Magazine*, 23(186):1479–1489, 1971.

Hornbogen, E. Inhibition of recrystallization in supersaturated solid solutions by large amounts of cold work. *Journal of Materials Science*, 12(8):1565–1572, 1977.

Hu, H. Direct observations on the annealing of Si-Fe crystals in the electron microscope. *Transactions of the Metallurgical Society of AIME*, 224(1):75–84, 1962.

Huang, X. and Winther, G. Dislocation structures. Part I. Grain orientation dependence. *Philosophical Magazine*, 87(33):5189–5214, 2007.

Huang, X., Tsuji, N., Hansen, N., and Minamino, Y. Microstructural evolution during accumulative roll-bonding of commercial purity aluminum. *Materials Science and Engineering: A*, 340(1–2):265–271, 2003.

Huang, X., Hansen, N., and Nobuhiro, T. Hardening by annealing and softening by deformation in nanostructured metals. *Metallurgical and Materials Transactions A*, 312(5771):249–251, 2006.

Huang, Y. and Humphreys, F. J. Measurements of grain boundary mobility during recrystallization of a single-phase aluminium alloy. *Acta Materialia*, 47(7):2259–2268, 1999.

Huang, Y. and Humphreys, F. J. Subgrain growth and low angle boundary mobility in aluminium crystals of orientation {110}<001>. *Acta Materialia*, 48:2017–2030, 2000.

Huang, Y. and Humphreys, F. J. Measurements of subgrain growth in a single-phase aluminum alloy by high-resolution EBSD. *Materials Characterization*, 47:235–240, 2001.

Huang, Y. and Humphreys, F. J. The effect of solutes on grain boundary mobility during recrystallization and grain growth in some single-phase aluminium alloys. *Materials Chemistry and Physics*, 132:166–174, 2012.

Huang, Y., Humphreys, F. J., and Ferry, M. The annealing behaviour of deformed cube-oriented aluminium single crystals. *Acta Materialia*, 48:2543–2556, 2000.

Hughes, D. A. Microstructural evolution in a non-cell forming metal: Al-Mg. *Acta Metallurgica et Materialia*, 41(5):1421–1430, 1993.

Hughes, D. A. The evolution of deformation microstructures and local orientations. In *Proceeding of the 16th Risø International Symposium on Material Science*, pages 63–85, 1995.

Hughes, D. A. and Hansen, N. High angle boundaries and orientation distributions at large strains. *Scripta Metallurgica et Materialia*, 33(2):315–321, 1995.

Hughes, D. A. and Hansen, N. High angle boundaries formed by grain subdivision mechanisms. *Acta Materialia*, 45(9):3871–3886, 1997.

Humphreys, F. J. A unified theory of recovery, recrystallization and grain growth, based on the stability and growth of cellular microstructures-I. The basic model. *Acta Materialia*, 45(10):4231–4240, 1997.

Humphreys, F. J. Review: Grain and subgrain characterisation by electron backscatter diffraction. *Journal of Materials Science*, 36(16):3833–3854, 2001.

Humphreys, F. J. Characterisation of fine-scale microstructures by electron backscatter diffraction (EBSD). *Scripta Materialia*, 51(8):771–776, 2004a.

Humphreys, F. J. Reconstruction of grains and subgrains from electron backscatter diffraction maps. *Journal of Microscopy*, 213(3):247–256, 2004b.

Humphreys, F. J. Nucleation in recrystallization. *Materials Science Forum*, 467–470:107–116, 2004c.

Humphreys, F. J. and Bate, P. S. The microstructures of polycrystalline Al-0.1Mg after hot plane strain compression. *Acta Materialia*, 55(16):5630–5645, 2007.

Humphreys, F. J. and Hatherly, M. *Recrystallization and Related Annealing Phenomena*. Elsevier Ltd., Kidlington, 2004. Second Edition.

Humphreys, F. J., Prangnell, P. B., Bowen, J. R., Gholinia, A., and Harris, C. Developing stable fine–grain microstructures by large strain deformation. *Philosofical Transactions of the Royal Society of London A*, 357:1663–1681, 1999.

Hurley, P. J. and Humphreys, F. J. The application of EBSD to the study of substructural development in a cold rolled single–phase aluminium alloy. *Acta Materialia*, 51:1087–1102, 2003.

Hutchinson, W. B. Recrystallisation textures in iron resulting from nucleation at grain boundaries. *Acta Metallurgica*, 37(4):1047–1056, 1989.

Hutchinson, W. B. and Duggan, B. J. Influence of precipitation on recrystallization and texture development in an iron–1.2% copper alloy. *Metal Science*, 12(8):372–380, 1978.

Ito, K., Lücke, K., and Rixen, R. The influence of pre-annealing and annealing temperatures on the recrystallization textures of cold rolled aluminium-iron alloys. *Zeitschrift für Metallkunde*, 67(5):338–347, 1976.

Ito, K., Abe, H., and Lücke, K. Electron microscopic identification of second phases precipitated during recrystallization annealing of dilute Al–Fe–Si alloys. *Journal of Japan Institute of Light Metals*, 32(5):235–240, 1982.

Ito, K., Musick, R., and Lücke, K. The influence of iron content and annealing temperature on the recrystallization textures of high-purity aluminium-iron alloys. *Acta Metallurgica*, 31(12):2137–2149, 1983a.

Ito, K., Seki, F., Abe, H., and Lücke, K. Influence of silicone addition on the recrystallization texture of Al-Fe alloy. *Zeitschrift für Metallkunde*, 74(12): 772–776, 1983b.

Jacquet, P. A. Electrolytic and chemical polishing. *Metallurgical Reviews*, 1 (2):157–238, 1956.

Jones, A. R., Ralph, B., and Hansen, N. Subgrain Coalescence and the Nucleation of Recrystallization at Grain Boundaries in Aluminium. In *Proceedings of the Royale Society of London. Series A, Mathematical and Physical Sciences*, pages 345–357, 1979.

Kubota, S., Kawai, M., Yamamoto, M., and Shiga, M. Effects of cold rolling and heat treatments on Fe precipitation in high purity aluminum studied by mössbauer spectroscopy. *Journal of Japan Institute of Light Metals*, 51(12): 635–639, 2001.

Kuhlmann-Wilsdorf, D. Theory of plastic deformation: - properties of low energy dislocation structures. *Materials Science and Engineering: A*, 113: 1–41, 1989.

Kuijpers, N. *Kinetics of the β-AlFeSi to α-Al(FeMn)Si transformation in Al-Mg-Si alloys*. PhD thesis, Delft University of Technology, Delft, 2003.

Kurz, W. and Fisher, D. J. *Fundamentals of Solidification*. Trans Tech Publications, Uetikon-Zuerich, 1998. Fourth Revised Edition.

Kwieciǹski, J. and Wyrzykowski, J. W. Kinetics of recovery on grain boundaries in polycrystalline aluminium. *Acta Metallurgica*, 37(5):1503–1507, 1989.

Labusch, R. Statistical theories of solid solution hardening. *Acta Metallurgica*, 20:917–927, 1972.

Lee, C. S., Duggan, B. J., and Smallman, R. E. A theory of deformation banding in cold rolling. *Acta Metallurgica et Materialia*, 41(8):2265–2270, 1993.

Lee, Y. C., Dahle, A. K., and StJohn, D. H. The role of solute in grain refinement of magnesium. *Metallurgical and Materials Transactions A*, 31(11): 2895–2906, 2000.

Lens, A., Maurice, C., and Driver, J. H. Grain boundary mobilities during recrystallization of Al-Mn alloys as measured by in situ annealing experiments. *Materials Science and Engineering A*, 403:144–153, 2005.

Li, J. C. M. Possibility of subgrain rotation during recrystallization. *Journal of Applied Physics*, 33:2958–2965, 1962.

Li, J.L. and Saimoto, S. Texture evolution in aluminum during continuous recrystallization. *Materials Science Forum*, 273:459–464, 1998.

Liu, Q., Juul Jensen, D., and Hansen, N. Effect of grainorientation on deformation structure in cold-rolled polycrystalline aluminium. *Acta Materialia*, 46(16):5819–5838, 1998.

Liu, W. C. and Zhai, P. P. Characterization of microstructures near grain boundary in hot deformed AA3104 aluminum alloy. *Materials Characterization*, 62:81–89, 2011.

Lücke, K. The orientation dependence of grain boundary motion and the formation of recrystallization textures. *Canadian Metallurgical Quarterly*, 13 (1):261–274, 1974.

Majumdar, A., Maurice, C., and Driver, J. H. Vertex dynamics simulations of orientation dependent recovery in deformed aluminium single crystlas. *Materials Science Forum*, 702–703:639–642, 2012.

Marshall, G. J. and Ricks, R. A. Role of iron during recovery and recrystallization of aluminium-iron alloys. *Materials Science Forum*, 113–115:245–250, 1993.

Marshall, G. J., Ricks, R. A., and Limbach, P. K. F. Controlling lower temperature recovery and recrystallisation in commercial purity aluminium. *Materials Science and Technology*, 7(3):263–269, 1991.

Masing, G., Lücke, K., and Nölting, P. Einfluss von kleinen Beimengungen auf das Rekristallisationsverhalten von Reinstaluminium. *Zeitschrift für Metallkunde*, 47(2):64–74, 1956.

Maurice, C. and Driver, J. High temperature plane strain compression of cube oriented aluminium crystals. *Acta Metallurgica et Materialia*, 41(6):1653–1664, 1993.

Maxwell, I. and Hellawell, A. A simple model for grain refinement during solidification. *Acta Metallurgica*, 23(2):229–237, 1975.

Metzger, M. and Levy, M. Internal friction of aluminium crystals containing iron. *Journal de Physique Colloques*, 46(C10):261–264, 1985.

Miki, I. and Warlimont, H. Morhoplogie und Wachstumskinetik der Ausscheidungen in aluminiumreichen Aluminium-Eisen- und Aluminium -Eisen-Silizium-Legierungen. *Zeitschrift für Metallkunde*, 59(4):254–264, 1968.

Modéer, B. and Odén, A. Recovery in aluminium studied by an in situ technique in a high voltage electron microscope. *Journal of Materials Science*, 10:223–233, 1975.

Mondolfo, L. F. *Aluminum alloys: structure and properties*. Butterworths, London, 1976.

Morris, D. G. The origins of strengthening in nanostructured metals and alloys. *Revista de Metalurgia*, 46(2):173–186, 2010.

Morris, P. L. and Duggan, B. J. Precipitation and recrystallization in an Al–1.8%Mn alloy. *Metal Science*, 12(1):1–7, 1978.

Mott, N. F. A theory of work-hardening of metal crystals. *Philosophical Magazine*, 43(346):1151–1178, 1952.

Murr, L. E. *Interfacial phenomena in metal and alloys*. Addison-Wesley, Reading, 1975. Second edition.

Nes, E. Recovery revisited. *Acta Metallurgica et Materialia*, 43(6):2189–2207, 1995.

Nes, E. and Hutchinson, W. B. Materials Architecture. In *Proceeding of the 10th Risø International Symposium on Material Science*, pages 233–249, 1989.

Nişancioğlu, K. Electrochemical behavior of aluminum-base intermetallics containing iron. *Journal of The Electrochemical Society*, 137(1):69–77, 1990.

Ólafsson, P., Sandström, R., and Karlsson, Å. Electrical conductivity of aluminium alloys. *Materials Science Forum*, 217–222:981–986, 1996.

Ørsund, R. *Nucleation of recrystallization and effect on texture in commercial aluminum alloys*. PhD thesis, The Norwegian Institute of Technology, Trondheim, 1989.

Paul, H. and Driver, J. H. Recrystallization nucleation in some channel die deformed, high symmetry aluminium bicrystals. *Materials Science Forum*, 467–470:171–176, 2004.

Paul, H., Driver, J. H., and Lens, A. Mechanisms of new orientation formation during recrystallization of old deformed aluminium bicrystals. *Materials Science Forum*, 495–497:1249–1254, 2005.

Perryman, E. C. W. Observations on the structural changes accompanying recovery in super-purity aluminium. *Acta Metallurgica*, 2(1):26–37, 1954.

Polmear, I. *Light alloys: From traditional alloys to nanocrystals*, page 198. Butterworth-Heinemann, Linacre House, Jordan Hill, Oxford, 2006. Fourth Edition.

Porter, D. A. and Easterling, K. E. *Phase Transformations in metals and alloys*. CRC Press, Boca Raton, 2004. Second edition.

Rajmohan, N. and Szpunar, J. A. Stored energy in can body aluminium alloy after cold rolling and stress relieving. *Materials Science and Technology*, 15: 1259–1265, 1999.

Read, W. T. and Shockley, W. Dislocation models of crystal grain boundaries. *Physical Review*, 78(3):275–289, 1950.

Rixen, R., Musick, R., Göker, H, and Lücke, K. Texturen bei der primären Rekristallisation hochreiner Aluminium–Mangan–Legierungen. *Zeitschrift für Metallkunde*, 66:16–26, 1975.

Rogers, D. H. and Roberts, W. T. Rolling textures in aluminium sheet. *Zeitschrift für Metallkunde*, 65:100–105, 1974.

Rosen, G. I., Juul Jensen, D., Hughes, D. A., and Hansen, N. Microstructure and local crystallography of cold rolled aluminium. *Acta Metallurgica et Materialia*, 43(7):2563–2579, 1995.

Ryen, Ø. *Work hardening and mechanical anisotropy of aluminium sheets and profiles*. PhD thesis, The Norwegian University of Science and Technology, Trondheim, 2003.

Ryen, Ø., Nijs, O., Sjölander, E., Holmedal, B., Ekström, H.-E., and Nes, E. Strengthening mechanisms in solid solution aluminum alloys. *Metallurgical and Materials Transactions A*, 37(6):1999–2006, 2006.

Sabin, T. J., Winther, G., and Juul Jensen, D. Orientation relationships between recrystallization nuclei at triple junctions and deformed structures. *Acta Materialia*, 51:3999–4011, 2003.

Sæter, J. A. *Substructure evolution and strengthening in cold rolled and annealed aluminium alloys*. PhD thesis, The Norwegian University of Science and Technology, Trondheim, 1997.

Sæter, J. A., Forbord, B., Vatne, H. E., and Nes, E. Modelling recovery and recrystallization, applied to back-annealing of aluminium sheet alloys. In *Proceedings of the 6^{th} International Conference on Aluminium Alloys*, pages 113–126, 1998.

Saimoto, S. and Jin, H. Effects of solubility limit and the presence of ultra-fine Al_6Fe on the kinetics of grain growth in dilute Al-Fe alloys. *Materials Science Forum*, 550:339–344, 2007.

Sampath, D., Miller, W. S., Van den Broeck, R., and De Smet, P. Microstructural reactions occurring during homogenisation of AA1050 alloy. *Materials Science Forum*, 217:747–752, 1996.

Sande, G. Softening behaviour of selected commercially pure aluminium model alloys. Master's thesis, 2012.

Sandström, R. On Recovery of Dislocations in Subgrains and Subgrain Coalescence. *Acta Metallurgica*, 25:897–904, 1977a.

Sandström, R. Subgrain growth occurring by boundary migration. *Acta Metallurgica*, 25:905–911, 1977b.

Sandström, R., Lehtinen, B., Hedman, E., Groza, I., and Karlsson, S. Subgrain growth in Al and Al-1% Mn during annealing. *Journal of Materials Science*, 13:1229–1242, 1978.

Sarkar, S., Wells, M. A., and Poole, W. J. Softening behaviour of cold rolled continuous cast and ingot cast aluminum alloy AA5754. *Materials Science and Engineering: A*, 421(1–2):276–285, 2004.

Schmidt, S., Nielsen, S. F., Gundlach, C., Margulies, L., Huang, X., and Juul Jensen, D. Watching the growth of bulk grains during recrystallization of deformed metals. *Science*, 305:229–232, 2004.

Schuh, F. and Heimendahl, M. v. Die Ausbildung der Versetzungsstruktur in Aluminium und deren Beziehungen zum Verformungsverhalten (Teil I). *Zeitschrift für Metallkunde*, 65:346–352, 1974.

Schwartz, A. J., Kumar, M., and Adams, B. L. *Electron backscatter diffraction in materials science*. Kluwer Academic, New York, 2000. First edition.

Schwartz, A. J., Kumar, M., Adams, B. L., and Field, D. P. *Electron backscatter diffraction in materials science*. Springer Science + Business Media, New York, 2009. Second edition.

Sha, G., Marceau, R. K. W., Gao, X., Muddle, B. C., and Ringer, S. P. Nanostructure of aluminium alloy 2024: Segregation, clustering and precipitation processes. *Acta Materialia*, 59(4):1659–1670, 2011.

Siebel, G. Einfluß von Eisen- und Siliziumzusätzen auf die Zipfelbildung von Aluminiumblechen. *Zeitschrift für Metallkunde*, 57(7):500–509, 1966.

Sjølstad, K. *Deformation and softening behaviour of commercial AlMn-alloys*. PhD thesis, The Norwegian University of Science and Technology, Trondheim, 2003.

Skjerpe, P. Intermetallic phases formed during DC-casting of an Al-0.25 Wt Pct Fe-0.13 Wt Pct Si alloy. *Metallurgical Transactions A*, 18:189–200, 1987.

Smith, C. J. E. and Dillamore, I. L. Subgrain growth in high-purity iron. *Metal Science*, 4(1):161–167, 1970.

Smith, C. S. Grains, phases, and interphases: an interpretation of microstructure. *Transactions of the Metallurgical Society of AIME*, 175:15–51, 1948.

Sollaci, L. B. and Pereira, M. G. The introduction, methods, results, and discussion (IMRAD) structure: a fifty-year survey. *Journal of the American Medical Association*, 92(3):364–371, 2004.

Somerday, M. and Humphreys, F. J. The Effect of Dispersoids on the Recrystallization Behavior of a High-Purity Al-1.3 Mn Alloy. *Materials Science Forum*, 331–337:703–714, 2000.

Somerday, M. and Humphreys, F. J. Recrystallisation behaviour of supersaturated Al-Mn alloys Part 1 - Al-1.3 wt-% Mn. *Materials Science and Technology*, 19:20–29, 2003a.

Somerday, M. and Humphreys, F. J. Recrystallisation behaviour of supersaturated Al-Mn alloys Part 2 - Al-0.3 wt-% Mn. *Materials Science and Technology*, 19:30–35, 2003b.

Stanford, N., Dunne, D., and Ferry, M. Effect of orientation stability on recrystallization textures of deformed aluminium single crystals. *Materials Science and Engineering: A*, 348(1–2):154–162, 2003.

Stickels, C. A. and Bush, R. H. Precipitation in the System Al0.05 wt pct Fe. *Metallurgical Transactions*, 2:2031–2042, 1971.

Straumal, B. B., Gust, W., Dardinier, L., Hoffmann, J.-L., Sursaeva, V. G., and Shvindlerman, L. S. Abnormal grain growth in Al of different purity. *Materials & Design*, 18(4/6):293–295, 1997.

Sukhopar, O., Kuzmina, M., and Gottstein, G. Investigation of the substructure evolution within grains of different orientations during recrystallization in a commercial Al alloy. *Advanced Materials Research*, 409:71–76, 2012.

Sulonen, M. S. Discontinuous mode of dissolution of a ß phase precipitate into a Cu-Cd solid solutions. *Acta Metallurgica*, 8(10):669–676, 1960.

Suzuki, T., Arai, K., Shiga, M., and Nakamura, Y. Impurity effect on cube texture in pure aluminum foils. *Metallurgical Transactions A*, 16(1):27–36, 1985.

Takata, N., Ikeda, K.-I., Nakashima, H., and Nobuhiro, T. In-situ EBSD analysis of grain boundary migration during recrystallization in pure aluminum foils. *Materials Science Forum*, 558–559:351–356, 2007.

Tangen, S. *Deformation and annealing behaviour of commercial non-heat treatable aluminium alloys*. PhD thesis, The Norwegian University of Science and Technology, Trondheim, 2004.

Tangen, S., Sjølstad, K., Furu, T., and Nes, E. Effect of concurrent precipitation on recrystallization and evolution of the P-texture component in a commercial Al-Mn alloy. *Metallurgical and Materials Transactions A*, 41(11):2970–2983, 2010.

Taylor, G. I. Plastic Strain in Metals. *Japan Institute of Metals*, 62:307–324, 1938.

Tilley, R. *Understanding solids*, page 395. John Wiley & Sons Ltd., Chichester, West Sussex, 2008.

Truszkowski, W., Król, J., and Major, B. Inhomogeneity of rolling texture in fcc metals. *Metallurgical Transactions A*, 11(5):749–758, 1980.

Turnbull, D. Theory of cellular precipitation. *Acta Metallurgica*, 3(1):55–63, 1955.

Vandermeer, R. A. A transient effect in grain-boundary migration during recrystallization in aluminum. *Acta Metallurgica*, 15(3):447–458, 1967.

Vandermeer, R. A. and Juul Jensen, D. Microstructural path and temperature dependence of recrystallization in commercial aluminum. *Acta Materialia*, 49(11):2083–2094, 2001.

Vatne, H. E. *Experimental investigations and modelling of recrystallization in two hot deformed aluminium alloys*. PhD thesis, The Norwegian Institute of Technology, Trondheim, 1995.

Verdier, M., Brechet, Y., and Guyot, P. Recovery of AlMg alloys: flowstress and strain-hardening properties. *Acta Materialia*, 47(1):127–134, 1999.

Wang, W., Helbert, A.-L., Baudin, T., Brisset, F., and Penelle, R. Reinforcement of the Cube texture during recrystallization of a 1050 aluminum alloy partially recrystallized and 10% cold-rolled. *Materials Characterization*, 64: 1–7, 2012.

Winther, G. and Huang, X. Dislocation structures. Part II. Slip system dependence. *Philosophical Magazine*, 87(33):5215–5235, 2007.

Wyon, G. and Marchin, J. M. Formation of etch pits on slip lines in aluminium. *Philosophical Magazine*, 46(381):1119–1122, 1955.

Xing, Q., Huang, X., and Hansen, N. Recovery of heavily cold-rolled aluminum: effect of local texture. *Metallurgical and Materials Transactions A*, 37A:1311–1322, 2006.

Yamamoto, A., Kato, T., and Tsubakino, H. Precipitation in an Al-300 ppm Fe alloy. *Materials transactions*, 45(11):3106–3113, 2004.

Young, C. T., Headley, T. J., and Lytton, J. L. Dislocation substructures formed during the flow stress recovery of high purity aluminum. *Materials Science and Engineering*, 81:391–407, 1986.

Zhang, J., Shu, D., Rao, Q., Sun, B., and Chen, G. Nucleation and growth of high purity aluminum grains in directional solidification bulk sample without electromagnetic stirring. *Transactions of Nonferrous Metals Society of China*, 16(1):1–7, 2006.